FORMATION MECHANISMS AND STRUCTURE OF INTERFACES IN MATERIALS VIA ELECTRON MICROSCOPY TECHNIQUES

by

RENAE N. GANNON

A DISSERTATION

Presented to the Department of Chemistry and Biochemistry
and the Division of Graduate Studies of the University of Oregon
in partial fulfillment of the requirements
for the degree of
Doctor of Philosophy

December 2021

DISSERTATION APPROVAL PAGE

Student: Renae N. Gannon

Title: Formation Mechanisms and Structure of Interfaces in Materials Via Electron Microscopy Techniques

This dissertation has been accepted and approved in partial fulfillment of the requirements for the Doctor of Philosophy degree in the Department of Chemistry and Biochemistry by:

Shannon W. Boettcher	Chairperson
David C. Johnson	Advisor
Amanda Cook-Sneathen	Core Member
Benjamin J. McMorran	Institutional Representative

and

Krista Chronister	Vice Provost for Graduate Studies

Original approval signatures are on file with the University of Oregon Division of Graduate Studies.

Degree awarded December 2021

DISSERTATION ABSTRACT

Renae N. Gannon

Doctor of Philosophy

Department of Chemistry and Biochemistry

December 2021

Title: Formation Mechanisms and Structure of Interfaces in Materials Via Electron Microscopy Techniques

For continued advancement in materials science, a deeper understanding of structure and interfaces is needed. This is true for a wide variety of materials systems and length-scales. This dissertation focuses on exploring the structure and interfaces of layered heterostructures, thin film compounds, and in multiphase systems such as those in battery stacks where interfaces exist between materials from a wide variety of classes. For layered heterostructures and thin film compounds, interface interactions become increasingly important. This dissertation first explores the use of electron microscopy techniques to investigate formation mechanisms and reaction pathways in layered heterostructures and thin compounds from picometer to nanometer length-scales. Next, failure mechanisms, structure, and interfaces were explored using electron microscopy in layered multiphase materials with components generally used in batteries on nanometer to millimeter length-scales.

This dissertation includes previously published and unpublished coauthored material.

CURRICULUM VITAE

NAME OF AUTHOR: Renae N. Gannon

GRADUATE AND UNDERGRADUATE SCHOOLS ATTENDED:

University of Oregon, Eugene
Drexel University, Philadelphia, PA

DEGREES AWARDED:

Doctor of Philosophy, Chemistry, 2021, University of Oregon
Master of Science, Applied Physics, 2018, University of Oregon
Bachelor of Science, Materials Science and Engineering, 2017, Drexel University

AREAS OF SPECIAL INTEREST:

Materials Science
Thin Film Synthesis and Characterization
Electron Microscopy

PROFESSIONAL EXPERIENCE:

Research Assistant, D.C. Johnson Research Group, University of Oregon, 2019-2021
Graduate Intern, Nanostructure Physics R&D, Sandia National Laboratories, 2020
R&D Intern, Thermo Fisher Scientific, 2018-2019
Research Aide, Argonne National Laboratory, 2015-2016

GRANTS, AWARDS, AND HONORS:

Knight Campus Transitioning Scholars Fellowship, University of Oregon, 2020

PUBLICATIONS:

Gannon, R. N.; Hamann, D. M.; Ditto, J.; Mitchson, G.; Bauers, S. R.; R. Merrill, D.; Medlin, D. L.; Johnson, D. C. Defects in Layered van Der Waals Heterostructures: Implications for Thermoelectrics. *ACS Appl. Nano Mater.* **2021**.

Choffel, M. A.; Gannon, R. N.; Göhler, F.; Miller, A. M.; Medlin, D. L.; Seyller, T.; Johnson, D. C. (2021). Synthesis and Electrical Properties of a New Compound $(BiSe)_{0.97}(Bi_2Se_3)_{1.26}(BiSe)_{0.97}(MoSe_2)$ Containing Metallic 1T-MoSe2. *Chemistry of Materials*. **2021**.

Jungjohann, K. L.; Gannon, R. N.; Goriparti, S.; Randolph, S. J.; Merrill, L. C.; Johnson, D. C.; Zavadil, K. R.; Harris, S. J.; Harrison, K. L. Cryogenic Laser Ablation Reveals Short-Circuit Mechanism in Lithium Metal Batteries. *ACS Energy Lett.* **2021**, *6*, 2138–2144.

Bardgett, D.; Gannon, R. N.; Hamann, D. M.; Roberts, D. M.; Bauers, S. R.; Lu, P.; Johnson, D. C. Understanding the Reactions Between Fe and Se Binary Diffusion Couples. *Chem. Mater.* **2021**.

Cordova, D. L. M.; Fender, S. S.; Hooshmand, M. S.; Buchanan, M. R.; Davis, J.; Kam, T. M.; Gannon, R. N.; Fischer, R.; Lu, P.; Hanken, B. E. The Instability of Monolayer-Thick PbSe on VSe2. *Chem. Mater.* **2020**, *32* (18), 7992–8003.

Mesoza Cordova, D. L.; Kam, T. M.; Gannon, R. N.; Lu, P.; Johnson, D. C. Controlling the Self-Assembly of New Metastable Tin Vanadium Selenides Using Composition and Nanoarchitecture of Precursors. *J. Am. Chem. Soc.* **2020**, *142* (30), 13145–13154.

Randolph, S. J.; Filevich, J.; Botman, A.; Gannon, R.; Rue, C.; Straw, M. In Situ Femtosecond Pulse Laser Ablation for Large Volume 3D Analysis in Scanning Electron Microscope Systems. *J. Vac. Sci. Technol. B, Nanotechnol. Microelectron. Mater. Process. Meas. Phenom.* **2018**, *36* (6), 06JB01.

Everett, W.; Ade, P. A. R.; Ahmed, Z.; Anderson, A. J.; Austermann, J. E.; Avva, J. S.; Thakur, R. B.; Bender, A. N.; Benson, B. A.; Carlstrom, J. E.; others. Design and Bolometer Characterization of the Spt-3g First-Year Focal Plane. *J. Low Temp. Phys.* **2018**, *193* (5), 1085–1093.

Pan, Z.; Ade, P.; Ahmed, Z.; Adam, A.; Austermann, J.; Avva, J.; Thakur, R. B.; Amy, B.; Benson, B.; Carlstrom, J. Optical Characterization of the SPT-3G Focal Plane. *arXiv Prepr. arXiv1805.03219* **2018**.

Avva, J. S.; Ade, P. A. R.; Ahmed, Z.; Anderson, A. J.; Austermann, J. E.; Thakur, R. B.; Barron, D.; Bender, A. N.; Benson, B. A.; Carlstrom, J. E.; others. Design and Assembly of SPT-3G Cold Readout Hardware. *J. Low Temp. Phys.* **2018**, *193* (3), 547–555.

Posada, C. M.; Ade, P. A. R.; Ahmed, Z.; Anderson, A. J.; Austermann, J. E.; Avva, J. S.; Thakur, R. B.; Bender, A. N.; Benson, B. A.; Carlstrom, J. E.; others. Fabrication of Detector Arrays for the SPT-3G Receiver. *J. Low Temp. Phys.* **2018**, *193* (5), 703–711.

Anderson, A. J.; Ade, P. A. R.; Ahmed, Z.; Austermann, J. E.; Avva, J. S.; Barry, P. S.; Thakur, R. B.; Bender, A. N.; Benson, B. A.; Bleem, L. E.; others. Spt-3g: A Multichroic Receiver for the South Pole Telescope. *J. Low Temp. Phys.* **2018**, *193* (5), 1057–1065.

Pan, Z.; Ade, P. A. R.; Ahmed, Z.; Anderson, A. J.; Austermann, J. E.; Avva, J. S.; Thakur, R. B.; Bender, A. N.; Benson, B. A.; Carlstrom, J. E.; others. Optical Characterization of the SPT-3G Camera. *J. Low Temp. Phys.* **2018**, *193* (3), 305–313.

Ding, J.; Ade, P. A. R.; Ahmed, Z.; Anderson, A. J.; Austermann, J. E.; Avva, J. S.; Thakur, R. B.; Bender, A. N.; Benson, B. A.; Carlstrom, J. E.; others. Thermal Links and Microstrip Transmission Lines in Spt-3g Bolometers. *J. Low Temp. Phys.* **2018**, *193* (5), 712–719.

Yefremenko, V.; Ade, P. A. R.; Ahmed, Z.; Anderson, A. J.; Austermann, J. E.; Avva, J. S.; Thakur, R. B.; Bender, A. N.; Benson, B. A.; Carlstrom, J. E. Impact of Electrical Contacts Design and Materials on the Stability of Ti Superconducting Transition Shape. *J. Low Temp. Phys.* **2018**, *193* (5), 732–738.

Carter, F. W.; Ade, P. A. R.; Ahmed, Z.; Anderson, A. J.; Austermann, J. E.; Avva, J. S.; Thakur, R. B.; Bender, A. N.; Benson, B. A.; Carlstrom, J. E.; others. Tuning SPT-3G Transition-Edge-Sensor Electrical Properties with a Four-Layer Ti--Au--Ti--Au Thin-Film Stack. *J. Low Temp. Phys.* **2018**, *193* (5), 695–702.

Ding, J.; Ade, P. A. R.; Anderson, A. J.; Avva, J.; Ahmed, Z.; Arnold, K.; Austermann, J. E.; Bender, A. N.; Benson, B. A.; Bleem, L. E.; others. Optimization of Transition Edge Sensor Arrays for Cosmic Microwave Background Observations with the South Pole Telescope. *IEEE Trans. Appl. Supercond.* **2016**, *27* (4), 1–4.

Posada, C. M.; Ade, P. A. R.; Anderson, A. J.; Avva, J.; Ahmed, Z.; Arnold, K. *Photonics*, **2016**; Vol. 9914, p 991417.

ACKNOWLEDGMENTS

I owe thanks to many people that I've encountered during my time at the University of Oregon. I would like to express sincere gratitude to all of the researchers whose collaborations have made this work possible. I owe a deep sense of appreciation and thanks my advisor, Professor David C. Johnson. I am grateful for your willingness to accept me into your group, and all of your guidance, advice, and motivation to help me be successful. I would like to express special thanks to of my colleagues past and present – Dr. Danielle Hamann, Marisa Choffel, Aaron Miller, and Mellie Lemon. Thank you all for your support and encouragement, this would not be possible without you. To the latest additions to the DCJ lab - Fischer Harvel, Hannah Hazel, and Sarah Rich, thank you for your support, I have thoroughly enjoyed working alongside each of you can am excited to see your continued success. A special thanks to undergraduate students who I've had the honor working alongside – Dylan Bardgett, Shannon Fender, Taryn Kam, and Jordan Joke. Your passion and motivation is inspiring. To all previous DCJ lab members – thank you for your hard work to lay the foundation for us to build from.

Funding for this work was supported in part by the U.S. Department of Energy (DOE), Office of Science, Basic Energy Sciences (BES) under Award #DE-SC0020095.

I have had the honor of working with incredible collaborators nationally and internationally. I owe thanks to Dr. Douglas Medlin and Dr. Ping Lu for assistance with microscopy experiments, guidance, and contributions to this work. Special thanks to Dr. Katherine Jungjohann for continued collaboration on such exciting work and for providing me with the opportunity to work as a research intern with Sandia National Laboratories, albeit remotely during the pandemic, I am eternally grateful! Warm thanks to my past group

at Thermo Fisher Scientific during my Master's internship. You sparked my passion for microscopy. Special thanks to Steven Randolph for mentorship during my Master's degree and continued collaboration during my dissertation. Your encouragement to pursue a Ph.D. was a huge factor in my decision. I owe sincere gratitude to Dr. Lorenz Kienle and his entire Synthesis and Real Structure Group for providing me with the opportunity to do research abroad collaborate and learn from such a talented group. Special thanks to Dr. Niklas Wolff, Dr. Ulrich Schürmann, and Christin Szillus for guidance and assistance with experiments during my time in Germany.

Thank you to all of the Knight Campus Internship, formerly Master's Industrial Internship Program, staff for continued support throughout my time at University of Oregon. I am grateful to each and every one of you for advice, guidance, and for lending an ear when it was needed most (especially Lynde Ritzow, I am forever grateful the support. You've been a lifesaver!).

Thank you to CAMCOR and the UO machine shop for your extensive knowledge and support. Special thanks to Steve Wiemholt for sharing your extensive knowledge and expertise and guidance in troubleshooting and fixing equipment.

To all of my past professors, research advisors, and post-doctoral mentors, thank you for helping shape me into the scientist I am today.

Thank you to my committee members for your time, patience, and wisdom. Thanks to the Department of Chemistry and Faculty for support and guidance.

Finally, I would like to thank my parents, family, my brother (and best friend), friends, and especially my fiancé Andrew. All your love and support has made this possible and helped me to continue forward when I thought I could not.

To Andrew, for always believing in me.

TABLE OF CONTENTS

LIST OF FIGURES

Figure

Page

Figure Page

Figure Page

LIST OF TABLES

Table Page

CHAPTER I

INTRODUCTION

1.0. AUTHORSHIP STATEMENT

This chapter was written for this work alone and will not be published elsewhere. David C. Johnson is my advisor and consulted in the preparation of this chapter. I am the primary author.

1.1. OVERVIEW

As advancements in materials innovation progress, subsequent advances in characterization techniques and analysis is needed. Obtaining useful and accurate in structural and interfacial information in materials is critical to overcoming challenges which prohibit implementation in devices. This is particularly important when considering the emergent low-dimension materials. This dissertation utilizes and proposes electron microscopy techniques which combine characterization techniques to understand critical formation mechanisms and interface structures in materials on picometer to millimeter length-scales. These methods are applied to several materials systems with a wide variety of applications, including layered heterostructures, thin film compounds, and multilayer stacks containing multiphase materials in battery components. For context, this chapter will provide brief introductions to these different materials systems and why they are of interest.

1.2. LAYERED HETEROSTRUCTURES

The foundation of materials science is to understand processing-structure-properties relationships - the materials paradigm. Recently, there has been a great effort to develop novel 2D materials and heterostructures to achieve unprecedented properties[1–3], but the investigation of processing-structure-properties relationships is only beginning. The most commonly used method for preparing 2D materials is mechanical exfoliation (scotch-tape method) where the size of monolayers is ~ 5μm.[4,5] Alternative approaches, such as MOCVD, are being developed to produce wafer-scale materials, however it is challenging to completely cover a surface with unit cell control of thickness.[6] Typically, a suitable substrate for epitaxy and finely controlled growth conditions are required to ensure lateral growth of domains to produce nearly continuous sheets. Controlling defect densities has proven to be challenging in these methods as there are many factors such as processing conditions and misorientation angle between domains.

Understanding the processing-structure-properties relationship becomes more complicated when considering heterostructures that consist of two or more of these atomically thin materials. Controlled heterostructure formation is in even earlier stages. Defects are not well understood, characterized with respect to types, or investigated with respect to their impact on properties. When considering the implementation of these materials into devices, which is the ultimate goal, it is critical to control defect concentrations that impact desired properties. Defects such as grain boundaries, vacancies, twin boundaries and substitutions will impact electronic and optoelectronic performance of these materials differently. Gaining insight into the self-assembly process and formation mechanisms of

defects in 2D materials and heterostructures is necessary to help elucidate the materials processing-structure-properties relationship.

This work used a wafer-scale, low temperature solid state synthesis route called Modulated Elemental Reactants (MER) to synthesize layered heterostructures.[7,8] MER involves the repeated deposition of a sequence of elemental layers to create a precursor with the nanoarchitecture of a targeted A_mB_n heterostructure. The precursors are annealed at low-temperatures to self-assemble the targeted metastable products. The final configuration depends on the structure and composition of the precursor, and the processing conditions. The idea is that the annealing temperatures are high enough for the atoms to move short distances to decrease their free energy, resulting in a metastable product which is a local minimum in the energy landscape. The temperatures need to be low enough that the atoms cannot move large distances and rearrange into the thermodynamic products.

1.3. THIN FILM COMPOUNDS

A growing demand for new materials to drive technological advancement has sparked projects such as the Materials Genome Initiative.[9,10] This initiative and its core programs such as the Materials Project[11] aim to streamline efforts in the prediction, screening, synthesis, and characterization of new compounds. A lack of understanding of how solid state reactions proceed has posed significant challenges to researchers attempting to synthesize theoretically stable compounds.[12,13] Traditional solid state synthesis is generally limited to thermodynamic products due to this lack of understanding how to precisely control composition, reaction pathways, and structure. In an attempt to direct systems to

specific metastable compounds rather than thermodynamic products, including those that are predicted to be theoretically stable, it is necessary to determine what atomic arrangement is needed in a precursor and what processing conditions are required to drive the system to the desired compound. One major consideration in developing this understanding is the ability to develop advanced characterization techniques and approaches to gain insight into formation mechanisms and structures in solid-state synthesis.

A recent report predicted and attempted to synthesize 24 candidate ternary transition metal selenides and sulfides materials which were predicted to be stable.[14] Experimental attempts to synthesize these ternary phases resulted only in the formation of binary phases. Molecular beam epitaxy was used to attempt the synthesis of three ternary Pb-Fe-Se compounds ($PbFe_2Se_3$, Pb_2FeSe_3, Pb_2FeSe_4). Samples characterized with X-ray diffraction suggested that only PbSe and Fe_3Se_4 formed. Given that we general synthesize transition metal selenides with MER, this work focuses on compounds containing Pb, Fe, and Se. An advantage to the MER approach is that it provides the ability to vary the precursor structure, layer thicknesses, composition, and processing conditions. Reactions at solid-solid interfaces and determination of whether or not predicted phases form can be investigated with experimental probes such as X-ray reflectivity, diffraction, and fluorescence, however these do not provide details into local structural or interface information. Experimental approaches which can elucidate necessary information to carefully follow solid-state reactions is critical to developing informed synthetic strategies for predicted compounds.

1.4. MULTILAYER AND MULTIPHASE MATERIALS SYSTEMS

Previous sections discussed the importance of the ability to investigate atomic to nanometer length-scale structural and interfacial information, however it is important to consider applications where materials beyond the thin film limit are implemented. Batteries are a perfect example of a system that typically combine nanometer and beyond length-scale features, which are generally comprised of multiple classes of materials and phases. For instance, consider a coin (or button) cell battery. Generally coin cells contain metal current collectors such as Al or Cu, liquid electrolyte, anode materials such as Li or Zn, and a separator made out materials such as a polymer Celgard membrane.[15] These active components are generally encased by hundreds of micrometers of hard materials such as stainless steel.

These interfaces and component morphologies play a critical role in performance.[16] In recent years, Li-ion and Li-metal batteries have been the subject of extensive research to in an effort to further advance energy storage.[17] Characterization techniques often require the disassembly of battery components to study interfaces and individual regions of interest. Methods that do not require disassembly often do not have the resolution to resolve small scale features that may contribute to failure or challenges with performance.[18] Advanced techniques to access full stacks of active components in their native state would bridge the gap between understanding of electrochemical performance and component structural and interfacial information.

1.5. DISSERTATION OVERVIEW

New approaches and strategies for materials characterization using a combination of electron microscopy and X-ray techniques are discussed throughout this work. Formation mechanisms and interface structures are resolved using these approaches on layered heterostructure materials, thin film compounds, and in multilayer systems containing multiphase materials on picometer to millimeter length-scales.

The first section is comprised of Chapters I and II, which focuses on an introduction and overview to the topics and materials discussed in this work, in addition to general experimental methods used in subsequent sections.

The next section, which includes Chapters III – VII, focuses on the use of electron microscopy techniques to gain insight into formation mechanisms of various layered heterostructures prepared with Modulated Elemental Reactants. Chapter III was published in *ACS Applied Materials and Interfaces* in 2021. Coauthors Danielle M. Hamann, Sage R. Bauers, and Devin R. Merrill synthesized heterostructures. Jeffrey Ditto, Gavin Mitchson, and Douglas L. Medlin collected electron microscopy data. Professor David C. Johnson is my adviser, and I am the primary author of the manuscript. This chapter proposes formation mechanisms for crystallographic defects as a function of layer constituent thickness in $([SnSe]_{1+\delta})_m(TiSe_2)_n$. This is the first exhaustive survey of defects in cross-sections of non-epitaxial heterostructures. Mechanisms proposed in this manuscript have influenced the approach and analysis to all chapters in this dissertation where thin film compounds and heterostructures were synthesized.

Chapter IV is under preparation for submission to the *Journal of the American Chemical Society*. Coauthor Marisa Choffel assisted with synthesis of compounds. Douglas L. Medlin

assisted with collection of electron microscopy data. Professor David C. Johnson is my adviser, and I am the primary author of the manuscript. This chapter tests proposed formation mechanisms discusses in Chapter III. Specific defect types were formed in $(PbSe)_1(MoSe_2)_1$ by controlling local composition in the middle of the film, providing confirmation of proposed formation mechanisms and further insight into the self-assembly mechanisms in compounds prepared with Modulated Elemental Reactants.

Chapter V was published in *ACS Chemistry of Materials* in 2021. Primary author Marisa Choffel synthesized and characterized compounds containing BiSe, Bi2Se3, and MoSe2 with X-ray diffraction, reflectivity, and fluorescence. Co-author Aaron M. Miller assisted with synthesis. Co-authors Fabian Göhler and Professor Thomas Seyller performed XPS measurements and analysis. Professor David C. Johnson is my advisor. I prepared TEM specimens, collected and analyzed HAADF-STEM/EDS data, wrote experimental and discussion sections for microscopy data, and edited the manuscript. This chapter discusses the requirements for precursor structure and composition to form a new compound $(BiSe)_{0.97}(Bi_2Se_3)_{1.26}(BiSe)_{0.97}(MoSe_2)$. HAADF-STEM/EDS confirmed the nanoarchitecture of the compound and presence of both MoSe2 polymorphs.

Chapter VI was published in the *Journal of the American Chemical Society* in 2020. Primary author Dmitri Cordova and co-author Taryn Kam prepared heterostructures and characterized samples with X-ray techniques. Ping Lu assisted with collection of HAADF-STEM/EDS data. David C. Johnson is my advisor. I prepared TEM specimen for HAADF-STEM and assisted with writing/analyzing data for sections pertaining to HAADF-STEM/EDS, in addition to editing the entire manuscript. This chapter discusses how

precisely controlling the number of atoms and nanoarchitecture elemental precursors enabled the selective synthesis of two closely related metastable tin vanadium selenides. This expands on the prior chapters, elaborating further on the impacts of nanoarchitecture and local composition on the formation of new compounds. HAADF-STEM data confirmed the nanoarchitecture of the $[(SnSe_2)_{0.80}]_1(VSe_2)_1$ sample and revealed small grain sizes likely attributed to large lattice mismatch and weak interaction between constituents. In addition, this chapter discusses the formation of VSe2 which is a constituent discussed in later chapters.

Chapter VII was published in *ACS Chemistry of Materials* in 2020. Primary author Dmitri Cordova and co-authors Shannon Fender, Mina Buchanan, and Taryn Kam prepared heterostructures and analyzed samples with various X-ray techniques. Co-authors Joshua Davis, Benjamin Hanken, and Mark Asta performed computational experiments. Robert Fisher and Ping Lu assisted with collection of HAADF-STEM/EDS data. David Johnson is my advisor. I prepared TEM specimen of all samples, assisted with HAADF-STEM/EDS data collection, analysis, and writing pertaining to those sections, in addition to editing the manuscript. This work includes compounds (PbSe, VSe_2) which will be discussed in later chapters of this dissertation. The number of PbSe monolayers was varied to target a variety of $[(PbSe)_{1+\delta}]_q(VSe_2)_1$ compounds. It was found that q = 1, 3, 5 PbSe monolayers was unstable, and would undergo significant rearrangement, which was evident via HAADF-STEM. All q = even and odd ≥ 7 PbSe monolayers were kinetically stable. These results were important to consider for later chapters where compounds containing PbSe and VSe_2 are discussed.

The third section, which includes Chapters VIII – XII, focuses on the use of electron microscopy techniques and X-ray characterization methods to understand reaction pathways in compounds that contain Pb, Fe, and Se. Chapter VIII was published in *ACS Chemistry of Materials* (doi.org/10.1021/acs.chemmater.1c00303). Primary author Dylan Bardgett and co-authors Danielle Hamann and Dennice Roberts prepared thin modulated Fe and Se precursors, collected and analyzed XRD, XRF, and XRR data. Ping Lu collected HAADF-STEM/EDS data. Sage Bauers edited the entire manscript. David Johnson is my advisor. I assisted with writing and editing the entire manuscript, prepared TEM specimen, and analyzed data from X-ray techniques and HAADF-STEM/EDS. This manuscript discusses the reaction of thin modulated Fe-Se precursors as a function of composition and annealing temperature, in contrast to thick precursors studied in Chapter VIII.

Chapter IX is under preparation for submission to *ACS Inorganic Chemistry*. Co-author Danielle Hamann assisted with deposition of precursors. Dylan Bardgett assisted with collection and analysis of XRD, XRR, and XRF data. David Johnson is my advisor. Ping Lu, Niklas Wolff, and Andriy Lotnyk collected HAADF-STEM/EDS data. I am the primary author of this manuscript, and prepared precursors, TEM specimen, analyzed HAADF-STEM/EDS data, and collected and analyzed XRD, XRR, XRF data as a function of annealing temperature. This chapter discusses the reaction of thick binary Fe and Se layers. It was found that when Se is deposited on Fe, a small interfacial reaction occurs but layers primarily remain elemental. When Fe is deposited on Se, samples completely react to form various Fe-Se phases depending on the composition.

Chapter X is under preparation for submission to *ACS Applied Electronic Materials*. Co-author Marisa Choffel prepared precursors containing PbSe and $MoSe_2$. Marisa Choffel and Hannah Hamovitz collected XRD, XRR, and XRF as a function of annealing for PbSe and $MoSe_2$ precursors. David Johnson is my advisor. Niklas Wolff and Andriy Lotnyk collected and assisted with analysis of HAADF-STEM/EDS data. I am the primary author of this manuscript and prepared thick PbSe and thin modulated PbSe and PbSe-VSe_2 precursors, TEM specimen, and collected XRD, XRR, and XRF data. This manuscript discusses the reaction of PbSe on various substrates (Si/SiO2, $MoSe_2$, and VSe_2) and the formation of crystallographically aligned PbSe upon deposition.

Chapter XI contains work that will be submitted to *ACS Chemistry of Materials*. Co-authors Dylan Bardgett prepared precursors containing Pb, Fe, and Se. Dylan Bardgett, Mellie Lemon, and Fischer Harvel collected XRD, XRR, and XRF data. Sven Rudin performed DFT calculations. David Johnson is my advisor. I am the primary author of this work and prepared precursors and collected/analyzed XRD, XRR, and XRF. This work discusses the reaction of Pb, Fe, and Se in modulated precursors with various layering schemes and compositions, building off of Chapters VII-X. A novel PbSe-$FeSe_2$ compound was formed, where $FeSe_2$ formed a hexagonal unit cell at low temperatures.

Chapter XII contains work that will be submitted to the *Journal of the American Chemical Society*. Mellie Lemon will be the primary author of the manuscript. Co-authors Dylan Bardgett and Fischer Harvel assisted with preparation of precursors and collection/analysis of XRD, XRR, and XRF data. Ping Lu collected HAADF-STEM/EDS data. David Johnson is my advisor. I prepared TEM specimen and analyzed HAADF-

STEM/EDS data. I wrote the results and discussion for samples with PbSe and Fe-doped VSe_2 and developed a methodology to use EDS data to determine atomic plane positions. This work discusses modulated precursors containing PbSe, VSe2, and Fe. Fe was found to be substituted and intercalated into VSe2, evident from EDS data.

The fourth section focuses on electron microscopy techniques used to investigate multiphase materials used in coin cell battery components. Chapter XIII contains work that will be submitted to *Microscopy and Microanalysis*. Co-authors Katherine L. Jungjohann, Katherine L. Harrison, and Laura C. Merrill prepared half-cell Li metal batteries. Steven Randolph assisted with collection of cryogenic laser ablation/PFIB/SEM data and experimental design. David Johnson is my advisor. I am the primary author of the manuscript, and assisted with experimental design and collection of cryogenic laser ablation/PFIB/SEM data. This work discusses the methodology and impact of various laser ablation parameters on interfaces in multiphase materials (half-cell Li metal batteries).

Chapter XIV was published in *ACS Energy Letters* in 2021. Katherine Jungjohann is the primary author of the manuscript. Co-authors Subrahmanyam Goriparti, Laura C. Merrill, Kevin R. Zavadil, Stephen J. Harris, and Katharine L. Harrison prepared half-cell Li metal batteries and collected/analyzed electrochemical data. Steven J. Randolph assisted with cryogenic laser ablation/SEM. David Johnson is my advisor and edited the manuscript. I assisted with writing/editing the manuscript and collecting/analyzing cryogenic laser ablation/SEM data. Using the methodology discussed in Chapter XIII, cross-sections of Li metal batteries cycled at different rates/different number of cycles were obtained. New failure modes were observed.

1.6. BRIDGE

Chapter 1 provided a general overview of the dissertation and the materials systems investigated in this work. The next chapter will focus on the experimental methods used to synthesize and characterize the materials discussed in Chapter 1.

CHAPTER II

EXPERIMENTAL PROCEDURES

2.0. AUTHORSHIP STATEMENT

This chapter was written for this work alone and will not be published elsewhere. David C. Johnson is my advisor and consulted in the preparation of this chapter. I am the primary author. This chapter discusses general experimental methods used throughout this work.

2.1. SYNTHESIS OF LAYERED HETEROSTRUCTURES AND THIN FILM COMPOUNDS

In typical solid-state chemistry, long reaction times and high temperatures result in thermodynamically stable products. The reaction steps involved in this process include interdiffusion, nucleation, and growth. Overcoming the barrier for nucleation is necessary to initiate crystal growth. Crystal growth involves atoms diffusing to specific sites on a developing crystal. The more bonds the atoms make with the growing crystal, the more stable and less mobile they are. Hence corner sites are more stable than edge sites, which are more stable that atoms on a surface. Ideally atoms have enough energy and time to find the most stable sites on the surface of the growing crystal.

Recently, an alternative, low temperature solid state synthesis route, called Modulated Elemental Reactants (MER), was developed and used to prepare numerous metastable compounds. MER synthesis is not as well understood or studied as traditional solid-state synthesis techniques. The MER method involves the preparation of a precursor

that contains a designed sequence of elemental layers where the number atoms of each layer is chosen to match that required to form a targeted structure. To prepare homologous series of compounds, different sequences of bilayers can be deposited. Typically, the materials prepared via this method are intergrowths of transition metal chalcogenides containing a transition metal dichalcogenide, such as $TiSe_2$, layered with a chalcogenide bilayer that takes on a rock-salt like structure, such as SnSe. An illustration of a pre-cursor that is designed to target a repeating structure of SnSe and $TiSe_2$ can be seen on the left in Figure 2.1. Figure 2.1. highlights a layered elemental precursor where the metal for one constituent is deposited, followed by the number of Se atoms necessary to form the desired compound and the then the metal for the second constituent is deposited followed by its respective number of targeted Se atoms. This sequence is repeated for the desired number of layers of each constituent in the desired layering pattern. When the precursor structure contains the targeted number of atoms with little error, annealing the precursor at a low temperature results in a near diffusionless transformation to form the targeted compound as shown schematically on the right in Figure 2.1.

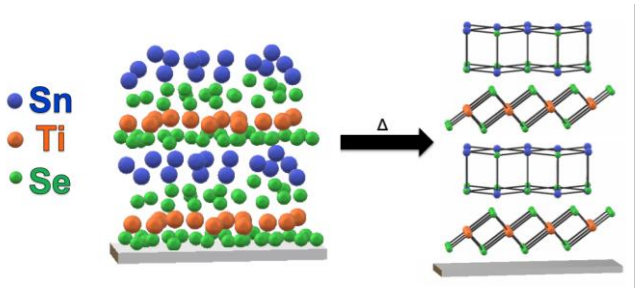

Figure 2.1. Schematic of MER synthesis method.

MER synthesis is done in a high vacuum custom physical vapor deposition system (< 5×10^{-7} Torr). Electron beam guns were used to deposit metals from high purity elemental

sources. A Knudsen effusion cell was used to deposited Se. Pneumatic shutters above each elemental source were controlled via custom LabVIEW software which controlled the deposition sequence and amount of time shutters were open and closed to deposit a desired thickness which was input.[1–3] After the desired thickness of the first element is met, the shutter for the next element opens, and this sequence continues. Quartz crystal microbalances were used to monitor the deposition rate and thickness, where rates at the substrate typically ranged from 0.1 – 0.9 Å/s. A schematic of the deposition system is shown in Figure 2.2. Here an example of an open shutter is shown where a plume of material (purple) is deposited onto the substrate at the top of the chamber. A rotating carousel (blue) holds substrates. Generally, substrates are pieces of single crystal Si wafers with native SiO_2 mounted onto a 6-inch Si support wafer which are mounted via the substrate door.

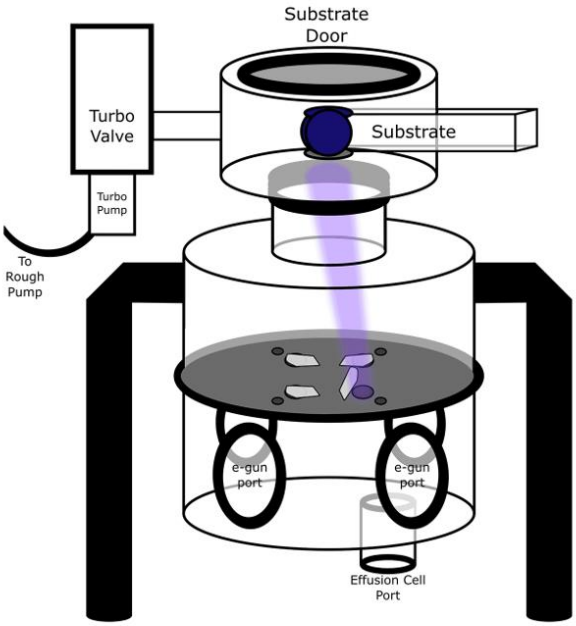

Figure 2.2. Schematic of custom PVD system used for MER.

For layered heterostructures, the amount of material deposited and sequence of elements in the precursor generally targets and mimics that of the desired crystallized heterostructure like that shown in Figure 2.1. discussed previously. For the case of other thin film compounds, a variety of layer thicknesses and sequences since samples did not necessarily target a specific layered heterostructure. Generally, total film thicknesses are ~ 30 nm to ensure there are enough interfaces and material for characterization. The easily programmable nature of layer thicknesses and sequences in this system allows for flexibility in targeted materials and compounds.

Thin film compound and layered heterostructure precursors were annealed on a calibrated hot plate to promote crystallization. In many cases, annealing studies were performed to determine the optimal annealing temperature for the desired compound or heterostructure.

2.2. X-RAY CHARACTERIZATION TECHNIQUES FOR LAYERED HETEROSTRUCTURES AND THIN FILM COMPOUNDS

A combination of X-ray diffraction (XRD), reflectivity (XRR), and fluorescence (XRF) are generally used to characterize all thin film compounds after deposition (AD) and as a function of processing conditions (annealing time and/or temperature). This provides information on the average structural information total composition in layered heterostructures and thin film compounds.

XRD and XRR are useful and powerful techniques which can provide information on average structural information in samples. Both techniques involve an incident beam of X-rays onto a film surface at some angle θ. X-rays with a wavelength λ are diffracted off of

atomic planes in the films, spaced apart by some distance *d*. For constructive interference to occur, Bragg conditions must be met, as described by Bragg's law: $n\lambda = 2d \sin\theta$.[4] The diffraction order *n* is generally equal to 1 for powder XRD. In specular XRD, (00*l*) superlattice reflections are present in well-ordered superlattices aligned to the c-axis of the substrate, such as many of the layered heterostructures discussed in this work. All XRD and XRR patterns in this work were collected on a Bruker D8 Discover (specular XRD, XRR) or a Rigaku Smartlab (in-plane and grazing incidence XRD). Both use Cu Kα X-rays (λ = 1.5406 Å).

In principle, XRR patterns are the result of the interference of partially reflected X-rays from interfaces in samples.[5,6] XRR is useful for determining layer thickness in multilayer films from frequencies of oscillations, or Kiessig fringes. Roughness can be determined by following Parratt equations.[5] Simulations for XRR patterns for multilayer thin film compounds and a layered heterostructure similar to those discussed in this work are shown in Figure 2.3. generated using GenX software.[7] Bilayer Pb|Se films on Si with native SiO_2 are shown in the top plot, where the effect of parameters such a layer thickness, total film thickness, and roughness are demonstrated. For the simulation with roughness, a root mean square roughness (R_q) of 10 Å of roughness was added to the surface of the Pb and Se layers. The bottom plot shows a simulated XRR pattern for a $(PbSe)_1(MoSe_2)_1$ on Si with native SiO_2. Roughness was not included. A Bragg reflection from the repeat unit (RU) thickness or c-lattice parameter of the RU is labeled. where the d-spacing that corresponds to that reflection at $2\theta \approx 7°$ that of 12.57 Å. This is equal to the sum of the c-lattice parameters of the individual constituents, and for experimental patterns is a useful tool to

probe the repeat unit structure. The number of maxima of oscillations or Kiessig fringes (22) before the Bragg reflection plus two is equal to the total number of RU in the sample (24).

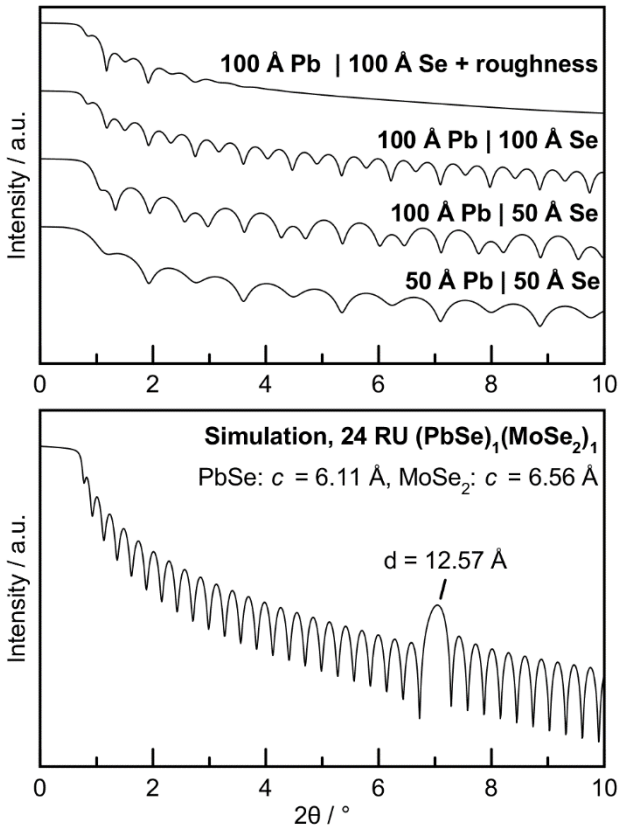

Figure 2.3. Simulated X-ray reflectivity patterns for thin film compounds with Pb and Se layers (top) and a layered (PbSe)1(MoSe2)1 heterostructure.

Specular XRD is particularly useful for layered heterostructures and to determine if preferred orientation or crystallographic alignment to substrates occurs in samples. Superlattice (00*l*) reflections can be used to determine the c-axis lattice parameter for the repeat unit structure in samples that form well-ordered heterostructures, similar to what is seen in Figure 2.3 where the (001) is present in the XRR pattern. In-plane and grazing

incidence XRD were particularly useful for thin film compounds which contained randomly oriented crystallites. It was possible to determine unit cell types and their lattice parameters with in-plane and grazing incidence XRD patterns, which was critical to understanding reaction pathways as a function of annealing temperature.

Lastly, all samples are characterized with X-ray fluorescence to determine the total number of atoms per unit area and composition in thin film compounds and layered heterostructures. In principle, an X-ray beam is directed at the thin film samples and compounds, with enough energy to eject a core shell electron. Outer shell electrons fill the vacancy, and this displacement produces the emission of an X-ray whose wavelength is characteristic to an element since orbital shell spacings are unique to atoms of each individual element. All XRF data was collected on a Rigaku ZSX Primus II wavelength dispersive X-ray fluorescence spectrometer with a rhodium X-ray source. Transitions from the L to K orbital shells is referred to as K_{α}, M to K as K_{β}, M to L as L_{α}, and so forth. Recently, our lab developed a method to quantify XRF in terms of total atoms per unit area for each element, which is described extensively elsewhere.[8] In short, calibration curves for each element (atoms per unit area versus intensity) in this work and used in our lab were developed from crystallographically aligned samples with integral unit cell thickness and a known number of units cells, determined by XRD. The total integrated intensities for each element in each sample is measured and background subtracted based on the samples bare substrate intensities. The ratio of background subtracted intensities (in counts per second) to the slope of calibration curves ([atoms/Å^2]/counts per second) provides us with the total

atoms/Å^2. Use of this method is key to determining deposition parameters and amount of material in samples.

2.3. ELECTRON MICROSCOPY TECHNIQUES

Atomic resolution structural and elemental analysis was performed on select samples throughout this work. While the X-ray characterization techniques in the previous section provided key structural and elemental information for thin film compounds and layered heterostructures, these methods provide a 'global' information. To confirm hypotheses based on results from X-ray characterization methods, particularly in samples where these results are more complex, electron microscopy techniques can access local information to compare to the global picture.

High Angle Annular Dark Field – Transmission Electron Microscopy (HAADF-STEM) was used throughout this work to obtain atomic resolution images of cross-sections of films, which is often used in materials analysis.[9] Simply put, transmission electron microscopy (TEM) involves the acceleration of an electron beam generated from the tip of a high brightness source through a series of electron lenses, which is focused to a small spot on the sample. For STEM, this spot is rastered across the sample (scanning). Electrons interact with and are transmitted through the ultra-thin sample (lamella). HAADF-STEM is used in this work because electrons scattered at high angles, primarily from Rutherford scattering close to the nucleus of atoms in the sample, are collected with an annular dark field detector. Therefore, contrast in images is dependent on atomic number (Z), where higher brightness = higher Z.[10] For many materials in this study, Z dependent contrast is useful for

qualitatively and quantitative analysis of different constituents, particularly in layered heterostructures. HAADFImageJ[11] was generally used for measurement and FFT analysis of HAADF-STEM images.

Achieving atomic resolution requires a specimen whose thickness is typically < 50 nm to allow transmission of electrons through the lamella thickness. Since we are interested in observing cross-sections in our samples, regions (~ 10 μm wide, ~ 2 μm thick) are lifted out of the specimen, mounted to a grid designed for TEM holders, and thinned to thicknesses less 50 nm. This is done in a Scanning Electron Microscope (SEM) using a Focused Ion Beam (FIB). Unlike TEM, SEMs produce images from electron beams which are scanned across and interact the sample surface and penetrate into the sample. Secondary electrons, backscattered electrons, and characteristic X-rays are produced as a result of this interaction, and detectors are used to detect these signals and construct an image.[12] FIBs are most commonly used for removal of material by sputtering with incident ions. Traditionally, Ga^+ liquid-metal ion sources (LMIS) are used in a focused ion beam because the high mass allows for relatively large volume removal in comparison to other sources and good spatial resolution.[13] Like the SEM, images are produced from the production of secondary electrons and ions from the interaction of the incident ion beam with the sample. Material can also be deposited using SEM/FIB assisted chemical vapor deposition.[13]

An overview of the lift-out process for a cross-section TEM specimen is shown in Figure 2.4. which begins with a top-down view in the SEM in the top left image. Protective caps (for this work was Pt or C) are deposited on the film surface using the electron/ion beams to ensure that damage from high energy beams is minimized, and to protect the

surface of the sample for thinning. Material on either side of the protective cap, and from below the sample surface into the Si substrate is removed with the FIB (top right). needle with a fine tip is inserted and positioned on the edge of the specimen. The needle is welded to the edge of the specimen by depositing material with the FIB. Then, the remaining regions where the specimen is still attached to the substrate are removed, leaving only the specimen on the needle. The needle is retracted, and the stage is moved to be positioned Cu TEM grid. The needle is inserted again, and the sample is carefully attached to the top of the Cu post by deposting material with the FIB. After the sample is secure on the grid, the FIB is used to remove material to detach the needle. All lamella in this work was prepared using a Helios Nanolab 600i DualBeam SEM/Ga^+ FIB and mounted onto Cu grids. Final lamella thinning was done with an accelerating voltage of 2 kV, using methods similar to those described in great detail elsewhere.[14] A TEM image of a thinned lamella where a thin film compound was deposited on Si is shown in Figure 2.5. Dark regions on the left and right of the lamella were not thinned, and therefore are not electron transparent. The thin film and Si are electron transparent. Several microscopes were used in this work and are specified in each chapter that includes HAADF-STEM/EDS.

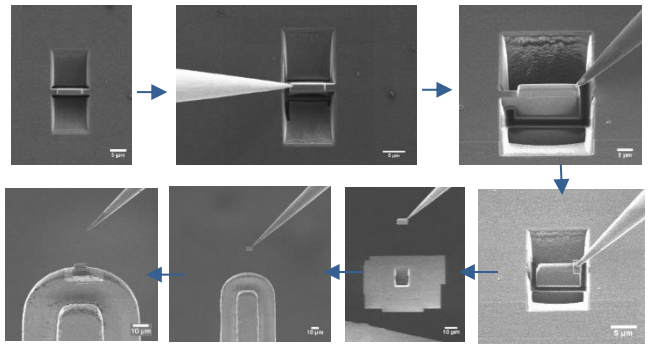

Figure 2.4. Standard lift-out process for cross-section TEM lamella starting from the top left and ending on the bottom left.

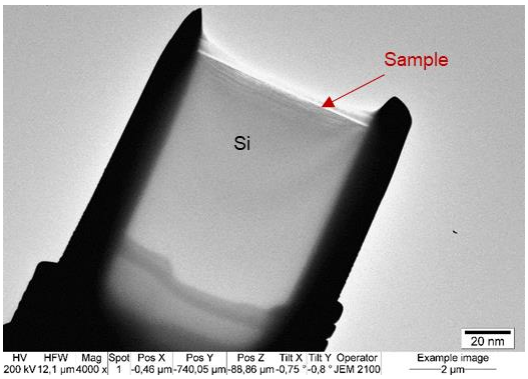

Figure 2.5. Thinned lamella in a TEM where a thin film sample is located at the top region.

Energy dispersive x-ray spectroscopy (EDS) is a technique that can be performed in an SEM or (S)TEM. The working principle of EDS is essentially the same as that of XRF – however an incident electron beam is used rather than an incident X-ray to cause ejection and displacement of core shell electrons. The benefit to EDS is the ability to produce elemental maps or line profiles in a local, specific region of interest where atomic resolution mapping is achievable when done in an (S)TEM.[15]

Lastly, large area and volume analysis was performed on half-cell coin cell batteries that contained stacks of Li metal, Cu current collectors, polymer separators, liquid electrolyte, and solid electrolyte interphase encased in stainless steel. The active region of interest was ~ 200 – 400 µm thick and buried under ~ 250 µm of stainless steel casing and the hundreds of microns, which is inaccessible for traditional SEM/FIB/plasma-FIB. Therfore, a system which combines an ultrafast pulsed laser with a SEM/PFIB was used to access these buried multiphase material stacks on prototype system based on a Helios G3 DualBeam SEM/Xe^+ PFIB.[16–18] Given the presence of liquid electrolyte, the addition of a cryogenic stage to this system was necessary to keep the liquid electrolyte frozen for analysis. An example of a

cross-section obtained on an intact coin cell is shown in Figure 2.6., whichis much larger scale (μm to mm length-scale) than those discussed using previous techniques for thin films. However, nanoscale features can still be resolved in the cross-section. This technique and methods are described in greater detail in Chapter XIII.

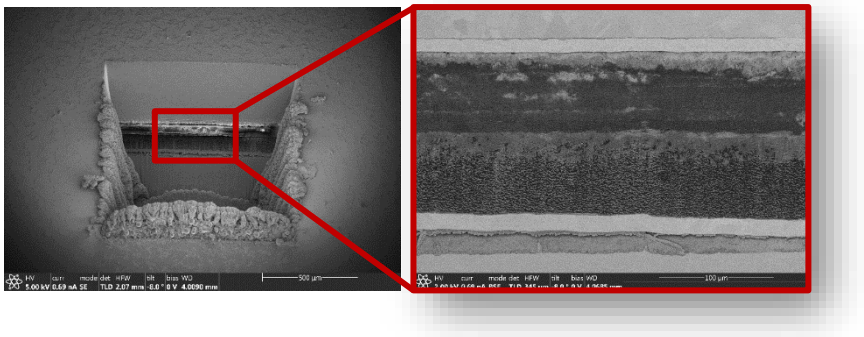

Figure 2.6. Overview SEM image of a cross-section through an intact half-cell coin cell battery where ~ 1 mm3 of material was removed to access the buried stack of components (right). SEM image of a polished stack of components, where large and small scale features and interfaces are resolved.

2.4. BRIDGE

General experimental methods for synthesis and X-ray characterization of layered heterostructures and thin film compounds were discussed in this chapter, in addition to an overview of the electron micrscopy techniques used throughout this dissertation. The next chapter utilizes the synthesis and characterization techniques discussed in this chapter to understanding defects in layered heterostructures. Formation mechanisms for defects analogous to those in standard crystal growth are proposed which provided insights into the overall self-assembly mechanism for the formation of these layered heterostructures and those discussed in future chapters.

CHAPTER III

DEFECTS IN LAYERED VAN DER WAALS HETEROSTRUCTURES: IMPLICATIONS FOR THERMOELECTRICS

3.0. AUTHORSHIP STATEMENT

Chapter III was published in *ACS Applied Materials and Interfaces* in 2021. Coauthors Danielle M. Hamann, Sage R. Bauers, and Devin R. Merrill synthesized heterostructures. Jeffrey Ditto, Gavin Mitchson, and Douglas L. Medlin collected electron microscopy data. Professor David C. Johnson is my adviser, and I am the primary author of the manuscript.

3.1. INTRODUCTION

There has been a great effort in recent years to develop novel 2D materials and heterostructures to achieve unprecedented properties. While graphene, a semimetal, was the first 2D material discovered and widely studied, interest in 2D materials has rapidly expanded to many systems including metals (e.g. VSe_2, $NbSe_2$), semiconductors (e.g. MoS_2, WS_2) and insulators (hBN).[1,2] Combining and stacking these 2D materials into heterostructures provides wider opportunities to achieve tunable and novel properties. These 2D compounds are often held together by out-of-plane van der Waals forces, which are much weaker than the in-plane covalent bonds of the constituent layers (ca. meV vs eV per bond). This enables the 2D compounds to be cleaved and assembled into a myriad nanoarchitectures whereby interlayer coupling results in tunable or emergent behaviors, such as in graphene-hBN systems.[3] The most common methods to prepare van der Waals

heterostructures are through mechanical assembly or via van der Waals epitaxy, however direct growth methods (e.g. CVD) are emerging.

While the library of 2D materials and van der Waals heterostructures grows, substantial efforts to minimize and understand the impact of defects on properties must be made in order to implement them reliably into devices.[1] The effect of defects on properties is exacerbated with reduced dimensionality, and therefore the ability to control defect types and densities is critical. In 2D materials prepared with methods such as mechanical exfoliation or MOCVD, defects such as vacancies, antisites, substitutions, adatoms, and grain boundaries are common.[4,5,6] These defects have been found to impact optical, electronic, and optoelectronic properties.[5,7] While defects in common 2D materials have been studied (e.g. graphene), defects in van der Waals heterostructures are not well understood, characterized with respect to types, or investigated with respect to their impact on properties. The frequency and distribution of these defects is also likely to depend on the thickness of the constituent layers, and the variety of defects is larger for systems with non-epitaxial interfaces. To functionalize such heterostructures, understanding and controlling defects is critical for controlling performance, reliability, and reproducibility.[1]

One of the most studied class of van der Waals layered heterostructures are those that contain transition metal dichalcogenides (TMDs), which are promising candidates for thermoelectric applications.[8] This paper examines defects in TMD-containing SnSe-$TiSe_2$ heterostructures, prepared as non-epitaxial, vertically stacked superlattices to probe the changes in the distribution and frequency of defects as a function of constituent thickness and to gain insight into the defect formation mechanisms. We employ the Modulated

Elemental Reactants (MER) synthesis method, which allows tailored architectures through room temperature layer-by-layer deposition of a precursor, followed by low-temperature annealing that crystallizes the material. The $([SnSe]_{1+\delta})_m(TiSe_2)_n$ system (where $1+\delta$ includes the difference in basal plane area between constituents) was chosen for this investigation since its base-line structure and properties are understood as function of the thickness of the SnSe and $TiSe_2$ layers.[9–14] Grain sizes in the individual layers are typically range between 50 and 200 nm.[9–14] Prior HAADF-STEM observations of the basic $([SnSe]_{1+\delta})_m(TiSe_2)_n$ nanoarchitecture are in excellent agreement with X-ray diffraction, X-ray reflectivity, and X-ray fluorescence measurements. This atomic resolution imaging also reveals a wide variety of defects in the idealized structure, which depend on the thickness of the constituent layers and the processing conditions.

As we discuss in detail here, the defects observed in the $([SnSe]_{1+\delta})_m(TiSe_2)_n$ system are generally analogous to those observed in traditional crystal growth and can be broadly categorized into two groups based on their proposed formation mechanisms. The first category results from the nucleation and subsequent diffusion-limited growth of the constituent layers within the precursor as the heterostructure self-assembles. This category encompasses grain boundaries, antiphase boundaries, and both coherent and incoherent twin boundaries. The second category of defects results from local or global variations in the amount of deposited material. Such spatial variations in the deposition disrupt the overall layering sequence giving perturbations that are analogous to line defects, such as dislocations and disconnections, that are observed in conventional crystalline materials. We propose formation mechanisms for these defects, which will be sensitive to processing parameters.

These insights suggest strategies for controlling the density and spatial location of specific defects, which could enable new approaches for defect-engineered electronic properties.

3.2. EXPERIMENTAL

The heterostructures for this study were prepared using the Modulated Elemental Reactant (MER) method.[15] Specific details concerning the synthesis, structure, and properties of the $([SnSe]_{1+\delta})_1(TiSe_2)_1$ films considered here have been presented previously.[9–14] In short, the MER method is a wafer-scale, low temperature, solid-state synthesis route that involves the repeated deposition of a sequence of elemental layers to create a precursor with the nanoarchitecture and local composition match that of the targeted A_mB_n heterostructure. For example, to synthesize $([SnSe]_{1+\delta})_1(TiSe_2)_1$, a compound containing alternating layers of SnSe and $TiSe_2$, a sequence of Ti|Se|Sn|Se layers is initially deposited by physical vapor deposition. In this sequence, the number of Ti atoms and Se atoms in the Ti|Se bilayer corresponds to the number required to make a single $TiSe_2$ and the number of Sn and Se atoms in a Sn|Se bilayer corresponds to the number of atoms required to make a bilayer of SnSe. The alternating thickness is repeated to get either films of ~ 50 nm or films that have a minimum of 10 repeat units. All samples were deposited onto Si <100> substrates with native SiO_2.

The deposited films are predominantly amorphous, with compositional modulation corresponding to the sequence of deposited layers. There is significant interdiffusion between the deposited layers as the elements react to form amorphous alloys. The structure of the as deposited precursors and their self-assembly into the heterostructures discussed in

this paper are discussed in detail in a sequence of prior publications.[9–14] After deposition of the precursors, the films were annealed at low-temperatures in an inert environment to transform the elemental layers into the targeted, metastable crystalline product. Annealing times and temperatures were low enough to promote short range diffusion, but not high enough to result in the thermodynamic product. The resulting films are single phase with respect to both X-ray diffraction (XRD) and X-ray reflectivity (XRR).

To access local structural information, atomic resolution electron microscopy techniques were used. High Angle Annular Dark Field – Scanning Transmission Electron Microscopy (HAADF-STEM) is used to obtain Z-contrast atomic resolution images of cross-sections of samples collected over several years from several operators using FEI Titan or Themis Z microscopes. Cross-sections with thicknesses < 50 nm were prepared with a Helios 600i DualBeam SEM-FIB using standard lift-out procedures.[16] A protective layer was applied to the surface of the samples using a permanent marker[17] before the use of SEM/FIB, followed by ion beam deposited carbon.

3.3. Results and Discussion

3.3.1. Baseline microstructure: $([SnSe]_{1+\delta})_1(TiSe_2)_1$

We begin by discussing the baseline microstructure in $([SnSe]_{1+\delta})_1(TiSe_2)_1$, which is the simplest of the heterostructures we examined (Figure 3.1). Figure 3.1a illustrates a precursor that targets $([SnSe]_{1+\delta})_1(TiSe_2)_1$, and contains the ideal product consisting of alternating layers of SnSe and $TiSe_2$. Figure 3.1b shows a HAADF-STEM image which confirms that annealing the precursor results in the targeted compound, containing

alternating SnSe bilayers and $TiSe_2$ trilayers (higher and lower intensity) throughout almost the entire film. There are thin (nm) impurity regions at the top and bottom of the film that are distinct from the repeating pattern of SnSe and $TiSe_2$ layers and can result from excess Sn, Ti, or Se, and can form additional compounds such as $SnSe_2$ at the surface.[13] The bottom layer of the film may also contain impurity compounds, such as Ti_2Se or Ti silicides, that form when the initial layer of Ti reacts with the subsequently deposited Se layer or with the substrate during the deposition or annealing processes.[18]

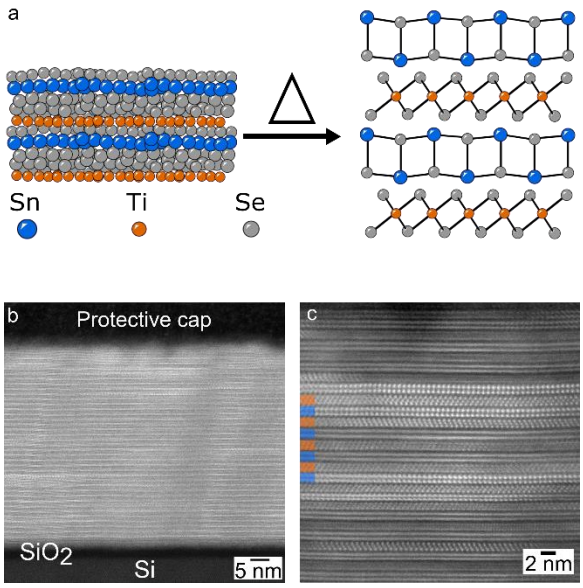

Figure 3.1. a) Schematic of an as-deposited precursor containing Sn, Ti, and Se followed by the final product $([SnSe]_{1+\delta})_1(TiSe_2)_1$. b) HAADF-STEM image of $([SnSe]_{1+\delta})_1(TiSe_2)_1$ showing the substrate (Si and native SiO_2) at the bottom. The sample consists of repeating units of $([SnSe]_{1+\delta})_1(TiSe_2)_1$, indicated by alternating layers of a higher intensity (SnSe) and lower intensity ($TiSe_2$). c) Higher magnification HAADF-STEM image of $([SnSe]_{1+\delta})_1(TiSe_2)_1$, which reflects the ideal product with no defects shown in a) and shows regions on and off zone axes within both constituents. Several SnSe and $TiSe_2$ layers are marked with blue and orange rectangles, respectively. Local crystallographic alignment between SnSe and $TiSe_2$ is also evident in the regions where neighboring layers are both locally oriented along a low-index zone axis.

The majority of the higher magnification image of $([SnSe]_{1+\delta})_1(TiSe_2)_1$ in Figure 3.1c contains the targeted repeating layer sequence which is marked with blue (SnSe) and orange

($TiSe_2$) rectangles to easily identify the difference in constituents for several repeat units. This region contains few obvious defects, despite the low temperature of the annealing (350°C, 30 minutes)[13] to self-assemble. This suggests there must be a significant interaction between the constituents which makes this compound at least a local free energy minimum and that there is an energy penalty to create ensemble defects. Considerable long-range diffusion must occur to eliminate local variations in the number of atoms deposited in each elemental layer in the precursor. The rest of the samples discussed in this paper have low densities of defects, similar to that shown in Figure 3.1b and 3.1c. The rest of this manuscript will focus on specific defects found in the samples, which were typically found by extensive searching of the TEM lamella prepared from each sample.

3.3.2. Rotational/Turbostratic Disorder: Domain boundaries

We begin by discussing the first class of defects we discuss are those resulting from rotational disorder within or between (turbostratic disorder) individual layers of the heterostructure, which can have important consequences for properties and the electronic structure of materials. Rotational disorder is typically random but can be discrete in cases where crystallographic alignment exists between constituents or there are crystallographic faults within a layer. Such rotational disorder has also been observed within single layer films of dichalcogenides in samples grown using vacuum deposition techniques.[19] More disorder is to be expected for heterostructures with lattice mismatch, either between two structures with the same structure but different lattice parameters or between two layers with different structures (for example a square and a hexagonal basal plane).[20] The lattice mismatch inherent between constituents of heterostructures[21] and weak van der Waals

bonding between layers makes it challenging to avoid rotational disorder in the growth of heterostructures. The bonding between constituents containing alternating layers of a rock salt constituent with a dichalcogenide ($([MX]_{1+\delta})_1(TSe_2)_1$, where M = Sn, Pb, Bi and T = Ti, V, Nb, Ta, Cr) is unusual, as the incommensurate structural misfit between constituents results in distribution of bond distances between the atoms at the interfaces.[22] While SnSe (90° angles in the basal plane) and $TiSe_2$ (hexagonal) are symmetrically incommensurate, $([SnSe]_{1+\delta})_1(TiSe_2)_1$ system has a near lattice match between <100> SnSe and <110> $TiSe_2$ [7], which favors a specific orientation between the constituents.

Rotational disorder is readily apparent by the variety of zone axis orientations present throughout the image in atomic resolution image of $([SnSe]_{1+\delta})_1(TiSe_2)_1$ shown in Figure 3.2.

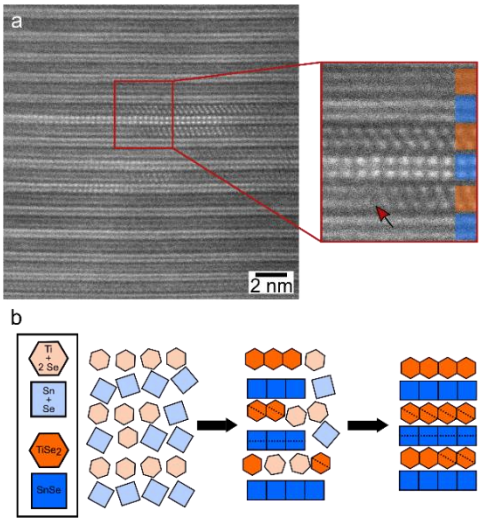

Figure 3.2. a) HAADF-STEM image of $([SnSe]_{1+\delta})_1(TiSe_2)_1$ which shows domain boundaries within layers as a result of turbostratic disorder. The second $TiSe_2$ layer from the bottom of the region highlighted with a red box shows a boundary (marked with an arrow) between 2 orientations within the same layer, illustrating rotational disorder, in addition to neighboring layers which are in different orientations. Several SnSe and $TiSe_2$ layers are marked with blue and orange rectangles, respectively. b) a schematic of the precursor (light shaded squares and hexagons) which represent Sn + Se and Ti

+ 2Se that has not crystallized (left), followed by a partially crystallized compound where nucleation and growth is occurring during annealing (middle). Dark shaded squares and hexagons represent crystallized regions. After annealing, the final turbostratically disordered crystallized compound (right) is illustrated to mimic the region in 2a highlighted in the red box. The dashed lines in the crystallized compound represent orientations of regions of each layer. The square and hexagonal symbols represent the symmetry of the different layers, not the orientation of the symmetry axes, which are perpendicular to the substrate.

We believe that this disorder results from crystallization during the low temperature annealing initiating at numerous nucleation sites with subsequent growth occurring randomly throughout the precursor. The rotational disorder is also likely supported by the weak orientational dependence of bond-strength between layers. The boundaries between these differently oriented domains thus form what is likely the most common type of defect in the MER deposited films. We can distinguish between the boundaries between differently oriented layers and those between differently oriented domains within a given layer (or packet of layers).

To illustrate, consider Figure 3.2, which shows an image of $([SnSe]_{1+\delta})_1(TiSe_2)_1$ from a different region of the same sample shown in Figure 3.1c. The occurrence of single layer grain boundaries in different positions in different layer further supports the idea that the crystallization from the precursor is initiating at multiple nucleation sites. An example of a grain boundary within a layer of $TiSe_2$ is shown in Figure 3.2 and marked with an arrow. The SnSe layers above and below do not have grain boundaries at the same location, suggesting that the growth of the two constituents is not interconnected or concurrent. The rotational disorder between constituents also implies that the energy difference between different orientations of neighboring layers is small. This lack of epitaxy between constituents results in different relative orientations of the constituents having different distributions of bond distances, which have similar energies as the average bond distance does not change

significantly. The interaction between the constituent layers must be strong, however, as many misfit layer compounds are thermodynamically more stable than a mixture of the constituent binary compounds.[22] This has been previously discussed in the literature, where both covalent and ionic bonding, in addition to van der Waals forces are suggested to explain the unusual stability of misfit layer compounds.[23] The accidental near lattice match in the $([SnSe]_{1+\delta})_1(TiSe_2)_1$ sample is unique among the samples investigated herein by having nanoscale regions of long-range order only found for m = 1, n = 1. This can be seen in the regions that are on-axis in Figure 3.2a. It is also apparent in Figure 3.1c by the large number of adjacent on-axis regions within the area shown.

The schematic in Figure 3.2b suggests a mechanism for forming a single layer grain boundary defect through a sequence of intermediate structures. The left side image illustrates the precursor structure with the ideal amount of material. The middle image indicates nucleation sites that form during the deposition or low temperature annealing of the precursor. The nucleation sites in the middle panel likely form in a sequential manner rather than simultaneously, however, for simplicity, only one panel is shown between the precursor and final product. The right image shows the final heterostructure. Light shaded blocks indicate amorphous regions. Dark shaded blocks indicate crystalized regions with the stripe indicating the crystallographic alignment of the domain.

In some cases, however, crystallization of the precursors occurs with orientation relationships between the differently oriented domains, giving for instance twin-related variants or anti-phase boundaries. For instance, a coherent twin boundary is highlighted in Figure 3.3 in the $([SnSe]_{1+\delta})_1(TiSe_2)_2$ system. The region highlighted in Figure 3.3a in the red

box shows two neighboring $TiSe_2$ layers that do not have a twin defect, where both layers have the same orientation. The red box highlighted in Figure 3b shows a region where there is a coherent twin boundary, where a 180° rotation about the [0001] axis exists between the neighboring $TiSe_2$ layers. Figure 3.3c illustrates how this defect may form, showing the transformation of the precursor to the final product for the regions shown in 3.3a and 3.3b. The top schematic in Figure 3.3c represents the region highlighted in Figure 3.3a, where a single nucleation site for $TiSe_2$ exists and both $TiSe_2$ layers grow from this nucleation site. This results in their having the same orientation, as indicated by the direction of the dashed lines. The bottom schematic represents a potential mechanism for the defect formation from the region in Figure 3b. Two different nucleation sites exist in the same layer, with two different orientations, resulting in the coherent twin boundary between the neighboring layers. The orientations of the nucleation sites may be influenced by the adjacent SnSe layers if they form first.

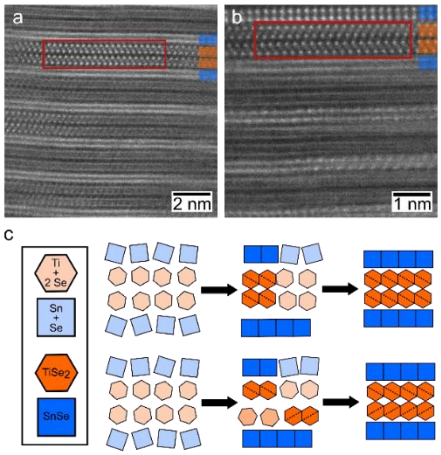

Figure 3.3. a) HAADF-STEM image of $([SnSe]_{1+\delta})_1(TiSe_2)_2$ highlighting a region with a red box of TiSe2 with no stacking defect, where the same grain orientation is observed for both TiSe2 layers. Several SnSe and TiSe2 layers are marked with blue and orange rectangles, respectively. b) HAADF-STEM image of $([SnSe]_{1+\delta})_1(TiSe_2)_2$ highlighting a region with a red box of $TiSe_2$ with a coherent

twin boundary type stacking defect. Here a 180° rotation about the [0001] axis is observed between the $TiSe_2$ layers. c) the top schematic illustrates the precursor (left) with lighter shading to demonstrate the amount of material, followed by the start of nucleation and growth of the precursor (middle) where the solid shapes represent material that is starting to crystallize and self-assemble during annealing. Dashed lines indicate a specific orientation and no dashed line indicates a random orientation, and lastly the final product (right) where the orientation of both $TiSe_2$ layers is the same.

The second defect in $TiSe_2$ is an incoherent twin boundary, which is shown in Figure 3.4 in the $([SnSe]_{1+\delta})_1(TiSe_2)_4$. Figure 3.4a shows a period of the repeating structure where an incoherent twin boundary exists, where the boundary exists within layers rather than between them. Figure 4b shows the region that is highlighted in the red box in 3.4a, where the boundary is marked with red lines.

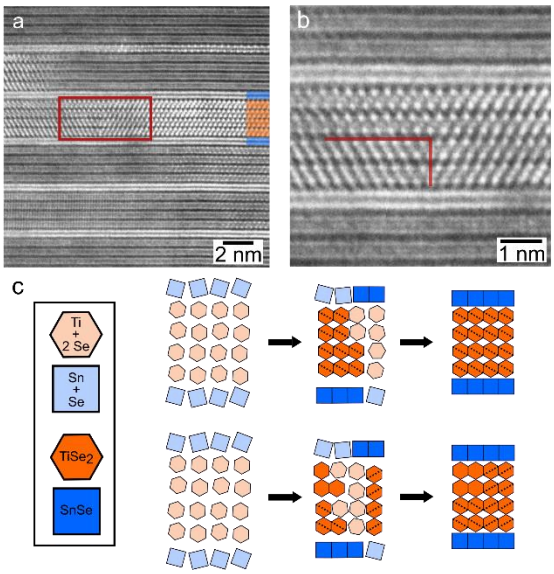

Figure 3.4. a) HAADF-STEM image of $([SnSe]_{1+\delta})_1(TiSe_2)_4$ highlighting a region with a red box of $TiSe_2$ with an incoherent twin boundary type defect. Several SnSe and $TiSe_2$ layers are marked with blue and orange rectangles, respectively. b) higher magnification of the region shown in 5a, which marks the twin boundary with a red line. c) the top schematic illustrates the precursor (left) with lighter shading to demonstrate the amount of material, followed by the start of nucleation and growth of the precursor (middle) where the solid shapes represent material that is starting to crystallize and self-assemble, dashed lines indicate a specific orientation and no dashed line indicates a random orientation, and lastly the final product (right) where the orientation of both $TiSe_2$ layers is the same. On the bottom, the same illustration is made, however 3 separate nucleation sites with different orientations for $TiSe_2$ are shown (middle). The first two $TiSe_2$ layers have a 180° between orientations, resulting in the incoherent twin boundary.

The vertical red line is where the boundary begins within layers where a reversal in the orientation within the two $TiSe_2$ layers is seen. The horizontal line indicates a boundary between neighboring $TiSe_2$ layers where a third orientation in this region of the repeating period is present. Figure 3.4c illustrates a possible growth mechanism that would result in the formation of the incoherent twin boundary. The top schematic depicts a repeating period where a nucleation site exists and has started to grow all 4 layers in the repeating period with the same orientation as indicated by the direction of the dashed lines. The bottom schematic depicts the repeating period shown in Figure 3.4a and 3.4b, where 3 nucleation sites are shown in the middle panel of the schematic. The 2 nucleation sites with dashed lines have the same orientation but mirrored, and the last nucleation site has a different orientation (no dashed line). In the last panel where the final product is shown, the 2 mirrored nucleation sites have grown to create a boundary within the layers.

$([SnSe]_{1+\delta})_1(TiSe_2)_2$ is a known thermodynamically stable compound in the ternary phase diagram. It has been prepared by the solid state reaction method in an evacuated quartz ampule by Song et. al.[24] Song et. al. did not comment specifically on twin boundaries in this compound. Their HRTEM image indicates a common zone axis for both the SnSe and $TiSe_2$ layers.[24] Refinement of the lattice parameters of this compound indicates that the SnSe and $TiSe_2$ layers have distorted such that the *b*- and *c*-axis lattice parameters are common while the a-axis lattice parameter is different.[24] When the $([SnSe]_{1+\delta})_1(TiSe_2)_2$ compound is prepared at low temperatures from designed precursors using the MER method discussed in this work, the structure is distinctly different despite having the same sequence of SnSe and $TiSe_2$ layers. The in-plane structures of the SnSe and $TiSe_2$ layers are

also structurally independent from one another, having different in-plane lattice systems, square and hexagonal respectively.[12] Many different orientations of both the SnSe and $TiSe_2$ layers are found in representative HAADF images, which likely lead to the presence of defects such as twin boundaries. The presence of many twin boundaries in $([SnSe]_{1+\delta})_1(TiSe_2)_2$ suggests that there is only a small energy penalty for their formation and/or they are kinetically stable.

The most common defects observed within SnSe bilayers in the $([SnSe]_{1+\delta})_m(TiSe_2)_n$ system appear to be antiphase boundaries (Figure 3.5). Establishing the formation mechanism is unclear due to complexity in the SnSe system. Bulk SnSe exists in two polymorphs, α-SnSe and β-SnSe. The phase transition from α-SnSe and β-SnSe is second order as there is a continuous displacement of Sn and Se atoms as temperature is varied due to a soft phonon mode.[25,26,27] Both the interaction between $TiSe_2$ and SnSe and changing layer thicknesses modify the phonon modes, impacting the relative stability of the two structures. The stable repeating structure of SnSe bilayers resembles the high temperature SnSe phase (β-SnSe). However, when the SnSe thickness is increased the SnSe structure becomes increasingly more like the low temperature structure (α-SnSe).[28] The consequence of this are local areas that have structures intermediate between the α-SnSe and β-SnSe phases. Identifying which phase is present locally is difficult due to similarities in the structures (Figure A.1). Therefore, we will limit our discussion of defects in the SnSe constituent to the most frequently observed defect. Figure 3.5a shows a region of SnSe that has an antiphase boundary type defect in $([SnSe]_{1+\delta})_3(TiSe_2)_2$, which is highlighted with a red box. Figure 3.5b shows the region highlighted in the red box in 5a, where Sn and Se atoms

are marked with blue and grey circles, respectively. The antiphase boundary defect is shown for layers where neighboring Sn atoms are stacked. Figure 3.5c and 3.5d are similar, except there are 2 antiphase boundaries present, which are located in the middle of the repeating structure in $([SnSe]_{1+\delta})_8(TiSe_2)_2$. One hypothesis for how the boundary could form is that it is a result of formation of the high temperature SnSe phase. Supporting this notion is the observation that the stacking along the [001] direction in the high temperature β-SnSe phase (Figure A.1) is consistent with the stacking at the antiphase boundaries. These layers could be surrounded by either [001] oriented α-SnSe or [100] β-SnSe.

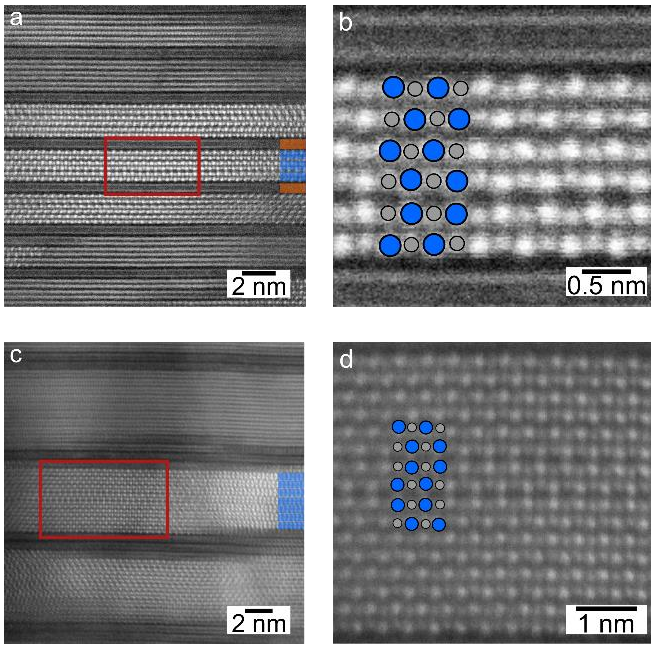

Figure 3.5. HAADF-STEM images of a) A region in $([SnSe]_{1+\delta})_3(TiSe_2)_2$ where an antiphase boundary exists in the SnSe highlighted with the red box. Several SnSe and TiSe2 layers are marked with blue and orange rectangles, respectively. b) higher magnification of the region shown in 5a, where blue and grey circles represent Sn and Se atoms, respectively. The first 2 SnSe bilayers from the bottom have Sn atoms stacked on top of one another, whereas the 3rd bilayer has stacking similar to a rock-salt structure. c) A region in $([SnSe]_{1+\delta})_8(TiSe_2)_2$ where an antiphase boundary exists in the SnSe highlighted with the red box. d) higher magnification of the region shown in 5c. The first 4th through 6th SnSe bilayers from the bottom have Sn atoms stacked on top of one another, all other bilayers have stacking similar to a rock-salt structure.

Finally, we consider a defect that is also a result of multiple nucleation sites but disrupts the overall repeating period. A rotated island in the $([SnSe]_{1+\delta})_1(TiSe_2)_{15}$ sample resulting from a misaligned grain of $TiSe_2$ in the layer adjacent to the substrate is shown in Figure 3.6. Figure 3.6a highlights the domain with a red dashed line, and Figure 3.6b shows this region at higher magnification. Figure 3.6c illustrates a potential formation mechanism for this grain boundary. Only part of the total repeating period is shown, and SnSe is not included for simplicity. The left panel of the schematic shows the precursor with Ti and Se on the Si + native SiO_2 substrate. The middle panel shows potential nucleation sites for this region, where the misaligned grain begins to grow in addition to surrounding nucleation sites that are aligned to the *c*-axis. The right panel depicts the region shown in Figure 3.6a and 3.6b (the number of layers differs from the image for simplicity) where the nucleation sites have grown to create regions that are aligned to the *c*-axis, and growth of the misoriented grain. The light shaded regions illustrate the boundaries between the aligned and misaligned regions.

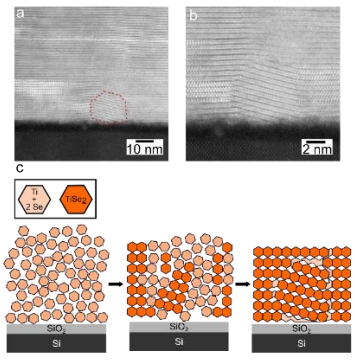

Figure 3.6. a) HAADF-STEM image of $([SnSe]_{1+\delta})_1(TiSe_2)_{15}$ highlighting a region with a red dashed line of a $TiSe_2$ grain that is not aligned to the *c*-axis on the substrate (Si + native SiO_2). Several SnSe

and $TiSe_2$ layers are marked with blue and orange rectangles, respectively. b) higher magnification of the region shown in 10a. c) the left panel shows the precursor with lighter shading to depict the Ti and Se. Not all layers for the repeating period or for the region in 10b are shown for simplicity. The middle panel illustrates potential nucleation and growth of the precursor where the solid shapes represent material that is starting to crystallize and self-assemble. The final product (right) shows the growth of the $TiSe_2$ grain that is not aligned, and light shaded regions at the boundaries between the aligned and misaligned regions.

This defect was only observed adjacent to the substrate in this sample and presumably forms through heterogeneous nucleation at the interface with the substrate. The misalignment of the grain may result from substrate roughness or the presence of an impurity layer at the substrate as discussed in Figure 3.1. Typically, these misoriented grains are smaller than the grains in the layers lying parallel with the substrate. This suggests that the initial nanoarchitecture of the precursor favors coarsening of grains parallel to the substrate, which would result in the consumption of these small grains with random orientation. The misoriented grain results in a variety of other defects in the surrounding regions, including dislocations, disconnections, and small domains of SnSe in the form of disconnection defects to accommodate the misaligned grain. Above this grain, the heterostructure is aligned to the *c*-axis and maintains the intended repeating period of $([SnSe]_{1+\delta})_1(TiSe_2)_{15}$.

3.3.3. Layer Thickness-related defects

So far, we have considered defects for which the individual layers of the precursor are all assumed to be ideally continuous. However, depending on the growth conditions there can be local and global deviations from the intended thicknesses of the individual layers within the precursor. Here, we distinguish between two types of thickness-related

defects as illustrated schematically in Figure 3.7. In the first case the number of layers is the same on both sides of the defect, but there is a step in the structure such that the phase changes within a layer. We refer to these defects as *layer-step defects*. In the second type of defect the number of layers is different on the two sides of the defect, resulting in a discontinuity of the layers. We refer to this type of defect as a layer-dislocation. Note that both of these types of defects are closely related to interfacial *disconnections*, a general class of interfacial line defect possessing both dislocation and step content.[29, 30] However, because of the possibility for rotational disorder between the different layers, the conventional three-dimensional crystallographic constraints that are normally applied in the analysis of disconnections at crystalline interfaces possessing a well-defined crystallographic orientation relationship, are not as applicable here.

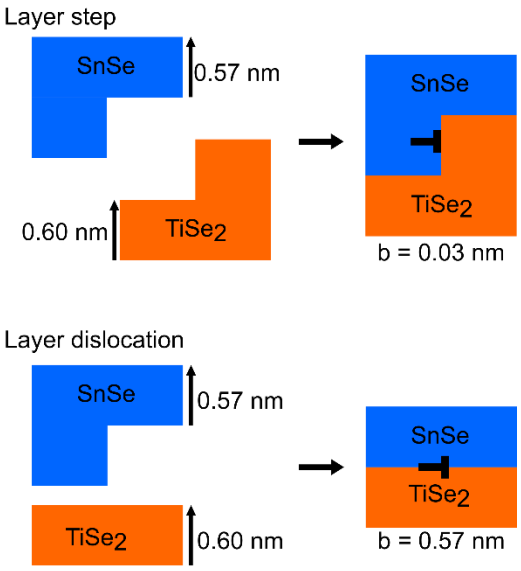

Figure 3.7. Schematics of a layer-step defect between SnSe and $TiSe_2$, where the Burger's vector (b) is small due to the similarity in the c-lattice parameters and s layer dislocation defect where the Burger's vector is larger because an additional partial layer of SnSe is present.

3.3.3.1. Layer-Step Defects

Figure 3.8 highlights a layer-step defect in $([SnSe]_{1+\delta})_2(TiSe_2)_1$ where an SnSe layer meets $TiSe_2$ at a grain boundary. The region in the red box on Figure 3.8a is shown at in Figure 3.8b and layers are labeled to highlight the disconnection. The dislocation content in this defect is small because the thicknesses of the SnSe (c =5.747 Å) and $TiSe_2$ (c = 5.998 Å) layers are similar, resulting in only a small mismatch in the step heights. In a system where there is a larger difference in c-lattice parameters, there would be larger dislocation content with consequences to the overall film thickness. Figure 3.8c shows a schematic of the formation of this defect from the precursor on the right. In the top schematic, the ideal amount of material to form the 2 bilayers of SnSe and 1 trilayer of $TiSe_2$ is shown, resulting in the desired product on the right. In the bottom schematic, the precursor locally has excess $TiSe_2$ relative to a single trilayer, and insufficient SnSe to form 2 complete bilayers. Since the layer thicknesses are approximately equal and the number of SnSe-$TiSe_2$ interfaces is conserved, we do not expect a significant energy penalty for this defect.

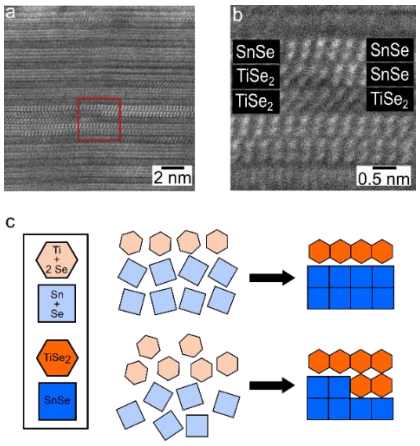

Figure 3.8. a) HAADF-STEM image of $([SnSe]_{1+\delta})_2(TiSe_2)_1$ highlighting a layer-step defect within the red box. b) higher magnification from the region highlighted in 4a, showing the disconnection

where SnSe and $TiSe_2$ exist within the same layer. c) the top schematic illustrates a precursor (light shaded squares and hexagons for Sn + Se and Ti + 2 Se, respectively) where the number of atoms in the precursor is equal to the number of atoms to form $([SnSe]_{1+\delta})_2(TiSe_2)_1$ and results in the desired structure (dark shaded squares and hexagons). The squares and hexagons do not correspond to orientation. The bottom schematic illustrates the formation of a disconnection, where the amount of SnSe in the precursor is deficient, and the amount of $TiSe_2$ is in excess to form one complete layer.

The number of layer step defects varies considerably as the thickness of the constituent layers are varied. Disconnections were not observed in the $([SnSe]_{1+\delta})_1(TiSe_2)_1$ cross section, presumably because there is an energy penalty for reducing the amount of SnSe-$TiSe_2$ interface area due to the strong interaction between constituents. These defects become increasingly frequent, however, as the period of the heterostructure increases, as shown in Figure 3.9 from a cross-section of an $([SnSe]_{1+\delta})_8(TiSe_2)_2$ sample. Layer step defects are evident throughout this image, particularly on the right-hand side. The high density of layer step defects results in significant variation in the local number of layers of each constituent in the repeating period, although the average thickness of the repeating period is that targeted by the initial precursor. Since the precursors are prepared by sequentially depositing m Sn|Se and n Ti|Se elemental bilayers, any systematic deviation in the number of atoms deposited in each bilayer relative to that required to form a bilayer of SnSe or a single trilayer of $TiSe_2$ becomes m or n times larger. This makes it experimentally more challenging to prepare "perfect" precursors as m and n become larger, resulting in the disconnections from either the shortfall or excess number of atoms in each SnSe or $TiSe_2$ block from that required to make m bilayers of SnSe or n trilayers of $TiSe_2$.

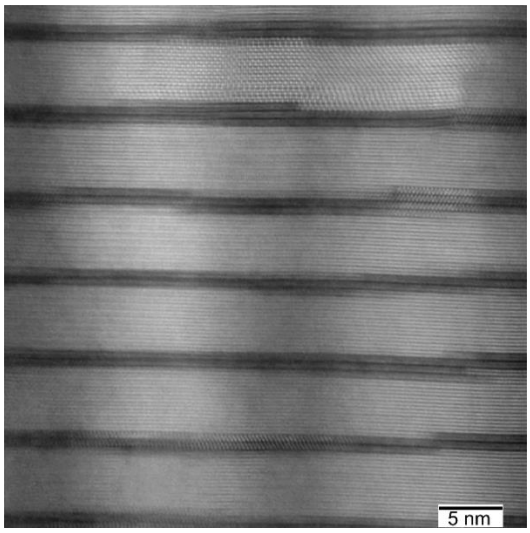

Figure 3.9. a) HAADF-STEM image of $([SnSe]_{1+\delta})_8(TiSe_2)_2$ which has a high density of layer-step defects, which are regions at grain boundaries of SnSe (light) to $TiSe_2$ (dark). The right-hand side of the image shows disconnections at every repeating period from the bottom to the top.

3.3.3.2. Layer Dislocations

Figure 3.10 highlights a layer-dislocation defect in $([SnSe]_{1+\delta})_1(TiSe_2)_2$ where a $TiSe_2$ trilayer is terminated. Layer dislocation defects were found in every sample investigated in this manuscript. The region in the red box on Figure 3.10a is expanded in Figure 3.10b and the dislocation is indicated with the dashed red lines. Figure 3.10c shows a schematic of the formation of this defect from the precursor on the right. The top schematic illustrates the ideal amount of material to form 1 bilayer of SnSe and 2 trilayers of $TiSe_2$, resulting in the desired product on the right. Similar to the layer disconnections, there is a non-integral number of layers in the precursor which is shown in the bottom schematic in Figure 3.10.

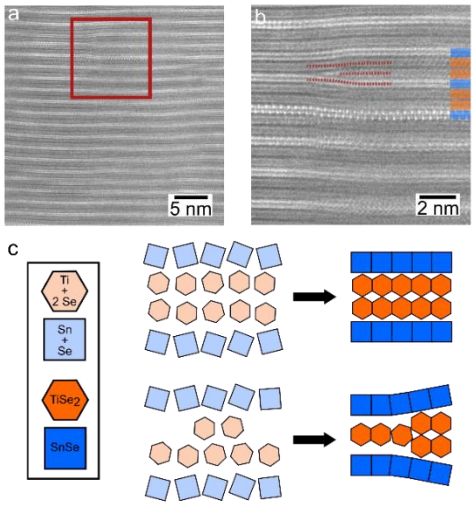

Figure 3.10. a) HAADF-STEM image of $([SnSe]_{1+\delta})_1(TiSe_2)_2$ highlighting a layer-dislocation type defect within the red box. b) higher magnification from the region highlighted in 5a, showing the dislocation type defect where a layer of $TiSe_2$ is terminated between complete layers of SnSe. Several SnSe and $TiSe_2$ layers are marked with blue and orange rectangles, respectively. c) the top schematic illustrates a precursor (light shaded squares and hexagons for Sn + Se and Ti + 2 Se, respectively) where the number of atoms in the precursor is equal to the number of atoms to form $([SnSe]_{1+\delta})_1(TiSe_2)_2$ and results in the desired structure (dark shaded squares and hexagons). The squares and hexagons do not correspond to orientation. The bottom schematic illustrates the formation of a dislocation, where the amount of SnSe in the precursor is the amount required to form complete layers, and the amount of $TiSe_2$ is insufficient to form 2 complete layers.

However, the final product does not form an integral number of layers due to locally insufficient amount of material, which is illustrated in the schematic with insufficient $TiSe_2$ to form 2 complete trilayers neighboring the ideal amount of SnSe to form 1 bilayer. The result is a partially complete layer of $TiSe_2$ which is terminated.

As with the layer step defects, our observations suggest the layer dislocation defects also become more frequent with increasing thickness of the constituent layers in heterostructures. For instance, consider Figure 3.11. In this $([SnSe]_{1+\delta})_8(TiSe_2)_2$ sample, Figure 3.11 contains a region where a layer of SnSe is terminated at the dislocation, in contrast with the $TiSe_2$ layer terminated in Figure 3.10. Disconnections and dislocations can

often be found in similar regions for samples with thicker periods, which is evident in the HAADF-STEM image of $([SnSe]_{1+\delta})_8(TiSe_2)_2$ shown in Figure 3.10.

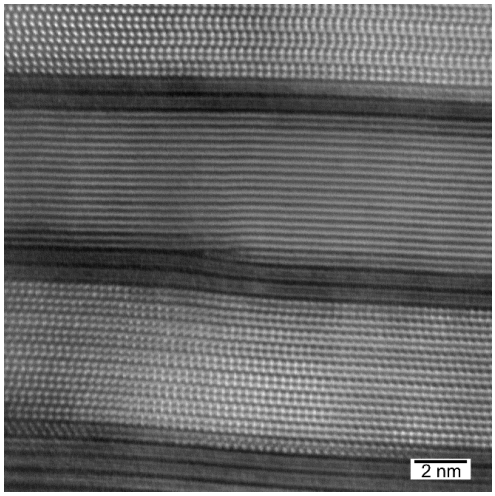

Figure 3.11. a) HAADF-STEM image of $([SnSe]_{1+\delta})_8(TiSe_2)_2$ with a region that has a layer-dislocation resulting from the termination of an SnSe bilayer. A disconnection defect is also apparent at the top of the image in the neighboring layer to the repeating SnSe bilayers.

The higher density of these defects is likely due to errors in deposition as depositing m or n layers that differ from the ideal composition by some amount, resulting in a larger global error. For example, in the $([SnSe]_{1+\delta})_8(TiSe_2)_2$ system if 1% more Sn and Se were deposited in each layer of the precursor, there would be 8% more Sn and Se than needed to form SnSe in the repeating period. In a $([SnSe]_{1+\delta})_1(TiSe_2)_1$ if the same error was present, there would only be 1% more material in the repeating period. The magnitude of the deviations, the diffusion rates of the elements, and the processing conditions will all impact the density of these defects in the self-assembled product.

It is also possible to precursor errors that give rise to less than a fully stochiometric layer, producing a locally faulted layer. An example is highlighted in Figure 3.12. For instance, an extra plane of atoms is trapped between the surrounding $TiSe_2$ trilayers. We

interpret this extra plane of atoms to be Ti based on the HAADF-STEM contrast. The region highlighted in the red box on Figure 3.12a is shown in Figure 3.12b, where the local extra plane of atoms is evident between [210] oriented $TiSe_2$ layers. These partial dislocations defects disrupt the periodic structure of the majority of the sample, like the dislocations discussed previously.

Figure 3.12c shows a schematic of how this defect may form during annealing, with the as deposited precursor illustrated on the right. For simplicity, only 4 of the 15 $TiSe_2$ layers in the repeating period are illustrated. Excess Ti relative to the targeted $TiSe_2$ stoichiometry is illustrated using light red shaded circles. The top schematic illustrates the ideal amount of material to form 1 bilayer of SnSe and 4 trilayers of $TiSe_2$, resulting in a defect-free product on the right. In the bottom schematic a possible formation mechanism for the partial dislocation is shown where excess Ti is present locally in the precursor which is trapped during self-assembly between domains of $TiSe_2$. The inclusion formed by the trapped Ti looks like a nanograin of TiSe, whose structure consists of alternating hexagonal planes of Ti and Se. These partial dislocations are likely only apparent for thick repeating periods for the same reason that high densities of the previous two defects were seen, that if each layer of Ti deposited is slightly off-composition there is a cumulative impact with a larger consequence to the overall repeating period. This defect could form if the thickness of Se layers was deficient or if the Ti layers were thicker than the amount needed to form $TiSe_2$. This defect could form if the thickness of Se layers was deficient or if the Ti layers were thicker than the amount needed to form $TiSe_2$.

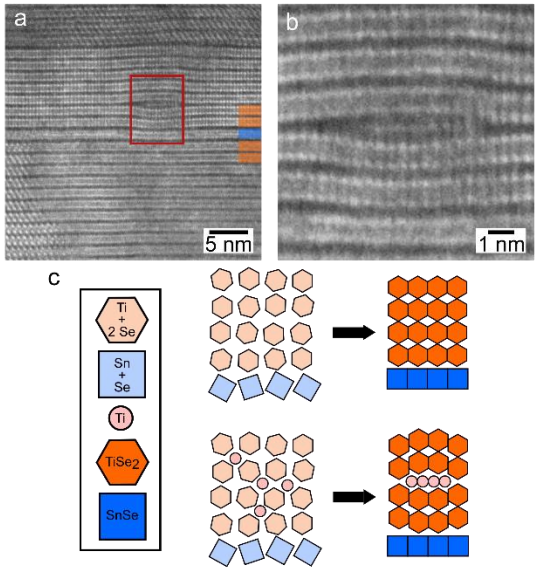

Figure 3.12. a) HAADF-STEM image of $([SnSe]_{1+\delta})_1(TiSe_2)_{15}$ highlighting a partial layer dislocation defect within the red box. Several SnSe and $TiSe_2$ layers are marked with blue and orange rectangles, respectively. b) higher magnification from the region highlighted in 11a, showing the Ti atoms are trapped between the [210] oriented $TiSe_2$ trilayers. c) the top schematic illustrates a precursor (light shaded squares and hexagons for Sn + Se and Ti + 2 Se, respectively, light shaded circles for Ti) where the number of atoms in the precursor is equal to the number of atoms to form 1 SnSe bilayer and 4 $TiSe_2$ trilayers and results in the desired structure (dark shaded squares and hexagons). The squares and hexagons do not correspond to orientation. The bottom schematic illustrates the formation of a partial layer dislocation, where excess Ti relative to $TiSe_2$ stoichiometry is present locally in the precursor, resulting in the small domain of Ti between $TiSe_2$.

3.4. Conclusions

The defects observed in cross-sections of $([SnSe]_{1+\delta})_m(TiSe_2)_n$ studied with HAADF-STEM are analogous to those observed in conventionally grown crystals, despite the diffusion limited growth during low temperature annealing from a designed precursor. The density and type of defects present were found to increase as the thickness of the constituent layers increased, providing clues as to the origin of defects. The defects result from either deviations in the amount of material deposited globally or locally in the precursor or by multiple nucleation sites being present during the self-assembly process.

Nucleation occurs at multiple sites within the precursors because any amorphous regions formed during deposition onto the nominally room temperature substrates are supersaturated with respect to the crystalline constituents. Several recent reports discuss methods to control nucleation rates/sites which could be used to reduce domain boundary and layer step defects.[6,31,32] Local variations in composition will always occur, therefore controlling layer step defects would require controlling processing conditions and diffusion rates.[18,33] Our results also suggest that it should be possible to control the type and density of defects in these heterostructures by controlling the precursor structure and processing conditions to influence properties. Defects are desirable in some cases, such as reduced lattice thermal conductivity which can be improved by increasing dislocation densities and decreasing grain size.[34] For other properties, such as increasing carrier mobility, one needs to reduce defect levels.[34]

3.5. BRIDGE

This chapter proposed formation mechanism for defects in layered heterostructures based on defects observed via electron microscopy. Two primary categories of defects were discussed, those that form as a result of self-assembly consistent with simultaneous nucleation and growth occurring throughout the sample during crystallization, and those that formed as a result of errors in local or global precursor composition. Understanding these defects and how they form has implications for tuning properties where specific defects are desired or need to be minimized. The next chapter tests the formation mechanisms proposed in this chapter. Intentional defects were formed at a specific site in a layered heterostructure by precisely controlling local composition.

CHAPTER IV

CONTROLLED DEFECT FORMATION IN TRANSITION METAL DICHALCOGENIDE CONTAINING HETEROSTRUCTURES

4. AUTHORSHIP STATEMENT

Chapter IV is under preparation for submission to the *Journal of the American Chemical Society*. Coauthor Marisa Choffel assisted with synthesis of compounds. Douglas L. Medlin assisted with collection of electron microscopy data. Professor David C. Johnson is my adviser, and I am the primary author of the manuscript.

4.1. INTRODUCTION

The ability to synthesize designed heterostructures is significantly limited. Fault lies on both the inability to accurately predict stable compounds and to synthesize kinetic products. Predictions are complicated because there are no systematic rules with which to understand coordination and bonding energies, like in molecular chemistry.[1] Computations may make approximations that result in systematic errors in formation energies. Other complications plague the synthetic attempts to synthesize predicted or designed structures. The synthetic attempts increase the complications as the different aggregate states and reactivities increase the energy of mixing unpredictably, increasing the energy of diffusion.[2,3] If diffusion is limited to the surface in synthetic methods like molecular beam epitaxy, the lattice match required for templating the next layer adds another synthetic obstacle.[4]

A previous study (Chapter III) discussed and proposed formation mechanisms for defects in heterostructures, providing clues to understand the self-assembly process using solid-state synthesis). Defects that mimic those in traditional crystalline materials such as dislocations, grain boundaries, steps, and antiphase boundaries were observed in cross-sections of heterostructures prepared with the Modulated Elemental Reactants (MER) method. MER is a low-temperature solid state synthesis route that involves the deposition of compositionally modulated layers of material. A precursor film is prepared with a nanoarchitecture that mimics that of the desired product, decreasing the diffusion lengths. Low-temperature annealing results in the self-assembly of the precursor structure to a kinetically stable product. Rotational disorder is generally present in all samples prepared through this method, likely as a result of a self-assembly mechanism where nucleation and growth of domains are occurring simultaneously. Nucleation does not occur solely based on the substrate. This work described two primary categories of defects – those that form as a result of the amount of material in the precursor, and those that form as a result of the self-assembly mechanism or transformation from precursor to product.

Heterostructures synthesized via MER have demonstrated desirable properties such as ultra-low thermal conductivity, charge density wave transitions, and superconductivity.[5–7] When considering implementation of materials prepared with MER into devices, it will be necessary to better understand the growth mechanisms to accurately interpret and predict physical properties. Depending on desired properties, precise control over specific defect types and densities must be achieved. For example, layer step defects were found via electron microscopy in heterostructures prepared $([SnSe]_{1+\delta})_1(VSe_2)_1$ compounds dependent

on the ratio of Sn/V, which had impact on the magnitude of the charge density wave.[8] Without known defect types and densities, determining the impact of defects on properties in these materials is not possible.

Here we present formation mechanisms for two types of defects that form in heterostructures as a result of local composition of the precursor structure. The system investigated for this study was $(PbSe)_m(MoSe_2)_n$, which is a semiconductor compound with tunable thermal conductivity dependent on the ratio of PbSe to $MoSe_2$ layers. For simplicity, we targeted $(PbSe)_1(MoSe_2)_1$, since it is well understood and it's structural and electrical properties have been studied as a function of constituent thickness.[9–12] Additionally, there is little concern that phases other than PbSe and $MoSe_2$ would form under these conditions. Intentional defects were prepared in samples by depositing repeating units of PbSe and $MoSe_2$, and varying the amount of material deposited only in the middle repeating unit in the film. The 'defect layer' in the center of the film was surrounded by repeating units with that targeted the correct amount of material required to form $(PbSe)_1(MoSe_2)_1$. One sample aimed to investigate defect formation that occurs as a result of varying the amount of material in only one constituent (PbSe), whereas another investigated varying the amount of both constituents (PbSe and $MoSe_2$) in neighboring layers. The hypothesis that layer step and dislocation defects form in these heterostructure materials due to errors in local composition. Layer dislocation defects form when the local amount of material for one constituent is higher or lower than the amount to form a single layer, and the amount of material to form a single layer of the other constituent is correct. Layer step defects form from error in the local amount of material to form both constituents.

4.2. METHODS

Samples were prepared with the Modulated Elemental Reactants (MER) method.[13] This method is a low-temperature solid-state synthesis technique where alternating elemental layers are deposited in a precursor, mimicking the desired nanoarchitecture. Precursors are then annealed to low temperatures (< 500°C) to crystallize a final compound or heterostructure. Elemental layers are deposited with physical vapor deposition (PVD) in a custom deposition system onto substrates, which for this study is a polished Si <100> wafers with native SiO_2.

A sequence of Mo|Se|Pb|Se was used, where the number of Mo and Se atoms in Mo|Se targets that required to form a trilayer of $MoSe_2$, and the number of Pb and Se atoms in Pb|Se targets that required to form a bilayer of PbSe. For intentional defect layers, the same sequence was used but the target number of atoms was varied. For the sample where one constituent's local composition was varied, a complete $MoSe_2$ trilayer and half of a PbSe bilayer was targeted. For the sample where both contstituents local composition was varied, half of the number of atoms to make $MoSe_2$ and half that required to make PbSe were targeted.

After deposition, samples were annealing in a nitrogen environment at 350°C for 15 minutes to promote self-assembly of the desired metastable heterostructure. This annealing temperature was chosen based on prior work and annealing studies on this system.[9,11,12] Before and after annealing, samples were characterized with x-ray fluorescence to determine the total number of atoms/$Å^2$ of each element by utilizing calibration curves described in

Hamann, et. Al.[14] Specular x-ray diffraction and x-ray reflectivity were used to investigate film quality and structure of the precursors and annealed samples.

In order to study local structural information and defect layers, cross-sections were prepared with an FEI Helios Nanolab 600i DualBeam SEM/FIB using standard lift-out procedures[15] for atomic resolution electron microscopy. A protective layer of permanent marker and SEM/FIB deposited carbon where deposited on the sample surface prior to liftout. Cross-sections were analyzed with High Angle Annular Dark Field – Scanning Transmission Electron Microscopy (HAADF-STEM) and Energy Dispersive X-ray Spectroscopy (EDS) on a Thermo Fisher Scientific Themis Z.

4.3. Results And Discussion

Precursors were prepared by depositing alternating layers of elemental Mo|Se and Pb|Se, where the amount of material in each layer targeted $MoSe_2$ and PbSe (with exception of intentional defect layers). A precursor with no defect layer was prepared to target $(PbSe)_1(MoSe_2)_1$ where the target amount of material deposited was the same for 24 repeat units of Mo|Se|Pb|Se. The next precursor targeted 12 RU $(PbSe)_1(MoSe_2)_1$ + $(MoSe_2)_1$ $(PbSe)_{0.5}$ + 12 RU $(PbSe)_1(MoSe_2)_1$. This precursor was deposited with the intention to determine what defects form as a result of insufficient amount of material to form one constituent locally (PbSe in this case). The last precursor targeted 12 RU $(PbSe)_1(MoSe_2)_1$ + $(MoSe_2)_{0.5}$ $(PbSe)_{0.5}$ + 12 RU $(PbSe)_1(MoSe_2)_1$. This precursor was deposited with the intention to determine what defects form as a result of insufficient amount of material to form both constituents locally. A schematic o each precursor structure is shown in Figure

4.1. Precursors were characterized after deposition (as-deposited) and after annealing with a variety of X-ray techniques.

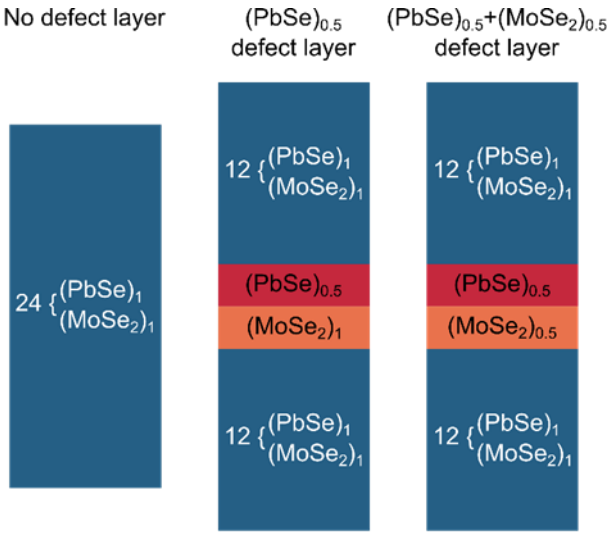

Figure 4.1. Schematic of precursors targeting no intentional defects (left), intentional defect targeting the incorrect amount of material to make one constituent locally (middle), and intentional defect targeting the incorrect amount of material to make both constituents locally (right).

X-ray fluorescence (XRF) was used to determine the total number of atoms/Å^2 for each element in the precursors before and after annealing. Table 4.1 contains the total atoms/Å^2 for each element before and after annealing. The number of possible repeat units was calculated based on the rate limiting element, assuming 0.1065 Pb and Se atoms/Å^2 are needed to form 1 bilayer of PbSe, and 0.1067 Mo atoms/Å^2 + 0.2135 Se atoms/Å^2 are needed to form 1 trilayer of $MoSe_2$. The 'no defect' sample has excess Pb after annealing. The defect layer samples have excess Pb, Mo, and Se within error for what is expected for the additional material deposited in the middle of the samples. In all samples, excess Se is lost with annealing as Se evaporates.

Table 4.1. Total atoms/Å^2 determined by XRF for each element. The integral number of repeat units of $(PbSe)_1(MoSe_2)_1$ was calculated based on the limiting element.

Sample		Total Pb atoms/Å^2	Total Mo atoms/Å^2	Total Se atoms/Å^2	Number of possible $(PbSe)_1(MoSe_2)_1$ repeat units
No defect layer	As-deposited	2.56(2)	2.33(3)	8.0(2)	23
	Annealed	2.57(2)	2.36(3)	7.0(2)	
$(PbSe)_{0.5}$ defect layer	As-deposited	2.46(2)	2.32(3)	6.9(2)	22
	Annealed	2.45(2)	2.32(3)	6.8(2)	
$(PbSe)_{0.5}$ + $(MoSe_2)_{0.5}$ defect layer	As-deposited	2.57(2)	2.57(3)	7.7(2)	23
	Annealed	2.55(2)	2.57(3)	7.3(2)	

Specular X-ray reflectivity (XRR) and X-ray diffraction (XRD) were used to analyze the sample structure prior to annealing. X-ray reflectivity patterns of each sample are shown in Figure 4.2a. The number of repeat units in the sample can be determined by the number of Kiessig fringes before the first Bragg reflection from the superlattice ($2\theta \approx 6.5 – 7.5°$) plus 2. For the 'no defect' sample, there are Kiessig fringes from 24 repeat units, which agrees with the structure of the deposited precursor. The defect samples have distinctly different patterns when compared to the sample with no intentional defect. The disruption of the periodic electron density in the middle of the sample results in an interference effect from Laue oscillations and Kiessig fringes. Models of the samples with and without defect layers show that this phenomenon agrees with what is observed in the XRR data (Figure B.1). This indicates that prior to annealing, the middle of the sample contains some thickness which is not identical to the surrounding repeat unit thicknesses. The number of Kiessig fringes

before the first Bragg reflection indicates the number of repeat units (excluding the defect layers), which is equal to 24 for both samples with intentional defect layers. This is consistent with the deposited precursor structure.

Specular X-ray diffraction patterns are shown in Figure 4.2b. Dashed lines are used to illustrate where expected superlattice reflections from $(PbSe)_1(MoSe_2)_1$. This assumes the predicted repeat unit thickness (12.584 Å) is equal to the sum of c-lattice parameters for 1 bilayer of PbSe (6.124 Å)[16] and 1 trilayer of $MoSe_2$ (6.460 Å).[17] The weak broad reflections indicate that the heterostructure began to self-assemble for all samples upon deposition, with reflections close to that expected for $(PbSe)_1(MoSe_2)_1$. The first reflection at $2\theta \approx 6.5 – 7.5°$ is from artificial layering of the precursor which is not fully crystallized, which is why it is shifted from the predicted position. The presence of defects is not obvious in the specular XRD patterns alone.

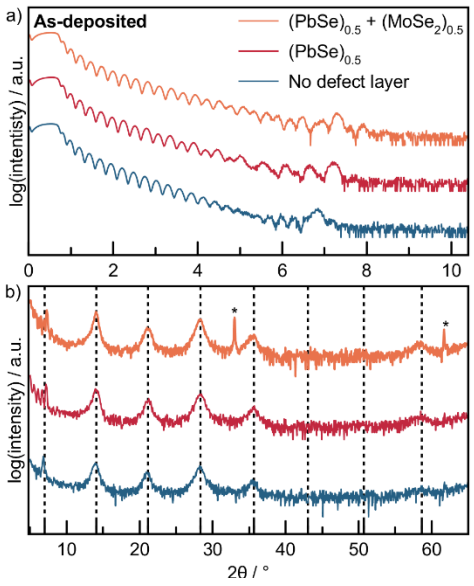

Figure 4.2. a) X-ray reflectivity patterns for each sample prior to annealing (as-deposited). b) Specular X-ray diffraction patterns for each sample prior to annealing. Dashed lines indicate where

00l superlattice reflections are expected. The legend in a) also applies to b). Asterisks mark reflections from the substrate.

Specular XRD and XRR were collected after annealing to investigate the crystallized heterostructure and determine if defect layers remained. Figure 4.3a shows XRR patterns for all samples after annealing. There are Kiessig fringes out to higher angles for all samples (> 10° 2θ), which indicates that all samples are smoother after annealing. Based on Kiessig fringes, all samples contain 23 repeat units after annealing. Based on XRF, there is only enough material to form 22 repeat units of $(PbSe)_1(MoSe_2)_1$ in the $(PbSe)_{0.5}$ however there is excess Pb and Se upon deposition. This suggests that additional PbSe layers could form in the sample (including the defect layer) which could account for the additional repeat unit thickness. The XRF data for the 'no defect' and $(PbSe)_{0.5}$ + $(MoSe_2)_{0.5}$ samples agrees excellently with this data. Both defect samples have the same interference phenomenon in the XRR pattern that was seen after deposition, which suggests the middle of the sample contains a different thickness (defect). Samples with defects have a slightly larger total film thickness determined by XRR than the sample without a defect layer (Table B.1).

Specular XRD patterns are shown in Figure 4.3b. Dashed lines are only shown for positions of even (*00l*) superlattice reflections for clarity of the patterns. All samples have narrower and more intense reflections than in the as-deposited samples that correspond to repeat unit thicknesses of 12.57(1)-12.61(3) Å. This is slightly smaller than previously reported for $(PbSe)_1(MoSe2)_1$ (12.658(2) Å), however these samples were prepared prior to having the ability to determine the total number of atoms/Å^2 of each element.[9] Laue oscillations are present to ~ 25° 2θ for all samples, which only occur if when a well-defined integral number of unit cells is present throughout the sample. Analysis of Laue oscillations

provides the number of unit cells present, which is equal to 23 for all samples. This agrees excellently with the XRR and XRF data. The defect layer samples have patterns where all odd (00*l*) reflections are split. Previous work modelled and showed experimental XRD data for a $[(SnSe)_{1.15}]_1[TaSe_2]_1$ with a VSe_2 layer in the middle, where peak splitting also occurred for odd (00*l*) reflections.[18] This occurs because scattered X-rays from regions with the ideal layer sequence are in phase for (00*l*), but are exactly out of phase for odd (00*l*) with scattered X-rays from the ideal regions separated by the additional layer thickness (defect). The peak splitting in defect samples is evidence that there are 2 blocks of ideal $(PbSe)_1(MoSe_2)_1$, with an additional thickness from defect layers in the middle.

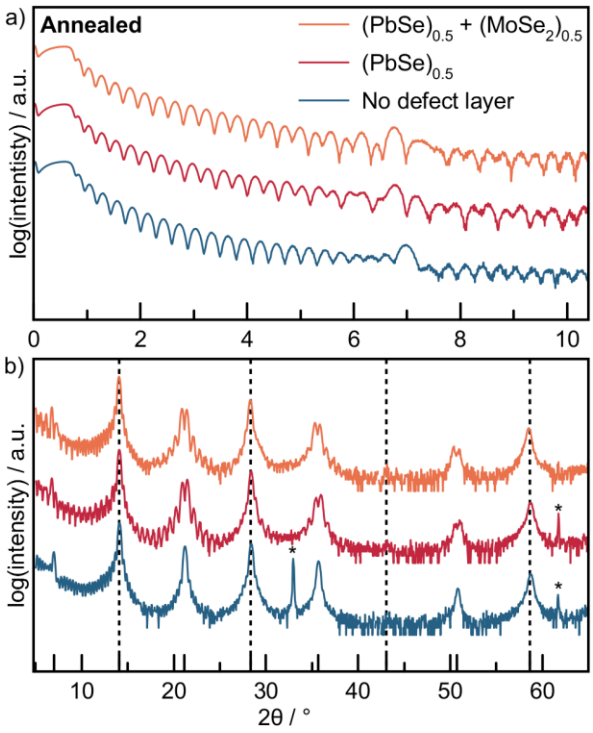

Figure 4.3. a) X-ray reflectivity patterns for each sample prior to annealing (annealed to 350°C for 15 minutes). b) Specular X-ray diffraction patterns for each sample prior to annealing. Dashed lines indicate only where even 00l superlattice reflections are expected for clarity. The legend in a) also applies to b). Asterisks mark reflections from the substrate.

X-ray techniques provided evidence that defects were in the middle of both samples where intentional defect layers were deposited, however does not provide detail on the structure of the defect layer. In order to determine what defects formed, cross-sections of each sample were prepared for investigation with HAADF-STEM. Figure 4.4 contains HAADF-STEM images of the sample without intentional defects. The entire film thickness is shown in Figure 4.4a. Contrast in HAADF-STEM is dependent on atomic number, where heavier elements appear brighter. PbSe bilayers appear brighter in this case, and $MoSe_2$ trilayers appear darker. Alternating PbSe and $MoSe_2$ layers can be seen throughout the entire thickness of the sample. Roughness at the bottom of the film from the substrate creates defects in the first several layers, which occurs in most films deposited with this method. This can result in partially incomplete layers in some regions, however this is resolved in this sample after the first ~2 layers. Rotational disorder is apparent from regions within constituent layers that are on and off zone axis, as there is no epitaxial relationship between constituents. This supports a self-assembly mechanism where simultaneous nucleation and growth is occurring. For this sample, this process begins during deposition since the sample began to crystallize before annealing.

While rotational disorder exists, layers are aligned to the substrate in the c-direction. The total sample thickness (Fig. S2) and number of repeat units of $(PbSe)_1(MoSe_2)_1$ agree excellently with XRR and Laue oscillations from XRD. Energy dispersive x-ray spectroscopy (EDS) showed that excess Pb/Se in the sample measured by XRF diffused to the surface of the film (Figure B.3). A higher magnification image is shown in Figure 4.4b. Aside from

grain boundaries within constituents from the rotational disorder, no obvious defects are present.

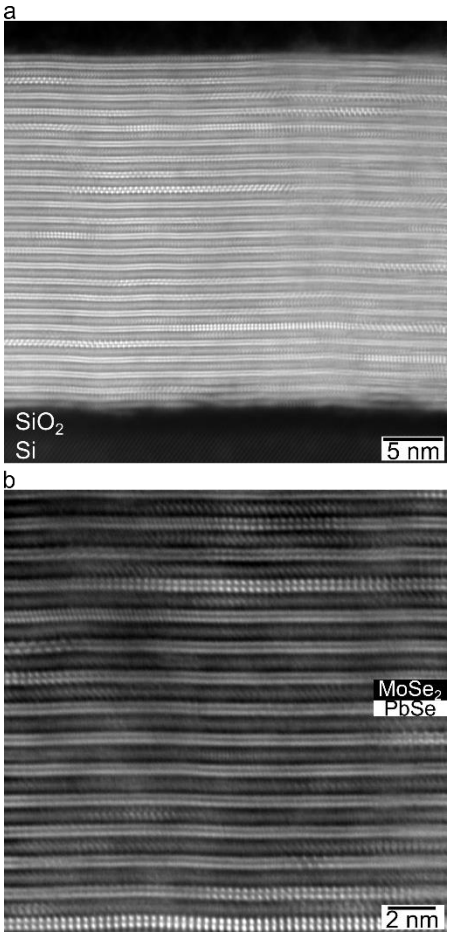

Figure 4.4. a) HAADF-STEM image of the entire $(PbSe)_1(MoSe_2)_1$ film with no intentional defects. b) Higher magnification HAADF-STEM image of the $(PbSe)_1(MoSe_2)_1$ with no intentional defects. One PbSe (brighter) and $MoSe_2$ (darker) layer are labeled. Aside from rotational disorder, no obvious defects are present.

Figure 4.5 contains HAADF-STEM images of the sample with the $(PbSe)_{0.5}$ defect layer. The entire film is shown in Figure 4.5a, where a defect in the middle of the sample (after 12 repeating units) is evident. Similar to the sample without a defect layer, rotational disorder and roughness at the substrate interface are present. The higher magnification

image in Figure 4.5b shows a layer dislocation defect in the middle of the sample. The dislocation type defect forms because $(PbSe)_{0.5}$ does not stay as a monolayer after annealing and rearranges to form a complete bilayer of PbSe in some regions. This defect also distorts layers above and below due to the local region with additional thickness. The region to the right of the dislocation defect remains flat, where there are two neighboring $MoSe_2$ layers without PbSe between them. This confirms proposed formation mechanisms for this defect type, which forms due to a local error in composition of one constituent (Chapter III).

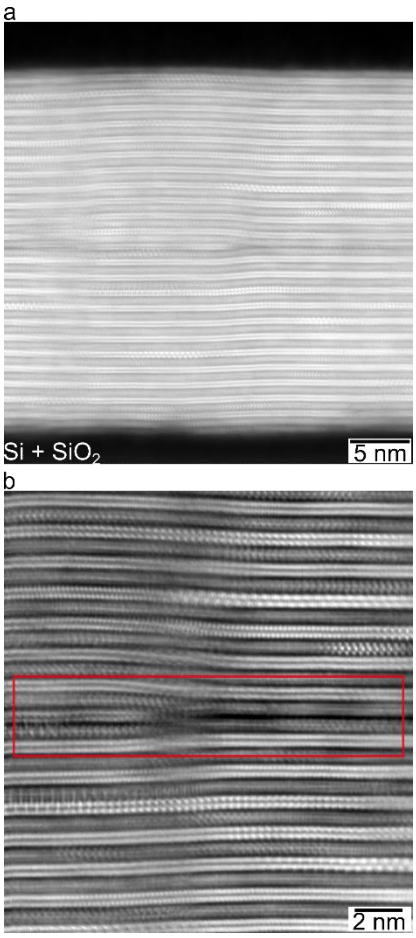

Figure 4.5. a) HAADF-STEM image of the entire (PbSe)1(MoSe2)1 with the (PbSe)0.5 defect layer. b) Higher magnification HAADF-STEM image of the (PbSe)1(MoSe2)1 with the (PbSe)0.5 defect

layer. A layer dislocation defect is highlighted in the red box, where a complete layer of PbSe formed on the left, and no PbSe is present on the right.

Figure 4.6 contains HAADF-STEM images of the sample with the $(PbSe)_{0.5}$ + $(MoSe_2)$ defect layer. Figure 4.6A shows the entire film thickness, where the middle of the sample (after 11 repeating units) has a larger van der Waals gap than the surrounding $(PbSe)_1(MoSe_2)_1$. A van der Waals gap between neighboring $MoSe_2$ regions which was also observed in Figure 4.5 is apparent due to weak interactions between $MoSe_2$ trilayers.

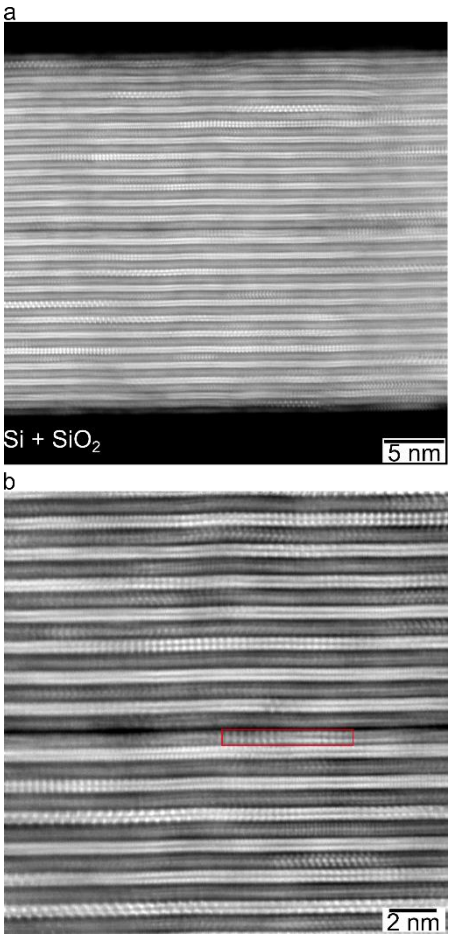

Figure 4.6. a) HAADF-STEM image of the entire $(PbSe)_1(MoSe_2)_1$ with the $(PbSe)_{0.5}$ defect layer. b) Higher magnification HAADF-STEM image of the $(PbSe)_1(MoSe_2)_1$ with the $(PbSe)_{0.5}$ defect layer. A dislocation type defect is highlighted in the red box, where a complete layer of PbSe formed on the left, and no PbSe is present on the right.

This is larger than that between PbSe and $MoSe_2$ as interactions between PbSe and $MoSe_2$ exist through bonding of Se in PbSe and $MoSe_2$, which has reported for PbSe and other transition metal dichalcogenides.[10] Unlike the $(PbSe)_{0.5}$, there is no significant distortion to the ideal regions in the sample and all layers remain smooth and flat. The higher magnification image in Figure 4.6b reveals a layer step defect in the middle of the sample. The layer step defect forms because $(PbSe)_{0.5}$ and $(MoSe_2)_{0.5}$ do not stay as a monolayer after annealing, and rearranges to form PbSe and $MoSe_2$ within the same layer. The region highlighted in the red box shows a small on-axis domain of PbSe surrounded by $MoSe_2$. There is little dislocation content in the layer step defect due to similarity in individual c-lattice parameters of PbSe and $MoSe_2$.This agrees with and confirms proposed formation mechanisms for this defect type, which forms due to a local error in composition of both constituents.

4.4. CONCLUSIONS

Defects observed in $(PbSe)_1(MoSe_2)_1$ heterostructures confirm formation mechanisms for variations in precursor composition for one or both constituents. When the local composition of one constituent is insufficient to form an integral number of bilayers or trilayers, layer dislocation defects form. When the local composition of both constituents is varied, layer step defects form. Using a nanoarchitecture where the defect layer was in middle of the sample generated phenomena in XRD and XRR patterns to providing confirmation that the defect layer was present prior to lifting out a cross-section for electron microscopy. Without confirmation of location and/or presence of a defect layer, finding a defect with microscopy could be analogous to finding a needle in a haystack. This work also

suggests that it is possible to target specific defect types and densities in other systems through precise control over the precursor nanoarchitecture and composition. This has implications for defect engineering to control properties where high or low defect densities are desirable. Site-specific defect layers could also be used to target a cleave plane in samples to obtain a specific number or type of layers after cleaving. In this system, cleaving would likely occur at van der Waals gaps between $MoSe_2$, since interactions between $MoSe_2$ trilayers is weaker than those between PbSe and $MoSe_2$ layers.

4.5. BRIDGE

Formation mechanisms for layer step defects and layer dislocations were confirmed in this chapter, where layer steps are the result of error in local composition of both constituents, and layer dislocations form as the error of only one constituent locally. This provided key insight into the overall self-assembly process of modulated precursors. The next chapter discusses the requirements for precursor structure and composition to form $(BiSe)_{0.97}(Bi_2Se_3)_{1.26}(BiSe)_{0.97}(MoSe_2)$. To confirm results from X-ray techniques, electron microscopy was used to access atomic scale structural information.

CHAPTER V

SYNTHESIS AND ELECTRICAL PROPERTIES OF A NEW COMPOUND $(BISE)_{0.97}(BI_2SE_3)_{1.26}(BISE)_{0.97}(MOSE_2)$ CONTAINING METALLIC 1T-$MOSE_2$

5.0. AUTHORSHIP STATEMENT

Chapter V was published in *ACS Chemistry of Materials* in 2021. Primary author Marisa Choffel synthesized and characterized compounds containing BiSe, Bi2Se3, and MoSe2 with X-ray diffraction, reflectivity, and fluorescence. Co-author Aaron M. Miller assisted with synthesis. Co-authors Fabian Göhler and Professor Thomas Seyller performed XPS measurements and analysis. Professor David C. Johnson is my advisor. I prepared TEM specimens, collected and analyzed HAADF-STEM/EDS data, wrote experimental and discussion sections for microscopy data, and edited the manuscript.

5.1. INTRODUCTION

Group 6 semiconducting transition metal dichalcogenides have been the subject of extensive research over the last several decades due to their potential applications in catalysis,[1-3] photovoltaics,[4] supercapacitors,[5] and rechargeable battery systems.[6] The structure of these MX_2 compounds (where M = Mo, W and X = S, Se) consists of a hexagonal layer of metal atoms sandwiched between two hexagonal chalcogen layers.[7-8] Depending on the stacking of these trilayers, several polymorphs are possible, with the semiconducting 2H polymorph being the most common with ABA BAB stacking. This stacking results in trigonal prismatic coordination of the metal.[9-10] The recent discovery that the Group 6 compounds transition from an indirect- to a direct- band gap semiconductor when the bulk

material is scaled down to a monolayer has created significant excitement as one of the first examples of an emergent property in a monolayer.[11-13] The transition from an indirect to a direct band gap semiconductor, which increases absorption and photoluminescence, has great promise for applications in optical devices.[12,14-16]

Ternary and higher order compounds containing the Group 6 X-M-X trilayers can also have ABC stacking of the layers, resulting in octahedral coordination of the metal and metallic conductivity.[3,17-20] These structural and electronic changes were first discovered in the alkali intercalation of the Group 6 compounds.[18,21-22] The ability to vary the intercalant, change carrier concentration by varying the amount of intercalate, and the discovery of superconductivity in these compounds resulted in a surge of activity.[18,23-24] Haering and coworkers recognized the potential of these compounds as battery cathodes, leading to the first commercialized lithium ion batteries.[25] More recently, there has been surge in publications on single and few layer 1T-MX_2 compounds due to improved catalytic properties for hydrogen evolution[2-3] and reduced contact resistances in 1T-2H-1T source-channel-drain field effect transistors.[19,26]

The high mobility and the volatility of alkali metal intercalants creates challenges in their synthesis and in subsequent processing steps when adjacent to other compounds.[27] An alternative way to create 1T-MX_2 layers is the presence of an adjacent strong electron donating layer. MSe layers, where M = Sb, Bi or a rare earth metal, have been reported to donate charge to neighboring dichalcogenide layers in misfit layered compounds.[28]These MSe layers have much lower vapor pressures than typical intercalants and are much less likely to diffuse. A recent paper on $(BiSe)_{0.97}(MoSe_2)$ reported a 40/60 ratio of 1T/2H

polymorph in the $MoSe_2$ layer, with a significant reduction in electrical resistivity relative to 2H $MoSe_2$.[29] To increase the fraction of 1T-MX_2, more charge donation is required. However, $[(BiSe)_{1+x}]_n(MoSe_2)$ compounds cannot be made, as multiple layers of BiSe are not stable next to each other.[30]

In this paper we report the synthesis, structure, and properties of $(BiSe)_{1+x}(Bi_2Se_3)_{1+y}(BiSe)_{1+x}(MoSe_2)$, probing how increasing the ratio of BiSe/$MoSe_2$ layers affects the percentages of 2H and 1T polymorphs in the $MoSe_2$ layer. $(BiSe)_{1+x}(Bi_2Se_3)_{1+y}(BiSe)_{1+x}(MoSe_2)$ was targeted as isostructural compounds have previously been reported.[31] The synthesis of the desired heterostructure is nontrivial, as it is only kinetically stable and avoiding the formation of $[(Bi_2Se_3)_{1+y}]_2(MoSe_2)$ requires excess Bi and Se in the precursor. The $(BiSe)_{1+x}(Bi_2Se_3)_{1+y}(BiSe)_{1+x}(MoSe_2)$ formed crystallographically aligned with respect to the substrate, but this is due to the morphology of the precursor, not epitaxial growth. The extensive turbostratic disorder between the constituent layers indicates that epitaxial growth does not dominate the self-assembly of the precursor into the heterostructure. High-angle annular dark field scanning transmission electron microscopy (HAADF-STEM) images confirms the layered nature of $(BiSe)_{1+x}(Bi_2Se_3)_{1+y}(BiSe)_{1+x}(MoSe_2)$ and indicates that two different polymorphs of $MoSe_2$ are present. X-ray photoelectron spectroscopy (XPS) data also indicates that 1T-$MoSe_2$ is present in increased quantities relative to $(BiSe)_{0.97}(MoSe_2)$. Resistivity measurements of $(BiSe)_{1+x}(Bi_2Se_3)_{1+y}(BiSe)_{1+x}(MoSe_2)$ show it is metallic, which are consistent with the increased amount of 1T$MoSe_2$ in the heterostructure. The Hall data is more complicated due to the heterogeneous mix of phases in the structures resulting in a change in carrier type as temperature is varied.

5.2. MATERIALS AND METHODS

Precursors targeting $(BiSe)_{1+x}(Bi_2Se_3)_{1+y}(BiSe)_{1+x}(MoSe_2)$ were synthesized *via* physical vapor deposition of the elements at pressures below 5 × 10-7 torr, using the repeating sequence Mo|Se|Bi|Se|(Bi|Se|Bi|Se)|Bi|Se. Bismuth and molybdenum were deposited using an electron beam gun and selenium was deposited using a Knudson effusion cell. A Si (100) wafer with a native oxide layer and fused quartz were used as substrates. The bulk crystalline structures of the individual constituents were used calculate the desired amount of material in each layer such that each Mo|Se layer had the number of atoms required to form a single Se-Mo-Se trilayer of $MoSe_2$, each Bi|Se layer had the number or atoms required to form a bilayer of a rock salt structured BiSe and each (Bi|Se|Bi|Se) had the number or atoms required to form a quintuple SeBi-Se-Bi-Se layer of Bi_2Se_3. A previously published calibration method[32] was used to optimize the deposition parameters. X-ray fluorescence (XRF) intensities were collected with a Rigaku ZSX Primus-II with a rhodium X-ray tube to determine the amount of each metal deposited. The proportionality constant between XRF intensity and amount of Mo and Bi the film was determined by preparing samples of $MoSe_2$ and Bi_2Se_3 and using the Se proportionality constant previously reported.[32]

X-ray reflectivity (XRR) and specular x-ray diffraction (XRD) data was collected on a Bruker D8 Discover diffractometer using Cu-*K*α radiation. Grazing incidence inplane XRD information was collected using a Rigaku SmartLab with a Cu source. Precursors were annealed at targeted temperatures for 15 minutes in a glove box with a nitrogen atmosphere

where O_2 pressure was below 0.5 ppm to promote their selfassembly into the crystalline products.

A cross-section of the sample was prepared with a FEI Helios Nanolab 600i DualBeam Scanning Electron Microscope (SEM)/Focused Ion Beam (FI) using standard lift-out methods.[32] A protective layer of Sharpie carbon and FIB deposited carbon was applied to the surface. High Angle Annual Dark Field-Scanning Transmission Electron Microscope (HAADF-STEM) images of the cross-section were collected on a probe-corrected Thermo Fisher Scientific Themis Z STEM at 300 keV.

Table 5.1. Amounts of material and repeating thicknesses for samples targeting the $(BiSe)_{1+x}(Bi_2Se_3)_{1+y}(BiSe)_{1+x}(MoSe_2)$ nanoarchitecture

Sample	Atoms / Å^2 per layer in precursor before annealing			Total Thickness (Å)	Number of Layers Deposited	Number of Layers Crystallized	Repeating Thickness (Å)
	Bi	M	Se				
Sample 1	3.88(8)	1.15(2)	6.5(3)	309.7(9)	11	10	28.37(2)
Sample 2	3.53(7)	1.37(3)	6.6(3)	308.7(5)	11	10	27.69(2)
Sample 3	3.19(6)	1.21(2)	7.6(4)	312.9(8)	11	10	28.49(2)
Sample 4	3.41(7)	0.90(2)	7.0(3)	291.2(7)	11	10	27.28(2)
Sample 5	3.46(7)	1.22(2)	7.0(3)	302.7(4)	11	-	27.78(2)
Sample 6	3.54(7)	1.15(2)	7.1(4)	315.0(8)	11	-	27.89(2)
Targeting $(BiSe)_{1+x}(Bi_2Se_3)_{1+y}(BiSe)_{1+x}(MoSe_2)$	3.71	1.18	6.8		11		28.06
	3.37	1.07	6.2		10		
Targeting $[(Bi_2Se_3)_{1+y}]_2(MoSe_2)$	2.87	1.18	6.8		11		25.56
	2.61	1.07	6.2		10		

X-ray photoelectron spectroscopy (XPS) measurements were carried out at room temperature at a pressure of less than 3×10^{-10} mbar using Al-Kα radiation from a SPECS XR- 50M X-ray source with SPECS Focus 500 crystal monochromator, and a SPECS Phoibos 150 MCD-9 hemispherical analyzer equipped with a nine channeltron detector. Cleaving of samples prior to XPS measurements was done by mounting the sample between two steel plates using a combination of low-degassing EPO TEK H72 and H22 epoxy resins. Breaking of the top plate under the flow of dry nitrogen in the load lock of the UHV system exposes the buried interfaces of the film. Spectral analysis was carried out by fitting the high-resolution core level spectra with multiple Voigt-profiles. Lorentzian lifetimes widths used in the fits were determined beforehand on commercially available single crystals as well as MER-grown binary samples. Temperature dependent resistivity measurements were collected on the samples between 24 and 298 K using the van der Pauw method on a home-built system.

5.3. Results And Discussion

Six precursors were deposited as we attempted to prepare $(BiSe)_{1+x}(Bi_2Se_3)_{1+y}(BiSe)_{1+x}(MoSe_2)$. The amounts of each element required to form 11 and 10 layers of a $(BiSe)_{1+x}(Bi_2Se_3)_{1+y}(BiSe)_{1+x}(MoSe_2)$ heterostructure were estimated using the lattice parameters and structures of the binary constituents and/or structurally related compounds (Table 5.1). The compositions, total thickness, and repeating layer thickness of each precursor are summarized in Table 5.1. The fluctuation of the measured amounts for

the precursors around the targeted values reflects the reproducibility of the deposition but is valuable as our initial target value is only an estimate. Compositions for each precursor were determined from the XRF intensities of each element for the total film and the previously described calibration method.[31] The precursors were closer in composition to the stoichiometry of $(BiSe)_{1+x}(Bi2Se3)_{1+y}(BiSe)_{1+x}(MoSe_2)$ than to the composition estimated for 11 or 10 layers of $[(Bi_2Se_3)_{1+y}]_2(MoSe_2)$, a potentially competing local free energy minima. The XRR patterns of all of the precursors contained a first order Bragg reflection from the sequence of deposited layers, indicating that the elements in the precursor did not completely mix during the deposition. The thicknesses of all of the repeating sequence of elemental layers were close to the estimated *c*-axis lattice parameter for the $(BiSe)_{1+x}(Bi_2Se_3)_{1+y}(BiSe)_{1+x}(MoSe_2)$ heterostructure (28.06 Å) determined by adding the *c*-axis lattice parameters of the constituents. The amounts of each element deposited in the repeating sequence Mo|Se|Bi|Se|(Bi|Se|Bi|Se)|Bi|Se suggests that forming 10 or 11 layers of $(BiSe)_{1+x}(Bi_2Se_3)_{1+y}(BiSe)_{1+x}(MoSe_2)$ would involve the smallest diffusion distances for the elements.

All of the samples were annealed to 350°C to quickly evaluate what compounds self-assembled from the precursors and the resulting specular and in-plane diffraction patterns are shown in Figure 5.1. The reflections observed in the specular diffraction patterns of samples 1 and 2 index to single families of (00*l*) reflections with *c*-axis lattice parameters of 27.97(1) Å and 27.79(2) Å, respectively. Both are close to the estimated *c*-axis lattice parameter of $(BiSe)_{1+x}(Bi_2Se_3)_{1+y}(BiSe)_{1+x}(MoSe_2)$ (28.06 Å). The in-plane reflections can be indexed as (*hk*0) reflections for three different constituents: two hexagonal unit cells and a

unit cell with a rectangular basal plane. The calculated lattice parameters ($a_{hex,1}$ = 4.170(3) Å, $a_{hex,2}$ = 3.311(4) Å, a_{rect} = 4.600(1) Å and b_{rect} = 4.238(1) Å) are consistent with those expected for Bi_2Se_3 (a = 4.178(1) Å), $MoSe_2$ (a = 3.32(1) Å), and BiSe (a = 4.61(1) Å and b = 4.26(1) Å), respectively.[29,31] This diffraction data indicates that $(BiSe)_{1+x}(Bi_2Se_3)_{1+y}(BiSe)_{1+x}(MoSe_2)$ formed from these precursors. Surprisingly, samples 3 and 4 formed $[(Bi_2Se_3)_{1+y}]_2(MoSe_2)$ instead of the targeted compound $(BiSe)_{1+x}(Bi_2Se_3)_{1+y}(BiSe)_{1+x}(MoSe_2)$ whose composition they were closest to.

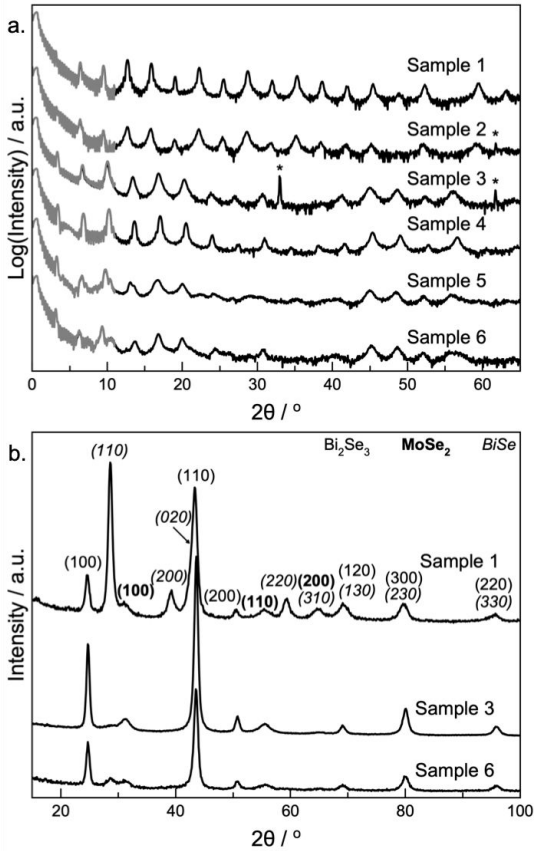

Figure 5.1. (a) XRR (gray) and specular x-ray diffraction and (b) representative in-plane x-ray diffraction patterns of the samples after annealing to 350°C. Asterisks in (a) mark the reflections that result from the Si substrate. The reflections for the different components are marked in (b) in varying fonts consistent with the labels in the top right corner.

The evenly spaced reflections in the specular x-ray diffraction yield c-axis lattice parameters of 26.38(1) Å and 25.96(1) Å, respectively, which are close to the estimated c-axis lattice

parameter for $[(Bi_2Se_3)_{1+y}]_2(MoSe_2)$ (25.56 Å). The in-plane maxima can be indexed as (*hk*0) reflections to two different hexagonal unit cells with *a*-axis lattice parameters of 4.154(2) Å and 3.309(5) Å, which are close to those expected for Bi_2Se_3 and $MoSe_2$, respectively.[29,31] Intensity at ~28.6° 2θ suggests that a small amount of BiSe may have formed. The specular diffraction scans for samples 5 and 6 have sharp reflections at low angles and broader diffraction maxima at high angles, suggesting that the samples have not fully self-assembled at this temperature. The high angle reflections yield *c*-axis lattice parameters of 26.32(1) Å and 26.27(1) Å for samples 5 and 6, respectively, which is close to the estimated *c*-axis lattice parameter of $(Bi_2Se_3)_{1+y}]_2[(MoSe_2)$. The reflections observed in the in-plane pattern of sample 6 can be indexed to two different hexagonal unit cells. The lattice parameters calculated from the peak positions (a_{hex} = 4.158(3) Å, a_{hex} = 3.304(7) Å,) are consistent with those expected for Bi_2Se_3 and $MoSe_2$. Higher intensity at ~28.6° 2θ suggests that more BiSe is present in this sample than found in sample 3. The different products formed shows how sensitive the reaction pathway is to the composition and structure of the precursors.

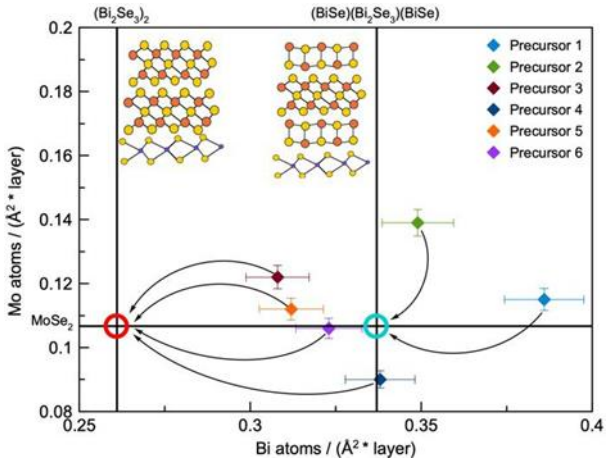

Figure 5.2. Amounts of Bi and Mo in the samples compared to the estimated amounts to form [(Bi2Se3)1+y]2(MoSe2) (red circle) and (BiSe)1+x(Bi2Se3)1+y(BiSe)1+x(MoSe2) (blue circle).

In conventional high temperature solid state synthesis, the composition of the starting mixture determines the product or ratio of products that form. In reactions of layered precursors, the local compositions and nanoarchitecture become important parameters as they control what nucleates and the diffusion lengths required for growth. Due to reactions with the substrate and/or oxidation at the surface, it is common to form one or more fewer unit cells of the intended heterostructure than the number of layers deposited.[34] We observed this in the precursors studied here, as the Laue oscillations around the (002) reflections in samples 1-4 indicate that 10 unit cells formed from the 11 repeating sequences deposited. Figure 5.2 graphs the amounts of Mo and Bi in each of the samples, normalized to the 10 unit cells that crystalized, and arrows are used to indicate whether they formed $(BiSe)_{1+x}(Bi_2Se_3)_{1+y}(BiSe)_{1+x}(MoSe_2)$ or $[(Bi_2Se_3)_{1+y}]_2(MoSe_2)$. Samples 1 and 2 have enough Bi and Mo to make the ten layers of $(BiSe)_{1+x}(Bi_2Se_3)_{1+y}(BiSe)_{1+x}(MoSe_2)$ that formed. Samples 3-6 are all deficient in one element compared to $(BiSe)_{1+x}(Bi_2Se_3)_{1+y}(BiSe)_{1+x}(MoSe_2)$. Instead of forming 9 unit cells of $(BiSe)_{1+x}(Bi_2Se_3)_{1+y}(BiSe)_{1+x}(MoSe_2)$, they instead evolve into $[(Bi_2Se_3)_{1+y}]_2(MoSe_2)$. We speculate that the significant excess of Se (5-13%) relative to the amounts of Bi and Mo in these precursors may have promoted the formation of Bi_2Se_3 rather than BiSe by Le Chatelier's principle. Since Laue oscillations are observed in samples 1- 4, long range diffusion is required to transport the excess amounts of Bi and Mo out of the coherent crystalline domains. The excess Se probably acts as a flux. Samples with excess Mo relative to the compound formed have broader diffraction maxima, which we speculate is due to $MoSe_2$ inclusions, which reduces the size of coherent domains. Excess Bi has been observed to form Bi_2Se_3 on the top of the sample in other Bi containing heterostructures,[30,35]

suggesting that it is more mobile than excess Mo. Our results indicate that the local free energy minima in the energy landscape for $(BiSe)_{1+x}(Bi_2Se_3)_{1+y}(BiSe)_{1+x}(MoSe_2)$ and $[(Bi_2Se_3)_{1+y}]_2[(MoSe_2)]$ are close in energy.

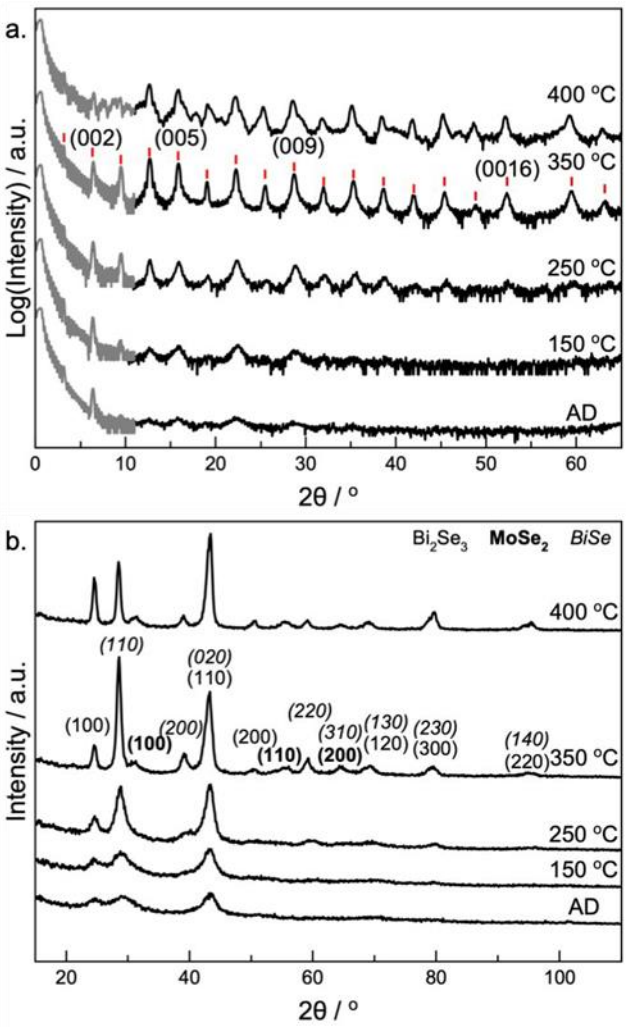

Figure 5.3. (a) XRR (gray) and specular XRD (black) patterns and (b) in-plane XRD patterns of Sample 1 as a function of temperature. The red lines indicate the 2θ values for reflections calculated using the *c*-axis lattice parameter of the structure (27.97(1) Å). Indices are indicated above some reflections.

Specular and in-plane XRD scans were collected on sample 1 as a function of annealing temperature to determine the optimal formation conditions for

$(BiSe)_{1+x}(Bi_2Se_3)_{1+y}(BiSe)_{1+x}(MoSe_2)$ (Figure 5.3). The specular XRD pattern of the as-deposited precursor contains reflections from two different sources. The sharp first order Bragg reflection results from the composition modulation of the precursor from the deposited sequence of elemental layers. The broader diffraction maxima at higher angles result from small crystalline domains that nucleated and grew during the deposition process. The broad diffraction maxima can all be indexed to a single family of (00*l*) reflections with a *c*-axis lattice parameter of 28.0(1) Å. This value is close to the estimated *c*-axis lattice parameter for $(BiSe)_{1+x}(Bi_2Se_3)_{1+y}(BiSe)_{1+x}(MoSe_2)$ (28.06 Å). Evidence for crystallization during deposition is also found in the in-plane XRD pattern. The broad reflections are consistent with the (100) and (110) reflections for Bi_2Se_3 and the (110) and (020) reflections for BiSe.[33] After annealing at 150°C, there are slight increases in intensity of the existing reflections in both the specular and in-plane XRD patterns, but no new reflections are observed. The XRR pattern has fewer Kiessig fringes, suggesting that there is an increase in the roughness of the film as atoms diffuse. After annealing at 250°C, the intensity of reflections in the specular and in-plane XRD patterns increase, linewidths decrease and additional reflections are visible in both patterns. Even more reflections appear after annealing at 350°C and the existing reflections in both patterns increase in intensity and decrease in linewidth. The XRR pattern indicates that the film smoothness increased during annealing at 350°C. Laue oscillations are now apparent between low angle Bragg reflections, indicating the sample is 10 repeating layers thick. The total thickness of the sample based on the Kiessig fringes in the XRR pattern is 306.9(3) Å. Based on the *c*-axis lattice parameter and the number of layers indicated from the Laue oscillations, the thickness of the crystalline BiSe-Bi_2Se_3-BiSe-$MoSe_2$ repeating structure is ~279.7 Å. The difference, ~27 Å, is

approximately the thickness of 3 quintuple layers of Bi_2Se_3, which is observed in the STEM images discussed next. The lattice parameters calculated from both patterns remain consistent with the formation of $(BiSe)_{1+x}(Bi_2Se_3)_{1+y}(BiSe)_{1+x}(MoSe_2)$ at this temperature. The (00*l*) reflections in the specular XRD pattern lose intensity, broaden, and new reflections appear after annealing at 400°C, indicating that $(BiSe)_{1+x}(Bi_2Se_3)_{1+y}(BiSe)_{1+x}(MoSe_2)$ is decomposing. The in-plane reflections of BiSe decrease in the intensity, suggesting that the decomposition of this layer is responsible for the deterioration of the heterostructure. The annealing study indicates that $(BiSe)_{1+x}(Bi_2Se_3)_{1+y}(BiSe)_{1+x}(MoSe_2)$ begins to self-assemble during the deposition and the self-assembly is completed and excess Bi and Se diffuse to the top of the film after annealing at 350°C.

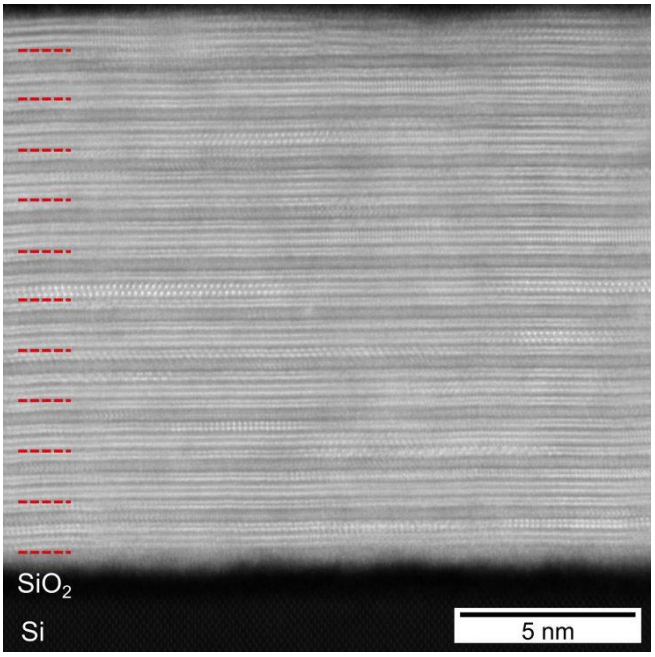

Figure 5.4. Representative HAADF-STEM image of the $(BiSe)_{0.97}(Bi_2Se_3)_{1.26}(BiSe)_{0.97}(MoSe_2)$ heterostructure annealed to 350°C on a Si substrate with its native SiO_2 surface layer. The 10 repeating sequences of layers resultingin Laue oscillations are indicated on the left with red dashed lines.

A HAADF-STEM image from a cross section of sample 1 annealed at 350°C is contained in Figure 5.4. The 10 repeating units of $(BiSe)_{0.97}(Bi_2Se_3)_{1.26}(BiSe)_{0.97}(MoSe_2)$, containing a quintuple layer of Bi_2Se_3, a bilayer of BiSe, a trilayer of $MoSe_2$, and a bilayer of BiSe are clearly visible. The 10 unit cells agree with the number determined from the Laue oscillations in the XRD pattern. There is a thin amorphous region present on the bottom of the film and two extra Bi_2Se_3 layers are present on the top of the sample. Similar diffusion of excess Bi and Se to the top of a sample forming Bi_2Se_3 layers was previously reported in other bismuth containing heterostructures.[30,35]

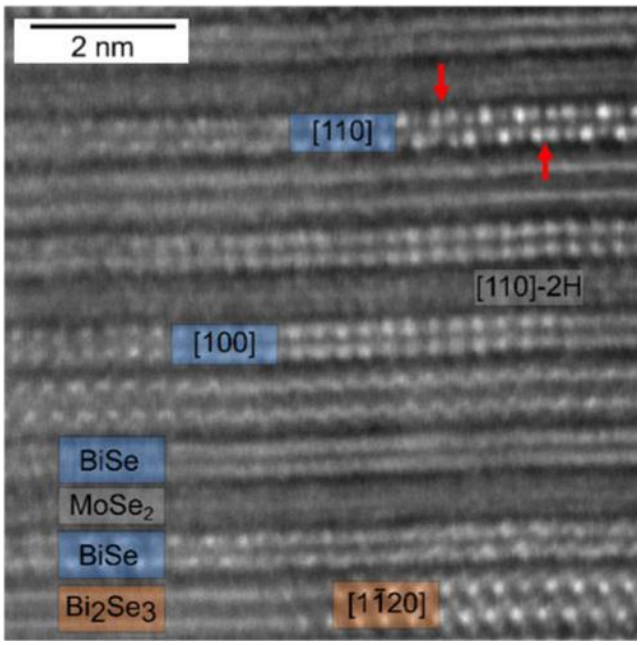

Figure 5.5. HAADF-STEM image of the $(BiSe)_{0.97}(Bi_2Se_3)_{1.26}(BiSe)_{0.97}(MoSe_2)$ heterostructure with zone axes labeled for each constituent. Antiphase boundaries are observed in regions of the film containing BiSe orientated along the [110] zone axis and marked with red arrows.

The first crystalline layer in the heterostructure above the substrate is Bi_2Se_3, which is surprising since a Mo|Se layer was first in the deposition sequence. The energy dispersive x-

ray spectroscopy (EDS) map shows that bottom of the film contains an amorphous mixture including Mo, Se, Si and O (SI). The intensity of Se on the bottom of the film is less than that of the Se intensity in $MoSe_2$ layers, suggesting that at least some of the Mo may react with the SiO_2 coated Si surface during deposition or annealing. Grain boundaries within layers and varying orientations within and between layers are present for all constituents, suggesting multiple nucleation sites. The resulting turbostratic disorder is commonly found in samples prepared from modulated precursors. [36-38]

A higher magnification HAADF-STEM image is shown in Figure 5.5 which clearly shows the atomically abrupt interfaces between the structurally different layers. Different layers having different zone axis orientations are observed, with the orientations changing both within and between layers. A single quintuple layer containing a Se-BiSe-Bi-Se stacking sequence is observed when the Bi2Se3 layer is oriented along a <11 0> zone axis. Antiphase 2 boundaries are clearly visible in BiSe layers when they are oriented along a <110> zone axis. The different orientations are thought to result from different nucleation sites both in the same and in different layers, resulting in the extensive rotational disorder observed. While not both contained in the image in Figure 5.5, we identified regions in the sample where small domains of the two different polytypes of MoSe2 could be identified when they are orientated down a <110> zone axis. The diagonal slashes shown in Figure 5.6a are consistent with an octahedrally coordinated 1T-MoSe2 polymorph and the chevrons in Figure 5.6b are consistent with a trigonal prismatic coordinated 2H-MoSe2 structure. That only small local regions are observable with these zone axis orientations reflects the small size of the MoSe2 grains.

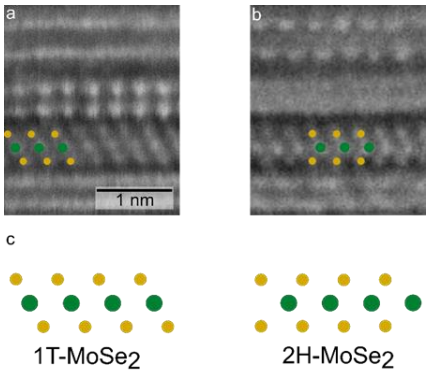

Figure 5.6. HAADF-STEM images which show a region of a) 1T-MoSe2 and b) 2H-$MoSe_2$. The schematics below the images show the expected [110] zone axis images for 1T-$MoSe_2$ and 2H-$MoSe_2$ [Mo (green) and Se (yellow)].

XPS of the Mo 3d, Se 3d, and Bi 5d core levels was collected on cleaved films to gain information about the electronic states found in $(BiSe)_{0.97}(Bi_2Se_3)_{1.26}(BiSe)_{0.97}(MoSe_2)$, and representative spectra are shown in Figure 5.7. Spectral analysis of the Mo 3d core level spectrum (Figure 5.7a) reveals contributions from two different components, with Mo $3d_{5/2}$ binding energies of 228.25 ± 0.05 eV and 228.93 ± 0.05 eV. An additional broad component centered at 229.47 ± 0.11 eV is required to account for the signal from an overlapping Se 3s core level. The Mo 3d binding energies are consistent with those reported previously for 1T- and 2H-$MoSe_2$, both in $(BiSe)_{0.97}(MoSe_2)$ (228.3 ± 0.1 eV and 228.9 ± 0.1 eV) and the individual polymorphs,[2,29,39] consistent with the observations in the HAADF-STEM images. The percentage of each polytype can be estimated from the relative intensities of the different $MoSe_2$ components in the spectrum. The amount of 1T-polymorph is found to be between 40 and 60%, which is higher than that observed in $(BiSe)_{0.97}(MoSe_2)$.[29] Se is expected to be in a Se^{2-} oxidation state regardless of whether it is found in the $MoSe_2$ polymorphs or the bismuth constituents.[40] Previous reports show that the Se 3d core levels of 1T- and 2H-$MoSe_2$ are found at slightly different binding energies, and that the chemical shift between

them is similar to that observed in the Mo 3d spectrum.[2] Any difference in binding energy for Se in Bi_2Se_3 and BiSe is too small to be distinguished. Our fit of the Se $3d_{5/2}$ spectrum is shown in Figure 5.7b, and the Se $3d_{5/2}$ binding energies (54.47 ± 0.05 eV for 2H-$MoSe_2$, 53.79 ± 0.05 eV for 1T-$MoSe_2$, and 53.57 ± 0.05 eV for Se bound to Bi) are consistent with those previously reported.[29] Two components are required to fit the Bi 5d spectrum (Figure 5.7c) as evident by the asymmetry of both the $5d_{3/2}$ and $5d_{5/2}$ lines towards lower binding energies. The position of the higher binding energy line (24.99 ± 0.05 eV) is consistent with Bi^{3+}, slightly larger than that observed in bulk Bi_2Se_3 (24.75 eV) and close to values reported for Bi atoms in BiSe (24.93-25.00 eV). The component at lower binding energy (24.13 ± 0.12 eV) has previously been assigned as Bi^0, due to Bi atoms at antiphase boundaries involved in Bi-Bi bonds between adjacent atoms (23.4-24.3 eV).29,41 From the relative intensity of the two components, we can estimate that approximately 30-50% of the Bi atoms in the BiSe layers are involved in Bi-Bi bonds at antiphase boundaries. The percentage of Bi involved in Bi-Bi bonds at antiphase boundaries in $(BiSe)_{0.97}(Bi_2Se_3)_{1.26}(BiSe)_{0.97}(MoSe_2)$ is similar to the $(BiSe)_{0.97}(MoSe_2)$ heterostructure,[29] however there are two BiSe layers for each $MoSe_2$ layer in $(BiSe)_{0.97}(Bi_2Se_3)_{1.26}(BiSe)_{0.97}(MoSe_2)$ while there is only one per $MoSe_2$ layer in $(BiSe)_{0.97}(MoSe_2)$. Therefore, more charge donation to $MoSe_2$ occurs in $(BiSe)_{0.97}(Bi_2Se_3)_{1.26}(BiSe)_{0.97}(MoSe_2)$, increasing the percentage of 1T-$MoSe_2$. This interpretation is supported by density functional theory and crystal orbital Hamilton to adjacent layers and antiphase boundary formation stabilize the BiSe rock salt structure by acting as "sinks" for excess electrons.[39] Charge donation from the BiSe layers to $MoSe_2$ layers stabilizes the octahedral 1T polymorph instead of the thermodynamic trigonal prismatic 2H polymorph.[19-20,29]

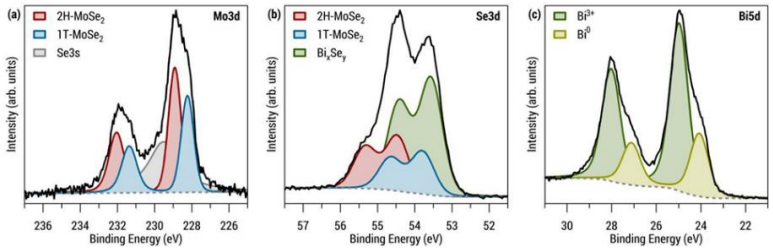

Figure 5.7. XPS analysis of the (a) Mo 3d, (b) Se 3d, and (c) Bi 5d core levels. Experimental data is shown as a solid black line, while the different components of the spectral analysis are in color.

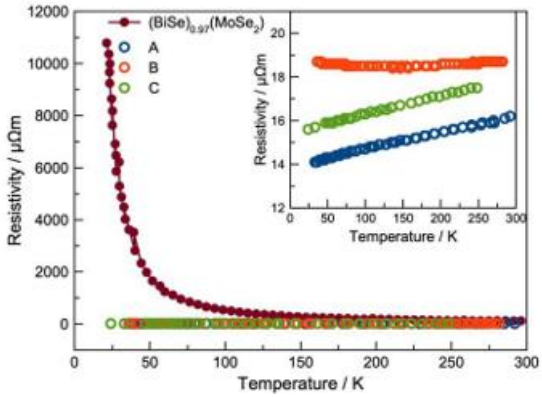

Figure 5.8. Temperature-dependent resistivity data of three $(BiSe)_{0.97}(Bi_2Se_3)_{1.26}(BiSe)_{0.97}(MoSe_2)$ samples (A, B, and C) from precursor 1 are plotted as a function of temperature for comparison with the $(BiSe)_{0.97}(MoSe_2)$ heterostructures. The inset figure graphs the data for the $(BiSe)_{0.97}(Bi_2Se_3)_{1.26}(BiSe)_{0.}97(MoSe_2)$ samples on an expanded scale.

In-plane electrical resistivity data for several $(BiSe)_{0.97}(Bi_2Se_3)_{1.26}(BiSe)_{0.97}(MoSe_2)$ samples are shown in Figure 5.8 along with the resistivity reported for $(BiSe)_{0.97}(MoSe_2)$. The two compounds have strikingly different temperature dependencies. The resistivity of $(BiSe)_{0.97}(MoSe_2)$ exponentially increases as the temperature is decreased, indicating an activated conduction mechanism typical for a semiconductor.[29] Since 2H-$MoSe_2$ is semiconducting in the bulk,[42] the amount of metallic 1T-$MoSe_2$[18-20] is not enough to create a continuous conducting network. In contrast, the room temperature resistivities of the $(BiSe)_{0.97}(Bi_2Se_3)_{1.26}(BiSe)_{0.97}(MoSe_2)$ samples are all very similar to each other, ~17(2) μΩm, with a near linear decrease in resistivity as the temperature decreases, indicating that this

compound is metallic. We suspect that the metallic conductivity results from a continuous network of1T-$MoSe_2$ across the sample, consistent with the significantly higher percentage of 1T$MoSe_2$ determined from our XPS data. While 1T-$MoSe_2$ is reported to be metallic,[18-20] we were unable to find resistivity data as a function of temperature for 1T-$MoSe_2$ reported in the literature. We used alkali metal intercalates of MoS_2, in which the MoS_2 has the 1T polymorph due to electron donation from the alkali metals, as a comparison instead. These compounds have room temperature resistivities ranging from 25 to 50 μΩm,[17] approximately twice the resistivity measured here for $(BiSe)_{0.97}(Bi_2Se_3)_{1.26}(BiSe)_{0.97}(MoSe_2)$, where the $MoSe_2$ sample is only ~ 20% of the volume of the unit cell.

In-plane Hall data was collected on $(BiSe)_{0.97}(Bi_2Se_3)_{1.26}(BiSe)_{0.97}(MoSe_2)$ to obtain more information about its electrical behavior. The Hall data is compared to a structurally similar $(BiSe)_{0.97}(Bi_2Se_3)_{1.26}(BiSe)_{0.97}(TiSe_2)$ in Figure 5.9, as Hall data was not reported for $(BiSe)_{0.97}(MoSe_2)$.[29,31]

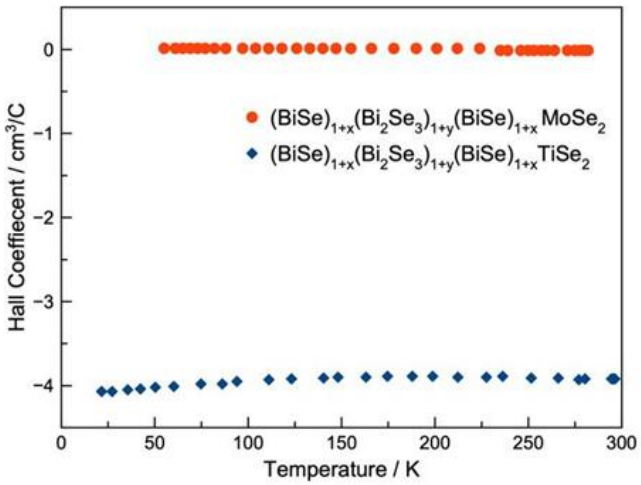

Figure 5.9. Temperature-dependent Hall data plotted as a function of temperature for $(BiSe)_{0.97}(Bi_2Se_3)_{1.26}(BiSe)_{0.97}(MoSe_2)$. Data for the structurally similar $(BiSe)_{0.97}(Bi_2Se_3)_{1.26}(BiSe)_{0.97}(TiSe_2)$ heterostructures is provided for comparison.

The Hall coefficient is negative for $(BiSe)_{0.97}(Bi_2Se_3)_{1.26}(BiSe)_{0.97}(TiSe_2)$ across the temperature range, indicating electrons are the majority carrier.[31] Charge transfer of electrons from BiSe to $TiSe_2$ was suggested as the source of the carriers, with the electrons in the $TiSe_2$ layers dominating the conductivity.[31] The Hall coefficient of $(BiSe)_{0.97}(Bi_2Se_3)_{1.26}(BiSe)_{0.97}(MoSe_2)$ is also negative at room temperature, but changes sign as temperature is decreased below 235 K. Interpreting the Hall and conductivity data for $(BiSe)_{0.97}(Bi_2Se_3)_{1.26}(BiSe)_{0.97}(MoSe_2)$ is complicated, since we know from the XPS data that this compound contains a heterogeneous mix of 2H- and 1T-$MoSe_2$. Based on prior reports that 1T-$MoSe_2$ is metallic and 2H-$MoSe_2$ is semiconducting, the current is likely concentrated in the portion of the sample that is the 1T polymorph, which forms a low resistivity percolation pathway through the film. The small value of the Hall coefficient is consistent with the metallic behavior observed in the temperature dependence of the resistivity data. Since the sign of the Hall coefficient changes with temperature, the small magnitude of the Hall coefficient may also be a consequence of the electrons in the 1T-$MoSe_2$ layer competing with holes in the two BiSe layers in the unit cell. The structural data, electrical transport data and XPS results are consistent with the BiSe layers donating charge to the MoSe2 layers in $(BiSe)_{0.97}(Bi_2Se_3)_{1.26}(BiSe)_{0.97}(MoSe_2)$. The XPS data shows that the amount of 1T-$MoSe_2$ relative to 2H-$MoSe_2$ is larger than that observed in $(BiSe)_{0.97}(MoSe_2)$, and the resistivity of $(BiSe)_{0.97}(Bi_2Se_3)_{1.26}(BiSe)_{0.97}(MoSe_2)$ is lower than that of $(BiSe)_{0.97}(MoSe_2)$.[29,31] However, our understanding of how the properties of monolayers change as a result of being adjacent to different substrates and constituents is limited. The Hall data indicates that at least two bands are contributing to the electrical conductivity. We have no data that indicates whether this contribution comes from the BiSe or the Bi_2Se_3 layers. Preparing homologous

compounds with thicker Bi_2Se_3 (m) or $MoSe_2$ (n) layers, $(BiSe)_{0.97}[(Bi_2Se_3)_{1.26}]_m(BiSe)_{0.97}(MoSe_2)_n$, and correlating the electrical properties and the resulting percentage of 1T and 2H polymorphs of $MoSe_2$ with the values of *m* and/or *n* might enable us to better understand the interaction between constituent layers.

5.4. CONCLUSION

The new metastable heterostructure $(BiSe)_{0.97}(Bi_2Se_3)_{1.26}(BiSe)_{0.97}(MoSe_2)$ was prepared by selfassembly from designed precursors. Excess Bi was required to obtain $(BiSe)_{0.97}(Bi_2Se_3)_{1.26}(BiSe)_{0.97}(MoSe_2)$, which diffused during growth to form a cap of Bi_2Se_3. The *c*-axis and in-plane lattice parameters are consistent with the formation of $(BiSe)_{0.97}(Bi_2Se_3)_{1.26}(BiSe)_{0.97}(MoSe_2)$. The HAADF-STEM imaging indicates that two different polymorphs of $MoSe_2$ form as small domains and that the BiSe layers contained antiphase boundaries. The XPS Bi 5d spectra contain intensity from two oxidation states of Bi, which is consistent with Bi^0 in Bi-Bi bonds at the antiphase boundaries of BiSe and Bi^{3+} in the Bi-Se bonds in Bi_2Se_3 and BiSe. Two oxidation states of Mo were also observed in the XPS Mo 3d spectra, consistent with the presence of both 2Hand 1T-$MoSe_2$. According to XPS, about 40- 60% of the $MoSe_2$ in the heterostructure was of the 1T polytype. The low resistivity values at room temperature and the metallic temperature dependence are consistent with the formation of a continuous network of 1T-$MoSe_2$. The heterogeneous mix of $MoSe_2$ polytypes complicates the interpretation of the Hall data. The low magnitude is consistent with the metallic behavior observed in the resistivity. The change in the carrier type as a function of temperature indicates that carriers in more than one band contribute to the conductivity. The thermal stability and metallic resistivity of

$(BiSe)_{0.97}(Bi_2Se_3)_{1.26}(BiSe)_{0.97}(MoSe_2)$ might make it useful as an ohmic contact for devices containing $MoSe_2$ layers.

5.5. BRIDGE

A new compound $(BiSe)_{0.97}(Bi_2Se_3)_{1.26}(BiSe)_{0.97}(MoSe_2)$ was successfully synthesized by controlling precursor structure and composition to nucleate the desired repeat unit. HAADF-STEM/EDS confirmed the presence of metallic and semiconducting $MoSe_2$ polymorphs, which is due to charge donation in the sample and was also seen using X-ray photoelectron spectroscopy. This work emphasizes the role of interfaces in layered heterostructures. The next chapter also discusses how precise control over nanoarchitecture in the precursor and composition enables the formation of new compounds. This is explored for layered heterostructures containing $SnSe_2$ and VSe_2.

CHAPTER VI

CONTROLLING THE SELF-ASSEMBLY OF NEW METASTABLE TIN VANADIUM SELENIDES USING COMPOSITION AND NANOARCHITECTURE OF PRECURSORS

6.0. AUTHORSHIP STATEMENT

Chapter VI was published in the *Journal of the American Chemical Society* in 2020. Primary author Dmitri Cordova and co-author Taryn Kam prepared heterostructures and characterized samples with X-ray techniques. Ping Lu assisted with collection of HAADF-STEM/EDS data. David C. Johnson is my advisor. I prepared TEM specimen for HAADF-STEM and assisted with writing/analyzing data for sections pertaining to HAADF-STEM/EDS, in addition to editing the entire manuscript.

6.1. INTRODUCTION

Molecular synthesis is powerful, with chemists being able to perform total syntheses of complex molecules through a series of carefully designed steps beginning from simple precursors.[1] Several important factors have contributed to the development and success of this field. One factor is the ability to predict the structure of potential kinetically stable compounds using simple bonding rules (the octet rule and the 18-electron rule).[2,3] A second factor is the diversity of reagents and catalysts that can be used to transform a single functional group, allowing a reaction to be possible for a large number of substrates. A third factor is the typically homogeneous nature of reacting systems, where reactants dissolve in solvents while maintaining their structure. Most of the structure of the different reactants is

preserved in the product molecules, as targeted reactions break and make specific bonds. NMR and other spectroscopies give detailed information about speciation, enabling the kinetics of the transformation from reactants to products to be investigated.[4,5] This has enabled molecular chemists to develop rules based on reaction mechanisms to modify reaction parameters to control reaction pathways.[6] Because intermediates in a multistep synthesis can be purified, a sequence of specific reactions can be planned using retrosynthetic analysis to synthesize complicated molecules.[7]

In contrast, solid-state synthesis is considered "as much art as science", because the process is mainly experience- and intuition-driven.[8] This reflects important differences between the synthesis of extended structures and molecules. For example, it is much more challenging to predict the structure of potential products, because many metallic elements can have a variety of oxidation states and coordination numbers.[9] The formation of an extended structure also involves the repeated formation of specific bonds to form crystals with macroscopic amounts of atoms. This self-assembly of the crystal structure cannot be done using stepwise reactions. Hence, synthesis approaches are less developed and the analytical techniques used to follow reactions often require specialized instrumentation.[10] While the synthesis approach of extended solids using fluids (fluxes, mineralizers, or supercritical fluids) as solvents is similar in many respects to molecular synthesis,[11-13] the reactants typically do not maintain their structure upon dissolution, and very little is typically known about the speciation that occurs in the liquid phase.[14] Spectroscopy and other reaction monitoring methods are also more difficult to implement due to typically higher reaction temperatures, opaque fluid phases, and more challenging NMR nuclei.[15,16] Rapidly

developing in situ techniques such as transmission electron microscopy and pair distribution function analysis from total scattering can provide insight into compound formation at the atomic level.[17-25] Diffusion is the rate-limiting step in the direct reaction of solids at high temperature,[26] where reactions occur at the interfaces between particles. Because many different interfaces with different crystallographic orientations are reacting between different elements (A-B, B-C, A-C), different reactions will be occurring at different interfaces forming different products at different rates.[27] Most analytical approaches only provide the sum of all of these reactions, making kinetic studies challenging. In most reactions to form extended solids, high temperatures and long times are typically used, resulting in the formation of only thermodynamically stable compounds.[28,29] While the importance of solid-state reaction mechanisms to develop kinetically controlled synthesis approaches has been recognized, the field remains understudied.[30,31]

In the field of 2D materials, there is significant interest in the synthesis of heterostructures, especially those containing layered dichalcogenides because of their diverse properties and exfoliable nature due to weak van der Waals interactions between strongly bonded Se-M-Se layers.[32] The system explored here, $[(SnSe_2)_{1+\delta}]_1(VSe_2)_1$, is interesting because the phase diagram of Sn-V-Se contains only one ternary equilibrium phase, $SnVSe_3$, the misfit layer compound $(SnSe)_1(VSe_2)_1$.[33] The metastable heterostructure $[(SnSe_2)_{1+\delta}]_1(VSe_2)_1$ lies on the tie line connecting $SnSe_2$ and VSe_2. The misfit parameter, $1+\delta$, reflects the difference in the in-plane unit cell size of between the two layers in the heterostructure[34] and is equivalent to the number of $SnSe_2$ unit cells per VSe_2 unit cell. There have been no reported studies exploring the formation of $Sn_xV_{1-x}Se_2$ solid solutions;

however, the large difference in a-axis lattice parameters (3.356 Å for VSe_2 and 3.811 Å for $SnSe_2$)[35,36] suggests that there is limited solid solubility.[37] The $[(SnSe_2)_{1+\delta}]_1(VSe_2)_1$ heterostructure and the $Sn_xV_{1-x}Se_2$ solid solution with $x \sim 0.43$ targeted here both cannot be synthesized using a classical high temperature solid-state synthesis route.

Here we use precursors made of a repeating sequence of Sn| Se|V|Se elemental layers to selectively form the metastable solids $[(SnSe_2)_{0.80}]_1(VSe_2)_1$ and $SnxV_{1-x}Se_2$ at low reaction temperatures. The precursors were designed to have different nanoarchitectures, defined as the sequence and thicknesses of the elemental layers deposited. While the layer sequence is the same, the modulation length of precursors I and II differ by a factor of 2. X-ray reflectivity and X-ray diffraction (specular and in-plane) were used to follow the self-assembly of $[(SnSe2)0.80]_1(VSe_2)_1$. Laue oscillations observed in the XRR patterns enable us to determine the number of unit cells of $[(SnSe_2)_{0.80}]_1(VSe_2)_1$ perpendicular to the substrate as a function of annealing temperature. In-plane XRD patterns enable us to independently follow the lateral growth of $SnSe_2$ and VSe_2. This data was used to develop an atomic scale picture of the reaction mechanism. The proposed reaction mechanism was tested by the different nanoarchitecture of precursor II, which formed the new metastable alloy, $Sn_xV_{1-x}Se_2$. Using an energy landscape, we rationalized why local composition and nanoarchitecture allowed us to discriminate between different reaction pathways.

6.2. EXPERIMENTAL

Thin film multilayer precursors were deposited on (100) oriented Si wafers with native oxide using a custom-built high vacuum physical vapor deposition (PVD) chamber with pressures maintained below 2 × 10-7 Torr. Se (Alfa-Aesar, 99.999%) was deposited

using a Knudsen effusion cell, while V (Alfa-Aesar, 99.7%) and Sn (AlfaAesar, 99.98%) were deposited using 6 keV electron beam guns. More detailed information about the instrument setup is found elsewhere.[38] The thickness of each element deposited at each step was monitored by quartz crystal microbalances found above each elemental source. A custom-made LabView code controls the opening and closing of pneumatic shutters to control the sequence and amount of each element deposited.

The areal density (in atoms/Å2) of each element was measured using X-ray fluorescence (XRF) on a Rigaku ZSX Primus II spectrometer. For each sample, the background signal was subtracted using the actual measurement from blank substrates as described by Hamann and co-workers.[39]

Precursors were annealed on a hot plate in a drybox with an inert atmosphere (O2 < 0.8 ppm). X-ray reflectivity (XRR) and specular Xray diffraction (XRD) patterns were collected on a Bruker D8 diffractometer equipped with Cu Kα radiation. One piece of precursor I was annealed for 5 min at various temperatures to determine the processing conditions to form $[(SnSe_2)_{0.80}]_1(VSe_2)_1$. A second piece of precursor I and precursor II were annealed at the optimum processing conditions. The Kiessig and Laue oscillations observed in the XRR pattern were used to calculate the thickness of the film via a modified form of Bragg's Law and the size of the coherently scattering domains, respectively. Grazing incidence in-plane diffraction (GIXRD) patterns were collected on a Rigaku Smartlab diffractometer also equipped with Cu Kα radiation. A model for the position of the atomic planes along the c axis was optimized by Rietveld refinement of the specular X-ray diffraction patterns using the GSASII.[40] LeBail fitting of the in-plane X-ray diffraction using

the FullProf Suite was used to refine lattice parameters.[41] A thin cross-section of the film was prepared with an FEI Helios NanoLab 600i DualBeam FIB-SEM using standard lift-out procedures. Scanning transmission electron microscopy data was collected on an FEI Titan G2 80-200 scanning transmission electron microscope (STEM) with a Cs probe corrector and ChemiSTEM technology (X-FEG and SuperX EDS with four windowless silicon drift detectors) operated at 200 kV. High angle annular dark field (HAADF) images were taken with an electron probe of size (fwhm)of about 0.13 nm, current of ~75 pA, convergence angle of 18.1 mrad, and using an annular dark-field detector with a collection range of 60-160 mrad.

6.3. RESULTS

Two multilayer precursors (I and II) with repeating structure Sn|Se|V|Se were deposited. The lattice parameters of bulk VSe_2 and $SnSe_2$ were used to calculate the required number of atoms in each Sn|Se|V|Se sequence to form Se-M-Se trilayers of both VSe_2 and SnSe2.[36,42] Precursor I used these targets and the Sn|Se|V|Se sequence was repeated 41 times. Precursor II contained the Sn|Se|V|Se sequence repeated 82 times, with each sequence containing one-half the number of atoms needed to form each Se-M-Se trilayer. The two precursors contain the same number of atoms but with a different nanoarchitecture. The total number of atoms of Sn, V, and Se per $Å_2$ (areal density) were measured using XRF and are summarized in Table 6.1 along with the targeted values. The measured values of Sn and V for both precursors are within theerror of the target amounts. Assuming a single-phased heterostructure product forms and that the excess/vacancies of Se is evenly distributed among the two phases, the precursor I stoichiometry is

$[(SnSe_2)_{0.78}]_1(VSe_2)_1$ and precursor II stoichiometry is $[(SnSe_{2.3})_{0.78}]_1(VSe_{2.3})_1$. In terms of a solid solution, precursor I's stoichiometry is $Sn_{0.43}V_{0.57}Se_2$ and precursor II's stoichiometry is $Sn_{0.43}V_{0.57}Se_{2.29}$.

Table 6.1. Number of Atoms per Unit Area Determined Using XRF Compared to Target Values Based on the Lattice Constants of Bulk $SnSe_2$ and VSe_2

		total number of atoms (Å^2)		
material	repeating units	Sn	V	Se
precursor I	41	3.3(1)	4.3(1)	14.6(4)
precursor II	82	3.13(9)	4.1(1)	16.6(5)
VSe_2[35]	41	0	4.203(3)	8.406(6)
$SnSe_2$	41	3.256(5)	0	6.52(1)

The limiting reagent in precursor I is Se, and there is enough Se to form 40(1) unit cells of the heterostructure or 80(2) unit cells of the alloy. In precursor II, the rate limiting reagent to form the heterostructure is Sn and there is enough Sn to form 39(1) unit cells of the heterostructure. With respect to the alloy, the metals are the limiting reagent and there is enough metal to form 79(1) unit cells of $Sn_xV_{1-x}Se_y$.

The evolution of a piece of precursor I was followed as a function of annealing temperature using XRF, XRR, and XRDto determine the conditions to form a single-phase $[(SnSe_2)_{1+\delta}]_1(VSe_2)_1$ sample (Figure 6.1). The XRR scan (Figure 6.1b) contains Kiessig fringes from the interference between the front and the back of the deposited film.[43] The spacing of the Kiessig fringes yield a film thickness of 550.8(6) Å, and the angle where the Kiessig fringes can no longer be observed yields a surface roughness of ~6 Å. The number of Kiessig fringes observed before the Bragg maxima from the modulation of the electron density in the precursor is consistent with the presence of 41 repeating sequences of

Sn|Se|V|Se layers. The position of the first two Bragg reflections from the Sn|Se|V|Se sequence of layers yields a modulation length of 13.5 Å. This is slightly larger than the sum of the c-axis lattice parameters of bulk VSe_2 and $SnSe_2$, 12.247(2) Å, because amorphous layers have a lower density than their crystalline counterparts. There is also a broad maximum at ~14°, suggesting that nucleation and coherent stacking of dichalcogenide layers occurs during deposition. Scherrer analysis of the line width suggests that the thickness of the coherent stacking is only a few layers thick. The XRR and XRF data (Figure 6.1a,b) indicate that the nanoarchitecture of the precursor is close to what was targeted and resembles the desired product.

The diffraction data (Figure 6.1c,d) collected on the as deposited precursor is consistent with the XRR discussion. The specular XRD pattern (Figure 6.1c) contains two narrow Bragg reflections from the repeating Sn|Se|V|Se sequence of layers and broad reflections from self-assembly occurring during the deposition of the precursor. The broad reflections at ~14° and 28° indicate that coherent domains have formed. The in-plane XRD pattern (Figure 6.1d) contains *hk0* peaks that can be indexed to two hexagonal unit cells, $SnSe_2$ and VSe_2, with *a*-lattice parameters of 3.78(1) and 3.39(1) Å. The peak widths of $SnSe_2$ is narrower than VSe_2, indicating that there are larger in-plane grains of $SnSe_2$ than VSe_2.

The data collected between 100 °C and 300 °C show that $[(SnSe_2)_{1+\delta}]_1(VSe_2)_1$ gradually self-assembles during this temperature range. The XRF data (Figure 6.1a) indicates that there is a small decrease in the amount of Se in this temperature range, which results from evaporation of Se while annealing. The XRR patterns (Figure 6.1b) contain an additional low frequency Kiessig oscillation due to the growth of an oxide at the surface of the film. The

film thickness calculated from the high frequency Kiessig fringes in the XRR indicate that the film thickness gradually decreases as annealing temperature increases, which is a consequence of both the loss of Se and the increasing density of the film. The first two diffraction maxima shift in angle on annealing at 100 °C and then increase in intensity and become narrower as annealing temperature increases. Laue fringes,[44,45] which originate from the finite number of unit cells in the coherently diffracting coherent domains of the film, are clearly visible on the diffraction maxima at 14° and become closer together as the annealing temperature increases. This indicates that the majority of the coherent domains are the identical thickness, which can be calculated from the frequency of the Laue oscillations. During the growth process, the low angle Bragg reflections from the artificial layering of the precursor disappears. The specular XRD patterns (Figure 6.1c) confirm the formation of $[(SnSe_2)_{1+\delta}]_1(VSe_2)_1$ and corroborate growth of the coherent domains perpendicular to the substrate. Starting at 100 °C, long-range order starts to develop as additional 00*l* reflections appear at higher angles. These 00*l* reflections increase in intensity, reaching a maximum at 250-300 °C. The positions of the 00*l* Bragg reflections yield a *c*-axis lattice parameter of 12.69(1) Å, which is slightly larger than the sum of the *c*-axis lattice parameters of bulk VSe_2 and $SnSe_2$, 12.247(2) Å, presumably due to the in-plane lattice mismatch preventing nesting of one constituent layer in the other. Laue oscillations, indicating a common size for the different $[(SnSe_2)_{1+\delta}]_1(VSe_2)_1$ domains after each annealing temperature, are observed on the first several Bragg reflections and will be discussed more fully in the next paragraph. The in-plane diffraction patterns (Figure 6.1d) reflect the in-plane crystal growth that also occurs during annealing. The $SnSe_2$ *hk*0 reflections exhibited only small changes in peak width and intensity, indicating that most of the SnSe2 is crystalline as deposited and the crystallite size

does not increase during the annealing. The VSe_2 *hk*0 reflections, however, noticeable increase in peak intensity and decrease in peak width as annealing temperature increases, indicating an increase in the amount of crystalline VSe_2 and growth of the in-plane grain sizes.

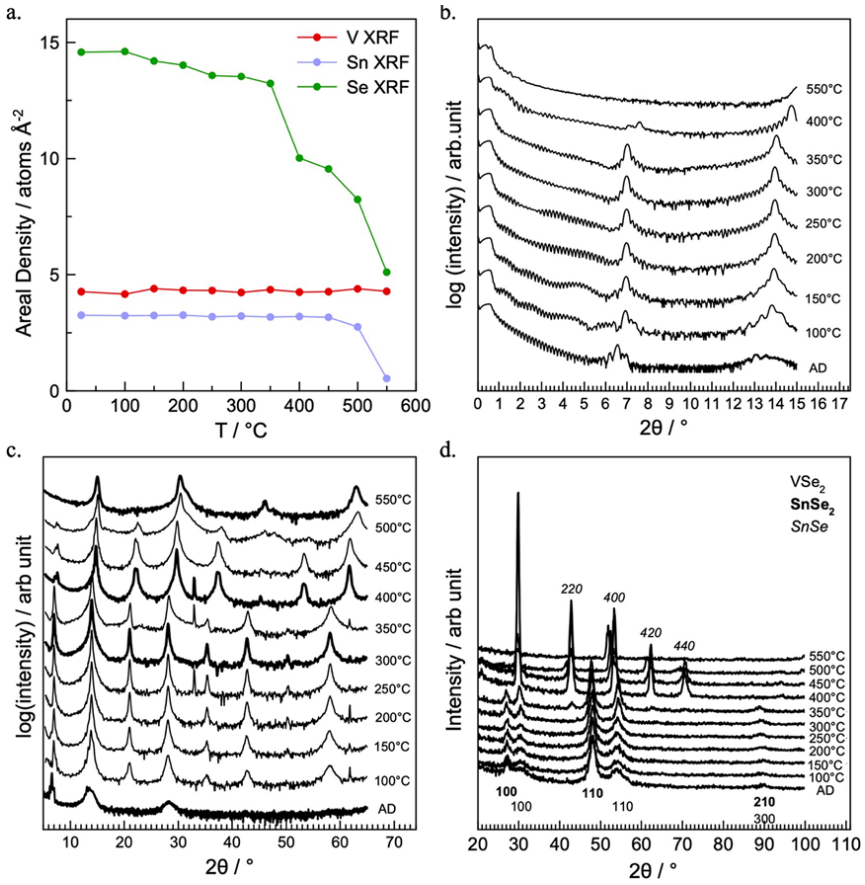

Figure 6.1. Evolution of Sn|Se|V|Se precursor annealed at di*ff*erent temperature steps. (a) The number of atoms per Å^2 of each element measured byXRF at each temperature step and calculated from the number of unit cells and *a*-lattice parameters at RT, 250 °C, and 400 °C. (b) X-ray re*fl*ectivity patterns showing the evolution of the overall *fi*lm structure (c) Specular X-ray di*ff*raction showing the evolution of the structure perpendicular to the substrate. (d) Grazing incidence in-plane X-ray di*ff*raction showing the evolution of the structure in the plane parallel to the substrate.

The characterization data in this temperature range provide a coherent picture of the self-assembly of $[(SnSe_2)_{1+\delta}]_1(VSe_2)_1$ from the as-deposited precursor. Figure 6.2a contains a

closer view of the Laue oscillations visible on the 002 reflection of $[(SnSe_2)_{1+\delta}]_1(VSe_2)_1$ after each annealing temperature. The presence of these oscillations indicates that a large majority of the suite of $[(SnSe_2)_{1+\delta}]_1(VSe_2)_1$ domains at each temperature are the identical size and an integral number of unit cells thick, which can be calculated from the spacing of the Laue oscillations. Figure 6.2b graphs the change in the size of the domains as a function of annealing temperature. At 250 °C, the number of unit cells reach its maximum value of 37. The number of unit cells formed is smaller than expected due to loss of Se and oxidation at the film surface. The overall film thickness (calculated from Kiessig oscillations) decreases by a small amount as the target product grows, due to densification of the film as it self-assembles and loss of some Se. The difference between the total film thickness and the thickness of 37 unit cells of $[(SnSe_2)_{1+\delta}]_1(VSe_2)_1$ at 250 °C is due to an oxide layer on the surface of the film. The areal density of Se measure using XRF is consistent with that expected for 37 unit cells of $[(SnSe_2)_{1+\delta}]_1(VSe_2)_1$ at 250 °C (solid green line, Figure 6.1a).

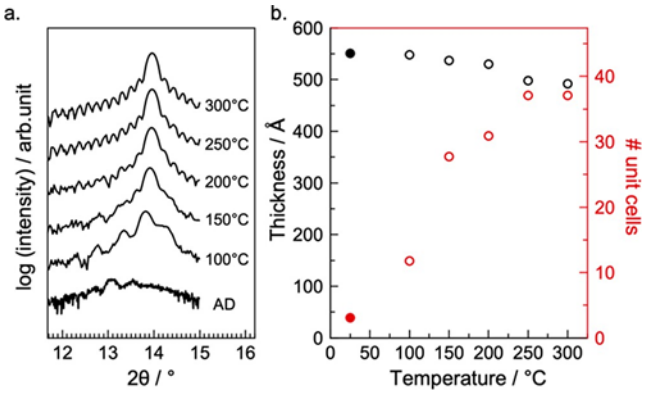

Figure 6.2. (a) Laue oscillations coming from the coherent film thickness at different temperatures. (b) Kiessig (black circles) and Laue (red circles, left axis) film thickness, and the number of unit cells (red circles, right axis) formed at each annealing temperature. The size of the coherent domain in the as-deposited sample (filled red circle) is estimated from the line width of the 002 reflection.

A growth mechanism consistent with the characterization data is shown in Figure 6.3. The most difficult fact to explain is that the majority of the film consists of domains of $[(SnSe_2)_{1+\delta}]_1(VSe_2)_1$ that are exactly the same integral number of unit cells throughout the annealing process. One possible explanation is that the coherent domains in the as-deposited film grow out from the substrate film interface as the film is deposited. This would provide a common starting point for all of the domains. The domains would stop growing as the film is deposited because metal atoms would need to diffuse through a thicker layer of amorphous Se and the increasing accumulated roughness as the film becomes thicker would decrease the coherence of the later deposited layers. The inplane diffraction patterns suggest that most of the $SnSe_2$ forms large 2D grains during the deposition. There are fewer and smaller domains of VSe_2 and unreacted V|Se layers between the $SnSe_2$ grains. As the precursor is annealed, the number of unit cells in the coherent domains near the substrate increase and an oxide layer forms at the film surface. The coherent domains grow at the same rates because the diffusion distances for atoms to arrive at the growth fronts are similar as a result of the nanoarchitecture of the precursor. Nucleation of the dichalcogenide takes place at the growth front near small crystallites because heterogeneous nucleation is easier due to the presence of an existing surface. Homogenous nucleation far away from the growth front is unfavorable because it would require the formation of a larger amount of additional surface area.[46] During this process, lateral growth of existing VSe_2 layers in the precursor occurs and additional VSe_2 layers selfassemble between existing $SnSe_2$ layers as charge transfer between the layers stabilize the intergrowth. Excess Se diffuses to the surface and evaporates. The difference in the selfassembly behavior of $SnSe_2$ and VSe_2 results in an interesting dynamic between lateral and perpendicular growth of $[(SnSe_2)_{1+\delta}]_1(VSe_2)_1$. Overall,

the formation of the heterostructure is enabled by the low reaction temperatures, which limit long-range diffusion so that the Sn|Se and V|Se layers are crystallized without losing the nanoarchitecture of the precursor. The strain energy associated with Sn substituting for V in VSe_2 or V substituting for Sn in $SnSe_2$, combined with compositional modulation in the precursor, limit the extent of alloy formation.

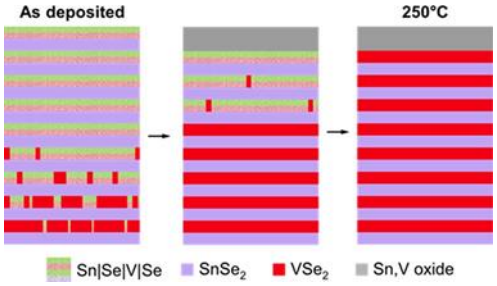

Figure 6.3. Proposed formation and growth mechanism for $[(SnSe_2)_{1+\delta}]_1(VSe_2)_1$.

Further annealing to 400 °C results in the decomposition of $[(SnSe_2)_{1+\delta}]_1(VSe_2)_1$ as Se is lost and $[(SnSe)_{1.15}]_1(VSe_2)_1$ forms. The XRF data (Figure 6.1a) shows a substantial drop in the number of Se atoms per $Å^2$ starting at 350 °C. This is close to the decomposition temperature of bulk $SnSe_2$ to SnSe (340 °C).[47] Changes in the XRR pattern (Figure 6.1b) from 300 °C to 400 °C demonstrate that the $SnSe_2$ layers have indeed decomposed. The decrease in the Kiessig fringe amplitude point to a change in the density of the film. The number of unit cells also decrease to 32, suggesting that not all of the $[(SnSe_2)_{1+\delta}]1(VSe_2)_1$ layers were converted to $[(SnSe)_{1.15}]_1(VSe_2)_1$. This is not at all surprising because SnSe has a higher atomic areal density of Sn than $SnSe_2$. The $SnSe_2$ decomposition does not reduce the number of VSe_2 layers, because VSe_2 is kinetically stable up to 400 °C.[48] The VSe_2 layers that are not in the heterostructure likely exist as small VSe_2 grains within the film. The retention

of the Kiessig fringes in the XRR pattern show that the film remains smooth during this transition. The *c*-axis lattice parameter of 12.02(1) Å after the 400 °C anneal is consistent with previously reported $[(SnSe)_{1.15}]_1(VSe_2)_1$.[49] The odd order reflections are broader than the even order reflections, presumably due to peak splitting from extra planes of VSe_2 separating domains of $[(SnSe)_{1.15}]_1(VSe_2)_1$ by half of a unit cell's thickness within the interior of the film.[50] The in-plane diffraction data (Figure 6.1d) supports the formation of SnSe.[49] After the 350 °C anneal, *hk*0 reflections from VSe_2, $SnSe_2$ and SnSe are present. After the 400 °C anneal, the $SnSe_2$ *hk*0 reflections are no longer present. The *a*-axis lattice parameter of the VSe_2 phase is 3.43(1) Å, consistent with previously studied $[(SnSe)_{1.15}]_1(VSe_2)_1$ (VSe_2 a = 3.414(3) Å).[49] SnSe has a square unit cell and an *a* axis-lattice parameter of 5.94(1) Å, which is also consistent with previous reports for $[(SnSe)_{1.15}]_m(VSe_2)_1$ (SnSe a = 5.91-5.92 Å).[51]

The last phase transition involves the disproportionation and subsequent oxidation of $[(SnSe)_{1.15}]_1(VSe_2)_1$ at temperatures greater than 450 °C, even though the sample was annealed in a drybox with low oxygen concentration. Another dramatic drop in Se atoms per $Å^2$ is observed during this last transition (Figure 6.1a). This transition coincides with an increase in oxygen XRF intensity and decrease in Sn atoms per $Å^2$. These stoichiometry changes suggest that the disproportionation is accompanied by the oxidation of and/or V and the loss of both Sn and Se through volatile species. The XRR data shows that the film roughness significantly increases. The 00*l* peaks in the XRD shift to higher angles and broaden starting at 500 °C. Odd order 00*l* reflections are completely diminished at 550 °C, and what remains are 00*l* reflections coming from a structure with a *c*-lattice parameter of 5.90(1) Å, consistent with some nonstoichiometric VSe_2 remaining in the film.[42] At the

highest temperature studied, only *hk*0 reflections (Figure 6.1d) from two closely related hexagonal lattices are observed, with *a*-lattice parameters of 3.46 and 3.52 Å, suggesting that the major phase present is VSe_2 with different values of x and y in the formula $V_{1+x}Sn_ySe_2$.

A second piece of precursor I was annealed at 250 °C for 5 min based on the annealing data, and its XRR pattern is shown in Figure 6.4a (black circles). The Laue oscillations around the first-order Bragg maximum are consistent with 39 layers of $[(SnSe_2)_{1+\delta}]_1(VSe_2)_1$ self-assembling during the anneal. Fewer layers oxidized during this single annealing step compared to the sequential annealing done on the first piece of precursor I. The total thickness determined from the Kiessig fringes is larger than 39 times the unit cell parameter of $[(SnSe_2)_{1+\delta}]_1(VSe_2)_1$, as two of the deposited precursor layers did not form the intended product. We modeled the XRR data using the program GenX to calculate the XRR pattern from our proposed structural model.[52]

The calculated pattern, shown in Figure 6.4a (red line), matches the experimental pattern, and the film parameters in the model are summarized in Table 6.2.

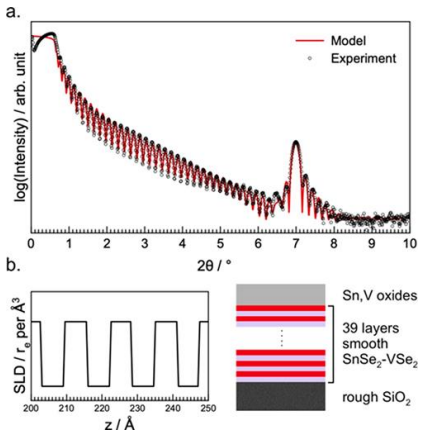

Figure 6.4. (a) XRR modeling of the optimized $[(SnSe_2)_{0.80}]_1(VSe_2)_1$ heterostructure. (b) Electron density pro*f*ile and schematic of the filmbased on the model.

The model contained 39 unit cells of $[(SnSe_2)_{0.80}]_1(VSe_2)_1$ with atomically smooth interfaces between the constituents, a rough layer of SiO_2 below the $[(SnSe_2)_{0.80}]_1(VSe_2)_1$ block, and a rough layer of tin/vanadium oxides above it. The thickness of the top oxide layer is approximately equal to that of the two missing unit cells, suggesting that they were mostly lost to oxidation. A thin interdiffusion region was required in the model to match the experimental pattern, which is consistent with a small amount of initially deposited Sn reacting with the SiO_2 surface during deposition.

Table 6.2. Thin Film Modeling Parameters Obtained from XRR Fitting (FOM = 0.141).

layer	no. of layers	thickness (Å)	density (FU per Å^3 × 10^{-2})	roughness (Å)	interdiffusion (Å)
Sn/V oxides	1	24.1(6)	1.6(1)	3.4(4)	–
VSe_2	39	6.31(4)	1.55(4)	–	–
$SnSe_2$		6.38(2)	1.28(4)	–	–
SiO_2	1	50(20)	1.7(5)	2(1)	4(1)

Rietveld analysis of the specular X-ray diffraction of $[(SnSe_2)_{0.80}]_1(VSe_2)_1$ is shown in Figure 6.5. Because only 00*l* reflections are observed, a Rietveld analysis only provides information on the atomic positions of the atomic planes in the heterostructures that are parallel to the substrate. To simplify the analysis, a model with V at zero and Sn at half the *c*-axis lattice parameter was used, with a mirror plane at the halfway point. The refined V-Se distance of 1.54 Å is close to those observed in other VSe_2 heterostructures such as $[(SnSe)_{1+\delta}]_1(VSe_2)_1$(1.48(2) Å),[49] $[(PbSe)_{1+\delta}]_1(VSe_2)_1$(1.54 Å),[53] $[(BiSe)_{1+\delta}]_1(VSe_2)_1$(1.52(1) Å),[54] and bulk VSe_2(1.57 Å).[35] The refined Sn-Se distance (1.59 Å) is close to that observed in $[(SnSe2)_{1+\delta}]_1(MoSe2)_1$ (1.57 Å)[55] and bulk $SnSe_2$ (1.53 Å).[36] The refined van der Waals gap of 3.21 Å is larger than those observed in either VSe_2 or $SnSe_2$ but smaller than the gap found in $[(SnSe_2)_{1+\delta}]1(MoSe_2)_1$ (3.35(1) Å).[55] The large van der Waals gap is a consequence of the large difference between the in-plane lattice parameters of VSe_2 and $SnSe_2$, which prevents

the Se atoms on either side of the van der Waals gap from nesting in between the Se atoms of the adjacent layers.

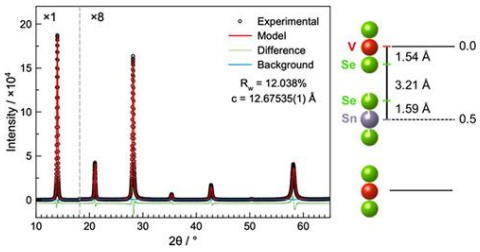

Figure 6.5. Rietveld refinement result of the specular X-ray diffraction of [(SnSe2)0.8]1(VSe2)1 and the atomic z-plane model of the average structure.

A LeBail fit of the in-plane X-ray diffraction data of the second piece of precursor I is shown in Figure 6.6. All reflections can be indexed as *hk*0 reflections from two different hexagonal unit cells. The calculated *a*-axis lattice parameter for the $SnSe_2$ constituent (3.79(1) Å) is only slightly lower than what is observed for bulk $SnSe_2$ (3.811 Å)[36] and in $[(SnSe)_{1+\delta}]_1(MoSe_2)_1$ (3.81 Å).[55]The calculated a-axis lattice parameter for the VSe_2 constituent (3.39(1) Å) is between the bulk value for stoichiometric VSe_2 (3.358 Å)35 and that reported for $[(SnSe)_{1+\delta}]_1(VSe_2)_1$ (3.414 Å). Using the in-plane lattice constants, a misfit parameter, 1+δ, of 0.80(4) is calculated. From this point on, the heterostructure crystallized from the second piece of precursor I is referred to as $[(SnSe_2)_{0.80}]_1(VSe_2)_1$.

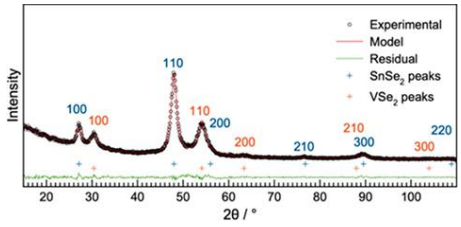

Figure 6.6. LeBail fit of the grazing incidence in-plane X-ray diffraction pattern of the $[(SnSe_2)_{0.80}]_1(VSe_2)_1$ heterostructure.

HAADF-STEM data were obtained on a cross-section of the $[(SnSe_2)_{0.80}]_1(VSe_2)_1$ film from the second annealed piece of precursor I to obtain information about the relative orientation of the dichalcogenide layers. Figure 6.7a contains an image of the entirety of the film, which shows that the film is homogeneous and smooth, consistent with the modeling of specular XRD and XRR. There are 38 layers of $[(SnSe_2)_{0.80}]_1(VSe_2)_1$ clearly visible, with another layer occasionally found at the top or bottom of the film. A closer look of the film at higher magnification, Figure 6.7b, contains alternating dark and bright layers that can be identified as VSe_2 and $SnSe_2$, respectively, because heavier elements appear brighter in HAADF-STEM data.[56] There are noticeably dark regions between the interfaces of the $SnSe_2$ and VSe_2 layers due to the van der Waals gap between the two constituents. The inset of Figure 6.5b shows a region of layers with high atomic resolution that happens to show zone axis views of both constituent layers. Only the ⟨110⟩ and ⟨120⟩ orientations of the two constituents are clearly resolved in the images. Both the VSe_2 and $SnSe_2$ layers exhibit octahedral coordination, which is consistent with the bulk structures of $SnSe_2$ and VSe_2. It is apparent from the microscopy data that there is a large degree of turbostratic disorder and lack of long-range order in the heterostructure. A close inspection of the entirety of the cross-section reveals that there are no large grains containing multiple repeating units crystallizing with a consistent orientation. Qualitative analysis of Figure 6.7b gives an estimated grain size of 5 nm, smaller than the grain sizes observed from other heterostructures that have long-range order.[57] These features can be traced to the large lattice mismatch and weak interaction between the constituents.

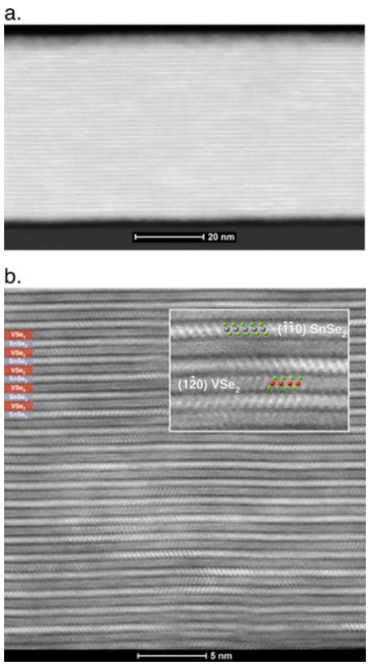

Figure 6.7. HAADF-STEM image of the (a) entirety and (b) large section of the film shows that it consists of $[(SnSe_2)_{0.80}]_1(VSe_2)_1$.

More information on the elemental distribution of the atoms within the layers was collected by EDX analysis of a small section of the film (Figure 6.8). The elemental EDX map confirms that there are alternating atomic layers of Sn and V separated by Se. However, there are regions where there is V-intensity in the Sn positions and vice versa. Because the unexpected intensities are not uniform across the analyzed region, it is likely due to inhomogeneous cross-substitution (e.g., VSe_2 replacing $SnSe_2$ or vice versa) across layers rather than homogeneous alloying (e.g., $Sn_xV_{1-x}Se_2$) within the layers. Substitutional defects of this type have been observed in nonstoichiometric $[(SnSe)_{1+\delta}]_1(VSe_2)_1$ when there are deliberate variations in global composition.[58] Homogenous alloys such as $[(SnSe)_{1+\delta}]_1(Ta_xV_{1+x}Se_2)_1[(SnSe)_{1+\delta}]_1(V_yTa_{1-y}Se_2)_1$ have clearly resolved V intensity peaks in Ta

positions and vice versa.[59] In $[(SnSe_2)_{0.80}]_1(VSe_2)_1$, we speculate this result comes from variations in local composition that are difficult to control during the deposition process.

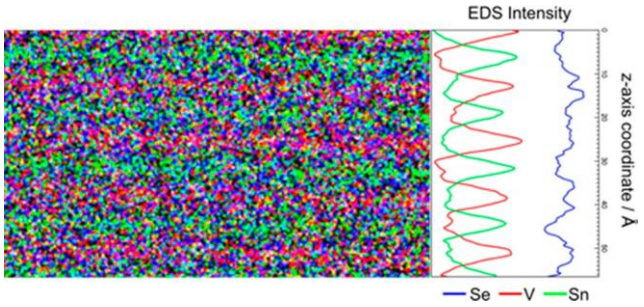

Figure 6.8. EDX elemental analysis of a section of the film showing atomic plane position of the elements.

The data presented above on precursor I and the mechanism for growth prompted us to prepare precursor II to probe the relative importance of composition versus nanoarchitecture on product formation. We intended precursor II to have the same composition as precursor I but half the initial modulation length of the deposited sequence of Sn|Se|V|Se layers. Our question was "what would form from this precursor?". Only short-range diffusion would be required to form the metastable alloy $Sn_xV_{1-x}Se_2$ and roughly twice that diffusion distance would be required to form the metastable compound $[(SnSe_2)_{0.80}]_1(VSe_2)_1$. Alternatively, small domains of VSe_2 interwoven with larger domains of $SnSe_2$ might form, or Se might segregate, enabling the thermodynamically stable compound $[(SnSe)_{1.15}]_1(VSe_2)_1$ to form. On the basis of the data from precursor I, we expected $SnSe_2$ would nucleate first, but the formation of large in-plane grains of $SnSe_2$ would be inhibited by increasing concentrations of vanadium atoms at the growth front.

Figure 6.9 contains diffraction data on precursor II. The experimental modulation length of the layering in the as-deposited precursor II was 7.27 Å, close to the *c*-axis lattice

parameters of tin and vanadium diselenides. Figure 6.9a contains the specular and in-plane diffraction patterns of precursor II after it was annealed at 250 °C. The specular diffraction pattern containing four reflections, that can be indexed as 00*l* reflections, yields a *c*-axis lattice parameter of 6.23(1) Å. The 110 reflection from the in-plane diffraction pattern (Figure 6.9b) of this sample is split, suggesting that the products are a vanadium-rich and a tin-rich dichalcogenide alloy. Vegard's law can be used to estimate the composition of the majority components from the resulting *a*-axis lattice parameters of *a* = 3.49(1) and 3.75(1) Å. The calculated compositions of the two phases observed are $Sn_{0.86}V_{0.14}Se_2$ and $Sn_{0.29}V_{0.71}Se_2$. We suggest that $SnSe_2$ nucleates and grows but incorporates some V due to the increasing concentration of V at the growth front. The increased concentration of V results in the nucleation of the vanadium-rich dichalcogenide. These events occur randomly and result in the random intergrowth of the two alloys rather than a precisely layered nanoarchitecture.

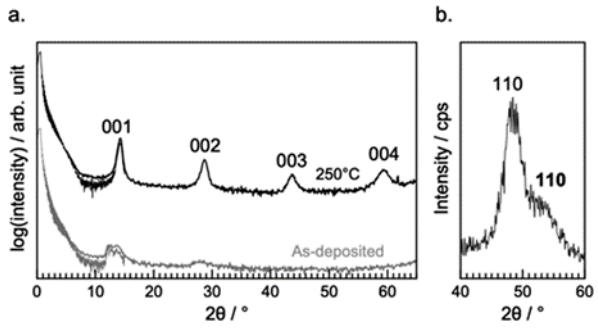

Figure 6.9. Synthesis of a new SnxV1-xSe2 alloy. (a) Specular X-ray diffraction of a precursor with half the number of required atoms per layer. (b) In-plane X-ray diffraction of the tin and vanadium diselenide alloy showing the presence of alloys with two different values of x.

6.4. DISCUSSION

Traditional materials synthesis approaches have few parameters that can be used to control a reaction pathway to a specific product, instead relying on changing the system conditions (temperature, pressure, composition) to make the desired product thermodynamically stable. The results presented herein indicate that both the local composition and nanoarchitecture of precursors, which controls the initial distribution of atoms, provide a means to choose between different self-assembly pathways. An energy landscape provides a useful tool to visualize key aspects reaction pathways, and Figure 6.10 contains an energy landscape consistent with the results of our study. Figure 6.10 shows the two kinetically stable phases formed in this study: $[(SnSe_2)_{0.80}]_1(VSe_2)_1$ and $Sn_{1-x}V_xSe_2$ exist as local minima and the misfit layer compound $[(SnSe)_{1.15}]_1(VSe_2)_1$ as the thermodynamic global minimum. Three different starting points are shown, corresponding to precursors I and II, and precursor A containing less Se with the nanoarchitecture designed to form the misfit layer compound $[(SnSe)_{1.15}]_1(VSe_2)_1$. As the layers in precursor I self-assemble to form $[(SnSe_2)_{1+\delta}]_1(VSe_2)_1$, the free energy drops as the system falls into the local minima (solid black line from site I). The formation of $SnSe_2$ during the deposition, facilitated by the local composition and nanoarchitecture of precursor I, selects this reaction pathway. Precursor II, while having the same overall composition, has a nanoarchitecture that does not provide enough Sn in any single elemental layer to form large grains of $SnSe_2$. When $SnSe_2$ nucleates, the growth front quickly becomes enriched in V, resulting in the formation of the metastable alloy, $Sn_{1-x}V_xSe_2$ (black dash dot line from site II). Precursor A, reported by Atkins and co-workers, had a nanoarchitecture similar to precursor I, containing alternating Sn- and V-rich layers but ~25% less Se.[49] This precursor forms $[(SnSe)_{1.15}]_1(VSe2)_1$, as there was not

sufficient Se to nucleate $SnSe_2$ during the deposition. There are large activation barriers between the different products initially formed because it would be necessary to create regions with the local composition required to nucleate the different alternatives, and this would require long-range solid-state diffusion which has a high activation energy.[49] The importance of local composition is also seen in a paper by Falmbigl and coworkers, which involved the reaction of a Sn|Se|V|Se precursor with a nanoarchitecture similar to that of precursors I and A but with an intermediate amount of Se.[60] In this precursor, annealing at 100 °C resulted in the simultaneous crystallization of $SnSe_2$, SnSe, and VSe_2 and all of these exhibited significant in-plane grain growth between 100 °C and 300 °C. The simultaneous formation of all three constituents suggests that the difference between the nucleation barriers for the three phases is small and controlled by the local Sn and Se composition.

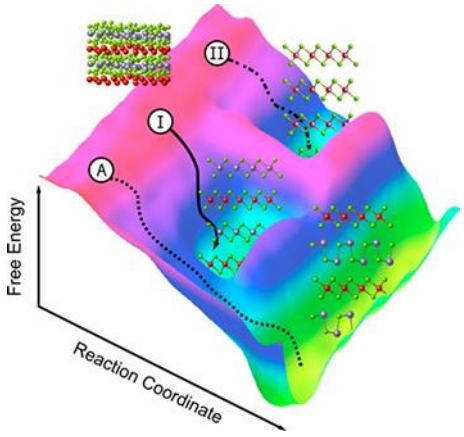

Figure 6.10. Free energy landscape of tin vanadium selenides.

6.5. CONCLUSIONS

In this work, in-plane diffraction measurements and Laue oscillations present in X-ray reflectivity scans of a designed precursor, as it evolved into a metastable heterostructure,

enabled us to determine the absolute size of the growing crystal as a function of temperature. This data provided insights into the self-assembly mechanism and defined optimum processing conditions to form a new kinetically stable misfit layer compound, $[(SnSe_2)_{0.80}]_1(VSe_2)_1$, with minimum oxidation. Controlling the local composition of the precursor enabled $[(SnSe_2)_{0.80}]_1(VSe_2)_1$ to preferentially form over $[(SnSe)_{1.15}]_1(VSe_2)_1$. Preparing a precursor with the same overall composition but different nanoarchitecture resulted in the formation of a new kinetically stable $Sn_xV_{1-x}Se_2$ alloy instead of $[(SnSe_2)_{0.80}]_1(VSe_2)_1$. The different reactions encountered from annealing studies of closely related multilayer systems were discussed in terms of an energy landscape as an effort to rationalize the different self-assembly pathways observed. The results show that nanoarchitecture and local composition are complementary design parameters to direct the self-assembly of new kinetically stable compounds along different reaction pathways in the energy landscape.

6.6. BRIDGE

This chapter builds on the ideas in previous chapters, which discusses the impacts of nanoarchitecture and local composition on the formation of new compounds. Two closely related metastable tin vanadium selenides were synthesized utilizing these ideas. HAADF-STEM/EDS confirmed the structure of the $[(SnSe_2)_{0.80}]_1(VSe_2)_1$ compound. The next chapter continues this expansion of how precursor structure, interfaces, and composition impact the formation of layered heterostructures. VSe_2 is used as one of the constituents in this next chapter, but now with neighboring PbSe layers to target a variety of $[(PbSe)_{1+\delta}]_q(VSe_2)1$ compounds.

CHAPTER VII

THE INSTABILITY OF MONOLAYER-THICK PBSE ON VSE_2

7.0. AUTHORSHIP STATEMENT

Chapter VII was published in *ACS Chemistry of Materials* in 2020. Primary author Dmitri Cordova and co-authors Shannon Fender, Mina Buchanan, and Taryn Kam prepared heterostructures and analyzed samples with various X-ray techniques. Co-authors Joshua Davis, Benjamin Hanken, and Mark Asta performed computational experiments. Robert Fisher and Ping Lu assisted with collection of HAADF-STEM/EDS data. David Johnson is my advisor. I prepared TEM specimen of all samples, assisted with HAADF-STEM/EDS data collection, analysis, and writing pertaining to those sections, in addition to editing the manuscript.

7.1. INTRODUCTION

The discovery of two-dimensional materials with the so-called emergent properties, those not observed in the constituent bulk compounds, has resulted in a boom in research on monolayers, heterostructures, and ultrathin materials.[1-4] The expansion of this field is fueled by the predictions of unusual quantum states and properties that might be observable in 2D materials, including unusual quantum spin Hall states,[5,6] Weyl fermions,[7] indirect-to-direct band gap transitions,[8] and topological states.[9] The surfaces and interfaces in 2D materials are responsible for many of the observed emergent properties. In monolayers, the lack of adjacent layers removes bonding and antibonding interactions between layers, which

can result in property changes such as the transition from an indirect to a direct band gap in MoS_2.[8] Interlayer coupling at the nonepitaxial interface between constituents in heterostructures can produce new properties. For example, charge transfer between constituents can cause modulation doping in heterostructures.[10,11] The interaction between layers can also prompt structural changes, such as the formation of octahedrally, rather than trigonal prismatically coordinated Mo in $MoSe_2$ when layered with BiSe.[12] Computational and experimental studies on the thickness-dependent properties of low-dimensional materials have revealed differences between odd- and even-layered thicknesses resulting from the stability of specific crystal surfaces and changes in symmetry.[13-17] The rapid development of this field experimentally was initially driven by the ability to obtain monolayers of naturally layered compounds via mechanical cleaving[18,19] and the ability to detect thicknesses rapidly using optical techniques.[20] The large interest in 2D materials as potentially important components of new technologies has resulted in the development of additional approaches to synthesizing films with a precise control of thickness and heterostructures with a controlled nanoarchitecture over wafer-scale surfaces.[19,21]

While initially focusing on layered materials with obvious cleavage planes, recent theoretical papers have predicted unusual properties associated with the 2D layers of materials with three-dimensional structures.[22-27] Preparing 2D layers of materials with 3D structures, however, is synthetically more challenging than preparing structurally 2D or naturally layered compounds. As a material becomes more 3D, cleaving thin layers in desired directions becomes increasingly more difficult. During the vapor phase growth, the strength of the interaction between the growing layer and the substrate is very important. If the

interaction is too strong, it will modify the electronic structure that is being targeted. If it is too weak, there will be a tendency to form islands rather than continuous thin films of uniform thickness.[28] Recent calculations have predicted that a free-standing monolayer PbSe could be a 2D topological crystalline insulator, with Dirac-cone-like edge states.[29] Ultrathin PbSe films have been grown on $SrTiO_3$ substrates by codepositing Se and Pb atoms, forming crystalline PbSe islands after postannealing.[30] A large compressive strain exists in these epitaxial few-layer PbSe islands, with the lattice parameters changing from 5.85 Å for a three monolayer-thick island to 6.1 Å for a nine monolayer-thick island. Bulk PbSe has a lattice parameter of 6.117 Å.[31] The large change in the lattice parameters indicates a strong epitaxial interaction between the substrate and PbSe; however, islands rather than constant thickness PbSe layers formed under the growth conditions used.

Here, we report our investigation of the growth of monolayers and a controlled thickness of PbSe layers between VSe_2 layers. This study was prompted by a previous investigation, where smooth PbSe films were grown on VSe_2.[32] This report and the thermodynamic stability of misfit-layered compounds containing well-defined bilayers of PbSe alternating with dichalcogenides suggest that a strong interaction exists between these constituents, even though the significant lattice mismatch prevents an epitaxial relationship between the constitutents.[33,34] Precursors were deposited to mimic the nanoarchitecture of $[(PbSe)_{1+\delta}]_q(VSe_2)_1$ heterostructures where q is an integer number of PbSe monolayers. The precursors with even layers and with $q \geq 7$ thicknesses exhibited the expected as deposited nanoarchitecture and evolved into the desired heterostructures. Surface diffusion during the deposition process of the $q = 1$, 3, and 5 precursors, however, resulted in more complex

initial nanoarchitectures. The computational and experimental findings reveal that for small values of odd *q*, the formation of odd PbSe rock salt layers has a higher energy compared to segregation into adjacent (*q*+1 and *q*-1) layers. The results suggest that the interaction between VSe_2 and PbSe is not strong enough to stabilize the monolayers, suggesting that its synthesis requires finding a substrate that has a stronger interaction with PbSe. The data presented support an odd-even effect in PbSe monolayers, a 2D structure derived from a bulk 3D structure, due to enhanced stability of even-thickness layers. This points to new opportunities to tune structures by varying the strength and type of interaction between the constituents, potentially opening up avenues for accessing novel properties by varying the layer thickness of 2D layers of compounds with 3D structures.

7.2. METHODS

Precursors were deposited on <100> Si wafers (3" × 1") with native oxide using a custom-built physical deposition chamber described by Fister and coworkers.[43] Elemental V (99.995%, Alfa Aesar) and Pb (99.8%, Alfa Aesar) were deposited using 6 keV electron beam guns while elemental Se (99.99%, Alfa Aesar) was deposited using a Knudsen effusion cell. Elemental layers were deposited by exposing the substrate to a plume of atoms from the heated sources. The time the substrate is exposed is controlled by pneumatic shutters that close after the desired thickness has been deposited. The desired thickness was measured using a quartz crystal microbalance and the sequence and thickness of elemental layers can be controlled using custom LabView software. The number of atoms of each element deposited is optimized by measuring the X-ray fluorescence (XRF) of the films ex situ using a Rigaku Primus II ZSX spectrometer. The measured XRF intensities are converted into the

number of atoms per unit area for each constituent as described by Hamann and coworkers.[35] The period of the deposited sequence of layers was measured using X-ray reflectivity (XRR).

Ex situ annealing was performed on a hot plate in an inert N_2 atmosphere (O_2 < 0.8 ppm). The changes as a function of annealing temperature and time were followed using X-ray diffraction. Specular X-ray diffraction (XRD) and X-ray reflectivity (XRR) patterns were collected using a Bruker D8 diffractometer with Cu-Kα radiation (λ = 0.15418 nm). The specular XRD scans contain substrate peaks at 2θ of ≈30 and 60°. The grazing incidence in-plane X-ray diffraction (GIPXRD) pattern was collected using a Rigaku Smartlab diffractometer, also with Cu-Kα radiation (λ = 0.15418 nm). LeBail fitting of the GIPXRD data was performed on FullProf Suite.[44]

An FEI Titan G2 80-200 STEM with a Cs probe corrector and ChemiSTEM technology (X-FEG and Super-X EDS with four windowless silicon drift detectors) operated at 200 kV was used in this study. High-angle annular dark-field (HAADF) images were recorded with an electron probe of size (FWHM) of about 0.13 nm, a convergence angle of 18.1 mrad and a current of ~75 pA, and an annular dark-field detector with a collection range of 60-160 mrad. Density functional theory (DFT) calculations were performed to compute the energy of PbSe slabs with different layer thicknesses of q = 1-8. For these calculations, the slabs were separated by 1.5 nm of vacuum to avoid interactions between the surfaces. To accommodate surface reconstructions, the dimensions of the slab supercells were doubled (relative to the conventional unit cell) in each direction parallel to the surface. The calculations made use of the projector augmented wave (PAW)[45] method as

implemented in the Vienna ab initio simulation package (VASP),[46] in conjunction with the generalized gradient-approximation exchange-correlation potential of Perdew-Burke-Ernzerhof (PBE)[47] modified for solids: PBEsol.[48] The choice of PBEsol was made based on previous works, which gave more accurate bulk properties of PbSe relative to PBE.[49,50] A planewave cutoff energy of 500 eV was employed. Wavefunctions were sampled using a Gamma-centered k-point grid of 8 × 8 × 1 (where the first two grid spacings are for directions in-plane and the last is normal to the surface) and a Gaussian smearing of 0.1 eV. The calculated lattice parameter for the rock-salt conventional unit cell using these settings is 6.103 Å, which matches well with the reported experimentally measured value of 6.1054(5) Å.[51] All atoms were fully relaxed in the slab supercells to a force convergence of 5 meV/Å, keeping the in-plane lattice vectors fixed to the scaled dimension of the optimized bulk lattice parameter. The charge-density self-consistency was iterated to an energy tolerance of 10-4 eV. These settings were found to be sufficient to converge the total energies to within 1 meV/FU and to converge the atomic displacements induced by the surface reconstructions (Figure D.3) to within 0.01 Å. Further information comparing the results from PBE and PBEsol can be found in Figure D.4, showing that although the total energies change significantly with the choice of these exchange-correlation functionals, the key results concerning the odd-even energy oscillations, the nature of the convex hull features, and displacement patterns are very similar.

7.3. RESULTS AND DISCUSSION

A sequence of precursors was designed containing the correct number of atoms of each element in a repeating sequence of elemental layers to mimic the targeted structures.

We calculated the number of atoms needed to form a monolayer of rock salt-structured PbSe in the <100> plane and a VSe_2 trilayer from the in-plane lattice parameters of each constituent in $[(PbSe)_{1+\delta}]_1(VSe_2)_1$, which contains a bilayer of PbSe alternating with VSe_2.[34] Figure 7.1 shows the calculated number of atoms of each element required to form $[(PbSe)_{1+\delta}]_q(VSe_2)_1$ compounds plotted as a function of *q*, the number of PbSe monolayers. To prepare compounds where *q* is even, we deposited a repeating unit (RU) of the sequence of elemental layers [V|Se + *q*/2(Pb|Se)] *r* times, where each V|Se bilayer is targeted to have the number of atoms required to form a VSe_2 layer and each Pb|Se layer is targeted to have the number of atoms required to form a PbSe bilayer. To prepare compounds where *q* is 1, 3, 5, 7, or 9 monolayers (1.5, 2.5, 3.5, and 4.5 bilayers), we deposited a similar sequence of elemental layers, where each Pb|Se layer contained either the number of atoms required to form a monolayer or a bilayer of PbSe such that the total number of layer atoms deposited equaled the value needed for *q* monolayers. For example, to prepare a *q* = 7 precursor, we deposited the RU sequence [V|Se + 3(Pb|Se)$_{bilayer}$ + 1(Pb|Se)$_{monolayer}$]. The compositions and structures of the deposited precursors were determined using XRF, XRR, and XRD.

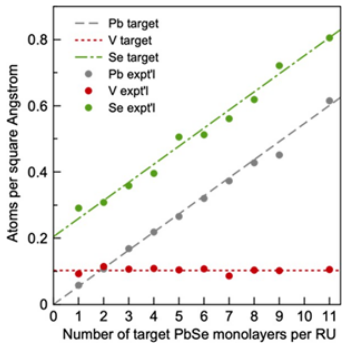

Figure 7.1. Targeted number of atoms per square Angstrom for each element per repeating unit for each of the designed precursors shown as lines. The circles are the amounts determined using XRF data.

The total number of atoms of each element deposited in each precursor was measured using XRF, and the average number of atoms per repeating unit was obtained by dividing the total number of atoms of each element by the number of repeating units deposited.[35] The measured number of atoms per unit area deposited for each precursor is shown as circles in Figure 7.1. The number of V and Pb atoms per unit area of all of the odd-numbered precursors is within 5% of the calculated values. The deviations from the calculated lines are a consequence of depositing the targeted numbers of atoms per unit area that are on the order of a monolayer for each element. Excess Se is observed in some precursors, which was anticipated to evaporate during the annealing process, and samples with deficient Se will likely have a small amount of metal oxides or incomplete unit cells. All the precursors contain close to the number of atoms of each element in the repeating sequence of layers to form the targeted compounds.

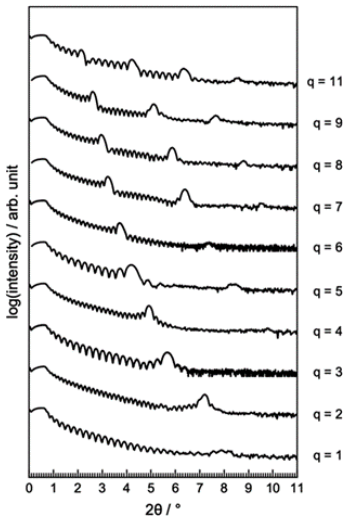

Figure 7.2. XRR patterns of the 10 as-deposited precursors. The patterns contain Bragg reflections from the nanoarchitecture of the precursor and lower intensity fringes from the interference pattern between the front and back of the sample combined with the incomplete destructive interference from a finite number of repeating layers.

The XRR patterns of the precursors contain intensity oscillations (Kiessig fringes) due to the finite thickness of the entire film and Bragg maxima due to the repeating sequence of elemental layers in the precursor (Figure 7.2). The position of the first-order Bragg reflection due to the layering of the precursor systematically shifts to a lower angle as the thickness of the PbSe layer (q) is increased. For the q = 1 sample, the Bragg maximum is much broader than for the other samples and shifted to a lower angle than expected, indicating that the repeating period is thicker than the targeted value. However, the precursor modulation length for the q = 1 sample calculated from the total thickness divided by the number of repeating units deposited is as expected from the deposition process (Figure 7.4). This difference suggests that long-range surface diffusion occurred during the deposition, resulting in the precursor having a different structure than targeted.

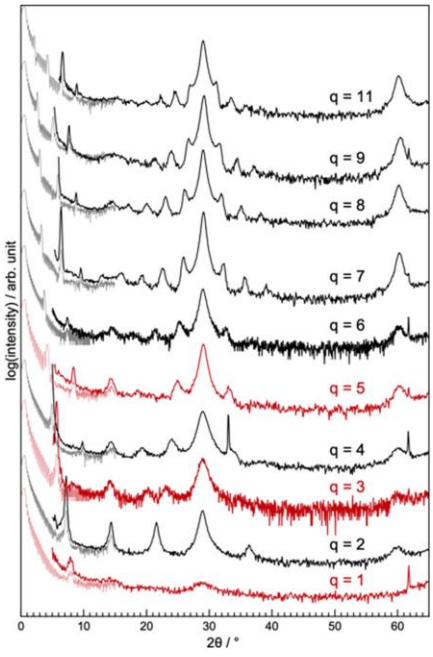

Figure 7.3. XRD patterns of the as-deposited precursors showing two different groups based on the relationship of the high-angle peaks with the precursor modulation length.

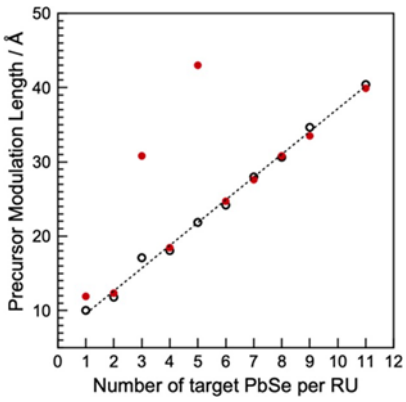

Figure 7.4. Dependence of the precursor modulation length on q, the targeted number of PbSe monolayers per repeating unit (RU). The black unfilled circles are the modulation lengths determined by dividing the total thickness by the number of deposited layers. The symbols in red are the modulation lengths determined by indexing the as-deposited high-angle reflections as 00l reflections. For q = 3 and 5, these different approaches yield different values, as described in the text.

The XRD patterns (Figure 7.3) of the as-deposited samples contain high-angle reflections that indicate that the samples have already begun to self-assemble during the deposition. The positions of these high-angle reflections divide the precursors into two groups. The reflections for the precursors with even-numbered q and odd $q \geq 7$ monolayers thick are at positions consistent with them being indexed as the 00l reflections yielding a c-axis unit cell size consistent with the precursor modulation length and the targeted nanoarchitecture. The with q = 1, 3, and 5 all have weak reflections in the high-angle scans that cannot be indexed as the 00l reflections from the precursor modulation length. For q = 3 and 5, the positions of the weak reflections indicate that the precursor modulation length is double than that expected from the deposition sequence. For the q = 1 sample, the weak reflections are not related at all to the precursor modulation length, consistent with segregation during the deposition process.

The data in Figure 7.4 reflects the differences in the targeted and actual nanoarchitecture deposited. It shows the precursor modulation length based on the deposition, determined by dividing the total thickness by the number of repeating units (black unfilled circles). The red filled circles are the modulation lengths (λ) determined by indexing the high-angle peaks as 00*l* reflections, which indicates the nanoarchitecture of the precursor that has crystallized upon deposition. The XRF, XRR, and XRD data indicate that the precursors with q = 2, 4, and 6 or larger all have the correct number of atoms of each element and the targeted nanoarchitecture. The XRD data for the precursors with q = 3 and 5 indicate that these precursors have a modulation length that is twice than that expected from the deposited sequence of layers. For these samples, half of the modulation length calculated from the high-angle 00*l* reflections falls where expected based on the deposition sequence, our XRF measurements, and the thicknesses of the even-layer thickness samples q = 2, 4, and 6. For the q = 1 sample, the modulation length calculated from the total thickness divided by the number of repeating units of the elemental layer sequence deposited is close to the extrapolated value from the even PbSe layer thickness samples. It has the required number of atoms; however, the high-angle XRD (Figure 7.3) data indicate that the nanoarchitecture is more complicated than the targeted sequence of a Pb|Se monolayer and a V|Se bilayer. The best-fit line between the precursor modulation length and the target number of PbSe monolayers (Figure 7.4, dotted line) has a slope of 3.07(8) Å, which is the thickness of an elemental Pb|Se layer that contains the number of Pb and Se atoms to yield a monolayer of PbSe. The intercept (6.5(5) Å) is the thickness of the elemental V|Se bilayer, which is slightly thicker than the thickness of a crystalline VSe_2 trilayer because the precursors are less dense than fully crystallized layers. The deviations from the linear

relationship shown in Figures 7.1 and 4 reflect our ability to reproducibly prepare targeted precursors. Three different behaviors were observed that depend on the targeted number of PbSe monolayers per repeating unit of the precursor.

Precursors with even-numbered q and odd ($q \geq 7$) monolayers evolved to form the targeted heterostructures. The XRR scans collected on the $q = 7$ precursor (Figure 7.5) collected as a function of temperature illustrate this behavior. The 001 and 002 reflections change in intensity and shift to lower angles as the annealing temperature is increased. The 003 reflection increases in intensity when the precursor is annealed between 150 and 350 °C. The 004 reflection first appears after the 150 °C annealing and grows in intensity up to and including the 350 °C annealing temperature.

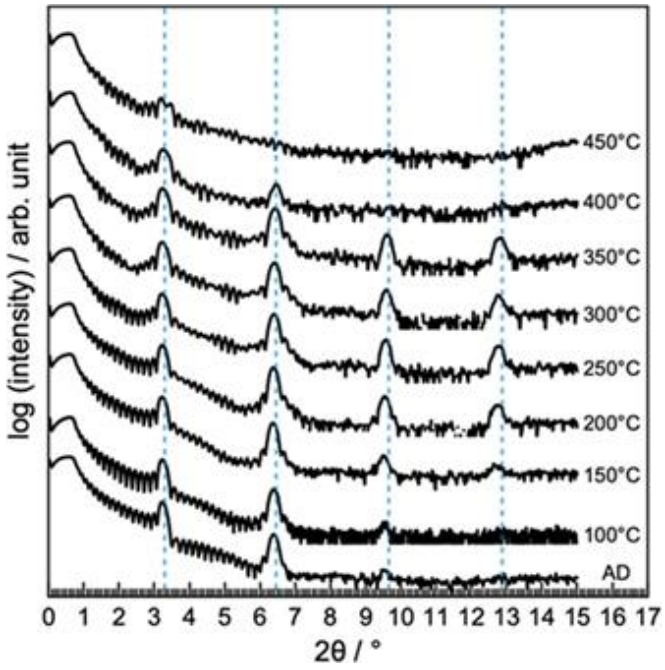

Figure 7.5. XRR data collected after annealing the q = 7 precursor at the designated temperatures. The blue dashed lines are the expected peak positions for the $[(PbSe)_{1+\delta}]_7(VSe_2)_1$ heterostructure.

These changes all indicate that the nanoarchitecture is preserved and the long-range order increases as the precursor self-assembles into the targeted heterostructure. Kiessig fringes due to the reflection of X-rays from the top and bottom of the films and the Laue interference pattern due to the finite number of unit cells in the films[36,37] are present at each step, suggesting that the films remain smooth throughout the annealing process. The film thickness decreases by a small amount (<5%) as the long-range order develops. The number of diffraction orders decreases when the precursors are annealed above 350 °C, indicating that the initial nanoarchitecture is being lost.

The specular diffraction patterns collected as a function of annealing temperature support the conclusions drawn from the XRR data. Figure 7.6 contains the data collected on the $q = 7$ precursor. Broad high-order 00*l* reflections (>15° 2θ) are observed in the as-deposited precursor, indicating that the sample forms domains with the significant long-range order during the deposition. The higher-angle reflections have the same periodicity (27.62(8) Å) as the low-order (<15° 2θ) 00*l* reflections (27.6(3) Å), suggesting that the nucleated structure has the same layering of the precursor. As the temperature is increased to 350 °C, the low- and high-order 00*l* reflections increase in intensity and converge to have similar peak widths. The *c*-axis lattice parameter calculated from the position of the reflections after the 350 °C annealing is 27.52(6) Å. At 400 °C, the 00*l* reflections start to diminish and we see the growth of a broad VSe_2 reflection at 2θ of ≈15°. At 450 °C, the high-angle scan contains only the 00*l* VSe_2, and the 002 and 004 PbSe reflections, while the XRR scan shows a very reduced intensity of the 001 reflection from the heterostructure.

This suggests that the heterostructure decomposes to thermodynamically most stable products.

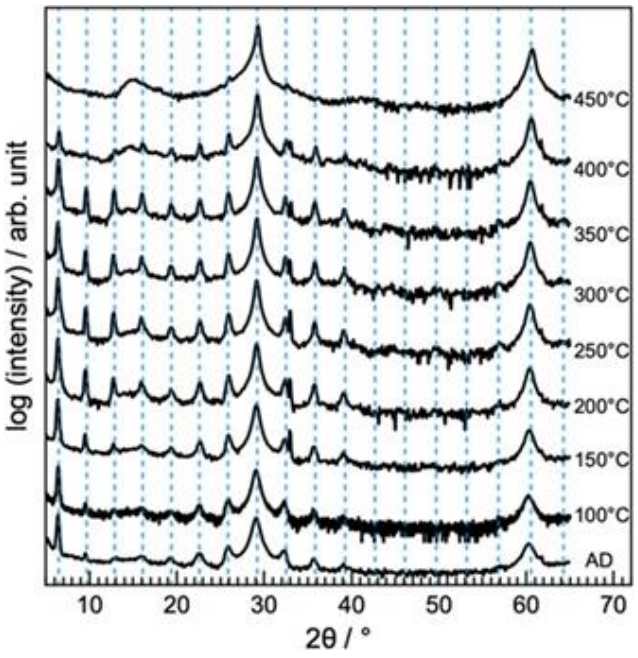

Figure 7.6. Specular XRD data collected after annealing the q = 7 precursor at the designated temperatures. The blue dashed lines are the expected peak positions for $[(PbSe)_{1+\delta}]_7(VSe_2)_1$.

Further evidence for the formation of the targeted heterostructures at moderate annealing temperatures comes from GIPXRD pattern of the precursors after annealing to 300 °C and the systematic change in *c*-axis lattice parameters of the products as *q* is varied. The in-plane diffraction of the $q = 7$ precursor after annealing at 300 °C, shown in Figure 7.7, is representative of the samples with even-numbered *q* and odd $q \geq 7$. All the observed reflections can be indexed as *hk*0 reflections from either a hexagonal or a square unit cell. The in-plane lattice parameter of the hexagonal unit cell (3.40(1) Å) is close to that reported for bulk VSe_2. The lattice parameter of the square unit cell (6.12(1) Å) is close to that reported for bulk PbSe (6.117 Å);[31] however, there are reflections observed that are

forbidden in the bulk unit cell, indicating that the structure distorts when *q* is small. Since only the 00*l* and *hk*0 reflections are observed in the specular and in-plane XRD, respectively, the heterostructure is crystallographically aligned to the substrate with the PbSe <100> and VSe_2 < 100> planes parallel to substrate. The *c*-axis lattice parameters of the annealed *q* = even and *q* ≥ 7 precursors are plotted against *q* and shown in Figure 7.8. The linear relationship between the *c*-axis lattice parameters and *q* suggests that heterostructures in this category can be predictably synthesized with the correct precursor. The slope (3.07(1) Å) is close to the value of half of the lattice parameter of a PbSe unit cell (6.117 Å).[31] The y-intercept (6.06(9) Å) is close to the *c*-axis lattice parameter of bulk VSe_2 (5.96-6.11 Å).[38]

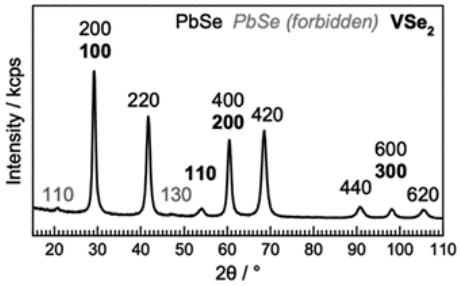

Figure 7.7. In-plane XRD pattern of a q = 7 precursor annealed at 300 °C. The indices are shown above the reflections.

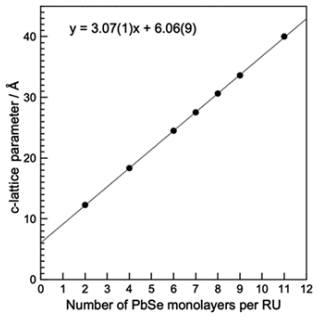

Figure 7.8. c-Lattice parameters of even and odd samples with q ≥ 7 monolayers plotted vs q.

HAADF-STEM images were collected for annealed precursors to provide additional structural information on the products formed. Figure 7.9 shows the representative images from the q = 7 sample. The whole film cross-section image (Figure 7.9a) shows that there is a consistent layered structure over the entire sample. The higher-magnification image (Figure 7.9b) shows that most of the sample consists of a repeating unit cell containing 1 VSe_2 and 7 PbSe monolayers.

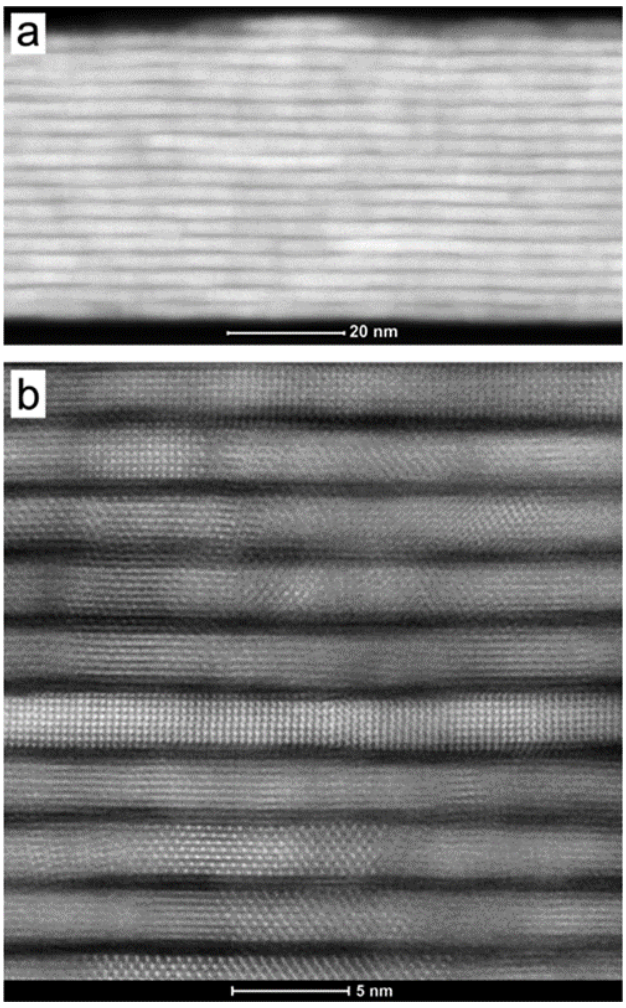

Figure 7.9. Representative HAADF-STEM images of the annealed q = 7 precursor. (a) Image of the entire film thickness. (b) Highermagnification images demonstrating the presence of mostly $[(PbSe)_{1+\delta}]_7(VSe_2)_1$ with small areas of $[(PbSe)_{1+\delta}]_6(VSe_2)_1[(PbSe)_{1+\delta}]_8(VSe_2)_1$.

There are local regions, however, where a repeating sequence of 6 PbSe monolayers-VSe_2-8 PbSe monolayers-VSe_2 (Figure 7.9b) replaces the 7 PbSe monolayers-VSe_2 sequence. This replacement occurs randomly throughout the sample. The local information obtained from the HAADF-STEM data is consistent with the average structure inferred from the diffraction data as discussed previously. The PbSe slabs in the film have various in-plane orientations since different zone axes are clearly seen in different slabs, indicating that the film has rotational disorder. The $q = 7$ sample forms mostly $[(PbSe)_{1+\delta}]_7(VSe_2)_1$ with local regions consisting of $[(PbSe)_{1+\delta}]_6(VSe_2)_1[(PbSe)_{1+\delta}]_8(VSe_2)_1$.

A different behavior as a function of annealing was observed for the $q = 3$ and 5 precursors, where the as-deposited precursors have reflections that suggest a doubling of the modulation length. XRR scans for the $q = 3$ precursor collected as a function of annealing temperature are shown in Figure 7.10. Superimposed on the diffraction scan are blue vertical lines indicating angles where reflections are expected from the targeted $q = 3$ precursor and red vertical lines showing where additional reflections are expected for a precursor with a doubled modulation length.

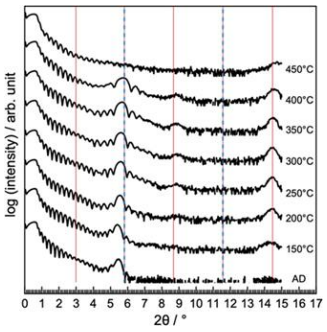

Figure 7.10. XRR data collected after annealing the q = 3 precursor at the designated temperatures. The blue dashed lines are the expected peak positions for a $[(PbSe)_{1+\delta}]_3(VSe_2)_1$ heterostructure, and the red solid lines are the expected positions for a heterostructure with twice this unit cell size.

The 001 reflection of the precursor persists up to 400 °C, but the expected second-order reflection from the precursor does not appear (at the blue vertical dashed line at ≈11.4° 2θ). Reflections do grow, however, at the approximate locations expected for the third-and fifth-order reflections from a doubled modulation length. The diffraction intensities decrease when annealed at 400 °C and only Kiessig fringes from the interference between the front and back of the film remain after the 450 °C annealing.

The specular diffraction data collected on the q = 3 sample, shown in Figure 7.11, provide additional information about the structural changes that occur during annealing. The diffraction pattern of the as-deposited sample contains several higher-angle reflections indicating long-range ordering that occurs during the deposition process to form a modulation length twice that which was expected. The high-angle 00l reflections intensify for annealing temperatures between 150 °C and 400 °C, and all of the observed reflections can be indexed as the 00l reflections of a unit cell with twice the repeating period expected from the deposited elemental layers. The positions of several reflections deviate from that calculated from the average c-axis lattice parameter (30.5(1) Å at 350 °C), which is probably a consequence of stacking faults apparent in the HAADF-STEM data discussed in a later paragraph. Only the 001 VSe2, and the 002 and 004 PbSe reflections are observed in the specular scan after annealing at 450 °C, indicating that the sample has segregated. The in-plane XRD data collected on the q = 3 precursor annealed at 300 °C contain maxima that can be indexed as the hk0 reflections from a hexagonal base (a = 3.42(1) Å) and a square base (a = 6.12(1) Å) (Figure D.1). These lattice parameters are consistent with the formation of VSe_2 and PbSe respectively. The XRR, specular, and in-plane diffraction data indicate that

the q = 3 and 5 precursors self-assemble to form superlattices with twice the expected c-axis lattice parameter. The unit cell consists of twice the number of crystallographically aligned VSe_2 and PbSe layers per repeating unit expected from the deposition sequence used to form the precursor.

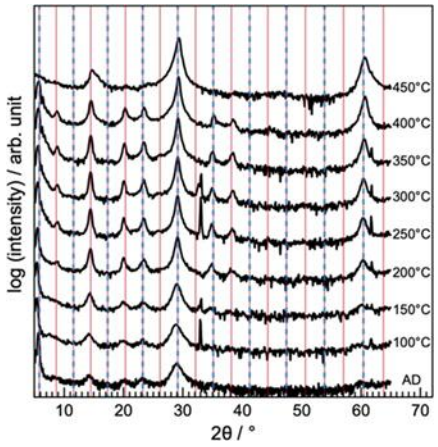

Figure 7.11. Specular XRD data collected after annealing the q = 3 precursor at the designated temperatures. The blue dashed lines are the expected peak positions for a $[(PbSe)_{1+\delta}]_3(VSe_2)_1$ heterostructure, and the red solid lines are the expected positions for a heterostructure with twice this unit cell size.

The HAADF-STEM images were collected to corroborate the structure of the self-assembled q = 3 precursor. The sample (Figure 7.12a) contains a surface region containing light and dark regions without a regular order above a layered film that contains light layers (PbSe) of various thicknesses separated by dark layers (VSe_2). Large Pb-rich and V-rich areas are observed at the top of the film indicating that some of the film has already segregated (Figure D.2). Within the layered part of the film, there are small domains that contain a regular local stacking pattern. The higher-magnification image (Figure 7.12b) shows that the light layers are rock-salt PbSe and the dark layers are CdI_2-structured VSe_2. Small regions with different stacking sequences appear adjacent to one another. For example, the regions

labeled as '2141' and '4121', representing $[(PbSe)_{1+\delta}]_2(VSe_2)_1[(PbSe)_{1+\delta}]_4(VSe_2)_1$ and $[(PbSe)_{1+\delta}]_4(VSe_2)_1[(PbSe)_{1+\delta}]_2(VSe_2)_1$, respectively, are adjacent to one another. These different stacking regions in the film cannot be distinguished using diffraction alone. The presence of these regions suggests that there are multiple nucleation sites and significant lateral diffusion during the deposition process. The HAADF-STEM sheds light on the structural features that cannot be deduced from the diffraction data, such as the presence of both layering sequences in the film and the domain size of regions of local order.

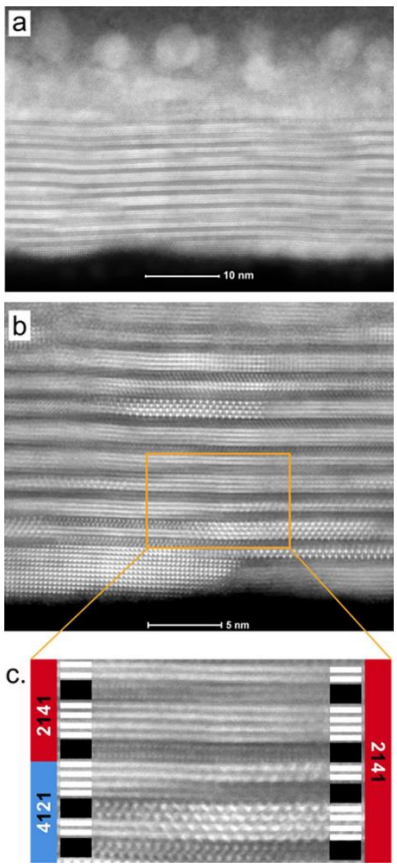

Figure 7.12. Representative HAADF-STEM images of the annealed q = 3 precursor. (a) Image of the entire film thickness, containing regions of $[(PbSe)_{1+\delta}]_2(VSe_2)_1[(PbSe)_{1+\delta}]_4(VSe_2)_1$ with many dislocations and stacking errors between them. (b) Atomic-scale resolution image of a selected region, which contains representative stacking errors. (c) Superposition of the image on a model of a

grain boundary between different stacking arrangements. Legend: black layers: VSe2 and white layers: PbSe.

We prepared a precursor targeting the $[(PbSe)_{1+\delta}]_2(VSe_2)_1[(PbSe)_{1+\delta}]_4(VSe_2)_1$ isomer to demonstrate the importance of designing a precursor where only short-range diffusion is required to form the targeted product. Specular diffraction and XRR patterns of the as-deposited and annealed precursors are shown in Figure 7.13a. The as-deposited precursor has significantly more long range order than the $q = 3$ precursor. The heterostructure forms at lower temperatures, and the diffraction maxima are significantly more intense and narrower than those shown in Figures 7.10 and 7.11, reflecting a more coherent structure. The cross-section HAADF-STEM image of the entire film thickness shown in Figure 7.13b containsvery distinct PbSe and VSe_2 layers and a regular stacking pattern across the entirety of the film. This microscopy data for this sample is similar to those obtained on films with even-order q and odd $q \geq 7$ monolayers, where only short-range diffusion in the precursor was required during the self-assembly process.

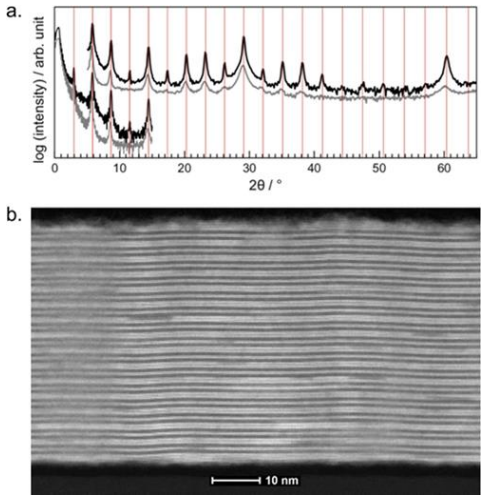

Figure 7.13. (a) Specular XRD and XRR patterns of the as-deposited (gray) and annealed (black) '2141' precursor. (b) HAADF-STEM image of the annealed precursor *f*ilm with a nanoarchitecture designedto form $[(PbSe)_{1+\delta}]_2(VSe_2)_1[(PbSe)_{1+\delta}]_4(VSe_2)_1$.

The precursor with $q = 1$ evolves differently than all of the other samples. The XRR data as a function of annealing temperature is shown in Figure 7.14. The vertical blue dashed lines indicate the position of reflections expected from a period calculated from the total thickness divided by the total number of layers deposited. The vertical red lines indicate the position of reflections expected for $[(PbSe)_{1+\delta}]_2(VSe_2)_1$. The angle of the first reflection observed is significantly smaller than expected in the as-deposited sample and shifts further to lower angles as the precursor is annealed at increasing temperatures. A second reflection appears after annealing at 150 °C and its intensity increases after annealing at higher temperatures. At 300 °C, both of these reflections can be indexed as the 00*l* reflections of a heterostructure with a 12.24(3) Å *c*-axis lattice parameter (red lines), which matches that expected for $[(PbSe)_{1+\delta}]_2(VSe_2)_1$. The specular diffraction data, shown in Figure 7.15, contains additional maxima that increase in intensity as annealing temperatures are increased. All of the reflections can be indexed as the 00*l* reflections from $[(PbSe)_{1+\delta}]_2(VSe_2)_1$ after annealing at 250 °C. The even-order reflections appear to have a narrower peak width than the other reflections and higher intensities compared to what is expected from $[(PbSe)_{1+\delta}]_2(VSe_2)_1$, suggesting that a second phase, VSe_2, is likely present. This is consistent with the XRF-determined composition of the film. After annealing at 500 °C, the XRR pattern contains only Kiessig fringes and the diffraction pattern contains maxima that can be indexed as the 001 reflection from VSe_2, and the 002 and 004 reflections from PbSe. The in-plane XRD data also suggest that the film contains crystallographically aligned PbSe and VSe_2 (Figure D.1).

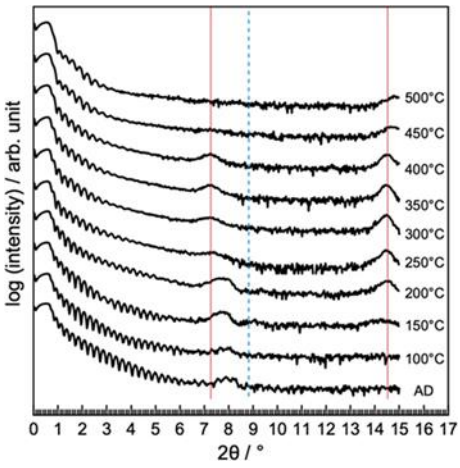

Figure 7.14. XRR data collected after annealing the q = 1 precursor at the designated temperatures. The blue dashed lines are the expected peak positions for the calculated modulation length, and the red solid lines are the expected positions for a $[(PbSe)_{1+\delta}]_2(VSe_2)_1$ heterostructure.

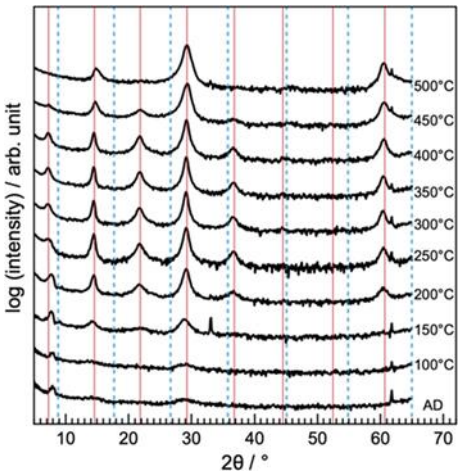

Figure 7.15. Specular XRD data collected after annealing the q = 1 precursor at the designated temperatures. The blue dashed lines are the expected peak positions for the calculated modulation length, and the red solid lines are the expected positions for a $[(PbSe)_{1+\delta}]_2(VSe_2)_1$ heterostructure.

The structure of the self-assembled $q = 1$ precursor was further probed by collecting the HAADF-STEM data. The whole film cross-section (Figure 7.16a) clearly demonstrates a different behavior from the others as the sample contains dark regions laterally separated

from the bright regions. This indicates the segregation of large grains of VSe_2 from PbSe. Figure 7.16b shows that the brighter regions consist of alternate layers of VSe_2 and PbSe bilayers while the darker regions consist of VSe_2. A higher magnification of the bright region (Figure 7.16b) suggests that the local structure of the film consists of a mixture of $[(PbSe)_{1+\delta}]2(VSe_2)_1$ and VSe_2. The segregation into these two distinct regions suggests that there is lateral diffusion taking place during deposition. A consistent theme from the HAADF-STEM data is that the formation of an even number of monolayers of PbSe appears to be favored over odd number of layers, especially for a small odd *q* value. The XRR and XRD data of the as-deposited sample suggest that the formation of even number of monolayers stems from the initial structure of the precursor.

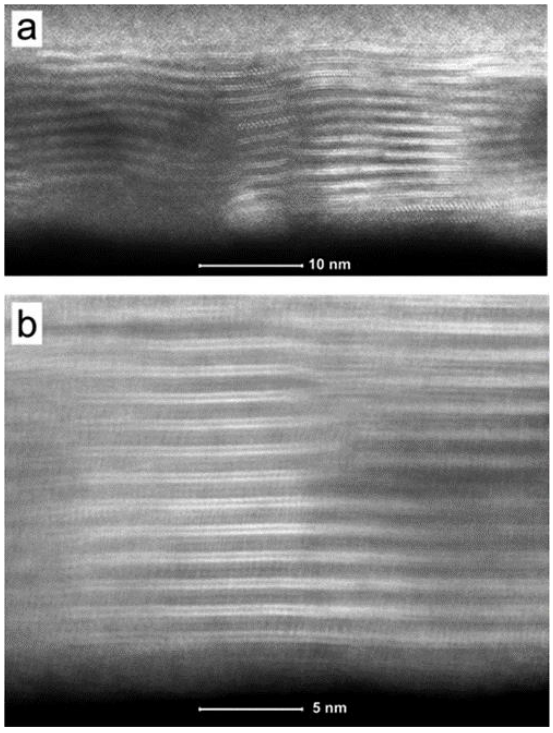

Figure 7.16. (a) Representative HAADF-STEM image of the annealed q = 1 precursor showing brighter regions of $[(PbSe)_{1+\delta}]_2(VSe_2)_1$ and dark regions containing only VSe_2. (b) Higher-magnification image of a bright region, showing the alternating layers of PbSe and VSe_2.

The underlying assumption of the synthesis approach used here is that the deposition process yields precursors with the nanoarchitecture of a specific target compound. These precursors are expected to form the targeted compounds because atoms do not need to move large distances to form this product relative to more stable alternatives that might require segregation. The nanoarchitecture of the precursor is experimentally controlled by the sequence of elements and the amount of each element deposited. In the system investigated here, the deposition sequence produced precursors close to the desired structure for q = even and $q \geq 7$, but the nanoarchitecture of the precursors with q = 1, 3, and 5 was different than expected from the deposition process. The data presented above suggest that the atoms in the Pb|Se layer in the q = 1, 3, and 5 samples underwent significant lateral surface diffusion during the deposition process to form PbSe layers containing an even number of PbSe monolayers. For the q = 1 sample, lateral diffusion of atoms in the V|Se layer is also required to explain the uniform thickness and the observed modulation length of the precursor. The precursors preferred to form a defect-rich film with bilayers rather than a more ordered film with a PbSe block containing an odd number of monolayers.

First-principles DFT calculations shed light on an energetic driving force consistent with this behavior. These calculations were used to compute the relaxed total energies of PbSe rocksalt slabs containing different layer thicknesses (q = 1-8), each oriented with the (001) surfaces. Figure 7.17 shows the plots of the calculated energies as a function of q. The energy of the monolayer is much higher than all of the others, consistent with the behavior of the q = 1 precursor discussed above. The energies of the odd-numbered layer thicknesses

are greater than those derived from the convex hull created by the blocks with even-numbered layers. The results thus indicate that it is more favorable to form a mixture of adjacent even-numbered blocks than odd-numbered blocks. The difference in energy between the convex hull and the odd-numbered block decreases as the thickness of the odd-numbered block increases. At high values of *q*, the energy difference between the convex hull and the odd-numbered blocks becomes negligible. There is also a general decrease in energy as the thickness of the block is increased, which is due to the larger number of internal atoms compared to those on the surface.

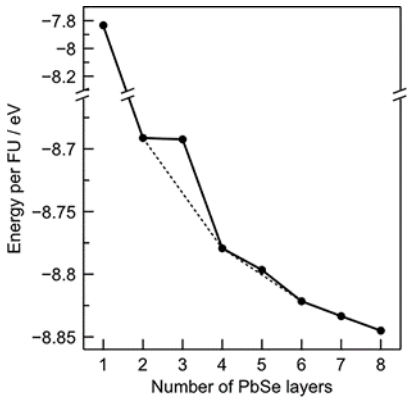

Figure 7.17. DFT-calculated energies of PbSe blocks in vacuum with varying numbers of monolayers (q). Note the discontinuity in the y axis. The dashed lines indicate the convex hull created by even-numbered blocks.

In DFT calculations, inter- and intra-layer displacements are observed in the relaxed structures due to the termination of the 3D rock-salt structure at the interfaces, as illustrated by the representations of each structure shown in Figure D.3. Within a monolayer, Pb and Se atoms deviate from the ideal rock-salt positions by a shift along the z-axis (normal to the surface), producing a "puckering" pattern in which the sign of the displacements are opposite for Pb and Se atoms. There is also a distinct alternation of short and long distances

between the monolayers in the even-thickness PbSe blocks, resulting in the formation of bilayers. The largest puckering occurs in the surface layer, regardless of the thickness of the PbSe block, and the magnitude of the distortion decreases as the PbSe monolayers approach the interior. Overall, the displacement observed reflect the trade-off between the surface reconstruction to lower the surface energy and distortions in the interior layers due to the surface reconstruction. In blocks with an odd number of monolayers, only the exterior slabs form bilayers as the surface reconstructs, resulting in their higher energy relative to the even-thickness PbSe layers. Thus, the slabs with even-layer thicknesses are able to accommodate the bilayer nature of the surface-induced displacements, while this pattern is frustrated in slabs with odd number of layers. We interpret this frustration as the origin of the energetic destabilization of the slabs with odd q values.

While the absolute energies and the distortions in the PbSe layers will be different if the vacuum is replaced by a dichalcogenide layer, these energy calculations suggest an explanation for the observed as-deposited structures and the final structures formed. For the $q = 1$ sample, the energy difference between a single PbSe monolayer between VSe_2 layers versus half the surface being a bilayer and half without PbSe is high enough that the system reconstructs during the deposition as the atoms diffuse on the surface. The instability of monolayer PbSe observed is consistent with the high energy calculated for this structure. Annealing results in continued segregation of the sample into $[(PbSe)_{1+\delta}]_2(VSe_2)_1$ and VSe_2, even though significant diffusion distances are required. For the $q = 3$ and 5 samples, the energy difference between regions with an odd monolayer thickness q versus alternating layers with $q - 1$ and $q + 1$ is still large enough to reconstruct the PbSe layer during the

deposition. Annealing continues the self-assembly of the favored even-layer thickness PbSe regions the precursor already has a bilayer nanoarchitecture. For q = 7, the energy difference is not enough to drive the system to segregate to a layer with a thickness of q monolayers into q - 1 and q + 1 layers during the deposition although layers with q = 6 and 8, in addition to q = 7, are observed in the HAADF-STEM images.

In the system investigated here, the stability of PbSe bilayers relative to odd-thickness PbSe blocks drives the diffusion of Pb and Se atoms during both deposition and self-assembly to form coherent bilayers. Similar odd-even alternation based on energy differences between even and odd conformations has been observed in self-assembled alkane monolayers melting points, and the dynamical behavior of liquid alkanes near their melting points.[39-42] The results obtained herein highlight the importance of calculations in determining the relative energy of different thickness-thin layers of 3D materials. Different surfaces exposed to the interface will change the relative energies and would aid experimentalists in choosing substrates, heterostructure constituents, and synthetic conditions.

7.4. CONCLUSION

The data presented here illustrates the importance of the nanoarchitecture of precursors in the self-assembly of the precursors to form heterostructures. The experimental evidence indicates that atoms can undergo long-range surface diffusion during the deposition process to form more favorable configurations than those targeted. Surprisingly, even though long-range diffusion occurs, the precursors evolve into metastable products

rather than completely segregating into a mixture of thermodynamically stable binary compounds. Limiting diffusion via low temperatures restricts the topology of the free energy landscape that can be explored, making the structure of the precursor critical in determining what products form. Precursors with a nanoarchitecture close to a specific local free energy minimum self-assemble during deposition and subsequent low-temperature annealing via a near diffusionless process. To form monolayers of compounds with bulk 3D structures, the strength of the bond between the constituents must be strong enough to favor the formation of a monolayer rather than localized islands and the temperature must be low enough to avoid more stable configurations.

7.5. BRIDGE

For q = 1, 3, 5 PbSe monolayers in $[(PbSe)_{1+\delta}]_q(VSe_2)_1$ was found to be unstable, and would undergo significant rearrangement. This was confirmed using a combination of computational experiments, X-ray techniques, and HAADF-STEM/EDS. Domains of excess PbSe that did not form in the layered heterostructure were observed on the surface in cross-sections, providing insight to how compounds with these elements will react depending on their precursor structure. and are important to consider for later chapters where compounds containing these constituents are discussed. The next chapter leads into the next section of this dissertation, where all results from chapters thus far are considered in the analysis and approach in chapters in this section. Modulated precursors with thicknesses < 10 Å, similar to those discussed to this point, were prepared and contained Fe and Se with varied composition. Annealing studies were performed to study reaction pathways in these binary diffusion couples.

CHAPTER VIII

UNDERSTANDING THE REACTIONS BETWEEN FE AND SE BINARY DIFFUSION COUPLES.

8.0. AUTHORSHIP STATEMENT

Chapter VIII was published in *ACS Chemistry of Materials* in 2021. Primary author Dylan Bardgett and co-authors Danielle Hamann and Dennice Roberts prepared thin modulated Fe and Se precursors, collected and analyzed XRD, XRF, and XRR data. Ping Lu collected HAADF-STEM/EDS data. Sage Bauers edited the entire manscript. David Johnson is my advisor. I assisted with writing and editing the entire manuscript, prepared TEM specimen, and analyzed data from X-ray techniques and HAADF-STEM/EDS.

8.1. INTRODUCTION

Recent advances in computational materials science and theory-based efforts have predicted numerous undiscovered materials with interesting properties.[1-4] However, the synthesis of many of these predicted materials has been challenging. Part of this challenge lies in the limited number of synthetic approaches, almost all of which yield only thermodynamically stable products.[5] We need to go beyond computational "materials by design" (what to make) to "reaction by design" (how to make) using both computation and experiment. One promising approach to synthesizing new materials is through nearly diffusionless crystallization of amorphous reactants, since any amorphous configuration is already higher in energy than any synthetically accessible crystalline phase.[6] A second factor is the limited understanding of solid-state reaction kinetics and the resulting inability to

control reaction intermediates.[7] The lack of control over reaction intermediates is evident in the limited number of ternary and higher order compounds that have been prepared, as the formation of stable binary compounds as intermediates limits products to those that are more stable than a mix of binary compounds.[8,9]

Ternary and higher order T-Fe-Se systems represent a field that has been intensively researched both theoretically and experimentally but still faces significant synthetic challenges using conventional approaches.[10-13] Binary iron selenides have been extensively investigated due to the discovery of superconductivity in PbO structured (P4/nmm) β-FeSe,[14] their potential as candidates in semiconductor/ferromagnet device applications,[13] and the discovery of their promise as photocatalysts in hydrogen evolution reactions.[15] The discovery of superconductivity enhancements arising from interfacial interactions between single layer β-FeSe prepared on perovskite-oxide substrates resulted in a boom in global interest and research.[16] Their potential applications resulted in the attempted synthesis of many heterostructures and superlattices containing iron selenides, but only limited variety have been successfully prepared.[13,17-19] The synthesis of these hierarchical structures, as well as ternary iron selenide compounds predicted from calculations to be stable, has been challenging,[17,20] presumably due to the lack of information concerning the kinetics of the reactions between Fe and Se, the subtleties of β-FeSe phase formation, and the influence of the adjacent phases.[7]

Here we report the composition dependence of the sequence of phase formation for the reaction between Fe and Se by depositing alternating layers of ultrathin Fe and Se on silicon substrates. All of the films formed crystalline Fe-Se compounds during the ambient-

temperature deposition and phase formation is found to be highly dependent on the local composition. Selenium rich films contained two previously unreported compounds, where the phase that formed depends on composition. Both of these compounds begin to decompose into thermodynamically stable binary compounds at very low temperatures (~ 100°C) for a solid state transformation. More iron rich precursors form crystallographically aligned β-FeSe, with the *c*-axis perpendicular to the silicon substrate. Annealing these films at elevated temperatures results in both increased grain size and better crystallographic alignment. The metastable phases may be useful intermediates for the synthesis of ternary iron selenides form precursors containing ultrathin layers of the three elements. Furthermore, the formation of crystallographically aligned FeSe during deposition suggests that heterostructures may be prepared from designed precursors via diffusionless transformations.

8.2. METHODS AND MATERIALS

The Thin film precursors of Fe and Se layered on (111) Si substrate wafers were prepared in a custom high vacuum ($<10^{-6}$ torr) physical vapor deposition chamber from elemental sources. A Knudson effusion cell was used to vaporize selenium (99.99%), while an electron-beam gun evaporated Fe from an iron target (99.95%). Programmed shutters positioned between the elemental sources and the substrate were used to control the amount of each element deposited onto the rotating Si substrate, while deposition rates were monitored at all times with quartz crystal microbalances. Fe and Se were sequentially deposited to form compositionally modulated precursors in accordance with the modulated

elemental reactants (MER) method.[21] Fe|Se bilayer, or repeat unit (RU), thicknesses were limited to less than 10 Å to minimize diffusion distances.

Samples were removed from the deposition chamber and stored in a nitrogen glove box (>0.2 ppm oxygen), where they were annealed or left as-deposited (AD). Annealing took place on a calibrated hot plate by resting the samples face up on the hot plate set to the desired temperature for 15 minutes. Subsequent annealing steps at higher temperatures were performed on the same sample using the process described above. Samples were temporarily removed from the nitrogen atmosphere as needed for characterization.

Specular (00*l*) X-ray diffraction (XRD) and X-ray reflectivity (XRR) patterns were collected on a Bruker D8 diffractometer with Cu Kα radiation in θ-2θ locked-coupled scan mode. Each specular XRD pattern was collected over a 2θ range of 5-65°. XRR patterns were collected in the same instrument geometry over a 2θ range of 0-11° to measure the total thickness of each film. Film thicknesses were determined using a linear least squares fit of the sequential positions of Kiessig fringes subject to the equation $\sin^2(\theta) = n^2(\lambda^2/4d^2) + \sin^2(\theta_{crit})$ with $\sin^2(\theta)$ as the ordinate and n^2 as the abscissa. Here, d is the thickness of the entire film and θ_{crit} is the critical angle. The thickness, d, was then determined from the slope of the fit and the uncertainty in d was propagated from the regression statistics of the fit.

Grazing incidence XRD (GIXRD) and in-plane diffraction patterns were collected on a Rigaku Smartlab diffractometer with Cu Kα radiation and parallel-beam/parallel slit analyzer (PB/PSA) and parallel beam (PB) optics, respectively. Each GIXRD pattern was collected over a 2θ range of 5-65° with an incident angle (ω) offset of 0.5° and a step-size of

0.04°. Similarly, each in-plane diffraction pattern was collected over a 2θ range of 15-110° with a step-size of 0.1°.

The number of atoms per unit area in each film was determined via an ultra-thin film X-ray fluorescence (XRF) technique elaborated at length by Hamann et al.[22] A series of two-dimensional transition metal selenide films with thicknesses well below the limit at which matrix absorption of fluoresced X-rays becomes significant (~ 200 nm) were prepared and used as calibration standards relating the XRF intensity of Se X-ray emission lines to the number of Se atoms per unit area through a linear relationship. The slope of this calibration curve allows for the facile determination of the areal density of Se atoms from the XRF intensity of a characteristic Se X-ray emission (Figure E.1). The calibration curve for Fe was created by preparing stoichiometric $FeSe_2$ and using the Se calibration to determine the Fe atoms per unit area of $FeSe_2$ films with varying thickness. The relative error in atoms per unit area was determined by adding the relative errors of the calibration slope and of the FeSe XRF standard in quadrature, giving a relative error of 0.8% for Fe atoms/Å^2 and 1.5% for Se atoms/Å^2. There was assumed to be no uncertainty in the number of repeat units because this in an integer number that is controlled during the deposition process.

The atomic percent composition of each film was determined by dividing the Fe atoms per unit area by the sum of the Fe atoms per unit area and Se atoms per unit area (Figure E.2). The uncertainty in the percent composition was nominally taken to be ± 1%, which is well above the uncertainty propagated from the determinations of atoms/Å^2 to account for additional sources of uncertainty.

Cross-sections of two samples were prepared with an FEI Helios NanoLab 600i DualBeam FIB-SEM using standard lift-out procedures. High angle annular dark field (HAADF) images were collected on an FEI Titan G2 80-200 scanning transmission electron microscope (STEM) with a Cs probe corrector and ChemiSTEM technology (X-FEG and SuperX EDS with four windowless silicon drift detectors) operated at 200 kV.

8.3. RESULTS

To explore the fundamental reaction dynamics between Fe and Se, a series of compositionally modulated Fe|Se thin films were prepared with varied compositions as shown as red tick marks on the Fe-Se phase diagram[23] provided in Figure 8.1 and summarized in Table 8.1. These samples span the composition range of known FeSe compounds in the binary Fe-Se phase diagram. The number of Fe|Se bilayers deposited and elemental compositions of the prepared samples are given in Table 8.1.

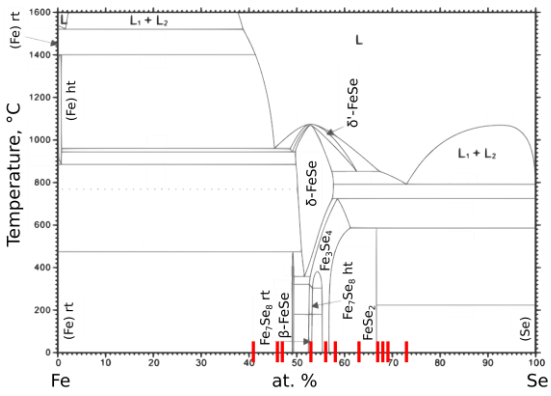

Figure 8.1. The compositions explored in this study marked on the iron-selenium phase diagram as red marks.

The thicknesses of the Fe|Se bilayers in the samples were determined by measuring the total thickness of the samples from their XRR patterns (Figure E.3) and dividing by the total

number of times the Fe|Se bilayer was deposited. In only one sample (31% Fe) with the largest RU of 9.2 Å we observe a peak in the XRR pattern corresponding to the artificial layering of the precursor (at $2\theta = 10.0°$), which agrees with the expected RU based on total thickness analysis. This indicates that the sample has not yet undergone complete mixing despite the nucleation of an unknown compound, as will be discussed later. The areal density (atoms/$Å^2$ per RU) of Fe and Se were measured using XRF, and the compositions of the samples ranged from 27-59% Fe (Table 8.1). The composition of precursors prior to annealing was determined based on the areal densities of each element. During subsequent annealing and the collection of diffraction data, selenium loss and oxygen incorporation into the films is observed.

Table 8.1. Sample Characteristics

*Composition (% Fe)	Total thickness (Å)	Number of RUs	RU thickness (Å)	Fe atoms/Å² per RU	Se atoms/Å² per RU
59	401(1)	83	4.8(1)	0.158(1)	0.110(2)
54	272(1)	50	5.4(1)	0.153(1)	0.132(2)
53	321(1)	51	6.3(1)	0.175(1)	0.156(2)
47	260(2)	54	4.8(1)	0.116(1)	0.132(2)
44	255(2)	50	5.1(1)	0.125(1)	0.162(2)
42	273(2)	48	5.7(1)	0.135(1)	0.187(3)
37	388(2)	83	4.7(1)	0.101(1)	0.169(3)
33	235(1)	101	2.3(1)	0.041(1)	0.081(1)

GIXRD patterns of each sample prior to annealing are provided in Figure 8.. The samples can be sorted into three main groups based on similarities in the GIXRD patterns. The first group shown at the bottom of Figure 8.2 spans the composition range of 27-33% Fe and is characterized by an intense reflection near 2θ = 15.0° and two broad reflections at 2θ = 30.7° and 55.5°, respectively. Together these reflections do not match any single known room temperature phase of FeSe.

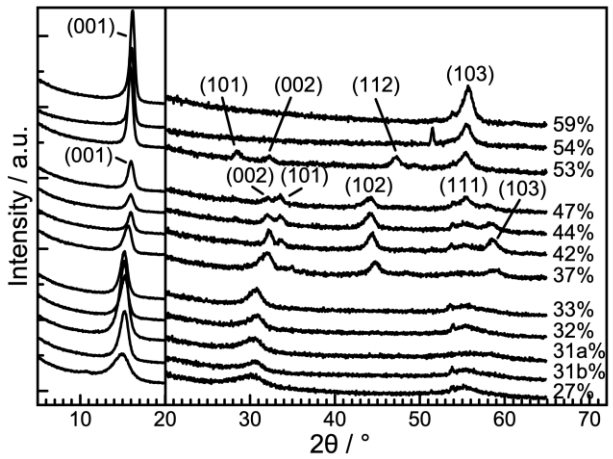

Figure 8.2. Grazing incidence XRD patterns of as-deposited samples plotted as a function of % Fe composition. For visualization purposes, the intensity at angles greater than 2θ = 20° has been artificially enhanced by a factor of 5.

The second group is centrally located in Figure 8.2 and spans the composition range of 37-47% Fe. This group is characterized by an intense peak at 2θ = 15.6-16.0°, two weak reflections at 2θ = 32.0-32.4° and 2θ = 33.4-33.6°, and another weak reflection at 2θ = 44.0°. The intensities of the higher angle reflections are highest for compositions between 42 and 44% Fe, although the first reflection reaches a maximum intensity at 47% Fe. The grazing incidence XRD pattern of the sample with 42% Fe can be indexed to a hexagonal

unit cell with a = 3.488(5) Å and c = 5.533(5) Å. Similarly, this unit cell does not correspond to any presently known FeSe compound.

The third group spans the composition range 53-59% Fe and is characterized by a strong reflection at 2θ = 16° and a weak reflection at 2θ = 55° that increases in intensity as the relative amount of Fe increases. With 3 more reflections than the other samples with higher Fe content, the 53% Fe sample can be indexed to a tetragonal unit cell with a = 3.771(5) Å and c = 5.549(5) Å, which is consistent with the unit cell of β-FeSe (P4/nmm, a = 3.7720(9) Å and c = 5.5161(5) Å).[24] The lack of (101), (002) and (112) reflections for the 54% and 59% Fe samples suggests β-FeSe crystallizes with preferred orientation as the composition of Fe is increased from 53% to 59%, as will be subsequently discussed. In the proceeding paragraphs, the structural evolution of samples in each of the three groups is followed as a function of annealing temperature using X-ray diffraction, HAADF-STEM, and XRF to closely monitor changes in structure and composition.

Figure 8.3 contains grazing incidence and specular XRD patterns for a representative sample, 31a% Fe, in the 27-33% Fe composition window collected after annealing at the indicated temperatures. All samples in this composition range formed an unknown reaction intermediate during deposition characterized by three broad reflections in the AD grazing incidence XRD patterns. The largest two reflections are also present in the specular diffraction patterns, indicating there may be little or no preferred orientation. The three reflections cannot be indexed to any simple cubic or tetragonal cell, but can be indexed to a hexagonal unit cell with lattice parameters a = 3.37(6) Å and c = 5.86(2) Å. With this unit cell, the reflections at 2θ = 15.0°, 2θ = 30.7°, and 2θ = 55.5° can be indexed to (001),

(002)/(100), and (111)/(103) reflections, respectively. The large uncertainties in the lattice parameters reflect the broad and potentially overlapping reflections. This unit cell is not consistent with any reported transition metal selenide phase in the literature, although an extrapolation of the work done by Kumar et. al. suggests that a similar unit cell may be achieved in δ-FeSe at very low temperatures (~ 10K) and high pressures (~ 10 GPa).[31] Further research will need to be conducted on these as-deposited structures before we can come to a conclusive structure determination. The intensity of the reflections decreases after annealing at 100°C, which prevents further structural analysis of this unknown compound. Local structural motifs of metastable Sb-rich phases are also observed in as-deposited Fe|Sb bilayers, even when it is compositionally unfavorable.[25] In films with the appropriate layer thickness and composition these local fragments can be ripened into crystalline phases.[26] This suggests it may be possible to isolate this new Se-rich $FeSe_x$ phase with a suitable precursor. Between 200 and 400°C, a new set of reflections is observed in all samples which can be indexed to an orthorhombic crystal structure with a = 4.800(2) Å, b = 5.775(1) Å, and c = 3.562(2) Å. These lattice parameters are close to the range reported for marcasite-type $FeSe_2$ (Pnnm, a = 4.804(2) Å, b = 5.784(3) Å, and c = 3.586(2) Å).[27-29] At 400°C, all samples temporarily rearrange to a new phase that can be described by a monoclinic unit cell with lattice parameters of approximately a = 6.156(3) Å, b = 3.54(1) Å, c = 11.22(1) Å, and β = 91.96(5) °. The formation of this new phase is accompanied by a substantial evaporation of Se during annealing at 400°C, driving the low temperature $FeSe_2$ phase towards compounds with lower Se content. These lattice parameters are close to those reported for monoclinic Fe_3Se_4, which crystallizes in the Cr_3S_4 structure type (I2/m) with lattice parameters a = 6.17(1) Å, b = 3.54(1) Å, c = 11.1(1) Å, and β = 92.0°.[30] All samples undergo an additional

rearrangement to a hexagonal crystal structure (a = 3.602(3) Å and c = 5.847(4) Å at temperatures above 450°C accompanied by a further loss of Se. These lattice parameters are slightly below the range of those reported for the thermodynamically stable δ-FeSe ($P6_3/mmc$) phase (a = 3.618 – 3.636 Å and c = 5.880 – 5.946 Å).[31,29]

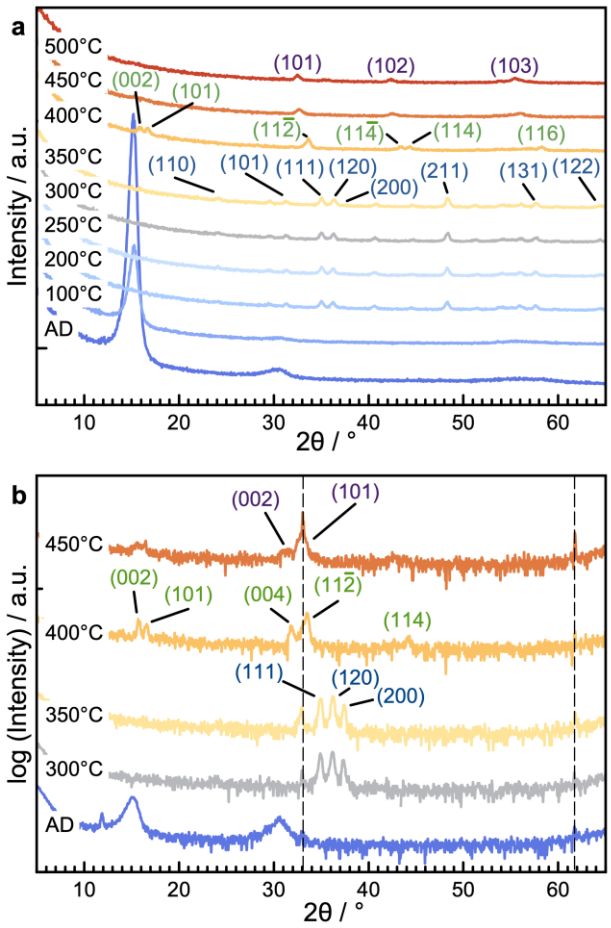

Figure 8.3. Representative (a) grazing incidence and (b) specular XRD patterns of the 27-33% Fe composition window as a function of annealing temperature. The colors of indices correspond to (blue) $FeSe_2$, (green) Fe_3Se_4, and (purple) δ-FeSe. Reflections marked with a dashed vertical line are an artifact of the Si substrate.

The similarity in grazing incidence XRD patterns between samples in the 33-31% Fe range suggest that, within the RU thickness range of 2.3 to 9.2 Å, diffusion distance does not have a significant role in phase formation at this nominal composition. The specular diffraction

patterns in Figure 8.3b also support the sequential evolution of the sample from an unknown as-deposited structure → $FeSe_2$ → Fe_3Se_4 → δ-FeSe as annealing temperature is increased. The similarity of grazing incidence and specular diffraction patterns at all temperatures suggests that the extent of preferred orientation, if any, is small.

Figure 8.4 provides representative grazing incidence and specular XRD patterns for the 37-47% Fe composition window as a function of temperature. The sample with 42% Fe is used as the representative sample at low temperatures. This sample was annealed up to 350°C after which it was accidentally exposed to excess oxygen and oxidized. The sample with 37% Fe, which has identical diffraction patterns at 300°C and 350°C, is used as a representative for this composition window at higher temperatures instead. The as-deposited GIXRD and specular XRD patterns contain several reflections whose positions do not correspond to any presently known structure in the Fe-Se phase diagram expected under room temperature and atmospheric conditions. The diffraction pattern can be indexed to a hexagonal unit cell with a = 3.488(5) Å and c = 5.533(5) Å. While dissimilar from the unit cell parameters of δ-FeSe under atmospheric pressure, these unit cell parameters are consistent with those of δ-FeSe at room temperature and 8.5 GPa of pressure (a = 3.4822(8) Å, c = 5.5069(5) Å) reported by Kumar et. al.[31] The as-deposited diffraction patterns in the 37-47% Fe composition window are notably distinct from those reported above in the 27-33% Fe window, indicating that these are two separate unknown phases. This structure mostly decomposes by 200°C and at 300°C the diffraction patterns can be indexed to an orthorhombic unit cell with a = 4.795(3) Å, b = 5.753(4) Å, and c = 3.570(3) Å, with the exception of a reflection at 2θ = 16°. This unit cell is similar to the structure observed at this

temperature in the 27-33% Fe composition window and the lattice parameters are close to the literature reported unit cell parameters for marcasite $FeSe_2$.[27] As suggested by the lack of reflections in the specular pattern compared to the grazing incidence pattern, there is not significant preferred alignment of this compound to the substrate. The weak intensity at 2θ = 16° could belong to residual quantities of the as-deposited structure or to β-FeSe or Fe_3Se_4, which both have known reflections at that angle. At 400°C, the sample undergoes another structure rearrangement accompanied by a significant loss of Se. Similar to the 27-33% Fe composition window at 400°C, the diffraction patterns can be indexed to a monoclinic unit cell with a = 6.183(2) Å, b = 3.504(2) Å, c = 11.263(4) Å, and β = 91.94(3)°, which is in close agreement with the literature reported values for Fe_3Se_4 (I2/m).[30]

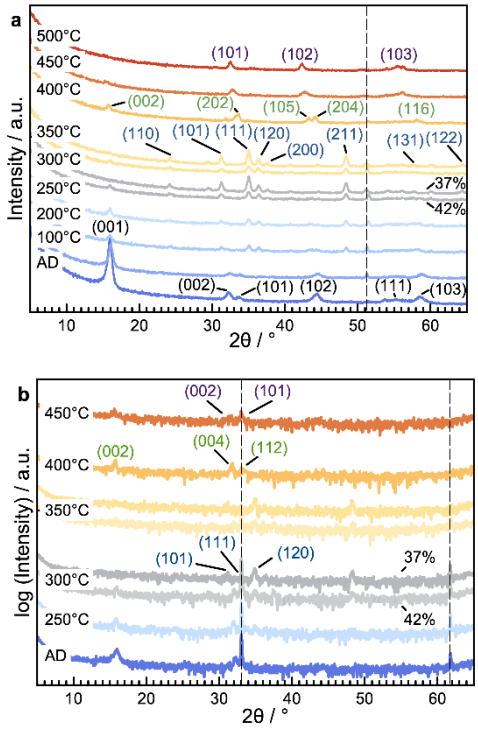

Figure 8.4. Representative (a) grazing incidence and (b) specular XRD patterns of the 37-47% Fe composition window as a function of annealing temperature. Diffraction patterns are provided of the 42% Fe sample for temperatures ≤ 350°C and of the 37% Fe sample for temperatures ≥ 300°C. The colors of indices correspond to (black) the unknown hexagonal

phase, (blue) $FeSe_2$, (green) Fe_3Se_4, and (purple) δ-FeSe. Reflections marked with a dashed vertical line are an artifact of the Si substrate.

The sample undergoes one more rearrangement at 450°C, resulting in nearly identical diffraction patterns to the high temperature patterns in the 27-33% Fe composition window belonging to the δ phase of FeSe.[28] We conclude that, once the samples in the 37-47% composition window form $FeSe_2$ at 200°C, they follow the same progression of $FeSe_2$ → Fe_3Se_4 → δ-FeSe as observed for samples in the 27-33% Fe composition window.

To further probe the microstructure in a sample which was not aligned to the substrate based on XRD, HAADF-STEM images were collected from a cross-section of the 37% Fe sample annealed to 350°C (Figure 8.5). Figure 8.5a contains a representative image of the entire film, which revealed large columnar grains with nearly vertical grain boundaries from the bottom to the top of the film. XRD indicated that the sample was not preferentially aligned to the substrate, however this provided insight into the microstructure that could not be obtained from XRD.

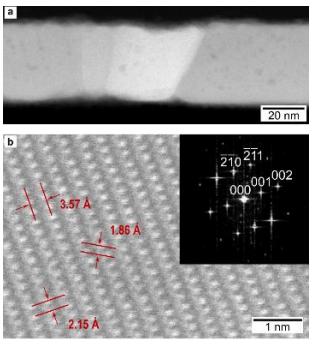

Figure 8.5. HAADF-STEM images of a cross-section of the 37% Fe sample annealed to 350°C. (a) Representative image of the entire film where several large grains and boundaries from the bottom to the top of the film are shown. (b) Image collected within a grain aligned to the $[1\bar{2}0]$ zone axis in $FeSe_2$. The spacings labeled in red correspond to d_{001} = 3.57 Å, $d_{\bar{2}10}$ = 2.15 Å, and $d_{\bar{2}11}$ = 1.86 Å which are close to literature values for $FeSe_2$. The FFT of this region is indexed in the upper right corner.

An on-axis grain is shown in Figure 8.5b, where the structure was resolved. The measured spacings between atomic columns from the image agree with literature values for $FeSe_2$, which were measured to be d_{001} = 3.57 Å, $d_{2\bar{1}0}$ = 2.15 Å, and $d_{2\bar{1}1}$ = 1.86 Å. An FFT from this region was indexed to the $[1\bar{2}0]$ zone axis in $FeSe_2$. Energy dispersive X-ray Spectroscopy (EDS) maps confirm that the sample is comprised of homogeneous Fe and Se, with an Fe-oxide layer at the film surface (Figure E.5).

Grazing incidence and specular XRD patterns of the FeSe samples in the 53-59% Fe composition window as a function of annealing temperature are provided in Figure 8.6, using the 59% Fe sample as representative of the structural evolution in the 53-59% Fe composition window. In-plane XRD patterns of the 59% and 53% Fe samples annealed at 300°C are additionally provided in Figure E.4. The two peaks in the as-deposited GIXRD pattern can't be indexed from the diffraction patterns at grazing incidence alone. The specular XRD patterns exhibit three evenly spaced reflections at 2θ = 16.2°, 32.6°, and 49.9°, suggesting they belong to the same family of (00*l*) reflections. The presence of a single family of reflections in the specular XRD pattern indicates preferred orientation of the sample with respect to the Si substrate. A rocking curve measurement on the first reflection has a line width of θ = 8.4° (FWHM), as provided in Figure E.4. The first reflection in both specular XRD and GIXRD patterns are at the same angle, which is consistent with the measured rocking curve width, indicating that this reflection should still be observed in a grazing incidence scan. These reflections all remain after annealing the precursor to high as 400°C. The in-plane XRD pattern at 300°C of the 59% Fe sample exhibits only two intense reflections at 2θ = 47.8° and 69.8°.

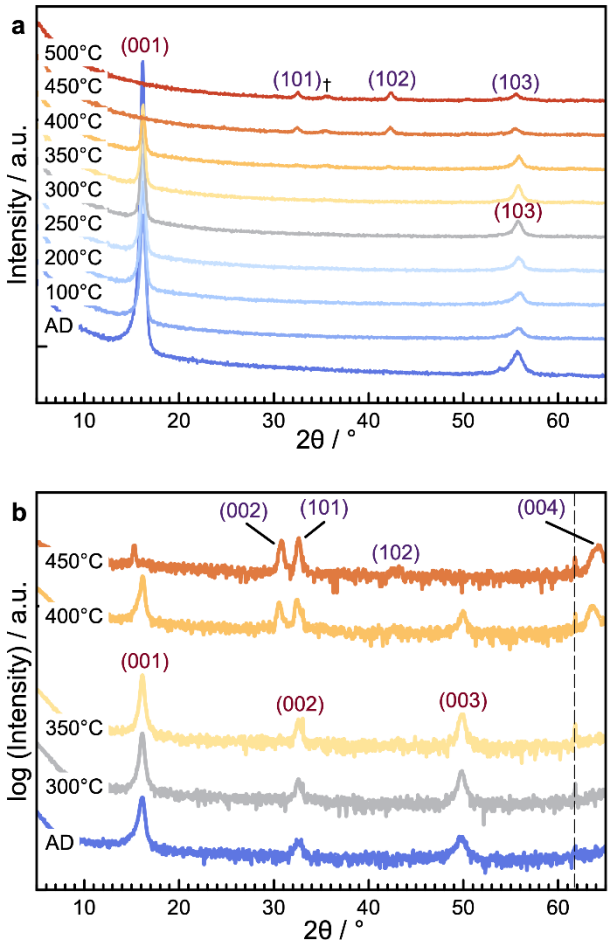

Figure 8.6. Representative (a) grazing incidence and (b) specular XRD patterns of the 53-59% Fe composition window as a function of annealing temperature. The colors of the indices correspond to (red) β-FeSe and (purple) δ-FeSe. Reflections marked with † likely belong to an iron oxide phase, while reflections marked with a dashed vertical line are an artifact of the Si substrate.

By refining the grazing incidence, specular, and in-plane diffraction patterns of the 59% Fe sample at 300°C together, and assuming a preferred orientation with the *c*-axis perpendicular to the substrate, the patterns can be indexed to a tetragonal crystal system with a = 3.78(1) Å and c = 5.492(1) Å. The calculated lattice parameters from the observed reflections are close to the lattice parameters reported in the literature for β-FeSe (a =

3.7720(9) Å and c = 5.5161(5) Å),[24] supporting the conclusion that all samples in the 53-59% Fe composition window contain β-FeSe. Above 400°C, the sample rearranges to form a new compound, and the diffraction patterns can be indexed to a hexagonal unit cell yielding lattice parameters of a = 3.77(2) Å and c = 5.916(8) Å. These lattice parameters are close to the range of values reported for δ-FeSe (a = 3.6361(9) Å and c = 5.907(2) Å) phase, which thermodynamically stable at this temperature and composition (*cf.* Fig 1).[31-33] The only difference between the evolution of structure in these three samples is the temperature at which the δ-FeSe phase becomes the dominate phase, which ranges from 250°C at 53% Fe to 400°C at 59% Fe (Figure E.4).

HAADF-STEM images were collected on a cross-section of the 59% Fe sample annealed to 350°C. Due to the thickness of the cross-section, high resolution images of this sample were not obtained. However, the c-axis thickness in the sample was observed in images collected after aligning the cross-section to the Si [110] zone axis (Figure 8.7).

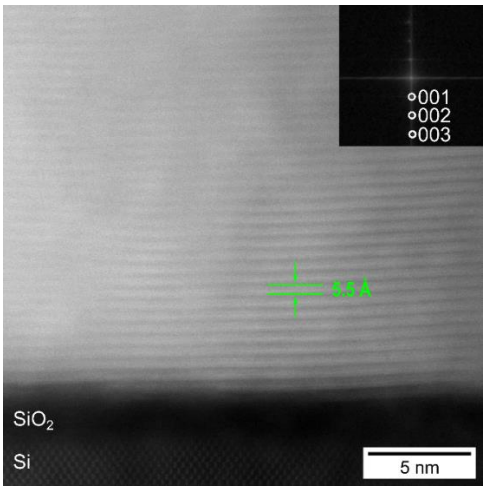

Figure 8.7. HAADF-STEM image of a thick cross-section of the 59% Fe sample annealed to 350°C. The cross-section thickness was too large to achieve atomic resolution. The Si and native SiO_2 are seen at the bottom of the image, followed by layers of β-FeSe which are aligned to the substrate.

The thickness labeled in green corresponds to the c-axis lattice parameter for β-FeSe. An FFT of this region is shown in the upper right corner, which contains only 001 reflections.

The thickness of β-FeSe layers was measured to be 5.5 Å, which is close to the literature β-FeSe c-axis lattice parameter. An FFT of this region shows spots which can be indexed to 00l reflections. This agrees with XRD collected from this sample and confirms that the β-FeSe is aligned to the Si + native SiO_2 substrate.

8.4. Conclusion

All binary Fe|Se precursors explored in this study crystallized during the deposition process despite being deposited on nominally room temperature substrates. Two novel, low temperature Fe|Se compounds form in the 27-33% Fe and 37-47% Fe composition windows. We speculate that these phases formed during deposition due to low barriers to nucleation and significant surface diffusion. Off-stoichiometry in the as-deposited 37-47% Fe precursor's hexagonal phase could cause the structure to resemble that of high-pressure δ-FeSe. The few, broad, and low intensity reflections in these diffraction patterns prevent us from refining the structures with the present data. Both of these compounds decomposed during annealing at 200°C forming an orthorhombic structure with lattice parameters that are close to the reported unit cell parameters for marcasite $FeSe_2$. $FeSe_2$ decomposes and Se is lost as the annealing temperature in increased, resulting in the formation of Fe_3Se_4 and, subsequently, δ-FeSe as the temperature is increased further. The temperature at which each phase decomposes depends on the composition of the precursor.

Samples in the 53-59% Fe composition window form β-FeSe with crystallographic alignment during the deposition. β-FeSe nucleates over a considerable composition range,

suggesting the precursors disproportionate into β-FeSe and pure Fe for iron rich compositions and into β-FeSe and more Se rich phases for selenium rich compositions The grains of β-FeSe increase in size as annealing temperature is increased, with the sample transforming into δ-FeSe after annealing at 400°C. The self-assembly of crystallographically aligned β-FeSe films from the precursors is a significant finding, as β-FeSe is a high temperature superconductor that has been intensively investigated.[15] Nucleation on the substrate indicates a non-epitaxial growth mode controlled only by local composition. The self-assembly of crystallographically aligned β-FeSe opens avenues to preparing heterostructures containing this compound.

The nucleation of binary compounds during the deposition of ultrathin Fe and Se layers in multilayer films also provides insights into the failure to prepare ternary compounds containing Fe and Se that were predicted to be stable or nearly so. The results here suggest that ternary compounds need to be more thermodynamically stable than a mixture of binary Fe-Se compounds and other phases, as binary Fe-Se compounds form immediately during reactions involving these elements. There is a strong driving force for mixing Fe and Se and nucleating binary compounds, as only the film with the thickest bilayer (9.2 Å) showed a Bragg reflection from the intended artificial modulation in the precursor but still crystalized during deposition. The weak intensity of this reflection indicates that there is only a small difference in local composition within the bilayers.

One possible approach to preparing ternary compounds containing Fe, Se, and a third element, T, would be to use a more complex layering sequence – Fe|T|Se|T – to prevent the immediate formation of binary Fe-Se compounds during the deposition.[34] The

formation of metastable compounds suggests the possibility of forming more interesting ternary compounds with Fe and Se using these metastable compounds as reaction intermediates. The metastable intermediate compounds would need to be intimately mixed with the ternary element to avoid having diffusion be the rate limiting step in the formation of a ternary compound. A key question is whether information obtained about binary diffusion couples enables the rational design of precursors that will avoid stable reaction intermediates in the reaction pathway towards metastable ternary compounds.

8.5. BRIDGE

This chapter follows a series of binary Fe–Se ultrathin diffusion couples via designed thin-film precursors and investigating their structural evolution as a function of composition and annealing temperature. Two previously unreported Fe–Se phases crystallized during the deposition process on a nominally room-temperature Si substrate in the 27–33 and 37–47% Fe (atomic percent) composition regimes. Both phases completely decompose after annealing to 200 °C in a nitrogen glovebox. At higher temperatures, the sequence of phase formation is governed by Se loss in the annealing process, consistent with what would be expected from the phase diagram. Films rich in Fe (53–59% Fe) crystalized during deposition as β-FeSe (*P*4/*nmm*) with preferred *c*-axis orientation to the amorphous SiO_2 substrate surface, providing a means to nonepitaxial self-assembly of crystallographically aligned, iron-rich β-FeSe for future research. ADF-STEM/EDS was used to investigate one of the samples that did not form with crystallographic alignment, and contained columnar grains of $FeSe_2$. The next chapter follows a similar study, but for Fe and Se bilayers and multilayers with thicknesses > 10 Å.

CHAPTER IX

ASYMMETRIC INTERFACES IN NANOSCALE BILAYER AND MULTILAYER FE-SE

9.0. AUTHORSHIP STATEMENT

Chapter IX is under preparation for submission to *ACS Inorganic Chemistry*. Co-author Danielle Hamann assisted with deposition of precursors. Dylan Bardgett assisted with collection and analysis of XRD, XRR, and XRF data. David Johnson is my advisor. Ping Lu, Niklas Wolff, and Andriy Lotnyk collected HAADF-STEM/EDS data. I am the primary author of this manuscript, and prepared precursors, TEM specimen, analyzed HAADF-STEM/EDS data, and collected and analyzed XRD, XRR, XRF data as a function of annealing temperature.

9.1. INTRODUCTION

While nucleation, diffusion, and growth in solid-state reactions have been widely studied[1], little is known about controlling reaction pathways. To successfully synthesize compounds predicted by projects such as the Materials Genome Initiative[2], a better understanding of reaction pathways and control over intermediates is necessary. When attempting to synthesize compounds predicted to be thermodynamically stable, intermediates formed which are generally binary compounds.[3] The formation of these intermediates prohibits the formation of these predicted compounds, which becomes more difficult when considering ternary or higher order phases. Since interdiffusion is classically the rate limiting step in solid state reactions, it is difficult to explore reaction pathways

experimentally due to the lack of experimental methods to follow the rearrangement of atoms.

Controlling interdiffusion and reactions at solid-solid interfaces is critical for current thin film technologies. For example, all microelectronics generally use metal silicide thin films as contact and electrode materials, diffusion barriers, and interconnects.[4,5] Controlling interdiffusion and reactions with subsequent layers is critical for forming and successfully implementing metal silicides in devices. Polycrystalline metal films deposited on single-crystal silicon can react at temperatures as low as 100°C, where diffusion or interface-reaction controls the growth.[4] Growth kinetics for a variety of metal silicides has been well studied and general reaction rules (based on the ordered Cu_3Au rule[6]) are followed to form reproducible metal silicides for implementation in devices. Generally, these rules state that nucleation of a new phase and if a nucleus can grow depends on a balance between the Gibbs free energy change of creating a nucleus of a new phase and the energy associated with forming the surface of the nucleus.[5] After nucleating and growing a new phase, interfaces and energetics are different for subsequent phases, altering the Gibbs free energy per unit volume of the new phase (Δg_v) and the surface energy change per unit area associated with creation of the nucleus (Δg_v). Simply, the ordered Cu_3Au rule applicable to metal silicides declares that the most mobile species should determine which phase forms first (Cu_3Au if Cu is more mobile than Au, $CuAu_3$ if Au is more mobile than Cu). For a system with phases A and B where A is more mobile (or Cu and Au), A_2B would be the first phase to nucleate and grow, followed by AB between A_2B and B. For thin films, the second AB phase will not form until A_2B exceeds a critical thickness.

Here we explore where those rules are followed for binary Fe-Se. There are four stable Fe-Se phases which include FeSe, $FeSe_2$, Fe_3Se_4, and Fe_7Se_8. There are two FeSe phases, which include β-FeSe (P4/nmm) and δ-FeSe (P63/mmc). The reaction of Fe and Se precursors with thicknesses much greater than 1 nm were investigated, in contrast to that reported for thin modulated precursors.[7] Different ratios of Fe-Se were deposited using physical vapor deposition with varying layering sequences on substrates nominally at room temperature. Samples were characterized with X-ray diffraction (XRD), reflectivity (XRR), and fluorescence XRF) before and after annealing to investigate phase formation, film structure, and composition.On select samples, High Angle Annular Dark Field – Scanning Transmission Electron Microscopy (HAADF-STEM) and Energy Dispersive X-ray Spectroscopy (EDS) were used to further probe structural information. We observed crystallization, complex XRR patterns, and varying amounts of oxygen for all samples upon deposition. HAADF-STEM/EDS revealed that in multilayer samples, the first layer of Fe did not react with the first Se layer deposited, however the next Fe layer deposited on Se reacted completely to form a unit cell consistent with β-FeSe, however with slightly larger lattice parameters. The surface of randomly oriented FeSe crystallites is relatively smooth, followed by a layer of Fe deposited on FeSe. Any remaining Se reacts with Fe, leaving a rough layer of Fe. This pattern of asymmetric interfaces continues through the entire sample. For the binary sample where Se is deposited on Fe and Fe is deposited on Se, a small interfacial reaction likely occurs upon deposition. This suggests that the initial substrate (Si with native SiO_2 (bilayer samples) versus Fe (multilayer samples) impacts the reactivity of elements upon deposition.

9.2. METHODS AND MATERIALS

Precursors containing Fe and Se on (111) Si substrates were prepared using a custom high vacuum (<10^{-6} torr) physical vapor deposition chamber from elemental sources. An electron beam gun was used to deposit Fe from an iron target (99.95%) and Se layers were deposited using a Knudson effusion cell. Shutters were used to control the amount of each element deposited, where deposition rates were monitored with quartz crystal microbalances. Substrates are nominally at room temperature. After deposition, samples were stored in a nitrogen glove box (>0.2 ppm oxygen). Annealing took place in the nitrogen glove box on a calibrated hot plate for 15 minutes at temperatures from 50 - 400°C. For characterization, samples were removed from the glove box.

X-ray reflectivity (XRR) patterns were collected on a Bruker D8 diffractometer with Cu Kα radiation in θ-2θ locked-coupled scan mode. Grazing incidence XRD (GIXRD) patterns were collected on a Rigaku Smartlab diffractometer with Cu Kα radiation and parallel-beam/parallel slit analyzer (PB/PSA) optics. The total number of atoms/Å^2 for each element was determined via an ultra-thin film X-ray fluorescence (XRF) technique elaborated at length by Hamann et al.[22] The composition of each film was calculated by dividing the Fe atoms Å^2 by the sum of the Fe atoms/Å^2 and Se atoms/Å^2.

Cross-sections of select samples were prepared with an FEI Helios NanoLab 600i DualBeam FIB-SEM using standard lift-out procedures. High angle annular dark field (HAADF) images were collected on the multilayer sample on an FEI Titan G2 80-200 scanning transmission electron microscope (STEM) with a Cs probe corrector and ChemiSTEM technology (X-FEG and SuperX EDS with four windowless silicon drift

detectors) operated at 200 kV. HAADF-STEM/EDS on the bilayer sample was collected on probe Cs-corrected Titan3 G2 60–300 microscope with 150% of the default resolution in all directions.[46–48]

9.3. Results and Discussion

Several precursors were prepared which did not target specific phases, but rather were used to investigate the Fe-Se reaction when varying thickness and deposition order. The first set of precursors were bilayer samples containing 1 layer of Fe and Se in order to study how Se deposited on Fe reacts, and how Fe deposited on Se reacts as a function of temperature. Sample B1 (bilayer) contains a layer of Se on Fe on a Si substrate with native SiO_2. Sample B2 contains a layer of Fe on Se, however a monolayer of V was deposited first on the substrate. It was necessary to deposit a metal first, because depositing Se on SiO_2/Si resulted in non-uniform islands of amorphous Se. Precursors containing multilayers of Fe and Se to increase the interface density taking advantage of the ability to obtain more information from x-ray diffraction techniques. Sample M1 (multilayer) was Fe-rich with Fe deposited first onto the substrate. Sample M2 is Se-rich with Fe deposited first onto the substrate. A schematic containing the precursor structures is shown in Figure 9.1

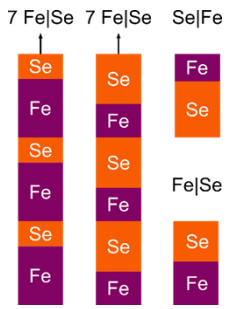

Figure 9.1. Schematic of Fe|Se precursors

A summary of the as-deposited characteristics in both sets of samples can be found in Table 9.1. X-ray fluorescence was used to determine the total number of atoms/ Å^2 of each element in the samples to determine the composition, which is defined as the % Fe. Varying amounts of oxygen were present in the AD samples.

Table 9.1. Total film thickness determined by XRR. Total atoms/Å^2 determined by XRF. Composition determined from total atoms/Å^2. Oxygen counts measured with XRF.

Sample		As-deposited Total film thickness (Å)	Total Fe atoms/Å^2	Total Se atoms/Å^2	As-deposited Composition (% Fe)	As-deposited oxygen counts (kcps)
B1	Bilayer, Fe|Se	312	5.29	4.85	52	0.0032(8)
B2	Bilayer, Se|Fe	336	5.54	11.00	33	0.0020(8)
M1	7 RU Fe|Se	895	40.10	17.60	70	0.0247(8)
M2	7 RU Fe|Se	1085	27.50	41.00	40	0.0025(8)

Grazing incidence X-ray diffraction (GXRD) and reflectivity (XRR) were used to characterize the film structure and determine if samples reacted upon deposition. XRR patterns of as-deposited samples (Figure 9.2a) are complex and difficult to interpret. The experimental patterns are not consistent with what would be expected for the simple bilayer or multilayer structure, which suggests rearrangement has occurred for all samples. An

example of a simulated XRR pattern for sample M1 with 7 RU of Fe|Se is in Figure F.1. The multilayer samples have Bragg reflections which are likely from repeating periods of electron density. For sample M1, these correspond to a d-spacing of 157(3) Å. The number of Kiessig fringes between Bragg reflections alternates between 4 and 5, where the number of Kiessig fringes plus 2 is equal to the number of repeating periods in the sample. Broader underlying Kiessig fringes correspond to a thickness of 64(2) Å, which could correspond to the thickness of an Fe layer. This agrees well given that 7 Fe|Se repeat units were deposited, however given the complexity of the pattern the as-deposited layering scheme is unknown based on these results. Sample M2 does not contain as many Kiessig fringes as M1, suggesting this film has higher sample roughness. Several Bragg reflections can be resolved, which correspond to a d-spacing of 252(4). Kiessig fringes between Bragg reflections cannot be resolved in the as-deposited sample.

GXRD patterns (Figure 9.2b) show that to some extent, all samples began reacting upon deposition. Multilayer samples contain several broad reflections. For the Fe-rich sample (M1), reflections can be indexed to a tetragonal unit cell with a = 3.72(3) and c = 5.70(3) Å, which are labeled with black indices. These parameters are slightly larger than those reported for tetragonal β-FeSe (P4/nmm, a = 3.7720(9) Å and c = 5.5161(5) Å).[8] The Se-rich sample (M2) has reflections which also can be indexed to a tetragonal unit cell with a = 3.77(3) and c = 5.69(3), which are labeled with black indices. Reflections at $2\theta \approx 44.5°$ are consistent with cubic α-Fe ($Im\bar{3}m$, a = 2.8604 – 2.861 Å), which are labeled with blue indices.[9] Bilayer samples contain few weak reflections upon deposition. It is not possible to index patterns with so few reflections, however based on multilayers we can assume that

weak reflections in sample B1 and B2 at 2θ ≈ 44.5° are from α-Fe, at 2θ ≈ 33.6° are the (011) reflection from a tetragonal FeSe unit cell, and in sample B1 the reflection at 2θ ≈ 15.5° is from (001) tetragonal FeSe. The presence of mixed (hkl) reflections indicates that there is no preferred orientation in crystallites upon deposition.

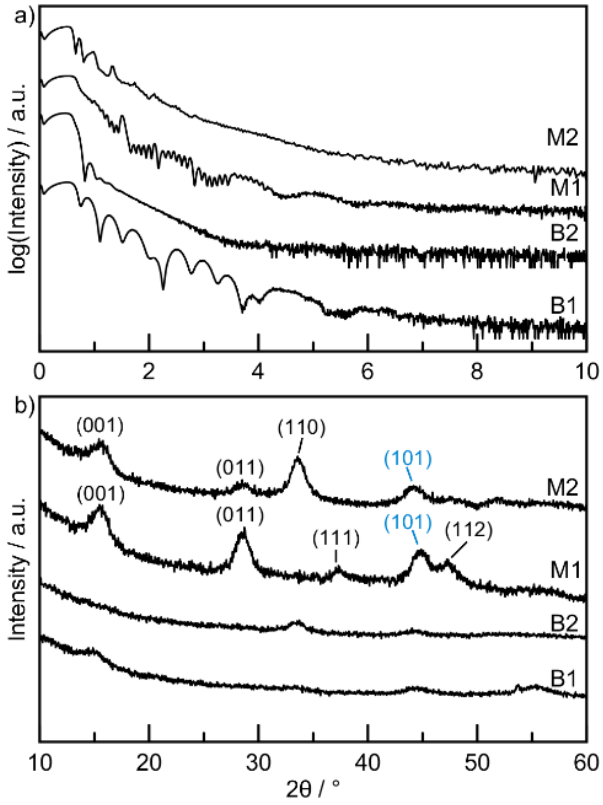

Figure 9.2. a) X-ray reflectivity patterns of as-deposited samples. b) Grazing-incidence XRD patterns of as-deposited samples. Black indices correspond to β-FeSe, blue indices to Fe.

Varying amounts of oxidation and complex XRR patterns lead us to collect HAADF-STEM/EDS of the multilayer Fe-rich sample (M1) which contained the most oxygen. Figure 9.3a shows a HAADF-STEM image of the entire as-deposited M1 sample, which provided several key insights into the precursor structure. First, it is important to note that the first Fe layer deposited does not react with the first Se layer deposited and instead

remains a relatively smooth layer of Fe. Based on GXRD of the Se on Fe sample (B1), it is also possible that a very small interfacial reaction occurred. Next, the second Fe layer is deposited on the first Se layer and reacts to form FeSe + excess Fe. Therefore, depositing A on B is not the same as depositing B on A. The interface between FeSe|excess Fe is relatively smooth, but the surface of the excess Fe is rough due to the formation of Fe domains on FeSe. This pattern is seen throughout the next 4 Fe|Se layers deposited. After the 6th Fe layer, Kirkendall voids are present in the sample where little to no excess Fe from the 7th layer deposited is present. Instead, two FeSe layers are neighboring, with a rough interface in between. EDS data of the entire film was collected (Figure F.1), which revealed that the surface layer on top of the sample contained Fe and O. Given that oxygen was present in the as-deposited XRF in conjunction with the HAADF-STEM/EDS data, we can assume that the excess Fe from the 7th deposited layer diffused to the surface to form Fe-oxide. This suggests that Fe is mobile through the FeSe layers. Given the complexity of the precursor structure and interfaces, it is not surprising that the XRR patterns were far from what was expected. Figure 9.3b shows a higher magnification HAADF-STEM image of the first Fe and FeSe layers. Randomly oriented crystallites of FeSe are present and the smooth Fe|FeSe versus rough Fe|FeSe interface is more obvious. The inset contains a fast Fourier Transform (FFT) of the region marked with a red square and corresponding d-spacings. The d-spacings measured in the FFT are consistent with (00*l*) reflections for a tetragonal unit cell with lattice parameters that agree with GXRD, providing confirmation that FeSe formed upon deposition.

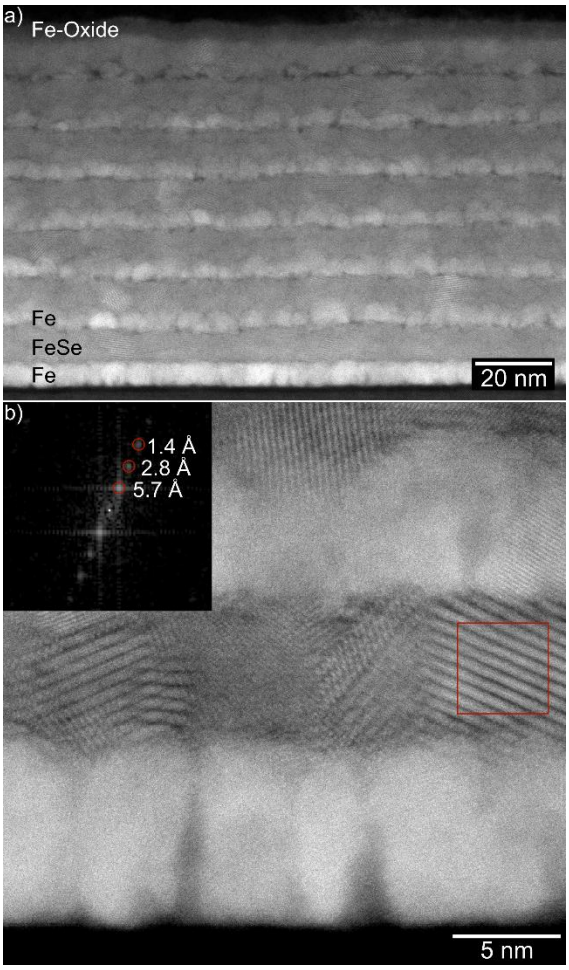

Figure 9.3. HAADF-STEM images of the as-deposited Fe-rich multilayer sample (M1) at a) lower magnification showing the entire film and b) higher magnification showing the first Fe|Se|Fe layers deposited.

To better understand the composition profile through the sample, a combination of XRF and EDS was used. Figure 9.4a contains intensity profiles of each element as a function of distance (including oxygen and the Si substrate) which were extracted from EDS maps (Figure F.2) from the Fe-rich multilayer sample. The film surface is at 0 Å and substrate is at 1000 Å. Alternating layers of Fe and FeSe are clear, where excess Fe layers have Fe maxima aligned with Se minima. Intensity of Fe and O at the film surface and absence of the 7th Fe layer confirm the hypothesis that Fe diffused to the surface and oxidized. An increasing

trend in intensity towards the top of the film is likely the result of a thickness gradient of the cross-section, which is difficult to control. In an attempt to quantify the EDS intensity profiles, we combined XRF and EDS data to obtain a composition in terms of atoms/unit volume as a function of distance in the sample. A plot of Fe and Se atoms/Å^3 versus distance in the sample is shown in Figure 9.4b. First, using the film thickness found from HAADF-STEM, the total number of atoms/Å^2 for each element from XRF measurements were converted to atoms/Å^3. The ratio of the XRF atoms/Å^3 to the average EDS intensities for each element were determined. Each point in the EDS intensity profile was then multiplied by this ratio to convert to units of atoms/Å^3. The dashed line on the composition plot indicates that our compound is has close to a 1:1 ratio of Fe:Se. An Fe-rich phase of FeSe is likely forming based on these results and GXRD data, which could explain why we see a higher Fe composition and slightly larger lattice parameters than known β-FeSe. The quantification of the EDS data across the sample enables the opportunity to model the complex XRR patterns using the atoms per unit volume for each element and distance. Attempts to do so are underway in addition to testing this methodology on ternary systems.

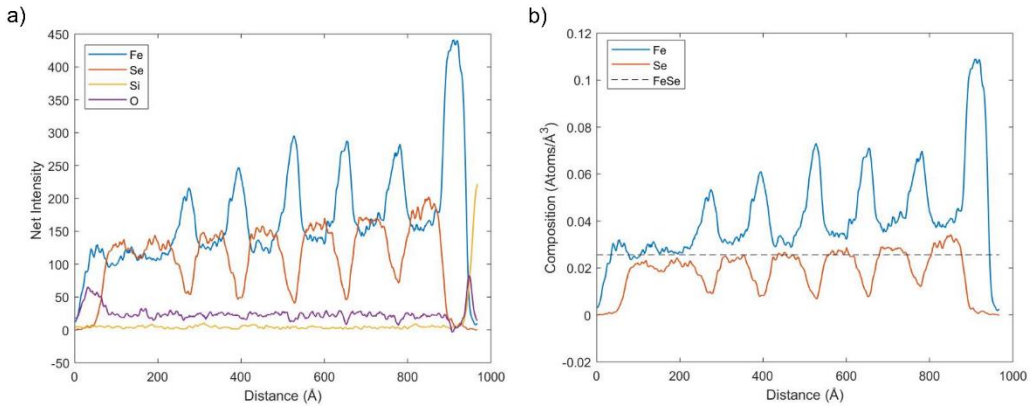

Figure 9.4. a) Distance versus net intensity from a profile extracted from EDS from the as-deposited Fe-rich multilayer sample (M1). On the x-axis, 0 is the surface (top) of the film and 1000 is the substrate (bottom) of the film. b) Distance versus composition for the as-deposited Fe-rich

multilayer sample (M1), where the composition was determined from XRF and EDS intensities. The dashed line represents the literature value for FeSe composition.

HAADF-STEM/EDS was also collected on the binary Se-rich sample (B2) where Fe was deposited on Se due to the lack of information obtained from XRR and GXRD. Figure 9.5a and 9.5b contain HAADF-STEM images of the entire film. The Se layer deposited remained amorphous, and does not form a smooth layer with uniform thickness. This explains the lack of Kiessig fringes in the XRR pattern and variation from what would be expected for a layer of Fe deposited on Se. EDS maps across the film (Figure F.3) show that the brighter layer in the HAADF-STEM image contains Fe and Se. Similar to the multilayer sample, the surface contains Fe and O, indicating that Fe-oxide formed upon deposition. A higher magnification image is shown in Figure 9.5c, where small lattice fringes are visible above the amorphous Se. The spacing of lattice fringes marked with black lines is 2.97 Å, which is close to what would be expected for the (002) reflection in FeSe based on GXRD results (2.85 Å). Given that the sample was only partially crystallized upon deposition and contained substantial amorphous Se, imaging under a high energy electron beam could have altered the same slightly. This could explain the discrepancy in the measured lattice fringe versus what was expected based on GXRD.

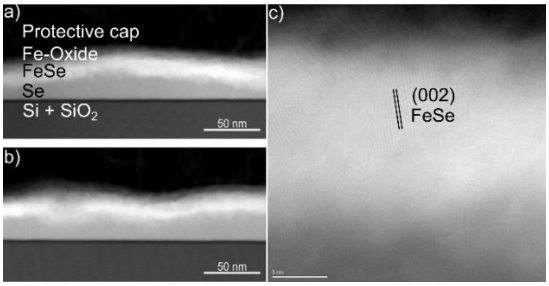

Figure 9.5. HAADF-STEM images of the Se-rich bilayer sample (B2) where Fe was deposited on Se where a) and b) show the entire film at low magnification and c) shows the top region in the sample at higher magnification

Samples were annealed and characterized with XRR, GXRD, and XRF. Figure 9.6 shows a plot of oxygen counts measured by XRF as a function of annealing temperature, which increase with temperature. The increase in oxygen was most substantial for the Fe-rich multilayer sample (M1). Based on HAADF-STEM/EDS results, this is likely due to the ability for excess Fe to diffuse through FeSe layers to the surface. With annealing, excess Fe from regions lower in the sample are likely able to move to the surface to oxidize. In the Se-rich multilayer sample, it is likely that there is little to no excess Fe to oxidize.

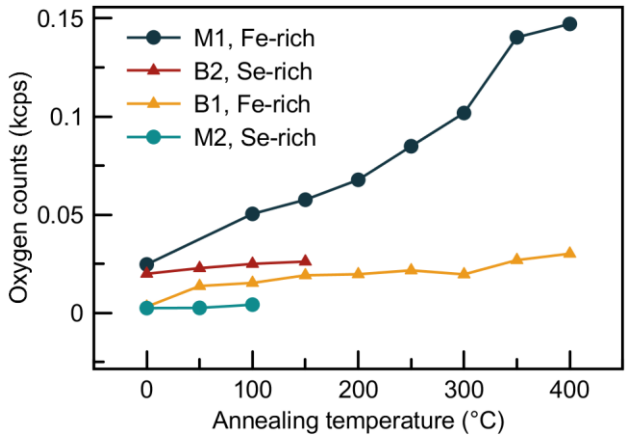

Figure 9.6. Oxygen counts from XRF as a function of annealing temperature

Figure 9.7 shows XRR and GXRD patterns as a function of annealing for the Fe-rich multilayer sample. Bragg reflections in XRR patterns (Figure 9.7a) from layering in the sample remains to 300°C, but is lost at 400°C. This suggests that there is little to no periodic structure left in the sample. Given oxidation in the sample, this could be from excess Fe between FeSe layers diffusing to the surface leaving the sample to be the first Fe layer, rough FeSe, and Fe-oxide. GXRD patterns are consistent with this hypothesis and with XRF data

(Figure 9.7b). Reflections labeled with black indices correspond to a tetragonal unit cell with lattice parameters a = 6.156(3) Å, b = 3.754(7) Å, c = 5.462(7) Å. These are slightly smaller than the lattice parameters in the as-deposited sample. This could be due to Se loss with annealing, where XRF Se atoms/Å^2 as a function of annealing temperature can be found in Figure F.4. A small reflection from Fe is still present at 400°C, which is likely from the first Fe layer deposited. Orange indices are consistent with Fe_3O_4 ($Fd\bar{3}m$, a = 8.34000 Å)[10], which should be expected given the substantial oxidation that occurred in this sample. Unlike thin modulated precursors, this sample does not go through a phase transformation during annealing and remains as β-FeSe, which is the superconducting phase.[7]

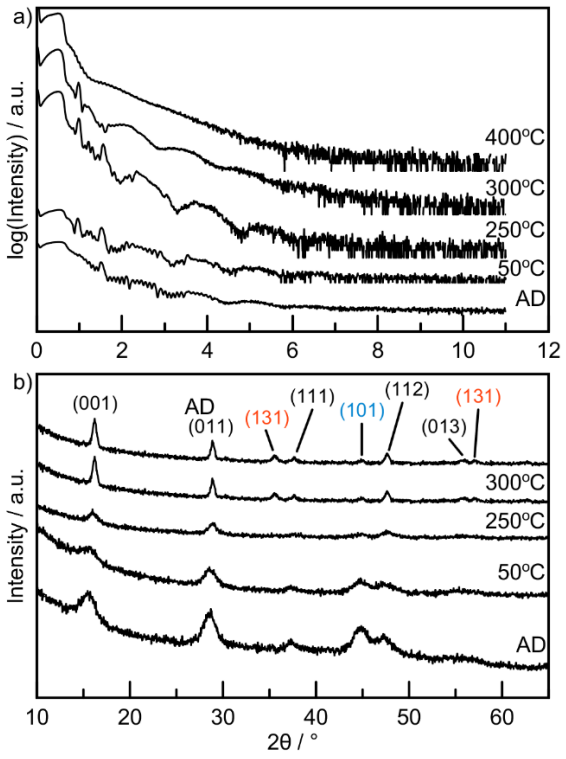

Figure 9.7. a) X-ray reflectivity patterns as a function of annealing temperature for the Fe-rich multilayer sample (M1). b) Grazing-incidence XRD patterns as a function of annealing. Orange indices correspond to Fe_3O_4. Blue indices correspond to Fe. Black indices correspond to β-FeSe.

XRR and GXRD patterns for the Se-rich sample are in Figure 9.8. This sample was only annealed to 100°C, which is the temperature where the as-deposited structure began change significantly. Bragg reflections are still present, similar to what was seen in the Fe-rich multilayer sample at similar temperatures, however the XRR patterns are difficult to interpret due to complexity (Figure 9.8a). Samples will be annealed to select higher temperatures to compare to the Fe-rich multilayer sample. The FeSe phase that formed upon deposition begins to break down at 50°C based on GXRD (Figure 9.8b).

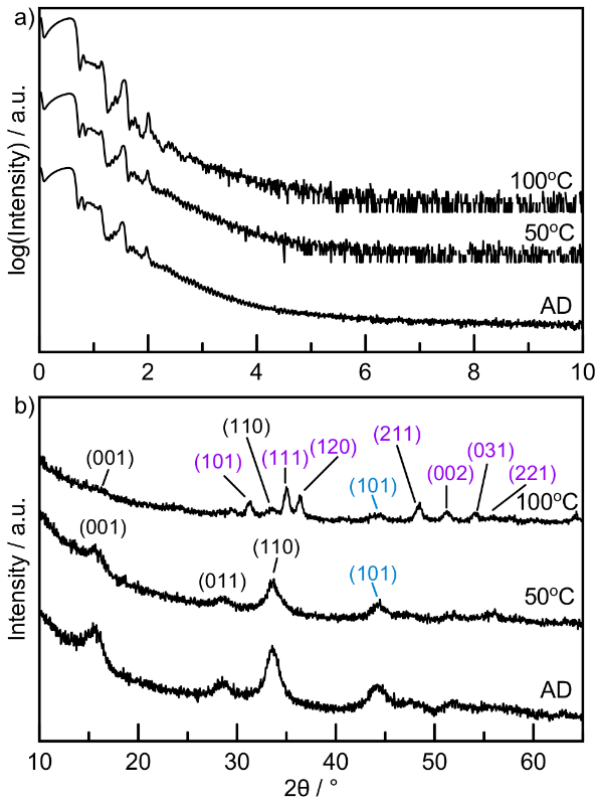

Figure 9.8. a) X-ray reflectivity patterns as a function of annealing temperature for the Se-rich multilayer sample (M2). b) Grazing-incidence XRD patterns as a function of annealing. Blue indices correspond to Fe. Black indices correspond to β-FeSe. Purple indices correspond to $FeSe_2$.

At 50°C, remaining reflections are consistent with the tetragonal unit cell (black indices) and α-Fe (blue). At higher 2θ (50 - 60°) weak reflections that do not correspond to a tetragonal unit cell began to grow in. At 100°C there are weak reflections from the initial FeSe phase (black) and Fe (blue), however reflections which agree with those expected for orthorhombic $FeSe_2$ (Pnnm, a= 4.80020 Å, b= 5.78230 Å, c= 3.58340 Å)[11] dominate the pattern (purple). This indicates that despite excess Se, the tetragonal phase is the first to form from Fe|Se|Fe, but is metastable. With excess Fe, the most Se-rich phase ($FeSe_2$) forms at relatively low temperatures. For thin modulated precursors, $FeSe_2$ formed in samples with similar overall composition at ~ 350°C. Like the Fe-rich sample, the reaction pathway is different in these precursors with thicker Fe and Se layers when compared to those modulated with layer thicknesses less than 10 Å.

XRR and GXRD patterns for the Fe-rich bilayer sample as a function of select annealing temperatures are shown in Figure 9.9. With annealing, XRR patterns become more consistent with what would be expected for a bilayer at 300°C (Figure 9.9a). At 300°C, Kiessig fringes from 2θ ≈ 0 – 2.5° correspond to a thickness of 206(4) Å. Kiessig fringes from 2θ ≈ 2.5 – 5°correspond to a thickness of 173(5) Å. Given what we know about Fe reacting on Se versus Se on Fe, it is likely that the smaller thickness corresponds to the Fe layer, and the larger thickness includes thickness of oxide and potentially a thin interfacial reaction. GXRD (Figure 9.9b) shows that similar to the multilayer Se-rich sample, the initial FeSe phase begins to break down as low as 50°C. While reflections are weak, those at 300°C (green) agree with those reported for thin modulated Fe-Se precursors which were described by a monoclinic unit cell (a = 6.156(3) Å, b = 3.54(1) Å, c = 11.22(1) Å, and β = 91.96(5)°).

This unit cell is similar to Fe_3Se_4 (I2/m, a = 6.17(1) Å, b = 3.54(1) Å, c = 11.1(1) Å, and β = 92.0°).[12] Evaporation of Se at higher temperatures is likely why this sample did not nucleate the most Se-rich phase ($FeSe_2$). Unlike the multilayer sample, Se was at the surface and did not have to diffuse to readily evaporate.

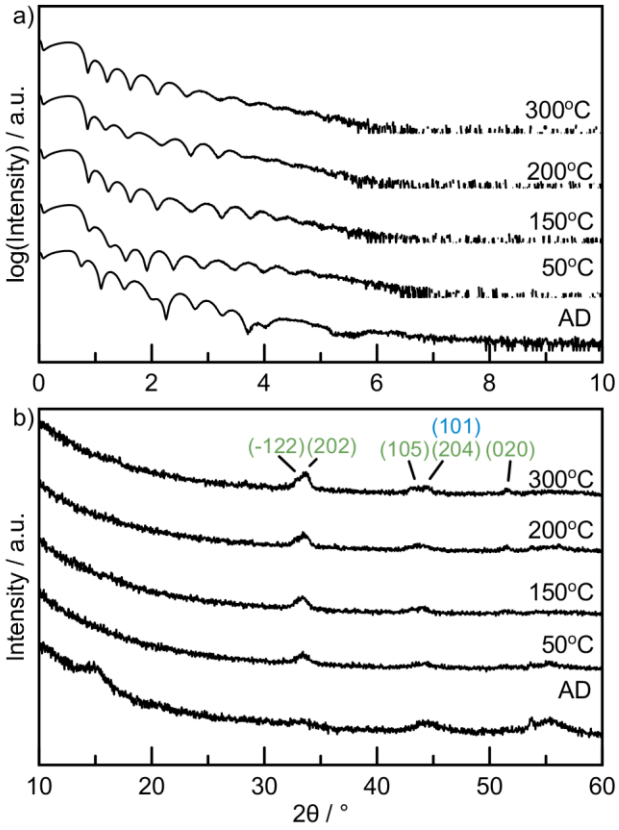

Figure 9.9. a) X-ray reflectivity patterns as a function of annealing temperature for the Fe-rich bilayer sample (B1). b) Grazing-incidence XRD patterns as a function of annealing. Green indices correspond to Fe_3Se_4. Blue indices correspond to Fe.

Lastly, annealed GXRD and XRR of the Se-rich sample (B2, Fe on Se) patterns are in Figure 9.10. Similar to the as-deposited XRR pattern, there is little information in the pattern that can be used to interpret the sample structure. We can assume that since the XRR pattern does not change drastically, the overall sample structure is similar to that seen

in the cross-section of the as-deposited sample from HAADF-STEM/EDS. At 50°C, the initial phase that nucleated is no longer present. Reflections that agree with those seen in the multilayer Se-rich sample grow in with annealing and are consistent with those expected for $FeSe_2$. When Fe is deposited on Se, with sufficient Se in excess, $FeSe_2$ is the second phase to nucleate.

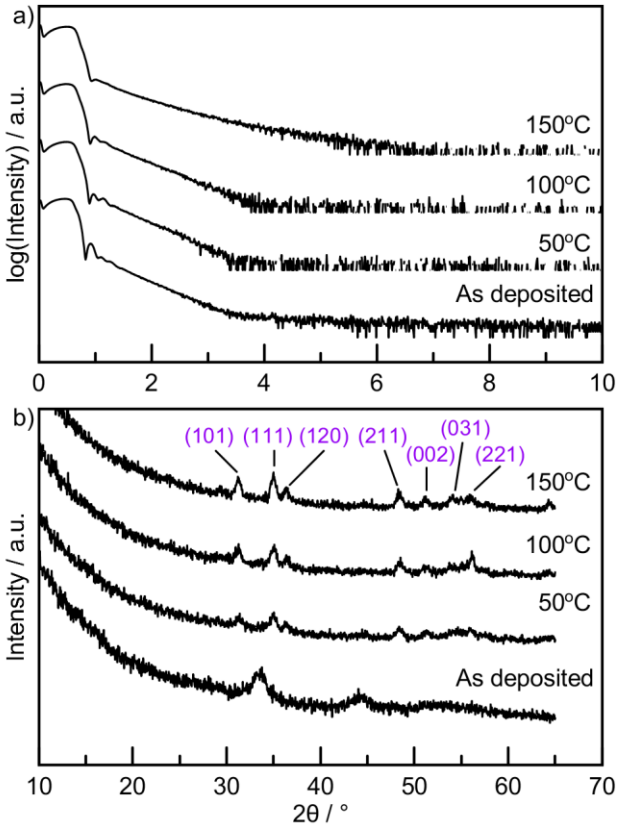

Figure 9.10. a) X-ray reflectivity patterns as a function of annealing temperature for the Se-rich bilayer sample (B2). b) Grazing-incidence XRD patterns as a function of annealing. Purple indices correspond to $FeSe_2$.

9.4. CONCLUSION

The reaction of Fe and Se for bilayer and multilayer binary Fe-Se precursors with larger layer thicknesses is different than that followed for modulated precursors with

thicknesses less than 10 Å. In all precursors, Fe and Se reacted to some extent prior to annealing. A unit cell consistent with β-FeSe was the first phase to nucleate, where lattice parameters varied slightly from those expected depending on the Fe:Se ratio. This was also seen for thin modulated precursors[7], suggesting that it is not possible to avoid reaction upon deposition. Unexpectedly, we concluded that small interfacial reaction occurs for when Se is deposited on Fe, but when Fe is deposited on Se – both layers mix completely and react upon deposition. For the case of multilayers, this results in an asymmetry of interfaces where the surface of unreacted Fe is rough, but FeSe is relatively smooth.

Ultimately, the reaction pathway in this system is more complex than the simplistic Cu_3Au rule and depends on several major factors. First, the reaction of A on B and B on A are not the same. Fe is mobile through reacted Fe-Se phases, but not through Se. Composition did not dictate the first phase that formed but did dictate the second phase to nucleate. For layer thicknesses >> 10Å, the same first phase nucleated, but for layer thicknesses < 10 Å,[7] the first phase to nucleate varied depending on overall composition. For both cases, the second phase to nucleate was $FeSe_2$ when the sample contained sufficient Se. For Se deposited on Fe, the second phase to nucleate was Fe_3Se_4, likely due to insufficient in the precursor and Se loss with annealing. Higher annealing temperatures were studied for the layers < 10 Å, where samples that nucleated $FeSe_2$ as the second phase rearranged to Fe_3Se_4 and δ-FeSe.

9.5. BRIDGE

Fe and Se with relatively larger layer thicknesses in bilayer and multilayers were explored as a function of composition, precursor structure. All samples nucleated a

tetragonal unit cell consistent with β-FeSe, with lattice parameters that varied dependent on composition. In the previous chapters, not all precursors nucleated the same phase first, but they did all react upon deposition. These results suggest that using these methods, it's not possible to avoid the reaction of Fe and Se during deposition. Surprisingly, asymmetric interfaces were revealed in asymmetric interfaces in Fe-Se were observed with electron microscopy. Additionally, we found that for samples in this chapter, Fe on Se reacts very little (a small interfacial reaction occurs) but Se on Fe mixes and reacts completely during deposition. A method to quantify EDS data in terms of atoms per unit volume as a function of distance by utilizing XRF data was proposed, which could be powerful in understanding samples with complex reaction pathways and their structures such as this one. The next chapter discusses the reaction of binary Pb and Se with varying layer thicknesses, precursor structures, and substrates.

CHAPTER X

GROWTH OF CRYSTALLOGRAPHICALLY ALIGNED PBSE OF CONTROLLED THICKNESS ON AN AMORPHOUS SUBSTRATE

10.0. AUTHORSHIP STATEMENT

Chapter X is under preparation for submission to *ACS Applied Electronic Materials*. Co-author Marisa Choffel prepared precursors containing PbSe and $MoSe_2$. Marisa Choffel and Hannah Hamovitz collected XRD, XRR, and XRF as a function of annealing for PbSe and $MoSe_2$ precursors. David Johnson is my advisor. Niklas Wolff and Andriy Lotnyk collected and assisted with analysis of HAADF-STEM/EDS data. I am the primary author of this manuscript and prepared thick PbSe and thin modulated PbSe and PbSe-VSe_2 precursors, TEM specimen, and collected XRD, XRR, and XRF data.

10.1. INTRODUCTION

Lead selenide (PbSe), a direct-bandgap semiconducting material with a cubic rock salt structure, is of interest to many due to its thermoelectric and photoconductive properties.[1–8] The high thermoelectric performance of doped PbSe films has led to exploring its potential use in efficient conversion of industrial waste heat into storable electrical energy.[9–11] PbSe has been investigated for photodetection applications because it absorbs a broad and uniform section of the electromagnetic spectrum.[6,12,13] Researchers have explored the changes in these properties as a function of changes in impurities, alloying extent, strain, and surface treatments trying to optimize performance.[9,14–22] Several investigations have reported that these properties depend on the thickness of PbSe.[8,20,23,24] Theoretical

investigations have also predicted that a monolayer of PbSe would be a two-dimensional topological insulator.[25]

Researchers have attempted to prepare monolayers of PbSe and smooth films of PbSe of controlled thickness using a variety of different synthetic approaches. Molecular beam epitaxy (MBE) has resulted in on a variety of different substrates has resulted in island growth of PbSe, leading to rough films.[26–28] A variety of single crystal substrates that are close to lattice matching PbSe have been tried, but island formation rather than smooth films were obtained. The substrates were heated to different temperatures to vary the mobility of the atoms deposited, but growth preferentially occurs on the first PbSe that forms rather than the substrate at all of the temperatures investigated. Another challenge that has impacted growth using MBE or ALD is the large difference in the thermal expansion coefficients of PbSe and most substrates that have been used, which results in the generation of dislocations upon cooling due to large mechanical strains.[18,29–31] The density of dislocations can be reduced by annealing after deposition or by using a patterned (111)-oriented silicon substrate, but the density remains too high for most applications.[28] Chemical bath deposition and solution based epitaxial methods, which also enable the mobile Pb and Se ions to explore multiple growth sites, experience similar problems despite reduced temperatures.[8,23,24,32] This has led researchers to explore to the use of buffer layers between substrate and PbSe.[18,33–35] For example, BaF_2/CaF_2 was used as a buffer layer to grow epitaxial PbSe layers with MBE on Si, but the resulting films cracked which is not suitable for device applications.[27] To obtain high quality crack-free PbSe on BaF_2/CaF_2, the buffer layers had to be grown with MBE and the PbSe with LPE in order to overcome mismatch

of thermal expansion coefficients.[27] The growth of single crystal of PbSe was accomplished using chemical solution deposition onto a buffer layer of PbS atop a GaAs substrate, however the quality of the films produced by this method had a dependence on the thickness.[32] An interesting recent reference reported the growth of nanoplatlets of PbSe on $MoSe_2$ monolayers, a non-lattice matched substrate.[36] Layers of PbSe a single bilayer thick were also reported in a number of different misfit layer compounds, $(PbSe)_1(TSe2)_n$, where T = Ti, V, Nb, Mo and W.[37–42] These compounds are called misfit layer compounds as there is not an epitaxial relationship between the two constituents.

The growth of PbSe via a Volmer-Weber mode where islands rather than smooth films form, indicates that the interaction between PbSe and the islands is stronger than the interaction between PbSe and the substrate. The ability to synthesize misfit layer compounds with PbSe that are thermodynamically stable and on MoS_2 suggests that the interaction between the PbSe layer and the dichalcogenide is stronger than the interaction of PbSe with itself. This led us to explore the growth of PbSe on amorphous V-Se and Mo-Se coated silicon (with native oxide) substrates. We deposited these layers on substrates that were nominally at room temperature. We found that PbSe formed during the deposition regardless of substrate or thickness. Samples deposited on Si with native SiO_2 formed rough films with no crystallographic alignment to the substrate. Samples deposited on the amorphous V-Se and Mo-Se coated substrates formed crystallographically aligned and atomically smooth PbSe. If the amount of PbSe deposited was close to an integral number of PbSe bilayers, Laue oscillations were clearly visible on the 002 reflection of PbSe. These

results suggest that a precise number of smooth and crystallographically aligned PbSe layers can be grown without epitaxy on amorphous substrates using physical vapor deposition.

10.2. MATERIALS AND METHODS

Precursors were deposited on rotating (111) Si substrates nominally at room temperature in a custom high vacuum ($<10^{-6}$ torr) physical vapor deposition chamber from elemental sources (Pb, Mo, V, Se). Electron beam guns were used to deposit Pb, Mo, and V. Knudson effusion cell was used to deposit Se. Shutters which were programmed to open and close based on the desired input thickness were used to control the amount of each element deposited. Quartz crystal microbalances were used to monitor the deposition rate and determine the amount of time shutters were open. Samples were transferred to stored and annealed on a hot plate in a nitrogen glove box (>0.2 ppm oxygen). Samples are exposed to air for transfer from the deposition system and characterization.

Specular X-ray diffraction and X-ray reflectivity (XRR) patterns were collected on a Bruker D8 diffractometer with Cu Kα radiation in θ-2θ locked-coupled scan mode. In-plane and Grazing incidence XRD (GXRD) patterns were collected on a Rigaku Smartlab diffractometer with Cu Kα radiation and parallel beam (PB) and parallel-beam/parallel slit analyzer (PB/PSA) optics, respectively. A method for determining the total number of atoms/Å^2 from X-ray fluorescence (XRF) was used which is described in detail by Hamann et al.[43]

Cross-sections of select samples were prepared with an FEI Helios NanoLab 600i DualBeam FIB-SEM using standard lift-out procedures. High angle annular dark field

(HAADF) images were collected on a probe Cs-corrected Titan^3 G2 60–300 microscope operating at an accelerating voltage of 300 kV.

10.3. RESULTS AND DISCUSSION

Bulk and modulated precursors were prepared to explore the growth of PbSe at low temperatures on a variety of substrates with a goal of preparing smooth ultrathin films with a precise number of unit cells. Bulk samples were deposited at nominally room temperature onto Si with native SiO_2 with Pb|Se and Pb|Se|Pb layering schemes where Pb was deposited first. Elementally modulated precursors with 8 and 16 repeating Pb|Se layers were deposited on Si with native SiO_2 where the amount of each element deposited in each Pb|Se layer sequence targeted a single bilayer of crystalline PbSe. To probe the impact of surface structure, elementally modulated precursors of Pb|Se were prepared on top of Mo|Se or V|Se layers, which were deposited on Si substrates with native SiO_2. The amount of Mo or V and Se deposited targeted per M|Se layer equaled that required for single $MoSe_2$ or VSe_2 trilayers, respectively. The number of Pb|Se layers in the precursor structure was varied to determine the effect of total thickness on the roughness of the PbSe that formed. The X-ray reflectivity patterns of all of these samples did not contain Bragg maxima, indicating that the Pb|Se layers intermixed completely during the deposition. The amount of material (atoms/Å^2) of each element was determined through XRF. For bulk samples, the overall sample composition was calculated, where the Pb|Se precursor was found to have an excess of Se and the Pb|Se|Pb precursor was found to have an excess of Pb relative to stoichiometric PbSe. For modulated precursors, the total experimental atoms/ Å^2 in the as-deposited precursor is reported in Table 10.1, where M is V or Mo. We also have calculated

the number of possible PbSe bilayers based on the amount of Pb in the precursors. This assumes that 0.1065 atoms/Å^2 of Pb and Se are needed to form one bilayer of PbSe.

Table 10.1. Total experimental atoms/Å^2 were determined via X-ray fluorescence, where Se also includes the amount used in M(Mo,V)|Se layers. The number of PbSe layers was calculated using the total Pb atoms/Å^2, where 0.1065 atoms/Å^2 are needed to form one bilayer of PbSe.

	Substrate	Precursor structure	Total Experimental Atoms/Å^2			# PbSe layers possible**	AD composition (% Pb)
			Pb	Se*	M		
Bulk	Native SiO_2 on Si	Pb|Se	1.570	4.666	-	-	25
		Pb|Se|Pb	3.585	2.176	-	-	62
Modulated precursors	Native SiO_2 on Si	8 Pb|Se	0.881	1.129	-	8	n/a
	4 repeating units V|Se	16 Pb|Se	1.671	2.843	0.415	15	
	8 repeating units Mo|Se	128 Pb|Se	12.573	14.598	0.823	117	
		64 Pb|Se	6.439	9.049	0.829	60	
		32 Pb|Se	3.191	5.690	0.827	29	
		16 Pb|Se	1.888	3.358	0.828	17	
		8 Pb|Se	0.823	2.476	0.821	7	

As a baseline to understand the reaction of Pb and Se, thick layers of each element were deposited and examined with a variety of techniques. X-ray reflectivity patterns of both samples (Figure 10.1a) contained only the first few Kiessig fringes, suggesting the samples are rough. Roughness was calculated from the XRR patterns using the formula derived by Parratt.[44] The Pb|Se|Pb sample has a higher root mean square roughness ($R_q \approx$ 33 Å) than that calculated for the Pb|Se sample ($R_q \approx$ 19 Å). Specular XRD of the as-deposited samples indicated that PbSe formed during deposition with no preferred alignment to the Si substrate (Figure G.1). All reflections in the grazing incidence X-ray diffraction (GXRD) patterns are consistent with the known rock-salt PbSe structure (Figure

10.1b). The resulting *a*- axis lattice parameter of 6.11(1) Å for the Pb|Se and Pb|Se|Pb samples agrees with that reported previously for PbSe (a = 6.117 Å).[45]

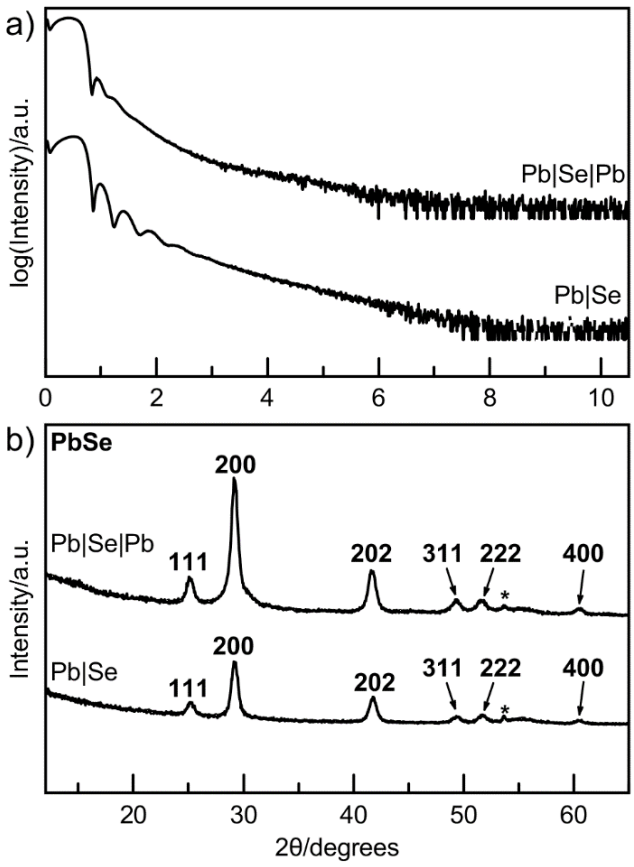

Figure 10.1. a) X-ray reflectivity patterns of as-deposited Pb|Se and Pb|Se|Pb precursors. b) Grazing incidence X-ray diffraction where labeled indices apply to as-deposited Pb|Se and Pb|Se|Pb precursors and are consistent with PbSe ($Fm\bar{3}m$). Asterisks belong to substrate peaks or are an artifact of the diffractometer.

A cross-section of the sample with the Pb|Se|Pb layering sequence was prepared and HAADF-STEM was used to investigate the sample to investigate the morphology of the sample roughness. The HAADF-STEM/EDS revealed the formation of PbSe islands coated with Pb(Se) oxides, presumably due to the exposure of the sample to air when transferring it to the instrument (Figure 10.2a). The images of the EDS maps (Figure G.2)

of the entire film revealed the presence of a thick surface oxide layer that contains mostly Pb and O, which is consistent with the difference in STEM intensities. The size of the PbSe islands and the resulting surface topology is consistent with the surface roughness calculated from the XRR data. A higher magnification HAADF-STEM image contains rectangular regions with lattice fringes (Figure 10.2b) that are consistent with PbSe or Pb(Se) oxides.

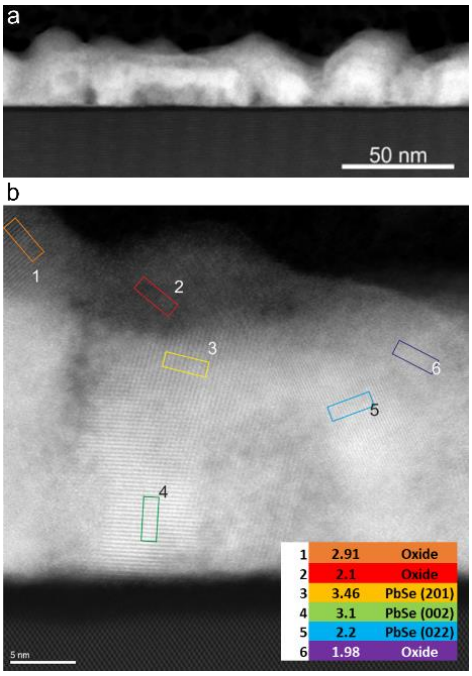

Figure 10.2. a) HAADF-STEM image of a cross section of the as-deposited Pb|Se|Pb (62% Pb) sample which shows PbSe islands. b) higher magnification HAADF-STEM image with regions that have lattice fringes consistent with Pb oxides or rock-salt PbSe.

The XRD and STEM data both show that PbSe forms during the deposition. After the first Pb layer is deposited, Se must reacts during deposition with the Pb layer and significant diffusion must occur during deposition, despite the fact that the substrate is not heated. As Se continues to be deposited, islands of PbSe form as Pb diffuses to the islands and away from the substrate. This island growth suggests that the interaction of the forming PbSe with the substrate must be weaker than bonding with the PbSe that has already

formed. When all of the first deposited Pb layer has reacted to form PbSe, the rest of the Se deposited forms an elemental layer which reacts as the 2nd layer of Pb is deposited. The excess Pb in the sample forms oxides from exposure to atmosphere as the sample is transferred to a dry box for storage, or as the sample is characterized using XRR and XRD. This data is consistent with prior reports of island growth of PbSe during MBE or during ALD growth on a variety of substrates, including SiO_2.[2,46]

Preparing elemental modulated precursors with thinner Pb|Se layers changes the diffusion lengths required to react Pb and Se during deposition. A sample with 8 bilayers of PbSe deposited on Si with native SiO_2 was prepared to investigate PbSe growth in a few-layer thick modulated precursor. The precursor was annealed to 300°C for 30 minutes, which were the annealing conditions used in the previous work with thicker PbSe layers.[41] After annealing, the sample contained 0.875 Pb atoms/Å^2 and 0.839 Se atoms/Å^2, which suggests that 8 bilayers of PbSe could form. Similar to the bulk PbSe samples, the XRR pattern of this sample (Figure 10.3a) indicates that the PbSe layer is rough ($R_q \approx 13$ Å), which suggests that island growth likely occurs during the deposition of the film. Specular XRD patterns of the as-deposited sample and after annealing to 300°C both contain reflections that can all be indexed as *hkl* reflections of PbSe, indicating that randomly oriented PbSe forms during deposition (Figure G.3). The reflections in the in-plane XRD pattern can also be indexed as *hkl* reflections of PbSe (Figure 10.3b). The systematic absences are consistent with the $Fm\bar{3}m$ space group, and the calculated *a*-lattice parameter of 6.11(1) Å agrees with that reported previously for PbSe (6.117 Å).[45] These results agree with

prior work where 16, 32, and 82 RUs of PbSe were deposited on Si with native SiO_2 yielding rough PbSe films where the grains are randomly oriented.[41]

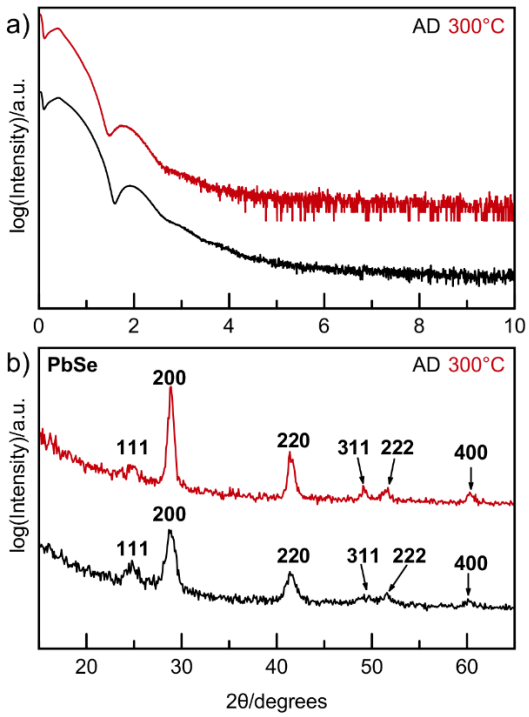

Figure 10.3. a) X-ray reflectivity pattern of the 8 Pb|Se precursor on Si with native SiO_2 as-deposited (AD) and annealed to 300°C. b) In-plane diffraction where labeled indices correspond to PbSe ($Fm\underline{3}m$).

To form atomically smooth layers, we speculated that we needed to switch the substrate to one with a stronger interaction with PbSe. $(PbSe)_1(VSe_2)_1$ is a known, thermodynamically stable compound and a recent investigation showed that Pb|Se layers deposited on VSe_2 form atomically smooth layers of PbSe. To expand this previous study, we prepared a modulated precursor containing 16 repeating layers of Pb|Se deposited on 4 RU of V|Se, which were deposited onto Si with native SiO_2. This precursor was annealed under the same conditions as the 8 Pb|Se precursor (300°C, 30 minutes). After annealing, the sample contained 1.655 Pb atoms/$Å^2$, 0.418 V atoms/$Å^2$, and 2.559 Se atoms/$Å^2$

measured by XRF. This is enough material to form 15 bilayers of PbSe and 4 trilayers of VSe_2, assuming 0.1026 V atoms/Å^2 and 0.2051 atoms/Å^2 are needed to make one trilayer of VSe_2. X-ray reflectivity patterns (Figure 10.4a) contains Kiessig fringes out to 5° 2θ, indicating that the as deposited sample is significantly smoother than those deposited onto native SiO_2 on Si. The XRR pattern after annealing is more complex as the VSe_2 crystallizes, leading to an interference pattern from the VSe_2 and PbSe layers. The as-deposited specular XRD (Figure 10.4b) pattern contains only 00*l* reflections from PbSe, indicating that the PbSe is crystallographically aligned and that the V|Se layers are amorphous. Laue oscillations are present on the 002 PbSe reflection of the as-deposited sample, which indicates that the majority of the film is an integral number of unit cells thick. The number of unit cells determines the spacing of the Laue oscillations, enabling us to calculate that 16 unit cells are present in both the as-deposited and annealed sample. This agrees with the number of PbSe layers possible calculated from the XRF data in Table 10.1. In-plane XRD (Figure G.4) contains only hk0 reflections from PbSe in the as-deposited sample, which confirms that PbSe formed crystallographically aligned on amorphous V|Se upon depostion. After annealing the sample at 300°Ç, the specular and in plane diffraction patterns indicate that VSe_2 crystallized. The VSe_2 is crystallographically aligned to the Si/SiO_2, as only 00l reflections are observed in the specular diffraction pattern and only hk0 reflections are present in the in plane diffraction pattern. The PbSe remaines crystallograpnically aligned, but the line widths decrease indicating that Ostwald riping occurs during the anneal. The spacing of the Laue oscillations remains the same as in the as deposited sample, indicating that 15 PbSe bilayers are still present after annealing.

The formation of crystallographically aligned films of constant thickness on an amorphous substrate during deposition surprised us. To confirm this result, we decided to investigate the formation of PbSe from Pb|Se layers deposited on Mo|Se layers. $(PbSe)_m(MoSe2)_n$ heterostructures are metastable, but form from precursors containing repeating sequences of m Pb|Se and n Mo|Se layers containing the number of atoms of Pb and Se in each Pb|Se layer required to form a bilayer of PbSe and the number of atoms of Mo and Se in each Mo|Se layer required to form a trilayer of $MoSe_2$. Binary $MoSe_2$ from modulated precursors does not begin to crystallize until temperatures are above 300°C, and annealing above 500°C in a Se atmosphere is required to form completely crystalized $MoSe_2$ layers.[47] The samples we prepared contain the same number of Mo|Se layers and between 8 and 128 Pb|Se bilayers.

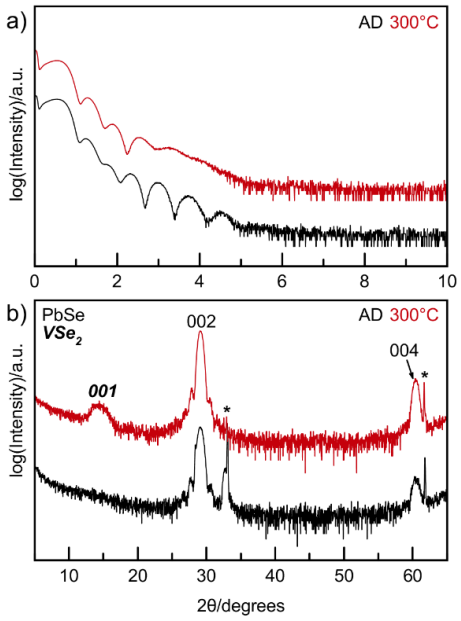

Figure 10.4. a) X-ray reflectivity pattern of the 16 RU Pb|Se precursor as-deposited (AD) and annealed on 4 RU V|Se. b) Specular X-ray diffraction pattern where labeled indices are consistent with only *00l* reflections from a PbSe ($Fm\bar{3}m$) unit cell or a hexagonal VSe_2 ($P\bar{3}m1$). Asterisks belong to substrate peaks or are an artifact of the diffractometer.

The specular XRD patterns for all of the as-deposited $(Mo|Se)_8(Pb|Se)_n$ samples are shown in Figure 10.5. The broad reflections at $2\theta \approx 13°$ are a result of the repeating Mo|Se layers in the precursor, which indicates that these layers are ~ 6.8 Å thick in each of the samples. The linewidth of this reflection is consistent in each of the samples due to the identical number of Mo|Se bilayers deposited. The intensity decreases as the number of Pb|Se bilayers deposited increases because of the reduced x-ray intensity that makes it through the Pb-Se layer. Observing the elemental modulation due to the repeated deposition of Mo and Se layers was observed previously.[47] Precursors with 8, 16, and 32 Pb|Se layers also contain only 00*l* reflections of PbSe, which indicates that crystallographically aligned PbSe forms during deposition on the amorphous Mo|Se substrate.

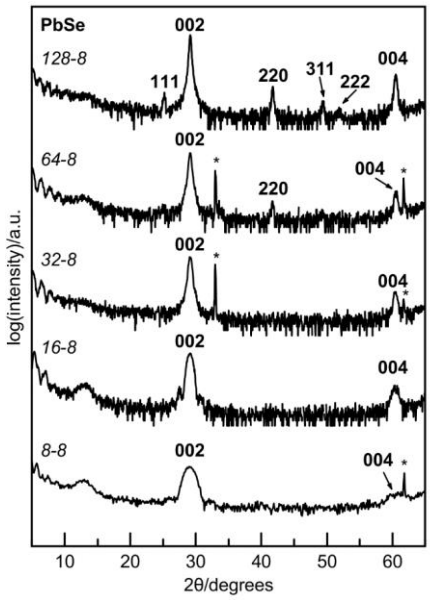

Figure 10.5. Specular X-ray Diffraction patterns for Pb|Se on Mo|Se precursors after deposition. Numbers in italics indicate the number of Pb|Se – Mo|Se layers deposited. All indexed reflections are consistent with a rocksalt PbSe unit cell. Reflections $2\theta \approx 13°$ is from artificial layering of Mo|Se layers.

Laue oscillations are present in the samples with 8 and 16 Pb|Se layers, indicating that the PbSe layers are smooth with a consistent, finite number of unit cells present across the majority of the film. Based on Laue oscillations, 7 and 15 PbSe unit cells (c = 6.13(5) Å) are present in the 8 Pb|Se and 16 Pb|Se precursors, respectively, which agrees with the amount of Pb deposited determined via XRF. Precursors with 64 and 128 Pb|Se layers contain non-00*l* reflections, indicating that randomly oriented PbSe crystallites form during the deposition, similar to what was seen in bulk samples deposited on the native SiO_2 layer on Si wafers. This suggests that the interaction with the substrate is important to prevent nucleation of grains that are not crystallographically aligned.

The 32 Pb|Se precursor is the thickest precursor that remained crystallographically aligned to the substrate, therefore we examined this precursor as a function of annealing temperature with specular XRR and XRD. The XRR and XRD patterns are shown in Figure 10.6. The as-deposited XRR pattern is complex for this sample, containing information on both the thickness of the Mo-Se layer and the Pb-Se layer. The broader Kiessig fringes at higher angle yield a thickness of ~55 Å, which is consistent with the expected thickness of the 8 Mo|Se bilayers deposited. The smaller period Kiessig fringes at lower angles yield a thickness of ~192 Å, which is consistent with the 32 Pb|Se bilayers deposited. The pattern evolves considerably as the sample is annealed at higher temperatures. The regularity and intensity of the smaller period Kiessig fringes increases while the intensity of the broader Kiessig fringes decrease as annealing temperature increases. The as deposited specular XRD contains only the 002 and 004 reflections from PbSe, which indicates that the PbSe

crystallized during the deposition, indicating that the PbSe is aligned to the Mo-Se layer before $MoSe_2$ has crystallized. Laue oscillations appear on the 002 reflection after annealing at 300° C and remain until annealing above 500°C. Analysis of Laue oscillations indicate that 29 PbSe unit cells formed after annealing, which agrees with the number of PbSe layers expected to form based on measurements of the amount of Pb present in the film from XRF data (S5). At 300°C, 001 and 003 reflections consistent with $MoSe_2$ begin to grow in, and their intensities increase with further annealing. The c-axis lattice parameter determined from these reflections, c = 6.52(4) Å, is slightly large than that reported for bulk $MoSe_2$ (6.46 Å).[48]

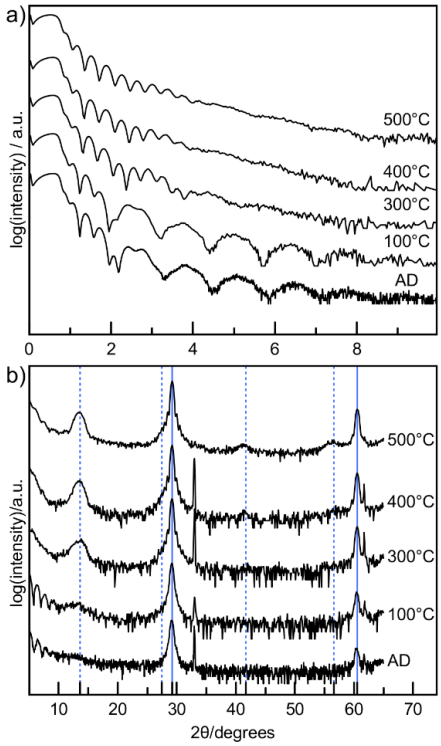

Figure 10.6. a) X-ray reflectivity patterns and b) specular X-ray diffraction as a function of annealing for the 32 Pb|Se – 8 Mo|Se precursor. Solid vertical blue lines represent the expected *00l* peak positions for a PbSe unit cell, and dashed vertical blue lines represent expected *00l* peak positions for $MoSe_2$.

All of the remaining samples were annealed at 400°C to explore the impact of annealing on the morphology of the films and the PbSe that formed on annealing. The number of layers expected to form after annealing were determined from measurements of the amount of Mo, Pb and Se present in the film from XRF for all samples, which can be found in the table in the supporting information (Table G.1). The number of $MoSe_2$ layers was determined by assuming Se was used to form the number of PbSe layers possible, and that 0.2135 Se atoms/Å^2 are needed to form one trilayer of $MoSe_2$. With Se loss after annealing, some excess elemental Mo may be present in precursors. Figure 10.7 contains XRR and XRD data from the 64 and 128 Pb|Se bilayer samples. Upon deposition, broader Kiessig fringes from the Mo|Se layers and smaller Kiessig fringes from PbSe in the precursor are present, as seen in previous samples.

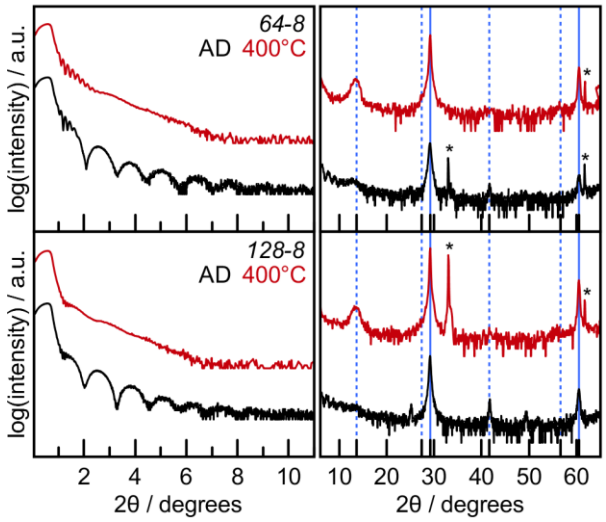

Figure 10.7. X-ray reflectivity patterns (left) and specular X-ray diffraction patterns (right) as a function of annealing for the 64 Pb|Se – 8 Mo|Se precursor (top) and 128 Pb|Se – 8 Mo|Se precursor (bottom). Solid vertical blue lines represent the expected *00l* peak positions for a PbSe unit cell, and dashed vertical blue lines represent expected *00l* peak positions for $MoSe_2$.

After annealing, both samples become smoother and the non-00l reflections are no longer present in the specular XRD pattern. This indicates that the PbSe layer are mostly crystallographically aligned to the partially crystalline $MoSe_2$ layers. Laue oscillations are not observed, indicating that the films are not consistently the same thickness across the area probed by the x-ray beam.

The diffraction scans collected on the samples with 8 and 16 Pb|Se layers after annealing at 400°C are shown in Figure 10.8. The XRR patterns remain complex after annealing, containing interference from both the PbSe and Mo|Se layers. The Kiessig fringes from the interference with the layers persists to higher angles after annealing, indicating that the samples become smoother. The high angle specular diffraction scans indicate that the PbSe layers remain crystallographically aligned after annealing.

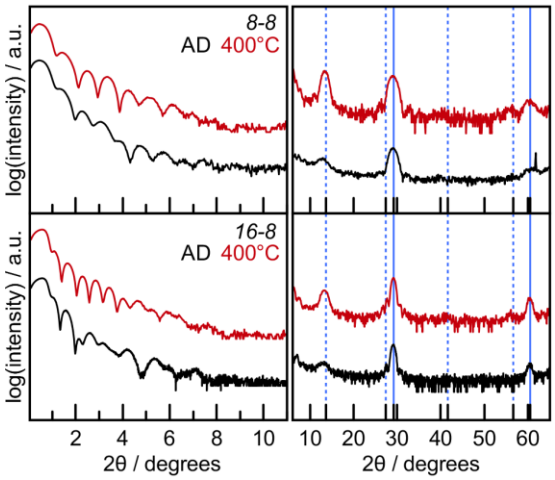

Figure 10.8. X-ray reflectivity patterns (left) and specular X-ray diffraction patterns (right) as a function of annealing for the 8 Pb|Se – 8 Mo|Se precursor (top) and 16 Pb|Se – 8 Mo|Se precursor (bottom). Solid vertical blue lines represent the expected *00l* peak positions for a PbSe unit cell, and dashed vertical blue lines represent expected *00l* peak positions for $MoSe_2$.

Laue oscillations are present in both samples after annealing. The number of unit cells calculated from the Laue oscillations was determined to be 7 and 15 unit cells in both the as-deposited and annealed samples corresponding to the 8 and 16 Pb|Se repeating bilayer thick precursors that were deposited, respectively. The difference between the number of unit cells formed and the number of Pb|Se layers deposited results from a shortage of Pb in the deposited bilayers. This data suggests that the morphology and structure of the PbSe layer does not change as the underlying $MoSe_2$ layer crystallizes.

10.4. CONCLUSIONS

This paper shows that suggest that strong interactions between substrate and growing film are necessary to form smooth, crystallographically aligned layers. The substrate does not need to be crystalline, as crystallographically aligned PbSe forms on amorphous Mo|Se and V|Se during deposition on substrates nominally at room temperature. The thicker PbSe bilayers can be annealed at low temperatures to increase the amount of crystallographic alignment. The number of PbSe bilayers formed depends on the amount of Pb (or Se) deposited. If the amount of Pb deposited is close to that required for an integral number of unit cells and there is an excess of Se, Laue oscillations are present in the as-deposited samples and they remain present after annealing. While prior studies typically explored epitaxial substrates, this study suggests that the substrate does not need to be crystalline to form smooth PbSe with crystallographic alignment. The crystallographic alignment and atomically smooth thicknesses of the PbSe formed contrasts with several prior results, where island growth occurred on substrates with near epitaxial relationships

with PbSe. We recognize that the drawback of using an amorphous substrate is that the orientation of different regions of the film can't be controlled.

10.5 BRIDGE

This chapter revealed several important considerations for PbSe growth. For relatively thick PbSe layers, it was found that PbSe follows island formation growth upon deposition, similar to that seen using other growth methods. Samples on Si with native SiO_2 did not form crystallographically aligned to the substrate, however samples on amorphous V|Se and Mo|Se layers did. This provides an avenue to form smooth, aligned PbSe layers at low temperatures at an integral number of unit cells thick. Unlike what was seen for Fe on Se vs. Se on Fe in the last chapter, Pb on Se and Se on Pb mix and react completely during deposition to form PbSe, which was confirmed with HAADF-STEM/EDS. The next chapter takes considerations from previous chapters into account in attempting to synthesize ternary Pb-Fe-Se compounds predicted to be theoretically stable. A layering scheme of Fe|Pb|Fe|Se was used to try and avoid the reaction of PbSe during deposition.

CHAPTER XI

REACTIONS IN TERNARY PB-FE-SE COMPOUNDS

11.0. AUTHORSHIP STATEMENT

Chapter XI contains work that will be submitted to *ACS Chemistry of Materials*. Co-authors Dylan Bardgett prepared precursors containing Pb, Fe, and Se. Dylan Bardgett, Mellie Lemon, and Fischer Harvel collected assisted with collection of XRD, XRR, and XRF data. Sven Rudin performed DFT calculations. David Johnson is my advisor. I am the primary author of this work and prepared precursors and collected/analyzed XRD, XRR, and XRF data.

11.1. INTRODUCTION

Thousands of new compounds have been predicted to be stable, but very few have been successfully prepared experimentally.[1] Theory and computational efforts have been driven by projects such as the Materials Genome Initiative (MGI) in recent years.[2–4] The goal of MGI is to rapidly advance materials discovery through complementary efforts in theory, computation, and experiment.[2] While many compounds and their structures have been predicted, their synthetic routes have not, creating a challenging task for experimentalists. In many cases, these predicted compounds are highly metastable and therefore synthesis would require a precise ability to navigate their energy landscapes. Controlling reaction pathways in solid-state synthesis is unlike that of organic chemistry, very little is known about how to control reaction kinetics and thermodynamics.[1] Greater efforts in understanding synthetic routes is crucial to achieving the goals of MGI and continued materials discovery.

Transition metal chalcogenides (TMCs) and dichalcogenides (TMDs) have been of great interest for a wide variety of applications in recent years. TMCs have been particularly of interest for use as electrode materials for energy storage/conversion, and have seemingly endless opportunity for tunable properties when layered with materials such as graphene.[5,6] Desirable physical properties such as superconductivity, charge-density waves, and thermoelectricity have been observed in many TMDs, making them attractive candidates for next-generation devices.[7] Only ~350 selenides and sulfides are reported on databases such as Inorganic Crystal Structure Database (ICSD), therefore efforts to predict and synthesize new selenides and sulfides should be made to continue to discover compounds and their interesting properties. For example, one study predicted and performed high throughput experiments to investigate unknown ternary systems (XYZ), where X was a cation (Ba, Ca, Sr, La, K, Bi, Pb), Y was a 3d transition metal, and Z was S or Se.[8] A list of 24 candidate compounds was determined by narrowing down thousands of structures based on stability. While their candidate structures were promising, synthesis of all 24 compounds was unsuccessful experimentally using solid state and gas flow reactions for bulk synthesis and molecular beam epitaxy (MBE) for thin film synthesis. Among the candidate phases predicted were three ternary lead iron selenides. Attempted synthesis of these compounds via MBE resulted in binary phases (PbSe, Fe_3Se_4).

In an attempt to synthesize ternary lead iron selenides, we employ the Modulated Elemental Reactants (MER) method in this work.[9,10] MER is a deposition technique that does not require an epitaxial substrate and allows for tuning of sequence of layering, layer thickness, and amount of material in each layer. This technique minimizes the diffusion

distance needed for atoms to nucleate and grow by designing precursors which mimic the desired structure, which is typically on the Å scale. Due to this, the rate-limiting step of the system is nucleation, instead of diffusion, which is typical for conventional solid-state synthesis. Precursors are prepared in custom physical vapor deposition system where substrates are nominally at room temperature, allowing the potential for kinetic products to form. Gentle annealing (< 500°C, < 1 hour) is used to promote the self-assembly of the targeted structure. Precursors with total compositions close to those of the predicted phases were prepared and the nanoarchitecture of the precursor was varied. These were studied with X-ray diffraction (XRD), reflectivity (XRR), and fluorescence (XRF) to determine what phases and film structures formed upon deposition and after annealing. Our experimental attempts also resulted in binary phases, however a new PbSe - hexagonal $FeSe_2$ phase was discovered. Despite the unsuccessful attempt at synthesizing the predicted compounds, this provides insight into the reaction pathways are for ternary Pb-Fe-Se thin films.

11.2. Materials And Methods

Precursors were created with varied layering and composition, targeting the compositions of the ternary phases predicted. The layering was adjusted by varying the sequence of elements deposited. Physical vapor deposition was used to deposit high-purity elemental layers of each element under high vacuum (< 10^{-7} Torr) onto a rotating Si with native SiO_2 substrate nominally at room temperature. Electron beam guns were used to deposit Pb and Fe layers, and a Knudsen effusion cell was used to deposit Se layers. Quartz crystal microbalances were used to monitor the deposition rate. Shutters over each source were programmed to open and close based on a desired input thickness. Further information

on this system are described elsewhere in detail.[11] The amount of material deposited was determined and optimized by using X-ray fluorescence (XRF) using a Rigaku Primus II ZSX. The total number of atoms/Å^2 of each element was determined by using methods described in Hamann, et. Al.[12]

Precursors are transferred to and stored in a nitrogen dry box (O_2 < 0.5 ppm), with the exception of removal for characterization. Annealing was performed in the dry box on a hot-plate. Precursors in their as-deposited (AD) and annealed states were characterized with a combination of XRF, X-ray diffraction (XRD), and X-ray reflectivity (XRR). A Bruker D8 diffractometer (Cu-Kα radiation, λ = 0.15418 nm) was used to collect specular XRD and XRR patterns. In-plane XRD patterns were collected on a Rigaku Smartlab diffractometer (Cu-Kα radiation (λ = 0.15418 nm).

11.3. RESULTS AND DISCUSSION

Three ternary compounds were predicted to be stable but have not been successfully prepared experimentally (Pb_2FeSe_3, $PbFe_2Se_3$, Pb_2FeSe_4). We prepared precursors with similar composition and various layering schemes to investigate the impact of nanoarchitecture on what phase(s) form during deposition. Figure 11.1 contains a Pb-Fe-Se ternary phase diagram where the predicted phases are marked with black circles.

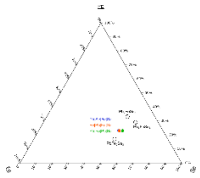

Figure 11.1. Ternary phase diagram for Pb-Fe-Se where predicted phases are marked with black circles, and experimental precursors with different nanoarchitectures are marked with colored circles.

The total composition for precursors with a Pb|Se|Fe|Se, Pb|Fe|Pb|Se, and Fe|Pb|Fe|Se layering scheme measured with XRF are marked with colored circles, which were closest to $PbFe_2Se_3$.

Specular XRD and XRR were collected for each sample after deposition. XRR patterns of the as-deposited precursors are shown in Figure 11.2a. Unlike many other modulated precursors prepared via this synthesis route, there is no Bragg reflection from the self-assembly of a periodic structure or from artificial layering in the precursor. Total film thicknesses were determined from XRR patterns, where the Pb|Se|Fe|Se precursor was ~ 293 Å thick and the Pb|Fe|Pb|Se and Fe|Pb|Fe|Se precursors were ~ 297 Å thick.

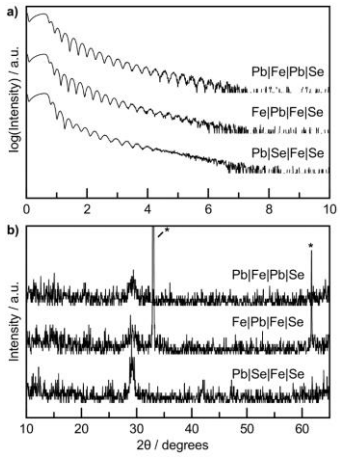

Figure 11.2. a) X-ray reflectivity patterns of as-deposited precursors with different layering schemes. b) Specular X-ray diffraction patterns of as-deposited precursors with different layering schemes.

The specular XRD patterns for these precursors all have weak reflections at $2\theta \approx 29°$, which is consistent with what would be expected for the (002) reflection in PbSe ($Fm\bar{3}m$, a = 6.117 Å).[13] This suggests that upon deposition, the same phase nucleates first regardless of the

layering scheme. With only one reflection present in the specular XRD pattern, very little information on the precursor structure can be resolved. However, we can assume that the precursor is partially crystallized after deposition, and there are no reflections consistent with a superlattice.

The Pb|Se|Fe|Se precursor was investigated as a function of annealing temperature, since this precursor had the highest intensity reflection at $2\theta \approx 29°$ in specular XRD upon deposition. Grazing incidence XRD (GXRD) and XRR patterns were collected as a function of annealing (Figure 11.3). At 150°C, the XRR pattern becomes more complex which could be due to increasing sample roughness and/or the film structure changing as nucleation and growth occurs. The pattern at 350°C is from a different piece of the sample than was used for the previous annealing steps, and was annealed directly from AD to 350°C rather than sequentially. This pattern is similar to the AD sample, which could suggest that annealing directly to a specific temperature can influence the film structure. One hypothesis for this is that sequential annealing steps could lead to more Se loss overall as Se evaporates. XRF data at the higher annealing temperatures should be collected in the future to test this. Based on previous work (Chapters IX, X), Pb-oxides and/or Fe-oxides are likely forming at the film surface, which could also contribute to the changes seen in the XRR patterns at higher annealing temperatures.

GXRD of the as-deposited precursor confirms that a cubic unit cell with parameters close to that of PbSe formed with a = 6.082(6) Å (labeled with black indices). For a typical rock-salt such as PbSe, the (001) reflection would be forbidden. This suggests that some distortion exists for the structure that is forming in these samples, which has been seen

previously for PbSe intergrowths previously.[14] In this case, this could be due to the addition of Fe into the structure, since there is no indication from XRD that Fe-Se phases are forming.

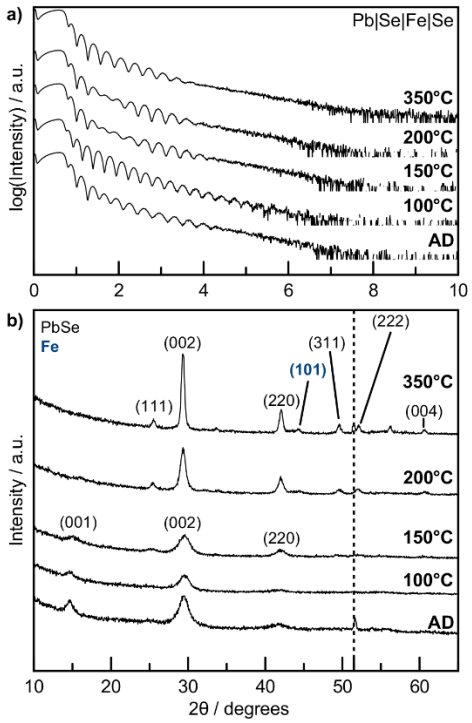

Figure 11.3. a) X-ray reflectivity patterns of the Pb|Se|Fe|Se precursor as-deposited (AD) and annealed up to 350°C. b) Grazing incidence X-ray diffraction patterns of the Pb|Se|Fe|Se precursor as-deposited (AD) and annealed up to 350°C. Black (hkl) indices correspond to a cubic unit cell with a = 6.082(6) Å, consistent with PbSe. Blue (hkl) indices are consistent with α-Fe. The dashed black line corresponds to reflections that are an artifact of the substrate.

At higher temperatures, a small reflection at 2θ ≈ 44° grows in, which is consistent with the (101) reflection in α-Fe ($Im\bar{3}m$, a = 2.8604 – 2.861 Å).[15] Analysis with HAADF-STEM/EDS should be done to confirm these hypotheses. Additionally, these should be compared to GXRD patterns of the precursors with different layering schemes annealed to higher

temperatures in the future to confirm that the layering sequence does not heavily impact what forms in this case.

After investigating various layering schemes, precursors with varying total composition were prepared which targeted the three predicted ternary phases. All precursors used an Fe|Pb|Fe|Se layering sequence in an effort to distance Pb and Se layers, as PbSe forms readily upon deposition. Figure 11.4 shows a ternary plot with the three predicted phases (black circles) and experimental precursors (colored squares) based on compositions determined from XRF. We will refer to these precursors as their compositions normalized to Pb ($PbFe_{1.84}Se_{2.98}$, $Pb_2Fe_{1.13}Se_{4.14}$, and $Pb_2Fe_{1.10}Se_{3.09}$).

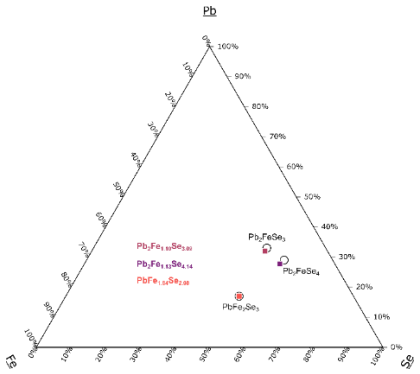

Figure 11.4. Ternary phase diagram for Pb-Fe-Se where predicted phases are marked with black circles, and experimental precursors with different compositions are marked with colored squares.

Specular XRD and XRR were collected on the as-deposited precursors (Figure 11.5). Unlike the samples with different layering schemes, all samples have Bragg reflections from artificial layering in the precursor in the XRR patterns (Figure 11.5a). In general, for heterostructures samples prepared with MER, these reflections correspond to the c-lattice parameter (or thickness) of the repeating unit. These parameters are marked for each

precursor, where the Pb-rich precursors ($Pb_2Fe_{1.13}Se_{4.14}$, $Pb_2Fe_{1.10}Se_{3.09}$) have an larger c-lattice parameter than the Fe-rich precursor ($PbFe_{1.84}Se_{2.98}$). This suggests that at these compositions, these precursors remain layered upon deposition.

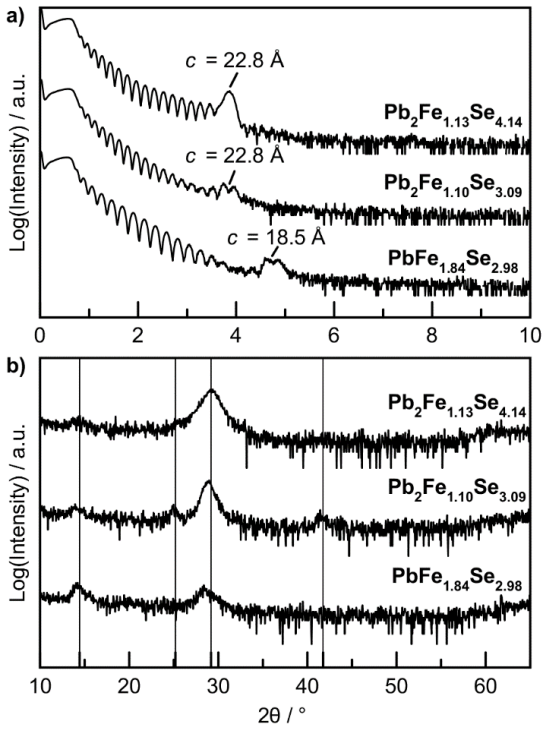

Figure 11.5. As-deposited precursors at different compositions (Fe|Pb|Fe|Se layering scheme). a) X-ray reflectivity patterns with *c*-lattice parameters marked for each initial layering reflection. b) Specular X-ray diffraction patterns where vertical lines correspond to positions of (001), (111), (002), (220) reflections expected for PbSe (c = 6.11 Å).

Specular XRD (Figure 11.5b) shows that like the previous precursors discussed, the samples began crystallizing upon deposition. Vertical lines correspond to the expected (001), (111), (002), (220) positions for PbSe (c = 6.11 Å). All samples contain weak and broad reflections consistent with a cubic unit cell with lattice parameters similar to that of PbSe. Based on this, we can speculate that upon deposition, the precursors contain bilayers of PbSe and some

additional thickness (from unreacted Fe and Se). While the exact precursor structure remains unknown, these results suggests that under these conditions, the predicted ternary phases cannot be prepared.

Although the predicted phases were not formed, these precursors were studied as a function of annealing temperature. First, we will discuss the $PbFe_{1.84}Se_{2.98}$ sample. Specular XRD and XRR patterns as a function of annealing are shown in Figure 11.6. From the XRR patterns in 11.6a, it is evident that the initial layering begins to break down at temperatures as low as 100°C and is lost at 200°C.

The specular XRD patterns (Figure 11.6b) show that the (001) reflection from the cubic unit cell, similar to PbSe (black vertical lines), is lost at 200°C and reflections consistent with β-FeSe (P4/nmm, a = 3.7720(9) Å and c = 5.5161(5) Å)[16] grow in (green vertical lines). Similar to the first set of precursors discussed, we can speculate that some distorted PbSe unit cell forms on deposit and breaks down into the binary compounds (PbSe, FeSe) at higher annealing temperatures. This is also likely why the initial layering reflection is lost at 200°C.

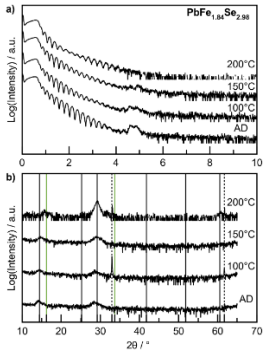

Figure 11.6. $PbFe_{1.84}Se_{2.98}$ precursor as a function of annealing. a) X-ray reflectivity patterns. b) Specular X-ray diffraction patterns where black vertical lines correspond to positions of (001), (111),

(002), (220), (222), (004) reflections expected for PbSe (c = 6.11 Å), respectively. Green vertical lines correspond with (001), (110) reflections expected for β-FeSe (a = 3.761 Å, c = 5.460 Å). Dashed black vertical lines are reflections from the sample substrate.

Next, specular XRD and XRR were collected on the $Pb_2Fe_{1.10}Se_{3.09}$ precursor annealed to the same temperatures (Figure 11.7). For this sample, the initial layering reflection is lost at 150°C. Similar to the previous sample, weak broad reflections consistent with β-FeSe begin to grow in at 150°C, and their intensities increase at 200°C (green vertical lines). All other reflections correspond to a unit cell close to PbSe (black vertical lines).

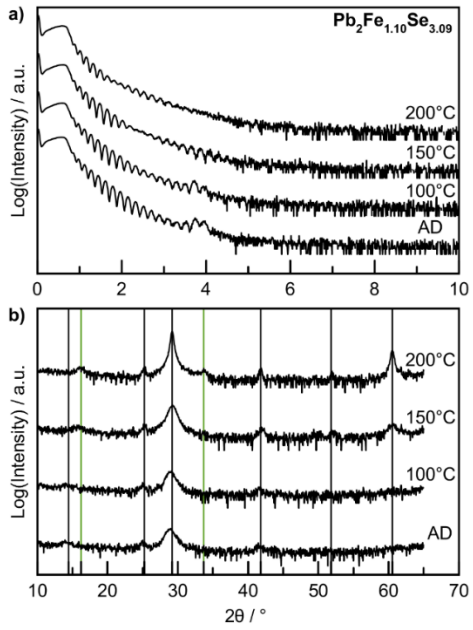

Figure 11.7. $Pb_2Fe_{1.10}Se_{3.09}$ precursor as a function of annealing. a) X-ray reflectivity patterns. b) Specular X-ray diffraction patterns where black vertical lines correspond to positions of (001), (111), (002), (220), (222), (004) reflections expected for PbSe (c = 6.11 Å), respectively. Green vertical lines correspond with (001), (110) reflections expected for β-FeSe (a = 3.761 Å, c = 5.460 Å).

Finally, specular XRD and XRR patterns for the $Pb_2Fe_{1.13}Se_{4.14}$ as a function of annealing temperature are shown in Figure 11.8. The initial layering reflection disappears at 200°C, which is similar to the other precursors in this set. This suggests that what forms

upon deposition is metastable and degrades at relatively low annealing temperatures. Further studies with smaller increments of annealing temperatures / different annealing times should be done to determine optimized annealing conditions. The specular XRD is more complex for this sample than the other precursors. While several reflections similar to PbSe are present (black vertical lines), additional reflections that do not relate to PbSe or Fe-Se phases exist below 200°C.

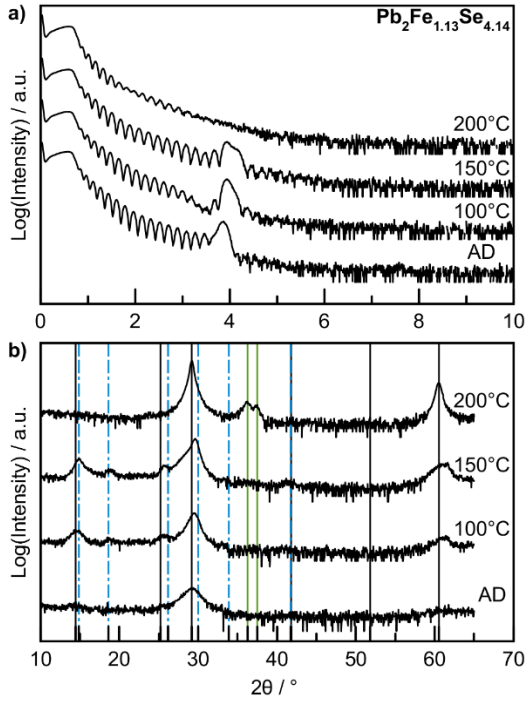

Figure 11.8. $Pb_2Fe_{1.13}Se_{4.14}$ precursor as a function of annealing. a) X-ray reflectivity patterns. b) Specular X-ray diffraction patterns where black vertical lines correspond to positions of (001), (111), (002), (220), (222), (004) reflections expected for PbSe (c = 6.11 Å), respectively. Green vertical lines correspond with (021), (002) reflections for $FeSe_2$ (a = 3.60(1) Å, b = 5.77(1) Å, and c = 4.79(1) Å). Dashed blue vertical lines correspond to (00l) reflections for a unit cell with c = 23.8 Å.

These reflections are consistent with a (00l) reflections from a superlattice (blue dashed vertical lines) that has a c-lattice parameter ≈ 23.8 Å, while the initial layering reflection is ≈

21.8 Å. Given the asymmetric shape of the initial layering reflection, peak shapes in XRD, and weak intensities, this suggests that a superlattice is forming in some regions, but with defects that are likely due to insufficient material locally or globally to form the structure. While the predicted phases did not form, this is the first indication that a Pb-Fe-Se superlattice can be prepared. This structure breaks down at 200°C, and reflections consistent with $FeSe_2$ (Pnnm, a = 4.804(2) Å, b = 5.784(3) Å, and c = 3.586(2) Å)[17] (green vertical lines) and PbSe (black vertical lines) were observed. For all samples, only binary phases are present at this temperature.

To further probe the structure, in-plane XRD was collected on the $Pb_2Fe_{1.13}Se_{4.14}$ annealed to 150°C (Figure 11.9). Vertical black lines are from (hk0) reflections that correspond to a cubic unit cell with c = 6.14 Å (close to PbSe). Only (hk0) reflections were observed, which suggests that the PbSe layers are crystallographically aligned to the substrate. One relatively intense reflection at 2θ ≈ 54° does not belong to those expected for PbSe, and does not correspond to any known Fe-Se phases.

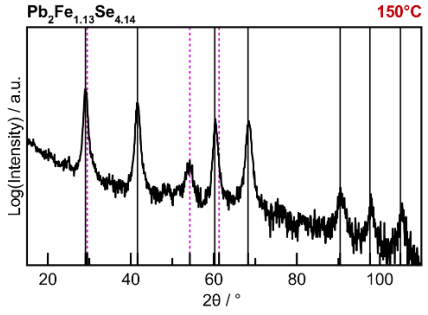

Figure 11.9. In-plane XRD pattern of the $Pb_2Fe_{1.13}Se_{4.14}$ precursor annealed to 150°C. Vertical black lines represent (200), (220), (400), (420), (440), (600), and (620) PbSe reflections (c = 6.14 Å), respectively. Dashed purple lines represent (200), (110), and (400) reflections for a hexagonal unit cell (a = 3.38, c = 6.05 Å) close to what would be expected for VSe_2.

In MER, typically a cubic rock-salt structure (like PbSe) is layered with a hexagonal transition metal dichalcogenide (like VSe_2).[14,18] With this knowledge, this in-plane XRD pattern was familiar in that the additional unknown reflection is similar to the (110) reflection that would be expected for a hexagonal unit cell such as VSe_2 (a = 3.40(1) Å, c = 5.96−6.11 Å).[19] Purple dashed lines represent (*hk0*) reflections for a hexagonal unit cell with a = 3.38, c = 6.05 Å. We speculate that rather than form orthorhombic $FeSe_2$, a new hexagonal $FeSe_2$ phase is forming when layered with PbSe.

To test our hypothesis, preliminary density functional theory (DFT) calculations were done to determine if a PbSe – hexagonal 1T-$FeSe_2$ structure would be stable. This was done by using an island approximation method which has been used for other systems containing VSe_2 and described in detail elsewhere.[20] Essentially, the structure was optimized by constructing the potential phases as islands which are allowed to relax between adjacent layers. Initial results suggest that a PbSe – 1T-$FeSe_2$ structure is stable, with a structure shown in Figure 11.10. Further work to optimize and study this structure are underway, however this provides further support for our hypothesis that a hexagonal $FeSe_2$ phase is forming in our precursor.

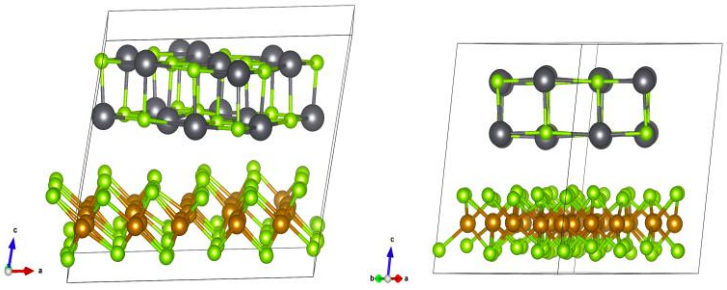

Figure 11.10. Theoretical structure of PbSe (Pb: gray, Se: green) and hexagonal 1T-$FeSe_2$ (Fe: orange, Se: green).

11.4. CONCLUSION

Preparation of three predicted ternary Pb-Fe-Se phases was unsuccessful with varying precursor nanoarchitecture and composition. This work suggests that despite increasing diffusion distance between Pb and Se, PbSe readily forms upon deposition, making it challenging to nucleate the predicted phases with more complicated unit cells. Depending on composition, precursors can form a structure which is initially layered. This layering is lost by 150 – 200°C, and the structure breaks down into binary phases (PbSe, β-FeSe, orthorhombic $FeSe_2$). Surprisingly, evidence of a superlattice was found in the $Pb_2Fe_{1.13}Se_{4.14}$ precursors. In-plane lattice parameters were consistent with PbSe and a hexagonal unit cell similar to hexagonal 1T-VSe_2, which we hypothesize to be $FeSe_2$. Preliminary density functional theory calculations (DFT) that PbSe layered with $FeSe_2$ in a hexagonal 1T structure is stable. Precursors that target these constituents are needed to form well-ordered layered heterostructures, as our precursor had insufficient material and layering sequence. Ideally, these precursors would contain Fe|Se|Pb|Se, where the amount of Fe and Se in Fe|Se contains the amount of material needed to form one trilayer of $FeSe_2$ and the amount of Pb|Se is the amount to form one bilayer of PbSe. Electron microscopy will be needed to resolve and confirm the structure, where HAADF-STEM/EDS methods to determine atomic plane positions could be used to develop starting positions for Rietveld refinement to compare to and optimize DFT calculations.

11.5. BRIDGE

This chapter discusses initial precursors used to study the reaction of ternary Pb-Fe-Se thin film compounds. Stable ternary compounds were predicted to be stable, but attempts to synthesize these experimentally have failed, including our own. Despite varying the precursor structure and compositions, PbSe forms upon deposition. Surprisingly, at select compositions, layered or partially layered heterostructures form which we've hypothesized to contain PbSe and hexagonal $FeSe_2$ (known $FeSe_2$ is orthorhombic). Initial computational experiments predict this to be stable. In the next chapter, these elements are layered with VSe_2 to understand if interfaces/substrate have influence on what phases nucleate from Pb, Fe, and Se.

CHAPTER XII

NOVEL TECHNIQUE FOR DETERMINATION OF INTERCALATION VERSUS SUBSTITUTION IN DOPED TMDS

12.0. AUTHORSHIP STATEMENT

Chapter XII contains work that will be submitted to the *Journal of the American Chemical Society*. Mellie Lemon will be the primary author of the manuscript. Co-authors Dylan Bardgett and Fischer Harvel assisted with preparation of precursors and collection/analysis of XRD, XRR, and XRF data. Ping Lu collected HAADF-STEM/EDS data. David Johnson is my advisor. I prepared TEM specimen and analyzed HAADF-STEM/EDS data. I wrote the results and discussion for samples with PbSe and Fe-doped VSe_2 and developed a methodology to use EDS data to determine atomic plane positions.

12.1. INTRODUCTION

Transition metal dichalcogenides (TMDs) have garnered significant interest over the last several decades because of their layered structure and interesting electronic properties that depend both on chemistry and number of layers.[1] The diverse and tunable properties of TMDs make them a highly attractive material for applications ranging from nanoelectronics and nanophotonics to catalysis and sensing.[2–4] An often-used strategy to invoke to further control of the properties of these materials is by doping with different atoms which substitute into the TMD structure or atoms or molecules which intercalate in the van der

Waals gap between layers.[5–7] By varying the amount of the substitution or intercalation, it is possible to control the electronic, magnetic, optical, and morphological properties of TMDs.

Synthesis techniques for doped TMDs are typically classical 'heat and beat' approaches that rely on the reaction of mixtures of chalcogen powders and either elemental metal to target specific compositions of dopants in TMDs.[8] Crystals are typically grown using physical vapor transport (PVT) or grown as films using chemical vapor deposition (CVD). For dopants that are similar in size and valence to the metal or chalcogen, either intercalation or substitution can occur.[9] The composition targeted in the product during synthesis is typically thought to control whether the dopant is incorporated substitutionally or in between layers as an intercalant. However, alternative structures could form with the same composition. For example, in a composition targeting intercalated dopant, the dopant could incorporate substitutionally and cause intercalation of the original metal between layers. There can also be a mixture of substitution and intercalation of the dopant and the metal in the dichalcogenide.

It is challenging to distinguish the type of dopant incorporation into the host structure using standard characterization techniques. In structural characterization with X-ray diffraction (XRD) of doped TMDs, the evidence for intercalation versus substitution is ambiguous for dopants that are similar in size and valence to the atoms in the layered TMD. Diffraction patterns of doped TMDs usually either closely resemble the pattern of the undoped host or show a small shift due to a change in lattice size. The shift induced by doping can be towards larger or smaller values for both intercalation and substitution

depending on the identity of the dopant and on charge transfer effects that alter the bond lengths or the size of the van der Waals gap between layers.[6,10] Both types of dopant incorporation can also affect the electrical or magnetic properties of the TMD by altering the bandgap or carrier concentration of the host TMD. This is further complicated in TMDs with reduced dimensionality, which are of high interest for modern device applications. In 2D TMDs, the effect of dopant incorporation on the electrical properties is often unpredictable.[7]

A method for distinguishing between intercalation and substitution is needed to establish structure – function relationships, which historically have facilitated improvements in material properties for applications such as catalysis. For catalytic TMDs, dopants can increase the density of catalytic sites either by inducing morphology changes that expose more sites or creating additional sites.[11] An understanding of how dopants are incorporated into the structure of specific catalytic TMDs would lead to insight into how to further improve efficiency through tuning the identity and concentration of the dopant. Recently, the catalytic efficiency of VSe_2 for the hydrogen evolution reaction (HER) was demonstrated to increase upon doping with a small amount of Fe.[12] Fe-doped VSe_2 had previously been studied by a few other groups who had targeted either substitution or intercalation of Fe in VSe_2 and had formed stable crystalline products with lattice parameters near those of VSe_2.[13,14] However, the extent of intercalation versus substitution of Fe in VSe_2 was not well explored. Each of the Fe-doped VSe_2 compounds synthesized showed electrical and magnetic properties that differ from those of pure VSe_2, but it is difficult to determine whether this arises from interlayer or intralayer interactions with Fe. Insight into the

structural incorporation of Fe in VSe_2 is needed to develop a fundamental understanding of how Fe improves HER catalytic efficiency.

This prompted us to prepare Fe-doped VSe_2 samples to investigate the use of HAADF-STEM and STEM-EDS cross section images of samples to clearly quantify the amount of substitution and intercalation. We used the modulated elemental reactants synthesis approach to prepare these samples, as this approach leads to preferred orientation of the resulting compound with the c-axis of the dichalcogenide perpendicular to the substrate.

12.2. MATERIALS AND METHODS

The multilayer thin-film precursors were deposited onto (100) oriented Si wafers using a custom-built high vacuum ($<10^{-6}$ Torr) physical vapor deposition (PVD) chamber from elemental sources. Electron-beam guns were used to evaporate Fe (99.95%) and V (99.99%) from targets, and a Knudson effusion cell was used to evaporate Se (99.99%). The deposition rates were monitored constantly by quartz crystal microbalances located above each elemental source. Pneumatic shutters positioned between the elemental sources and the spinning substrate were programmed to open and close to control the sequence and amount of material deposited. Thin layers of V, Fe, and Se were deposited sequentially and the number of V|Fe|Se repeat units was designed to target a film thickness of approximately 300 Å. Prepared samples were stored in a nitrogen glovebox (>0.2 ppm O_2) to prevent oxidation.

X-ray fluorescence spectroscopy (XRF) was carried out on a Rigaku Primus II spectrometer. XRF spectra measured were used to calculate the number of atoms per $Å^2$ of each element present with a technique previously described by Hamman and coworkers.[15] The calculated compositions were used for an initial estimate of the extent of intercalation versus substitution.

Annealing of the samples took place inside the glovebox on a calibrated hot plate set to the desired temperature. The samples were placed inside a closed container alongside a Se source during annealing to maintain a Se atmosphere and prevent Se loss. A piece of each sample was annealed at varying time and temperature in order to determine the optimal processing conditions for crystallization. The samples were temporarily removed from the nitrogen glovebox as needed for characterization. X-ray reflectivity (XRR) and specular X-ray diffraction (XRD) patterns were collected on a Bruker D8 diffractometer equipped with Cu Kα radiation in θ−2θ locked-coupled scan mode. XRR patterns were collected over a 2θ range of 0-11°, and specular XRD patterns were collected over a 2θ range of 5-65°. The Kiessig fringes observed in the XRR patterns were used to calculate the film thickness using a modified form of Bragg's law. Laue oscillations present in the specular XRD pattern were used to calculate the size of coherently scattering domains. In-plane XRD patterns were collected on a Rigaku Smartlab diffractometer with Cu Kα parallel-beam/parallel slit analyzer (PB/PSA) and parallel-beam (PB) optics over a 2θ range of 20-70°.

Cross-sections were prepared with an FEI Helios NanoLab 600i DualBeam FIB-SEM using standard lift out procedures. The prepared cross-section will be imaged in high-

angle annular dark-field (HAADF) scanning transmission electron microscopy (HAADF-STEM) mode at 300kV with a Thermo Fisher Scientific Themis Z.

12.3. RESULTS AND DISCUSSION

This work was motivated by previous work where unexpected results due to rearrangement in samples containing Pb, Fe, V, and Se were observed. Initially, a sample was prepared with a V|Se|Pb|Fe|Pb|Se layering scheme which targeted a $(PbFe_{0.5}\ Se_{1.5})_1(VSe_2)_1$ heterostructure, which will be referred to as the 1.5-1 sample. Upon deposition and after annealing, it was evident that the sample did not form the intended heterostructure and instead had rearranged to form a superlattice with a larger c-lattice parameter than expected for the targeted structure. Initially, the hypothesis was that two repeat units of $(PbFe_{0.5}\ Se_{1.5})_1(VSe_2)_1$ combined to form a larger structure comprised of $(VSe_2)_1(PbSe)_1(VSe_2)_1(PbSe)_1(FeSe)_1$. To test this hypothesis, a second sample was prepared with a V|Se|Pb|Se|V|Se|Pb|Se|Fe|Se precursor structure targeting the hypothesized ABABC repeat unit structure, where A = VSe_2, B = PbSe, and C = FeSe.

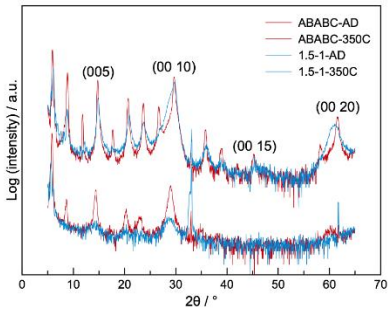

Figure 12.1. Specular XRD patterns of as-deposited (AD) and samples annealed to 350°C for 15 minutes.

Specular XRD of as-deposited (AD) and annealed 1.5-1 and ABABC samples is shown in Figure 12.1 above. Overlaying both patterns confirms that both samples rearranged with the same repeat unit. Reflections from the superlattice (00*l*) are labeled, with a c-lattice parameter of 30.03(7) Å (repeat unit thickness).

To determine if the sample did rearrange to form an ABABC repeat unit structure, a cross-section of the ABABC sample was prepared for analysis with HAADF-STEM/EDS. Figure 12.2 contains a low magnification HAADF-STEM image where the vertical arrow represents the line profile obtained from EDS maps collected over the area shown in the STEM image. Rather than taking an EDS line scan, line profiles of intensity versus distance for each element were extracted from maps to minimize sample damage which are shown on the left. Surprisingly, this confirmed the sample rearrangement but not to an ABABC repeat unit structure. From HAADF-STEM alone, the repeat unit structure appears to be $(PbSe)_1(VSe_2)_1(PbSe)_1(VSe_2)_2$ based on contrast and structure. This posed the question – where is the Fe in the sample? The EDS line profiles show that Fe is within (and for the second repeat unit between) VSe_2 layers. These results suggest that rather than nucleate FeSe, Fe intercalated and substituted into VSe_2.

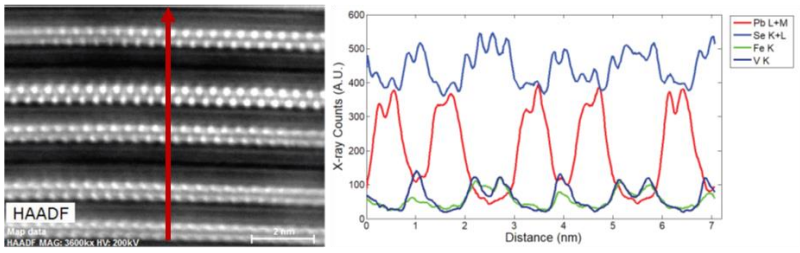

Figure 12.2. HAADF-STEM image (left) of a cross section of the ABABC sample and corresponding line profiles extracted from EDS maps from the region on the right. The red arrow is used to represent the profiles shown on the right.

An additional EDS map was collected over the entire film thickness, where a HAADF-STEM image and extracted line profiles from EDS are shown in Figure 12.3. In the HAADF-STEM image (left), the left region of the image is the top of the film and right region is the bottom/substrate. The top of the sample is at begins at 0 nm in the EDS line profiles for each element (right). With exception of the top and bottom of the film, the entire film contains the repeat unit structure discussed from Figure 12.2.

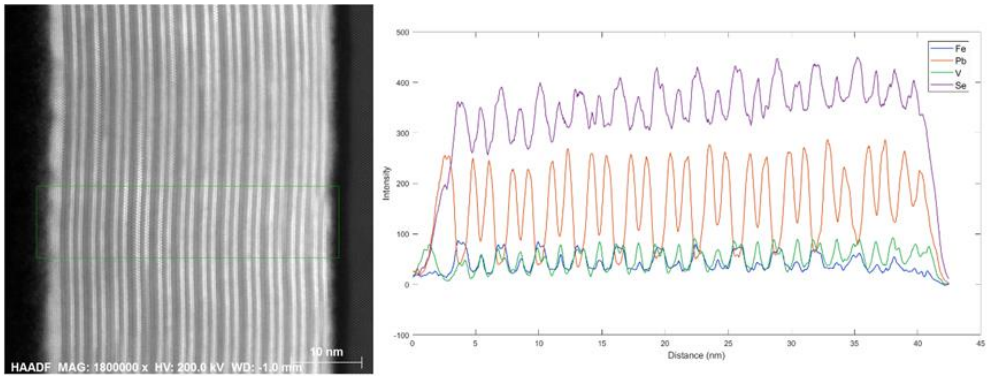

Figure 12.3. HAADF-STEM image (left) of a cross section of the entire film thickness of the ABABC sample and corresponding line profiles extracted from EDS maps from the region on the right.

The EDS line profiles from repeat units in the middle region of the film were averaged for each element to ultimately determine atomic plane positions for use in Rietveld refinements. This is necessary in this system in particular since the atomic plane positions for Fe cannot be determined from HAADF-STEM alone. An example of averaged line profile data for Pb for both PbSe bilayers in the repeat unit for 10 total repeat units is shown on the left in Figure 12.4. The dashed line is the averaged profile. This process was done for each element, then peaks of averaged data for each element were fit to a Gaussian model. Gaussian models for each element are shown on the right in Figure 12.4. Averaging all

repeat units in this sample did not contain the resolution needed to resolve several key features including individual PbSe plane in the bilayer, and individual Se layers in the Fe-doped VSe_2. Current work to combine the averaged data and data from the EDS map collected at lower magnification from Figure 12.2 is underway in attempt to determine the atomic plane positions currently missing. Peak coefficients can be used to determine atomic plane position for the repeat unit structure, which can be used as a starting point for Rietveld refinement.

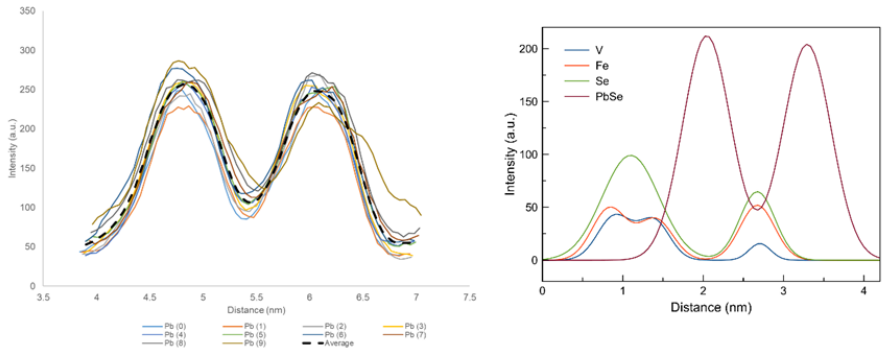

Figure 12.4. Example of averaged repeat unit profiles for Pb, where the dashed line is the average of 10 repeat units (left) and Gaussian models from fits of averaged profile data for each element.

To further investigate Fe intercalation and substation in VSe_2, three amorphous precursors were prepared by sequential deposition of V|Fe|Se elemental layers. The number of repeat units of V|Fe|Se elemental layers was controlled to target a total film thickness of approximately 30 nm. The deposition parameters for each precursor were adjusted to target a 1:2 ratio of total metal atoms to Se atoms. For the total metal atoms, two precursors were deposited targeting 30% Fe and 70% V and the third precursor was deposited targeting 60% Fe and 40% V. The composition of each sample was determined using X-ray fluorescence spectroscopy (XRF), and the stoichiometric formulas were calculated from the total amount

of metal and Se atoms per Å^2 of each of the precursors. As-deposited compositions are summarized in Table 12.1. Each repeat unit contained enough metal and Se atoms to form a Se-M-Se trilayer structure with the metal layer consisting of a mixture of Fe and V near the targeted percentages.

Table 12.1. Compositions and thicknesses of deposited amorphous precursors calculated from XRF and XRR measurements

Sample	Total Atoms/Å^2			Formula	Film Thickness (nm)	Film Roughness (nm)	Repeat Unit Thickness (nm)
	V	Fe	Se				
A (5C)	3.43(7)	1.4(1)	10.2(3)	$Fe_{0.27}V_{0.67}Se_2$	29.01(6)	0.747	0.580(1)
B (3B)	3.08(7)	1.5(2)	9.5(3)	$Fe_{0.32}V_{0.65}Se_2$	27.68(6)	0.797	0.554(1)
C (3C)	2.17(6)	2.8(2)	9.9(3)	$Fe_{0.57}V_{0.44}Se_2$	29.00(4)	0.747	0.580(1)

X-ray reflectivity (XRR) and specular X-ray diffraction (XRD) patterns for the as-deposited 6samples are shown in Figure 12.5. The XRR patterns show Kiessig fringes extending to ~6° 2θ for each sample before disappearing. The angle at which the fringes can no longer be resolved can be related to the film roughness via the Parratt equation, and gives a roughness of ~0.7-0.8 nm for each film. The as-deposited film thicknesses are summarized in Table 12.1. Peaks in the specular XRD patterns can be indexed to a family of 00*l* reflections, demonstrating that the $Fe_xV_{1-x}Se_2$ compounds crystallize aligned to the c-axis upon deposit. This is consistent with previous results that showed crystallization of pure VSe_2 aligned to the c-axis on deposit.[16] The c-axis lattice parameters calculated from the as deposited 00*l* reflections range between 0.615-0.619 nm.

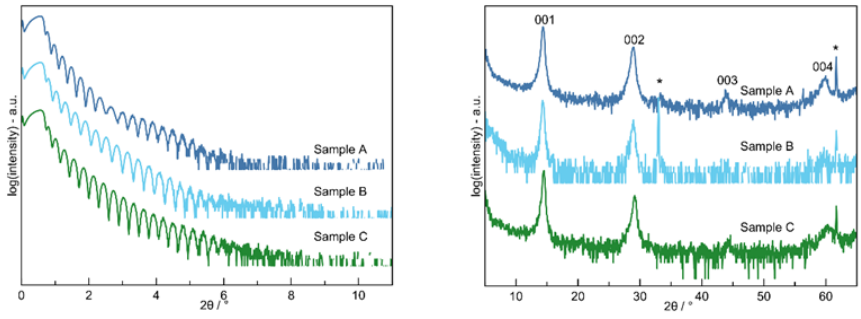

Figure 12.5. XRR and specular XRD patterns of as-deposited samples targeting $Fe_{0.3}V_{0.7}Se_2$ Reflections marked with an asterisk are from the Si substrate.

Annealing studies were carried out on the samples to determine the optimal temperature for crystallization. Specular and in-plane XRD measurements were carried out at each step of the annealing study to track changes in lattice parameters and reflection intensity with each sequential increase in temperature. The specular and in-plane diffraction patterns for a characteristic annealing study of Sample A are shown in Figure 12.6. The diffraction patterns for Sample B and C can be found in the SI, and are similar to those of Sample A.

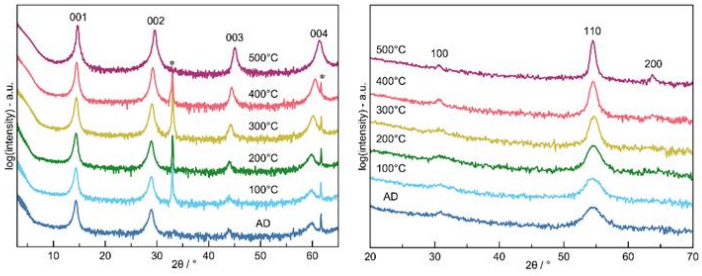

Figure 12.6. Specular (left) and in-plane XRD (right) patterns for annealing study of Sample A.

For each sequential annealing step, the intensity of the peaks increases and the full width at half max (FWMH) decreases, showing that the sample is becoming more crystalline

at each higher temperature. The samples became fully crystalline at the optimal temperature of 500°C. Specular and in-plane XRD patterns for each sample at 500°C are shown in Figure 12.7.

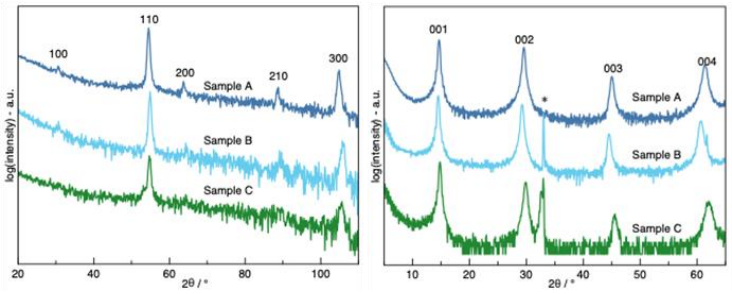

Figure 12.7. In plane and specular XRD patterns for each sample annealed at 400°C (In-plane XRD samples 3B and 3C, specular XRD for 3B) 500°C for 15 minutes in Se atmosphere

For each sample, the c-axis lattice parameter decreased as temperature increased and the a-axis lattice parameter stayed near constant. The c-axis lattice parameter was smaller for crystalline samples with higher Fe content. A summary of the a- and c-axis lattice parameters in the as-deposited precursors and the samples annealed at 500°C is show in in Table 12.2. For each sample, the values are near the reported c-axis and a-axis lattice parameters for pure VSe_2 of 6.108 Å and 3.359 Å and near the similar $Fe_{0.2}V_{0.8}Se_2$ compound of 6.090 Å and 3.367 Å, respectively.

For each sample at the optimal annealing condition, the 00*l* reflection in the specular XRD pattern also shows Laue oscillations as can be observed from the smaller peaks on either side of the Bragg peak shown in Figure 12.8. Laue oscillations arise from the incomplete destructive interference from a finite number of crystallographically aligned unit cells. At the Bragg condition, the reflections from each unit cell are interfering completely constructively,

but for a certain finite number of unit cells there are only so many combinations that lead to complete destructive interference between Bragg peaks. The incomplete destructive interference gives rise to oscillations on either side of the reflection which can provide information about the thickness of the crystallized portion of the sample.

Table 12.2. Summary of lattice parameters for samples as deposited and annealed at 500°C

Sample	a-axis lattice (Å)		c-axis lattice (Å)	
	As deposited	500°C	As deposited	500°C
A (5C)	3.34(2)	3.371(3)	6.175(6)	6.029(3)
B (3B)	TBD	TBD	6.188(1)	TBD
C (3C)	TBD	3.362(9)	6.152(1)	5.977(3)

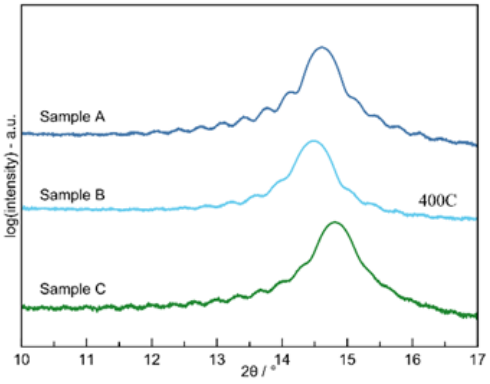

Figure 12.8. Laue oscillations on either side of the 001 reflection in the specular XRD for each sample

The number of oscillations between Bragg reflections, which can be calculated from the spacing of the visible oscillations, is equal to 1 less than the number of layers. The thickness of the crystallized portion of the sample can also be determined from the location of the Laue oscillations using Bragg's law. Dividing this thickness by the c-axis lattice parameter of the unit cell gives the number of crystalline layers. This number of layers can also be determined by calculating the number of oscillations between the first and second Bragg reflection from the spacing between oscillations. The number of layers derived from Laue oscillations can be compared to the possible number of layers that could be formed from the amount of V and Fe present determined from XRF. This will give information about the amount of Fe substituting into the VSe_2 layers. The Laue thicknesses and V and Fe compositions are summarized in Table 12.3.

Table 12.3. Thicknesses of samples calculated from XRR and Laue oscillations and summary of crystalline layers

Sample	Thickness from XRR (Å)	Thickness from Laue (Å)	Number of Crystalline Layers	Enough V for x layers	Enough Fe for y layers
A (5C)	263.1(7)	260.4	43	33	13
B (3B)	TBD	TBD	TBD	TBD	TBD
C (3C)	269.2(1)	269.0	45	21	26

12.4. FUTURE DIRECTIONS

Cross-sections of a piece of Sample A that has been annealed at optimal conditions will be used for HAADF-STEM imaging and EDX line mapping. The average structure and atom positions in the $Fe_{0.27}V_{0.67}Se_2$ layers will be calculated from the EDX line map and this data will be used to fit the diffraction pattern using Rietveld refinements. The results of this study should serve as a proof of concept for the proposed technique to determine the extent of substitution and intercalation in doped TMDs. This will have implications for research into the modification of TMD properties for specific applications such as catalysis.

12.5. BRIDGE

This chapter revealed that PbSe-$FeSe_2$-VSe_2 did not form, nor did any predicted phases, in precursors containing elemental layers of Pb, Fe, Se, and V. Samples instead rearranged to form a well-ordered layered heterostructure containing PbSe and Fe-doped VSe_2. In the previous chapter, $FeSe_2$ formed with a hexagonal unit cell similar to that of VSe_2. Here, rather than nucleate $FeSe_2$, Fe instead was intercalated and substituted into VSe_2 layers. This was found using HAADF-STEM/EDS and method to use EDS data to determine atomic plane positions was discussed. Samples which only contain Fe, V, and Se were prepared to target VSe_2 layers with varying amount of Fe-doping. HAADF-STEM/EDS data is needed to determine the amount of intercalated versus substituted Fe in VSe_2. This chapter concludes the third section of this dissertation. The fourth section and subsequent chapters discuss larger scale interface challenges through the use of a new

characterization technique, cryogenic femtosecond laser cross sectioning and subsequent scanning electron microscopy on intact coin cell batteries. The next chapter discusses the technique in detail, including impact of laser parameters on quality of the cross-sections (and resolvable features).

CHAPTER XIII

ULTRAFAST PULSED LASER ABLATION WITH CRYO-SCANNING ELECTRON MICROSCOPY: LARGE-FIELD 2D and 3D ANALYSIS OF NANOSCALE MULTIPHASE MATERIALS

13.0. AUTHORSHIP STATEMENT

Chapter XIII contains work that will be submitted to *Microscopy and Microanalysis*. Co-authors Katherine L. Jungjohann, Katherine L. Harrison, and Laura C. Merrill prepared half-cell Li metal batteries. Steven Randolph assisted with collection of cryogenic laser ablation/PFIB/SEM data and experimental design. David Johnson is my advisor. I am the primary author of the manuscript, and assisted with experimental design and collection of cryogenic laser ablation/PFIB/SEM data.

13.1. INTRODUCTION

Characterizing multiphase materials and their interfaces is a challenging yet necessary to understanding their systems and applications. One primary example of multiphase materials systems are batteries which are comprised of stacks of different materials types, including components such as polymers, metals, liquid electrolyte, and solid electrolyte interphase.[1,2] Interfaces and morphology play a critical role in the performance of batteries, requiring advanced methods to characterize the structure and properties.[3] Particularly for heterogeneous materials, accessing specific sites is critical. Generally, methods such as microcomputed tomography (MicroCT), electron microscopy (EM) and cryogenic-EM methods (cryo-EM), X-ray microanalysis, and neutron scattering techniques are used to

characterize such materials.[4] Each method has benefits and challenges, and often a combination of methods is necessary. For example, MicroCT is non-destructive, but resolution is generally limited to ~ 700 nm.[5] Cryo-EM methods can be used to resolve sub-nm scale features[6], but requires disassembly and is limited to small regions (several μm).

In recent years, ultrashort pulsed lasers (UPL) have driven advancements in micromachining, tissue modification, spectroscopy, and material processing through rapid and athermal material removal.[7–11] A system that combines UPL with a DualBeam Scanning electron microscope (SEM)/Plasma-focused ion beam (PFIB) was developed for rapid analysis of large areas and volumes in an electron microscope.[12,13] However, cryogenic ultrafast pulsed laser ablation has not been explored, which allows for cross-sections to be analyzed in multiphase samples where organics or liquids are present with metals and polymers, such as the electrolyte in a battery. No concern for ion-implantation, beam induced heating at high currents, or amorphization damage like with a FIB. Surface texturing, often referred to as laser induced periodic surface structures (LIPSS)[14], occurs on most materials and can mask nanoscale features. However, in this system the PFIB can be used to remove small surface structures on a region of interest. Differential milling due to sputter yields when used only a FIB appears more pronounced than differential ablation due to differences in ablation threshold. In short, the UPL is beneficial for rapid removal of material to obtain relatively flat cross-sections and the PFIB is beneficial for removing small scale surface texturing to resolve nanoscale features. Here we present a method for cryogenic ultrafast pulsed laser ablation combined with a scanning electron microscope to obtain large area cross-sections of intact half coin cell batteries which contain a variety of layers spanning several

different classes of materials. In order to image these coin cells in their native state, disassembly cannot occur. This requires the ability to mill through microns of stainless steel casing to access the active area, which the UPL has the capability to do. This is possible due to the high average pulse energy and repetition rates in the laser system, which is analogous to having a high current available in a traditional FIB. The athermal, ultrashort pulse is a key characteristic of the UPL that allows access through the stainless steel without thermally destroying the more beam sensitive active areas. This allows one to rapidly and coarsely approach the area of interest with minimal collateral damage. Laser parameters can be adjusted so as to provide a much improved surface quality in a final laser polishing step. If required, an additional step of using the PFIB to further refine the cut face may be performed.

13.2. METHODS AND MATERIALS

13.2.1. Sample Preparation

Half-cell Li metal coin cell batteries (20 mm diameter) were assembled and prepared using methods described in extensive detail elsewhere.[15] Coin cell batteries were mounted to pre-tilted holders which were designed to hold 20mm 2032 diameter coin cell batteries. Several iterations of pre-tilted stubs were used and optimized. In general, coin cells were mounted to metal copper now (aluminum or copper) stubs with a pre-tilt (21 – 26 degrees) to compensate for the limitations in stage tilt, which only go to -10 degrees in the prototype system. The use of a pre-tilted stub results in a cross section that's as close to vertical as possible for this configuration. The optimized holder includes a platinum RTD to measure temperature local to battery with a -26 degree pretilt. Countersunk screws capture < 1mm from the edge of battery to ground cathode and firmly secure without placing undue load on

the device. The bottom of recessed area for battery mount is electrically isolated via a layer of polyimide tape to ensure the cell is not shorted.

Initially, samples were mounted to the stub and plunge frozen in liquid nitrogen. The sample and stub were then transferred in air to a Quorum cryo-stage. The cooling process was optimized by a combination of improving the mount design to allow for easier coin cell mounting and by cooling the coin cell incrementally. The most recent and reproducible method has been to keep the batteries in a 0°C freezer until ready for processing. Then a LN_2 bath is made in Styrofoam insulating container. Two nested Pyrex beakers are placed in the LN_2 bath and the coin cell in the inner beaker. This double layer of glass slows the heat transfer from the LN_2 bath to the coin cell reducing the possibility of thermal shock and delamination. It's held in this condition for approximately 30 minutes before being moved directly into LN_2. All of this is being done while the wedge and stage have been precooled to at least -150°C. The system is vented and the cell is quickly transferred.

13.2.2. System

The prototype system is configured on a Helios G3 Xe^+ PFIB platform. The femtosecond laser has a wider vastly different parameter space than a FIB, which includes tunable wavelength, pulse energy, polarization and repetition rate. In addition, there are patterning parameters such as pixel spacing and effective dwell times that are somewhat analogous to FIB. This laser can operate at 1030 nm or using second harmonic generation, 515 nm with pulse durations < 300 femtoseconds. The pulse energy ranges from nJ range to a maximum of 59.817 μJ for 1030 nm and 37.489 μJ for 515 nm, with a range of repetition

rate from 1 to 60 kHz. The average power can be varied by changing pulse energy and repetition rate, where the maximum pulse energy can be used with reduced repetition rate to lower the thermal load to the sample. Since these samples contain polymers and frozen electrolyte, this is critical. Laser is nominally athermal, but it is definitely possible to causer thermal damage at higher repetition rates. Normally polymer processing is done at 500Hz – 3kHz.

Additional optics were added to the beam path to further increase the parameter space. This includes waveplates which allow for changing the beam polarization, which can be set to horizontal (S), vertical (P), or circular. Important to note that we are processing in oblique mode, so vertical (P) polarization is only partially P while S is pure S polarized. In addition, an objective lens which is positioned inside of the chamber is capable of moving in the Z-direction (in or out) and is designed to focus both laser wavelengths at a desired position. Nominally this is at eucentric position of the stage and coincident with both the PFIB and SEM.

The patterning was designed to mimic the patterning options on a DualBeam system as best as possible. This includes changing the shape, size, size, pitch, and scan type. For the 'fine mode' patterning, a 'pulse per pixel' (PPP) can be input, which defines the number of laser pulses used on each pixel in the pattern. For soft materials, this approach is beneficial because pulses can be delivered in a very deteriministic fashion so as to allow fewer or 1 PPP will allow for minimal heat generation and damage. Alternatively, in 'coarse mode' patterning, a dwell time can be input, which defines an ablation time per pixel and a delay

time between patterning loops. This approach is best suited for reducing ablation time and ablating through hard materials, such as stainless steel, rapidly.

Laser pattern control is primarily driven by a fast scanning mirror (FSM) that adjusts the angle of incidence of the beam onto the back focal plane of a telecentric objective with antireflective coatings. The rapid adjustment of the beam angle onto the objective translates into lateral displacement of the beam at its focal point. The telecentricity of the objective is responsible more minimizing spot distortions as the beam travels far from the optical axis.

Similar to automated slice and view FIB routines, automated laser slice and view can be obtained. This routine can also include automated laser/PFIB/EBSD/EDS collection, but for this application only laser slice and view was used. In this case, a laser pattern is defined that is used for each slice. Then stage positions are saved for both SEM imaging and laser slicing. The ability to automate this process allows for collection of serial section data (with laser only, PFIB only, or combination of both. The method presented here relies on stage positioning to define the laser slice thickness. However, it is entirely possible to automate the process to allow for slice placement via the fast scanning mirror.

13.3. RESULTS AND DISCUSSION

13.3.1. Large Multiphase Areas

One of the major challenges with the characterization of multiphase materials and interfaces is accessing a representative area. With the exception of MicroCT, other methods generally require interfacial disassembly. For coin cell battery characterization, disassembly of

the multiphase stack is not necessary as the UPL is capable of ablating through the 250 μm-thick stainless steel casing.

On this prototype system in this configuration, stage tilt and rotation were limited due to inherent design limitations on the Quorum cryo-stage. Modern cryo stages use copper heat transfer connections instead of plastic tubing that flows liquid nitrogen boil-off to allow for full tilt and rotation. This opens up the possibility of more advanced workflows (e.g. those including EDS, EBSD, or PFIB polishing steps) on cryogenically-maintained cells. Additionally, the need to minimize thermal mass on the cryo stage as well as the geometric limitations of the stage do not allow us to perform cross-sectioning normal to the battery surface. To do so would require a pre-tilt of at least 50 degrees on this prototype tool. The footprint of such a pretilt 2032-coin cell holder is prohibitive due to collision with the plasma FIB pole piece, so a design choice was made to create a coin cell holder at -26 degree pretilt, which can be seen schematically in Figure 13.1. This allows the coin cell to be accessed as close to normal as possible, while also allowing for access near the center of the coin cell.

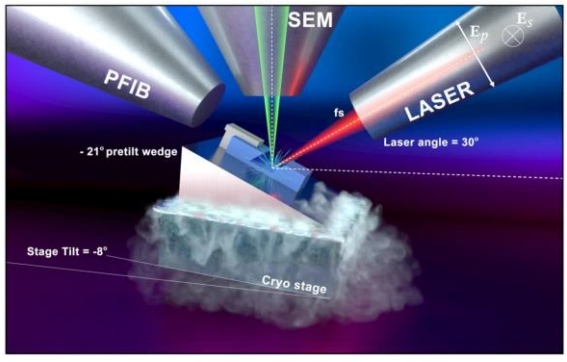

Figure 13.1. Schematic of the Helios laser plasma focused ion beam equipped with a cryo-stage and pretilt sample holder.

Despite design limitations, high quality cross-sections were obtained on coin cells. An example is shown in Figure 13.2. Figure 13.2a contains an overview of the cross-section with a ~ 1 x 0.9 x 0.7 mm region in a coin cell battery removed with UPL ablation. The multiphase ROI is marked with a red box in Figure 13.2a and contains a stainless steel casing, Cu current collectors, electrolyte and solid electrolyte interphase (SEI), a polymer separator, and Li metal. Each component is distinguishable in the higher magnification, polished cross-section shown in Figure 13.2b. False color was applied to the image to illustrate each material in the stack. Based on energy dispersive x-ray spectroscopy and the image contrast from the laser-induced texturing (which will be discussed later), deposits of Li metal can be identified in the top electrolyte + SEI layer.

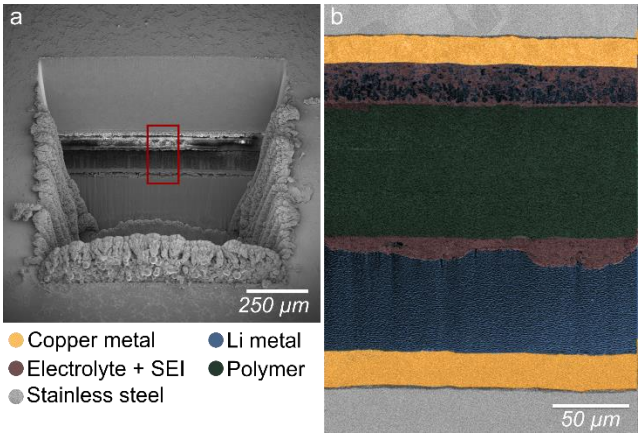

Figure 13.2. a) Overview of a cross-section Cryo-SEM SE image collected at 5kV, 0.69 nA of a ~ 1 x 0.9 x 0.7 mm region in a coin cell battery removed with UPL ablation where the ROI is marked with a red box. b) higher magnification Cryo-BSE image of the ROI collected at 2kV, 0.69 nA.

These high-quality cross sections were obtained in ~10-20 minutes of UPL ablation by using several polishing steps, similar to Ga-ion FIB. First, a coarse cut or bulk mill was used to remove the material of the targeted volume. To reduce time, the longer wavelength (1030nm), higher repetition rates (15kHz), higher pulse energy (60uJ), larger pitch, and

patterning in coarse mode was used. Next, an intermediate polish similar to standard Ga-ion cross sectioning was done to remove the redeposited material from the face of the cross-section and to move further into the sample to remove redeposition from the coarse cut. Smaller pattern dimensions in the y-direction, smaller pitch, and a lower repetition rate (6kHz) in fine patterning mode were used for this intermediate polish. Finally, the fine polishing step usually involved some experimental work due to the varied nature and morphology of the batteries being analyzed. Lower repetition rates and pulse energy were more favorable for most of the components in the stack, such as the polymer separator materials, to reduce the likelihood of damage and heat generation from parameters that result in higher average power (which can be outside of the athermal ablation regime).

The best known method for all steps also includes adjusting the focus of the laser to sub-surface in order to optimize cut quality and reduce time spent polishing areas outside of the ROI. The ability to change the position of the objective lens (which can be viewed as the laser 'pole piece' for comparison) is unique to the laser system, as there is no FIB equivalent. Rather than focusing at the surface on the stainless steel, the objective lens was moved in towards the sample, focusing just above the top of the battery stack layers or ROI. This allows for a significant reduction in time spent on the polishing, because it is not necessary to polish the entire 250 μm stainless steel casing. By reducing the volume that needs to be fine polished and by milling multiphase materials with a reduced ablation threshold, lower repetition rates, pulse energy, and pitch were used without increasing the polishing time. Additionally, the quality of the cut face can be improved in some cases by changing the angle of incidence of the laser using stage tilt, similar to performing an under or over-cut in a

traditional Ga-ion FIB. The current best known method involves using a stage tilt of -5 degrees (total tilt of -31 degrees including pre-tilted holder) for the coarse cut, -6 degrees (total tilt of -32 degrees) for the intermediate polish, and -8 degrees (total tilt of -34 degrees) for the final fine polish. This allows for reduced redeposition onto the ROI. These steps and conditions are generally applicable to all of the coin cell batteries in this study, however, laser ablation parameters could easily be changed based on needs. For example, patterning time could be further reduced by sacrificing cut-face quality, or increased to improve quality by changing parameters such as pitch.

13.3.2. Large Multiphase Volumes

When considering complex multiphase materials systems such as the coin cells discussed here, especially after cycling the battery creates more heterogeneity [ref ACS Energy Lett pub], it is beneficial to not only analyze representative areas but also volumes. High quality automated slice-and-view data can be collected and reconstructed to obtain a 3D dataset by removing material with the laser and imaging with the SEM. Laser slice-and-view can be done by moving the beam or stage positions by the desired slice thickness. As mentioned previously, more advanced automated workflows that include additional steps such as EDS/EBSD are possible in the TriBeam, but not possible with this prototype tool configuration given the limitations from the cryo-stage.

Laser slice-and-view was collected on a coin cell by moving the stage by the desired slice thickness of 2.5 μm. BSE images were collected at each slice, which were cropped from a 500 μm field of view to 316 μm due to redeposition filling in at the edges of the sliced field of view. Preparing a post where material is removed from both sides of the ROI would

eliminate redeposition filling in, however was not done for this sample. Images were aligned referring to the Cu current collectors and polymer separator, then reconstructed with Avizo software. The total reconstructed volume was 316x281x152 μm. The laser slice-and-view workflow is shown in Figure 13.3, which illustrates the ROI, followed by a stack of images, reconstructed volume from aligned images, and finally segmented reconstruction for Cu, Li metal, and the polymer separator.

The volume reconstruction allows for morphological understanding through the volume while retaining nanoscale resolution for each material in the multiphase stack. For example, the uniformity of the Cu current collectors can be determined from the segmentation. In this case, roughness and thickness variation in the Cu current collector was qualitatively observed. In addition, the top and bottom Li morphology can be studied, where in this case pits on the bottom correspond to regions on the top where Li grains are protruding, which is not obvious when only looking at a single frame of the cross sectional area.

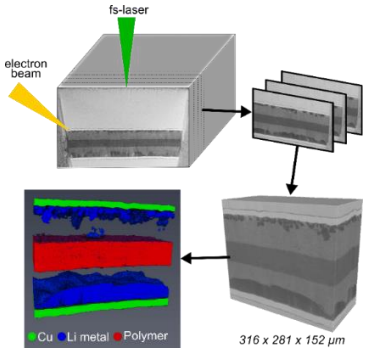

Figure 13.3. Schematic and results for automated laser slice-and-view collection in a coin cell. From top left: illustration of region for slice-and-view with dashed lines indicating various slices, followed by illustration of aligned slices cropped to the ROI. Bottom right showing the reconstructed 316 x 281 x 152 μm volume, bottom left showing segmented Cu (green), Li metal (blue), and polymer (red) from the volume.

13.3.3. Laser Cross-Sectional Surface Polishing

In addition to polishing methods discussed previously, the wavelength and polarization of the laser influences the surface of the cross-section. The ability to select the wavelength and polarization used for ablation in this system is not only beneficial for tuning the time and parameter space available, but can be beneficial for the quality of the cross-section. In some sense, selecting the wavelength and/or polarization is like selecting the ion species in a FIB, as one wavelength may be more beneficial for particular materials or applications. The influence on quality of the cut face stems from a phenomenon that occurs with UPL ablation, the generation of laser induced periodic surface structures (LIPSS) or aperiodic laser texturing. LIPSS generally appear as ripple-like features on a UPL ablated surface, and can appear on most classes of materials but are usually more obvious on metals and semiconductors. LIPSS are classified based on the period (Λ) of the structures into low-spatial frequency LIPSS (LSFL) and high-spatial frequency LIPSS (HSFL). LSFL are usually perpendicular to the incident laser polarization and have a pattern periodicity approximately equal to the laser wavelength. HSFL can be aligned perpendicular or parallel to the incident laser have a pattern periodicity significantly less than the laser wavelength. LIPSS are important artifact to consider when using this method because some features of interest are smaller than the spatial periodicity of the LIPSS texture which means that those features could be masked by LIPSS. However, LIPSS can be useful when identifying materials, particularly those that are embedded within materials which do not contain LIPSS.

13.3.3.1. Laser Wavelength

A polished region of a battery using 515 nm UPL is shown on the left in Figure 13.4a. LIPPS (LSFL) were primarily observed on the stainless steel, Cu current collectors, and Li metal were primarily observed on the coin cells using this method, with an average spatial of ~ 400 nm. Texturing is also evident on the polymer separator materials and SEI/electrolyte, but is generally aperiodic. Figure 13.4b shows the same region polished with 1030 nm, where the LIPSS are more prominent on the Li metal and Cu, with a spatial periodicity of ~ 1 μm. Given that the interface between the SEI and Li metal is significantly clearer using 515 nm to polish, this wavelength was generally used for the final polishing in order to obtain a cut face that appears smoother, and to better resolve these smaller features. While the period of LIPSS for 1030 nm is larger, this wavelength can access higher pulse energy and average power, which is advantageous for reducing the milling time. Additionally, higher pulse energy is helpful for removing hard to mill materials, such as the stainless steel casing in the battery stacks. A brief PFIB polish at glancing angles can be used to remove LIPSS to further resolve small features[13] and will be discussed later. It is important to have the ability to rapidly change the laser wavelength from 1030 nm to the second-harmonic 515 nm for access to various parameters and change in LIPSS.

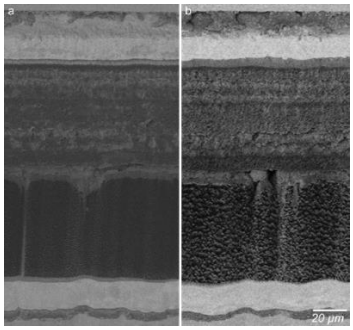

Figure 13.4. Cryo-SEM BSE images of an uncycled (pristine) coin cell battery ablated with 515 nm (a) and 1030 nm (b).

13.3.3.2. Laser Polarization

Multiple beam paths and waveplates which are integrated into software allow for the instantaneous change in polarization of the laser. The polarization also varies the orientation of LIPSS, as well as the cut face angle (the result of which is a function of the material's reflectivity for a given polarization). As mentioned previously, LIPSS are typically perpendicular to the polarization of the laser. The generation and appearance of LIPSS is not yet fully understood, particularly when working in this geometry.

Figure 13.5 shows comparisons of polarization in high magnification regions of coin cells. Figure 13.5a contains a region which was polished with p-polarized light (515 nm). The Li metal has LSFL that appear as ripples that are perpendicular to the polarization. Unlike the Li metal, LiH deposits that are present have HSFL that appear as ripples perpendicular to the polarization. The SEI/electrolyte does not have apparent LIPPS, although the general texture is varied. Figure 13.5b shows the same region in 6a, but polished with s-polarized light (515 nm). In this case, the Li metal does not have ripples but does have surface structures that are generally vertical. The LiH deposit has HSFL that appear as vertical ripples. Similar to the p-polarized light, the SEI/electrolyte do not have LIPSS. Figures 13.5c and 13.5d show a region with Li metal, SEI/electrolyte, and polymer separator from a different coin cell than shown in 6a and 6b. In 6c, p-polarized light (1030 nm) was used to polish the surface and LSFL can be seen on the Li metal. In 5d, circularly polarized light (1030 nm) was used to polish the same region. LSFL with ripples that are diagonal can be seem on the Li metal. Slight variations in texture to the SEI/electrolyte and polymer separator are visible when compared to 6c.

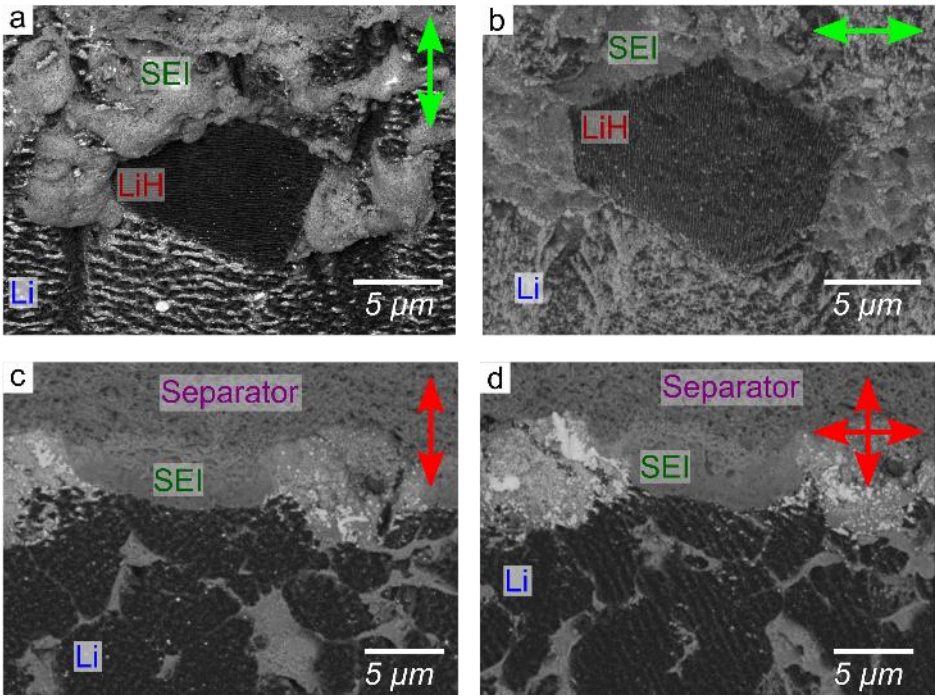

Figure 13.5: Cryo-SEM BSE images of a coin cell battery. a) region with Li metal, SEI/electrolyte, and LiH deposits polished with p-polarization (515nm) and b) polished with s-polarization (515 nm). c) region with Li metal, SEI/electrolyte, and polymer separator polished with p-polarization (1030 nm) and d) polished with circular polarization (1030 nm).

The appearance of LIPSS allows for the ability to identify different materials based on presence and periodicity. For example, LIPSS made Li metal domains and LiH deposits readily apparent and distinguishable from one another due to the difference in periodicity. Even when embedded in SEI/electrolyte, ripples on Li metal makes the Li domains easily identifiable, serving as an alternative contrast mechanism. Small Li metal deposits in SEI/electrolyte are shown in Figure 13.6. The LIPSS on the Li metal in a sample polished with 515 nm make the Li obvious and identifiable amongst voids and other texture on the SEI/electrolyte. The region in the right in Figure 13.6 shows the highlighted region from the left, where Li deposits were highlighted with blue.

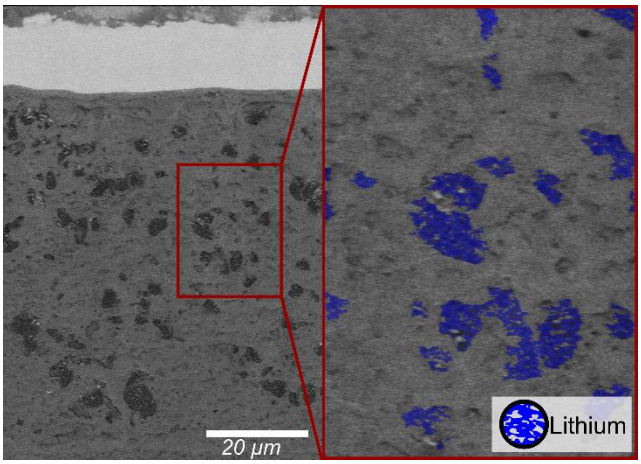

Figure 13.6: Cryo-SEM BSE images of a coin cell battery with Li metal deposits in SEI/electrolyte. The region highlighted in red on the right image is shown on the left. Li metal deposits are highlighted with blue on the right.

13.3.4. Plasma FIB Cross-Sectional Surface Polishing

After accessing large areas with the UPL, regions of interest or specific interfaces can be polished using the Xe^+ Plasma-FIB. This method could also be applied to finding regions to target for cryo-liftout and TEM preparation, but is not possible in the prototype system. Due to cryo stage limitations, it was not possible to rotate and tilt to glancing angles to polish with the PFIB without venting and manually rotating the sample. This is a cumbersome process and is alleviated using modern cryo-stages with rotation capability. However, to illustrate the value of additional PFIB polishing we have included the results from this manual rotation process after which the PFIB was used to remove the resulting ice formation and to further polish the laser cut face.

Figure 13.7a and 13.7b contain a region which was polished with the laser. The region in Figure 13.7b is a higher magnification image from the region in the red box marked

in 13.7a. This cross-section was obtained in coin cell where failure occurred in the polymer separator, similar to that discussed in (ref to Energy Letters). Due to this failure and Li metal morphology observed in the laser cut region, this area was polished with PFIB, which is shown in 8c and 8d. Figure 13.7d contains a higher magnification image of the region marked with a red box in 13.7c. All LIPSS were removed from the surface, which revealed small Li metal domains that were not evident in the laser cut area. In addition, features and Li domains in the SEI/electrolyte which were not observed in the laser cut area are prominent in the PFIB polished region, which is particularly evident in 8d.

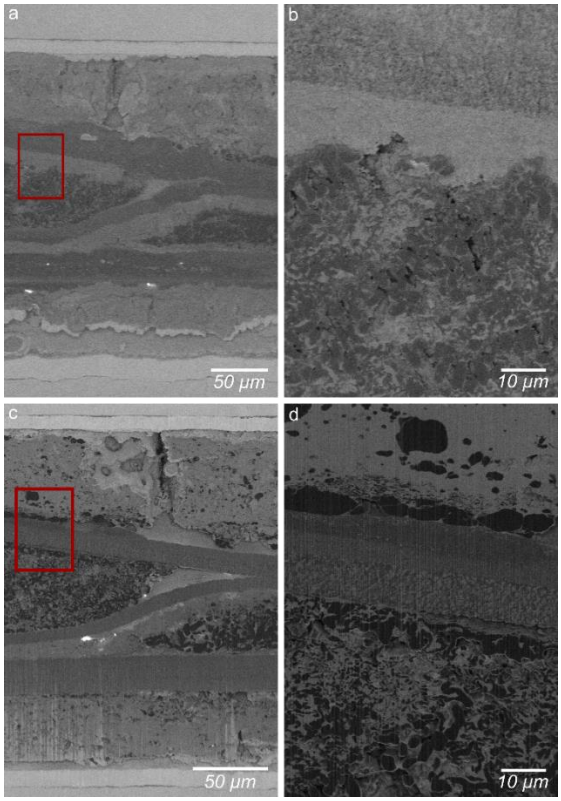

Figure 13.7: Cryo-SEM BSE images of a coin cell battery with Li metal deposits in SEI/electrolyte. The region highlighted in red on the right image is shown on the left. Li metal deposits are highlighted with blue on the right.

13.4. CONCLUSION

We have successfully developed a method for large area and volume analysis of complex multiphase materials systems using UPL combined with SEM/PFIB. This work demonstrated the benefits/drawbacks of a wide variety of laser parameters and their impacts on different classes of materials. Similar methodology could be applied to a wide variety of use cases such as beam sensitive materials, hard metals, and composites, where operating under cryogenic conditions may or may not be necessary. Critical nanoscale features were resolved by using the PFIB to polish laser-cut surfaces, which would not be accessible with PFIB alone. There are accessible improvements that can be made to this methodology which would allow for more advanced analysis and better resolution. On non-prototype systems, cryo-stage limitations with respect to rotation and tilt should be alleviated, which would allow for rotation and tilt for polishing with the PFIB and cross-sections which are closer to vertical. With fewer limitations on stage rotation and tilt, it would be possible to use the UPL/PFIB to target a specific ROI with cryo-PFIB liftout for cryo-TEM analysis. Additionally, integration of Energy Dispersive X-ray Spectroscopy to 3D slice and view routines is possible, which would allow for 3D chemical mapping.

13.5. BRIDGE

The fourth section of this dissertation which includes this chapter and the next discuss methods and analysis of intact coin cell batteries containing multiphase materials with a new characterization technique. This method combines cryogenic ultrafast pulsed laser ablation with SEM/PFIB. This chapter discusses the method in detail which involves several steps to obtaining high quality cross-sections on a millimeter length scale which can resolve nanoscale features. The impacts, benefits, and drawbacks of laser parameters such as

wavelength, and polarization were discussed. Laser slice and view was used to obtain 3D data through a coin cell, and slice and view data was reconstructed. Li-metal, polymer separator, and Cu current collectors were segmented to investigate the interfaces and morphologies through a volume. PFIB was used to remove laser surface texturing, allowing small scale features to be resolved. These methods could be applied to materials, multiphase systems, or samples with buried regions of interest not accessible or practical using other methods. The next chapter discusses the observation of electroplated Li-metal morphology and the accompanying solid electrolyte interphase (SEI) into and through the intact coin cell battery's separator, gradually opening pathways for soft-short circuits that cause failure. We found that separator penetration by the SEI guided the growth of Li dendrites through the cell. A short-circuit mechanism via SEI growth at high current density within the separator is provided. These results will inform future efforts for separator and electrolyte design for Li-metal anodes.

CHAPTER XIV

CRYOGENIC LASER ABLATION REVEALS SHORT-CIRCUIT MECHANISM IN LITHIUM METAL BATTERIES

14.0. AUTHORSHIP STATEMENT

Chapter XIV was published in *ACS Energy Letters* in 2021. Katherine Jungjohann is the primary author of the manuscript. Co-authors Subrahmanyam Goriparti, Laura C. Merrill, Kevin R. Zavadil, Stephen J. Harris, and Katharine L. Harrison prepared half-cell Li metal batteries and collected/analyzed electrochemical data. Steven J. Randolph assisted with cryogenic laser ablation/SEM. David Johnson is my advisor and edited the manuscript. I assisted with writing/editing the manuscript and collecting/analyzing cryogenic laser ablation/SEM data.

14.1. MAIN TEXT

The demand for more energy-dense lithium-ion (Li-ion) batteries[1,2] is so intense that even small improvements are the subject of considerable research efforts. Replacing the graphite anode with a Li-metal anode results in an impressive 50% improvement in energy density;[3] however, Li-anode prototypes cycled at high energy density have consistently failed at low cycle numbers. The failure mechanisms are a matter of rigorous debate. The common theory postulates that ultimately failure lies with poorly controlled, electroplated Li-metal morphology, in the form of Li dendrites that can grow through the nanoscale tortuous pathway of the polymer separator.[4-7] However, the Monroe-Newman model, that neglects solid electrolyte interphase (SEI) properties, suggests that even large (>1 μm in diameter) dendrite formations cannot penetrate through the submicrometer diameter pores of the

separator,[8] and recent cryogenic electron microscopy images have demonstrated that Li dendrites with submicrometer diameters are effectively deflected by the separator.[9] Therefore, the mechanism of how short circuits develop remains in question: if Li metal does not have the mechanical integrity to puncture through the porous separator, what is the pathway by which Li bridges the two electrodes through the separator?[10]

Alternatively, Li-anode failure has been attributed to the poor Li-ion transport properties of the SEI, a passivation film composed of organic and inorganic Li-containing species that forms during cell cycling.[4,11] The growth and propagation of SEI remains unclear because of the extreme difficulty of achieving unaltered, nanoscale characterization of the solid-liquid, air-sensitive, electrode-electrolyte interfaces. For example, microcomputed tomography (microCT) can acquire nondestructive structural images of the complete battery stack,[12,13] but only at ~700 nm resolution, and it cannot provide compositional mapping. In contrast, cryo-focused ion beam (FIB) preparation for cryo-scanning transmission electron microscopy provides nanoscale structural and compositional mapping,[14] but it can characterize sections only <50 μm^2 and the interfaces of interest must be severed during sample preparation, preventing representative and unperturbed imaging.

In this work, we demonstrate that high current densities cause soft shorts (parasitic electronic bridges in the cell), creating SEI inclusions within the separator that mechanically tear the separator and form open networks for Li-metal plating between the opposing electrodes. While Li metal is soft and should not be able to penetrate a separator, SEI capping and envelopment of the electroplated Li metal appears to aid in separator tearing.

We have discovered this mechanism through the first implementation of a structural/compositional characterization method that captures nanoscale interactions between the different battery layers over representative cross sections, all without disassembling the battery stack along interfacial boundaries. Because our goal was to understand the interaction between the Li-metal anode and the separator (particularly at high rates that commonly lead to short circuits), we constructed half cells of 2032 coin cell batteries, each containing a 50 μm thick layer of Li-metal on a copper (Cu) foil counter electrode, with a 9 μm thick Cu current collector as the working electrode. The electrodes were stacked on either side of a pair of 25 μm thick trilayer Celgard 2325 separators for increased tortuosity; each separator had two polypropylene layers that sandwiched a central polyethylene layer.[15] Cells were cycled at a high rate of 1.88 mA/cm^2 to a capacity of 1.88 mAh/cm^2, so that we could observe changes in the Li metal/separator interfaces as a function of cycle number.

We characterized representative area (0.5 mm^2) samples from intact coin cells using a Helios laser plasma focused ion beam (Laser PFIB) system (Thermo Fisher Scientific, Figures H.1- H.3) to spatially map the Li-metal, polymer separator, volatile electrolyte [~2.8 M lithium bis(fluorosulfonyl)imide in 1,2-dimethoxyethane],[16] and SEI layers. Sectioning was achieved using the athermal ultrashort pulse laser (UPL, removal rates >15 000× compared to a conventional Ga FIB) on the Laser PFIB tool.[17] This significant enhancement in material removal rates with the UPL was crucial to enabling cross-sectioning through the coin cell casing (250 μm of stainless steel). To maintain the layers of the battery stack and volatile electrolyte in a solid state, the coin cell was placed in a custom, pretilted aluminum

battery mount; the coin cell- mount assembly was frozen in liquid nitrogen, and the sample's temperature was controlled using a cryo-stage (<-100 °C, Figure H.4).[18] Because of the angle between the mount and laser optical axis (Table S1), the SEM images are at the perspective of a 59°-angled section (Figure H.5), and because the coin cell samples are flooded with excess electrolyte, varying quantities of electrolyte are visible between the top Cu and stainless-steel layers (Figure 14.1a,c). In Figure 14.11, the coin cell components are observed in the SEM images (Figures H.6-H.11; replicates of failure Figures H.13- H.17), where false color has been superimposed to reflect the energy dispersive X-ray spectroscopy (EDS) maps (Figures H.18- H.23).

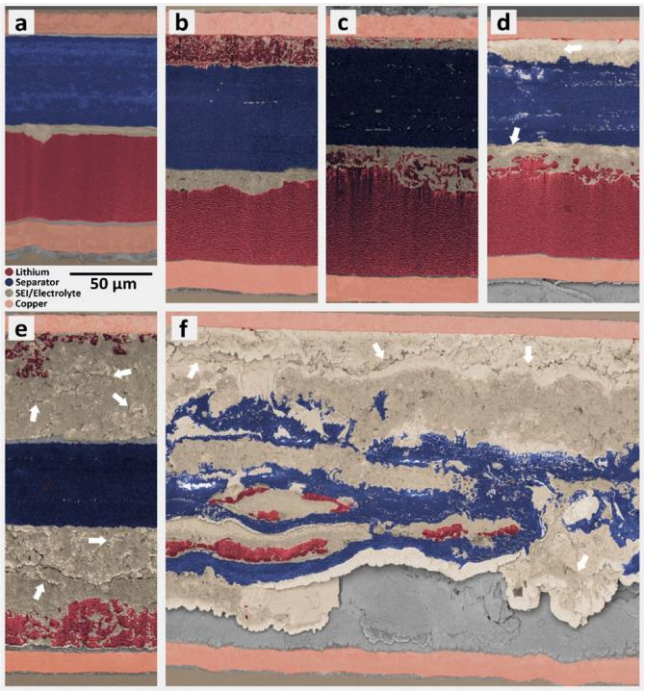

Figure 14.1. Scanning electron micrographs of intact angled-sections of high-rate cycled Li-metal half cells. (a) Uncycled cell, including: stainless-steel cap, Cu current collector, stack of two Celgard 2325 separators, Li metal, bottom Cu current collector, and lower stainless- steel disc, (b) 1st Li plating, (c) 1st Li stripping, (d) 11th plating, (e) 51st plating, and (f) 101st plating step. White arrows indicate cracks in the SEI matrix and gray regions indicate structures out-of-plane from the cut face.

We observed a consistent increase in distance between the top and bottom Cu foils with increased cycling, as the mossy Li deposits and SEI grows with each plating and stripping step (Table H.2). The correlation between cycling and SEI growth is a known phenomenon,[19] but the SEI's distribution and the extent of the growth were previously unquantifiable because ex situ measurements required the buried electrode/separator interfaces to be dismantled.

Our results show that copious SEI growth occurs over relatively few cycles at high-rate cycling. Even the first Li plating cycle (Figure 14.1b) shows that a fraction of the dark Li layer has moved across the separator and deposited on the Cu current collector at the top. A fully dense Li film should be only 9 μm thick, so the newly deposited 16 μm thick Li film must be either porous (filled in with electrolyte) and/or composed of both Li and SEI. Notably, small SEI deposits can already be observed within the separator, presumably resulting from conductive pathways (unresolved in these SEM images) that allowed small Li deposits to plate and react with electrolyte, forming these SEI inclusions.[20]

The first Li stripping cycle (Figure 14.1c) shows that after the Li is driven from the top Cu electrode, roughly 7 μm of SEI/ electrolyte/dead-Li-residue remains, filling the region between the top Cu electrode and the separator. More pronounced SEI deposits are seen in the separator. Below the separator, Li plates on top of the fully dense Li-metal surface as a low-density matrix, coated in SEI and filled with electrolyte. By the 11th Li plating cycle (Figure 14.1d), there are small Li deposits on the top Cu electrode, and the far denser SEI matrix now causes deformation of the separator. Inclusions of large SEI deposits appear within the separator (on the scale of several micrometers), above an increasingly thick

SEI layer and the roughened surface of the fully dense Li-metal layer. At the 51st Li-plating cycle (Figure 14.1e), the plated Li on the top Cu electrode again forms a low-density matrix of Li grains mixed with an extremely dense SEI matrix, which comprises most of the gap between the top Cu electrode and the separator. Interestingly, the separator retains its margins and structure, with only a few SEI inclusions. Below the separator, the electrolyte-filled SEI film is now much thicker than the fully dense Li-metal layer, which is being converted into a coarse SEI-filled network. At this point, there is clear evidence that copious SEI has formed by consuming large amounts of bulk active Li and electrolyte, with small embedded fragments of dead Li encased in the SEI.[20] Catastrophic cell failure is seen in the 101st plating cycle (Figure 14.1f), where the separator is completely shredded by SEI and large Li-metal deposits can be seen within the separator's interior boundaries. These images repudiate the long-held assumption that a single Li dendrite spans the cell and creates a hard short; instead, these images indicate that the primary failure mechanisms are widespread SEI inclusions and separator shredding.

Our electrochemical data validates the structural/chemical maps, suggesting that the soft shorts formed during cycling caused the growth of SEI inclusions within the separator. As expected, the disintegration of the coin cell's internal structures coincided with the battery's obvious electrochemical failure, which we analyzed using chronopotentiometric data generated from cycling prior to Laser PFIB characterization (Figure H.24, and replicates in Figures H.26- H.40). In the high rate cycled cells, the Coulombic efficiency measurements often exceed 100% and are likely indicative of soft short formation (Figure 14.2a,b). While random error or dead Li (stranding and reconnecting) could explain some of the variation

shown above and below 100% Coulombic efficiency, the fact that the cumulative stripped capacity exceeds the cumulative plated capacity until cycle 46 strongly suggests that some of the charge passed is due to soft shorts. In the separator, widespread SEI inclusions indicate conductive paths (likely composed of small Li-metal fragments weakly connected in the SEI matrix),[20] which allow electron transport into the separator and enable the soft shorts.

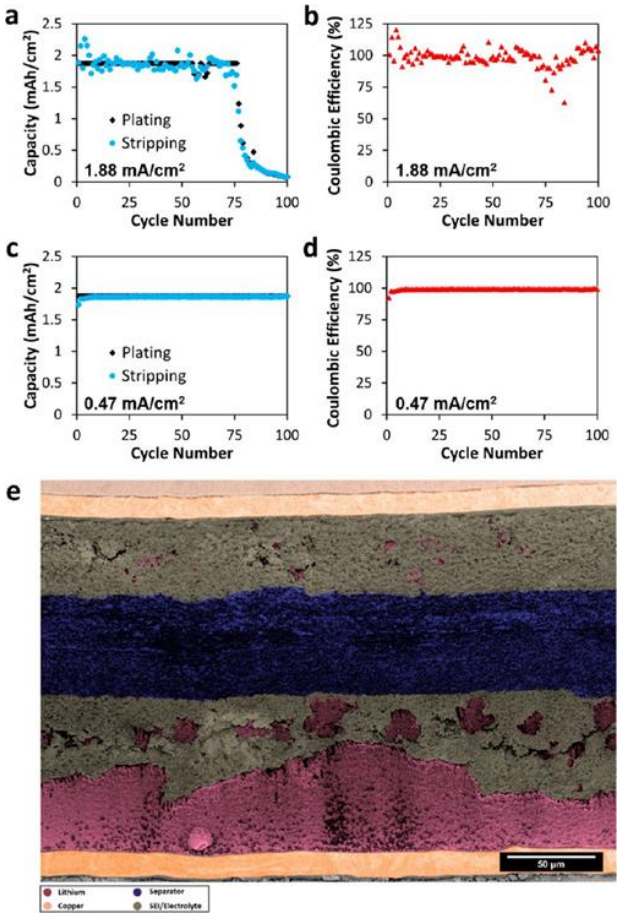

Figure 14.2. Electrochemical performance of the 101st Li plating sample. (a) Capacity of the plating and stripping cycles, for Li plating at a high rate of 1.88 mA/cm2 up to the 101st plating step. (b) Coulombic efficiency of each full cycle, exhibiting the battery's ability to efficiently recapture Li, even after the quantity of plated Li significantly decreases at ~75 cycles. Capacity (c) and Coulombic efficiency (d) of the plating and stripping cycles at a low rate of 0.47 mA/cm2 to a capacity of 1.88 mAh/cm2. (e) Scanning electron micrograph of an intact angled-section of the 101st Li plating low-rate cycled half-cell. The brown layer at the top of the image is the stainless-steel cap, and the gray contrast indicates structures out-of-plane from the cut face.

A few cycles before the cell failed, the Coulombic efficiency dropped, likely indicating the cell's impending inability to plate to the specified capacity. However, after the cell began to fail, the Coulombic efficiency briefly recovered, which suggests that the loss in capacity is fundamentally decoupled from the loss in Coulombic efficiency. It should be noted that when the cell was unable to plate to the specified capacity, because of depletion of the accessible Li inventory (dead Li or blocked Litransport pathways), the remaining Li inventory could still be efficiently cycled. This cell failed because of inaccessible or depleted Li inventory rather than from a hard short circuit caused by a dendrite.

Because most studies concentrate on low-rate cycling, the experiment was reproduced at 25% of the high-rate cycling to determine whether the same failure mechanisms pertained. Results (Figure 14.2c,d) demonstrate very steady capacity and Coulombic efficiency (>99%), even at high cycle numbers. At this lower current density, battery performance was very repeatable from cell to cell and showed no signs of failure (Figure H.25, and replicates in Figures H.41- H.43), which is consistent with the literature.[16] Furthermore, there appears to be a correlation between the observation of SEI and Li inclusions in the separator and the electrochemical data showing higher-than-expected stripping capacity, which we attribute to soft short formation. At the low-rate cycling, there was no significant oscillation around 100% Coulombic efficiency and the cumulative stripped capacity was always lower than the cumulative plated capacity. The SEM image (Figure H.12) shows no evidence of SEI or Li inclusions in the separator at low-rate cycling (Figure 14.2e), which is consistent with the electrochemical data. Additionally, important

differences between the high- and low-rate cycled 101st Li plating step coin cells can be seen in the separator structure, SEI thickness, plated Li-metal morphology, and the remaining counter-electrode Li thickness. Difference in the Li metal morphology may explain why less Li metal was consumed during the low-rate cycling. Visible cracks and crevices in the SEI may also indicate localized electrolyte consumption, which would reduce Li-ion transfer pathways during high-rate cycling.

Recent findings suggest that Coulombic efficiency is much more closely correlated to the quantity of inactive Li isolated from the current collector by SEI formation than to the amount of SEI formation.[20] This experiment validates that assumption because an abundant amount of SEI formed in the high-rate cycled cells within just a few cycles, yet the depleted Li inventory did not cause an immediate drop in the very high Coulombic efficiency. The prevailing literature almost always attributes high-rate Li-metal anode cell failure to the formation of a single Li dendrite[21] that punches through separator pores in the battery stack.[22,23] However, our electrochemical data and cross-sectional images clearly demonstrate that the SEI forms inclusions within the separator, which gradually destroy the separator and create pathways for Li metal to plate within the separator.

Small SEI deposits protruding into the separator between the separator's polypropylene and polyethylene trilayers (Figure 14.3a, b) and small internal SEI inclusions (Figure 14.3c-f) can cause dramatic horizontal tearing along the trilayer interfaces (Figure 14.3g), creating compromised intertrilayer separator interfaces. This phenomenon demonstrates inadequate adhesion between the trilayers[24] and/or softening of the separator upon electrolyte saturation.[25] Large SEI inclusions also formed along the separator's top and

bottom surfaces, punching vertically through the trilayers (Figure 14.3e), which resulted in further horizontal tearing. Because SEI formation can occur only with electrons at the required reduction potential, conductive paths (masked by SEI or too small to resolve in the SEM images) must be laced through the separator, providing all the components necessary to form SEI within the separator's trilayer structure (optical image in Figure H.44).

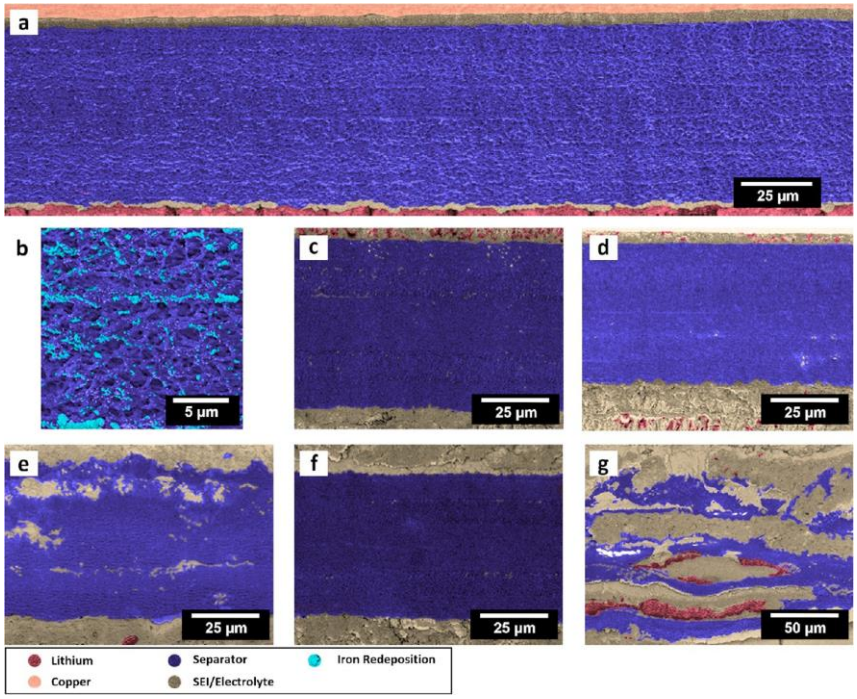

Figure 14.3. Scanning electron micrographs of high-rate cycled angled-sections showing failure within two stacked Celgard 2325 separators. (a) Uncycled cell and (b) higher-magnification image of the separator porosity (with the lighter contrast indicating iron redeposition from laser ablation), (c) 1st Li plating, (d) 1st Li stripping, (e) 11th plating, (f) 51st plating, and (g) 101st plating step.

Under high-rate conditions, SEI formation in the separator can typically be observed very early in the Li-cycling process. Figure 14.f (51st plating) shows few SEI inclusions compared to Figure 14.3e (11th plating), which demonstrates the stochastic nature of these processes, both within and among identically fabricated coin cells. However, while cell-to-cell variation

was observed, many duplicate cells failed catastrophically between 75 and 100 cycles (Figures H.13- H.17 and H.26- H.40). Complete destruction of the trilayer separator before the 101st lithiation was evident in Figure 14.3g, clearly demonstrating that, for high-rate cycled Li-metal anodes, the trilayer separator was not mechanically sufficient to withstand SEI evolution.

Our full-stack nanoscale characterization points to a failure mechanism which had not been previously considered in theoretical modeling:[26] the SEI's mechanical properties create pathways that allow soft Li metal to penetrate into and tear the separator, with Li-metal plating providing the force for penetration (Figure 14.4).

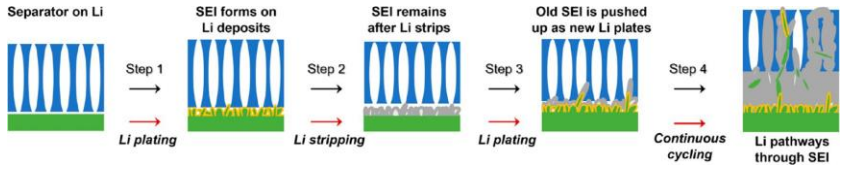

Figure 14.4. Schematic short-circuit mechanism for conductive Li pathways through the polymeric separator via SEI formation and subsequent deformation of the separator. SEI formed during the current plating step is colored yellow; SEI that formed in a prior step is colored gray.

We believe that the extensive SEI formation is itself a product of the conductive pathways that form between the small Li-metal fragments embedded within the SEI. During the first plating step, some high-aspect ratio Li grains deposit and grow with a capping SEI film. We believe it is possible that the hard, sharp SEI tips can bore into the separator's small pores and even puncture the separator (results from carbonate electrolyte in Figures H.45 and H.46 and alternative separator in Figures H.47- H.55). Once there is a complete conductive pathway through the separator, the cell-scale electronic bridge causes numerous soft shorts.

More mechanically robust separators may mitigate this failure mode; however, uncontrolled SEI growth may still cause electrolyte redistribution and Li-ion transport blocking.

In summary, our structural images and elemental maps, paired with our electrochemical data, definitively indicate that degradation of the Li cycling performance is prompted by the destruction of ion-transport pathways between the stacked electrodes and consumption of Li metal by excessive SEI formation. Cycling causes the formation of small SEI inclusions with small Li-metal grains, creating delicate conductive pathways that form within the separator. These pathways cause numerous soft shorts, which then accelerate SEI formation causing physical disfigurement (and subsequently destroy) the separator's functionality. Although Li dendrites do not have the toughness to pierce the separator, the SEI can carve routes through the separator, opening pathways for more soft shorts by plating Li along those pathways. To prevent this from happening, future research must focus on minimizing SEI formation and improving the integrity of the separator for high-rate cycling Li-metal batteries. Our new characterization approach allows for nanoscale structural/chemical mapping of intact battery stacks without destroying the interfaces between the solid/liquid/polymer composite stack, preventing air or water vapor exposure that would otherwise alter the sensitive battery stack materials.

14.2. EXPERIMENTAL METHODS

14.2.1 Coin Cells

2032-coin cells were fabricated with 16 mm diameter and 9 μm thick Cu current collectors as the working electrodes. The Cu was acid treated in 1.2 M hydrochloric acid for

10 min, washed with deionized water and acetone, dried, and then immediately transferred to an Ar-filled glovebox. The counter electrodes consisted of 16 mm diameter electrodes with 50 μm thick Li laminated to 10 μm thick Cu (Albemarle). Two layers of Celgard 2325 separators were placed between the two electrodes. The cells were flooded with 100 μL of ~2.8 M lithium bis(fluorosulfonyl)imide (LiFSI, Oakwood Chemicals) in 1,2 dimethoxyethane (DME, Sigma-Aldrich, anhydrous, 99.5%). The LiFSI salt was dried at 60 °C overnight in a heated antechamber connected to the glovebox. The DME was dried over activated alumina for at least 2 days before preparation of the electrolyte. The dry DME was extracted through a filter to remove any activated alumina; the DME and LiFSI were then mixed in a 2.4:1 molar ratio (DME:LiFSI) to make a ~ 2.8 M solution based on interpolation between previously documented electrolyte preparation procedures[16] The solution was stirred on a hot plate at 50 °C overnight. The cells were compressed with a precompressed wave spring and 1.8 mm total thickness of stainless steel spacers. The coin cells were allowed to rest for 24 h following fabrication before being tested on Biologic and Arbin battery cyclers. Coin cells were cycled at a current density of 1.88 or 0.47 mA/cm2 to a capacity of 1.88 mAh/cm2 during Li plating. A -1 V limit was programmed for plating, and stripping was allowed to continue until a voltage limit of 1 V was reached. A time limit was set to double the time required to strip the plated Li, so that if there was a short circuit, it would be easier to identify from higher-than-expected stripping capacity. Additional electrochemical data is presented in Figures H.24 and H.25 (with replicate cell data in Figures H.26- H.40 and H.41- H.43), detailing the voltage versus time curves for the cells imaged in Figure 1f

and Figure 2e, respectively, with corresponding capacity and Coulombic efficiency data shown in Figures 14.2a,b and 14.2c,d, respectively.

14.2.2 Cryogenic Helios Laser PFIB

The Helios system was equipped with a cryogenic cooling stage from Quorum (Quorum Technologies, Newhaven, U.K.). Inherent sample size, geometry, and motion limitations were imposed using the cryogenic cooling stage in conjunction with the laser. Therefore, it was necessary to develop some nonstandard cross-sectioning techniques to access maximum sample area on the batteries and to allow better line-of-sight to the EDS detector. The experimental process consisted of coating the battery anodes with insulating paint (nail polish) then mechanically clamping them to a grounded, aluminum wedge via a copper clip. The mounting wedge was cut into a pretilt at -21° to accommodate for the limited negative tilt (toward the laser) on this prototype tool. Because the laser delivery was oriented 30 degrees from horizontal, the net cut-face angle into the batteries' surface was 51°, plus any additional negative stage tilt that was applied by the stage (Figure H.4). The entire sample/stub was plunge frozen in liquid nitrogen for 15 min and then transferred in air to the precooled cryo-stage. Once the sample was mounted into the SEM chamber, immediate pumping to vacuum limited ice growth on the sample by the air. The precooled stage was kept at a temperature range between -100 °C and -120 °C during laser ablation and characterization. Within the Helios, the sample was brought to eucentric height and the stage was tilted to -8° for laser processing. Figure H.4 shows a schematic of this technique, which we call "oblique" cross-sectioning. Laser ablation followed a three-step procedure: (1) A large volume of material was removed using the 1030 nm laser at a large pulse energy and

spot size. (2) The protective coverslip was replaced to allow more transmittance to the sample for polishing. (3) The cut face was polished using the 515 nm beam at a lower pulse energy and reduced pulse repetition rate (details in Table S1).

14.2.3 Image Processing

To highlight the different battery components, the SEM images were cropped and imported into Adobe Photoshop. Color layers were added to the assembly of images, where individual layers were representative of the different coin cell components: stainless steel, copper, separator, SEI/electrolyte, and Li metal. The identification of each region to color was guided by energy-dispersive X-ray spectroscopy maps (Figures H.18- H.23). The contribution of iron redeposition was removed from all the images, except for Figure 14.3b, to minimize distraction from focus on the configuration between the Li metal, separator, and SEI/electrolyte. We acknowledge that the iron redeposition was mostly observed in the high-rate 51st and 101st plating images, as the iron redeposition could not be removed from cracks and crevices in the sample, which were caused by either factures in the SEI or gas evolution that resulted in a void during laser ablation.

CHAPTER XV

CONCLUSIONS AND FUTURE OUTLOOK

This dissertation began with an overview of the need for new characterization techniques and approaches in order to continue advancements in materials science. An introduction to the materials covered in this work was provided, which includes layered heterostructures, thin film compounds focusing on those that contain Pb, Fe, and Se, and multiphase materials systems used in battery components. These structures and interfaces General experimental methods used for materials synthesis and characterization throughout this work were discussed.

The second section (Chapters III – VII) covered the use of atomic resolution microscopy techniques to obtain insights into formation mechanisms and defects in various layered heterostructures prepared with Modulated Elemental Reactants (MER). The insight gained in these chapters has implications for the development of further precision and approaches to synthesizing materials with this and other solid-state methods. The ability to control and synthesize layered heterostructures with or without defects would provide a wide opportunity to explore emergent properties and drive implementation into devices.

The third section (Chapters VIII – XII) focused on understanding reaction pathways in compounds containing Pb, Fe, Se and included several with V and Mo. First, reaction pathways for various layer thicknesses and precursor structure were explored for binary Fe-Se and Pb-Se. The importance of the use of a wide variety of X-ray characterization methods and electron microscopy techniques was established throughout. This section demonstrated

how powerful these techniques can be when combined – further emphasizing their complementary nature. Together, the reaction pathways for these systems became clear. The most surprising results included asymmetric interfaces in Fe-Se that were observed using electron microscopy, which were not anticipated and could not be discovered with results from X-ray characterization alone. A method for quantifying energy dispersive X-ray spectroscopy (EDS) data in terms of atoms per unit volume as a function of distance in the sample was proposed, which could be used to model complex XRR patterns and better understand composition profiles and diffusion lengths in as-deposited precursors. The formation of PbSe upon deposition on amorphous substrates provided an avenue to avoid island growth, a feat which had not been overcome using most synthesis methods. While the synthesis of ternary Pb-Fe-Se compounds which are predicted to be stable was unsuccessful, a new PbSe (cubic) - $FeSe_2$ (hexagonal) compound was synthesized. When layering these three elements with V|Se layers, sampled rearranged to form PbSe with Fe-doped VSe_2. Intercalated and substituted Fe in VSe_2 was resolved using EDS line profiles, which were collapsed to one unit cell and fit to Guassians, which were used to find atomic plane positions which could be used as starting points for Rietveld refinement.

The last section discussed a new method for cryogenic ultrafast pulsed laser ablation (UPL) of intact Li-metal half-cell coin cell batteries in a Scanning Electron Microscope/Plasma-FIB. Large area and volumes were analyzed from cross-sections of intact cells for the first time. Studies of laser parameters on surface texturing and overall cross-section quality were investigated. Surface structures (ripples) were generated on Li-metal from UPL but not on solid electrolyte interphase and other components, which

allowed Li-metal domains apparent from SEM imaging alone. Failure mechanisms which would otherwise remain unknown were found from this work.

APPENDIX A

SUPPORTING INFORMATION FOR CHAPTER III

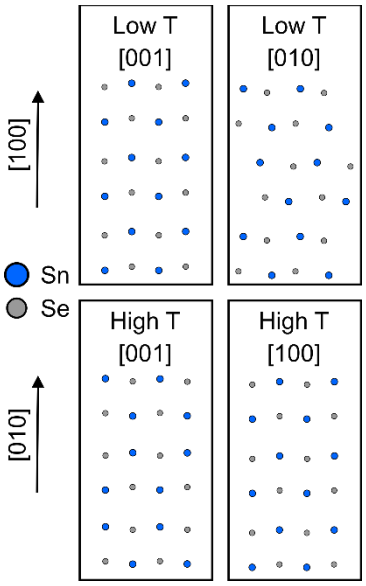

Figure A.1. Structure projections for low temperature (Low T) SnSe and high temperature (High T) SnSe for similar arrangements. In High T [001], note that the cations are stacked on top of each other.

APPENDIX B

SUPPORTING INFORMATION FOR CHAPTER IV

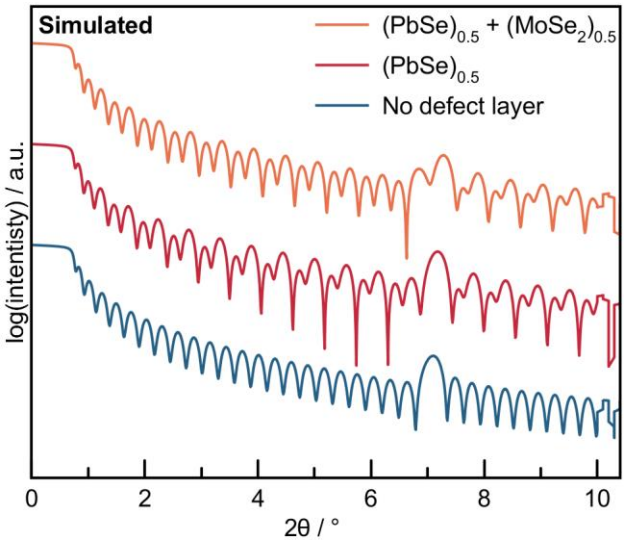

Figure B.1. Simulated X-ray reflectivity patterns for each sample. These simulations do not include any roughness and assume layer thicknesses and densities based on bulk parameters for PbSe and $MoSe_2$. Defect layers were inserted in the middle of the sample with thicknesses which were half of the c-lattice parameter (layer thickness) of PbSe and $MoSe_2$.

	XRR Total Thickness (nm)	**HAADF-STEM Thickness (nm)**	**c-lattice parameter (nm)**
No defect	28.8	29.6	1.257(1)
0.5 PbSe defect	29.4	30.1	1.257(2)
0.5 PbSe + 0.5 $MoSe_2$ defect	29.5	30.1	1.261(3)

Table B.1. Total film thickness measured by XRR and HAADF-STEM, and c-lattice parameters (repeat unit thickness) determined by XRD for each sample.

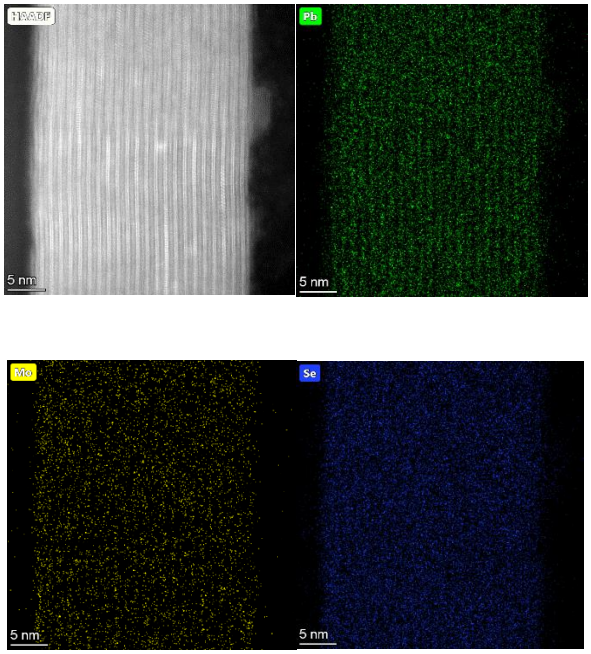

Figure B.2. HAADF-STEM image and corresponding energy dispersive x-ray spectroscopy data for each element across the entire film thickness. An island of PbSe is at the surface of the film, resulting from excess material in the precursor.

APPENDIX C

SUPPORTING INFORMATION FOR CHAPTER V

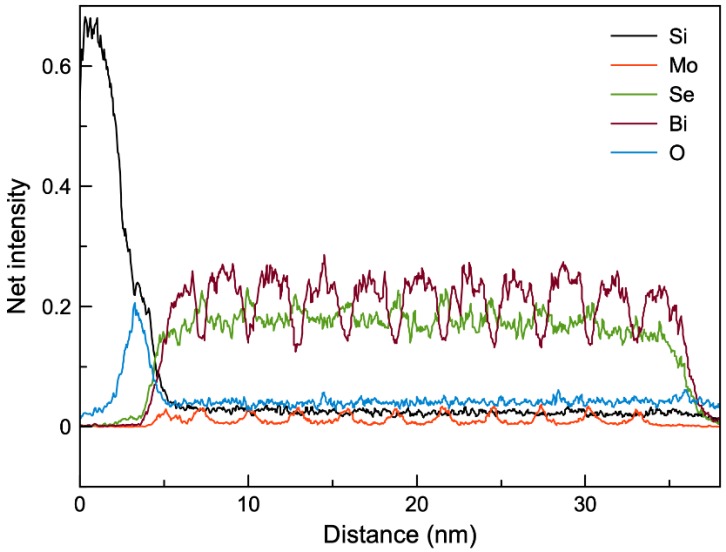

Figure C.1. Electron dispersive x-ray spectroscopy (EDS) line profile from substrate to surface of $(BiSe)_{0.97}(Bi_2Se_3)_{1.26}(BiSe)_{0.97}(MoSe_2)$.

APPENDIX D

SUPPORTING INFORMATION FOR CHAPTER VII

q	ilm Thickness / Å
1	332(1)
2	484(1)
3	342(1)
4	488(1)
5	306(1)
6	484(1)
7	504(1)
8	490(1)
9	485(1)
11	323(1)

Table D.1. Thickness of each annealed sample determined via analysis of XRR data.

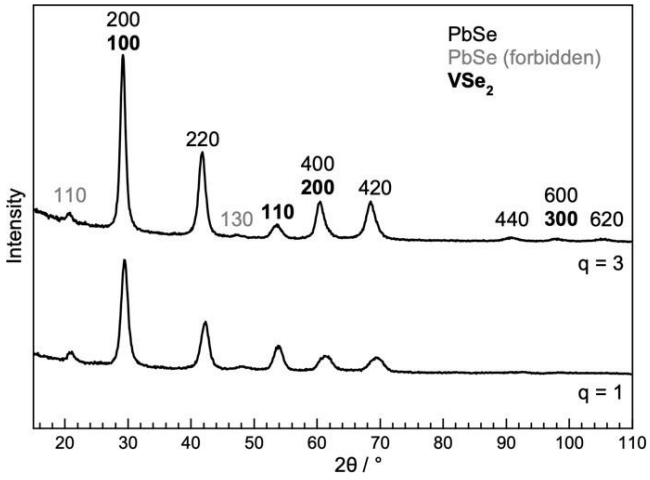

Figure D.1. Grazing incidence in-plane x-ray diffraction patterns of the annealed q = 1 and 3 precursors show that both films also consists of crystallographically aligned PbSe and VSe_2.

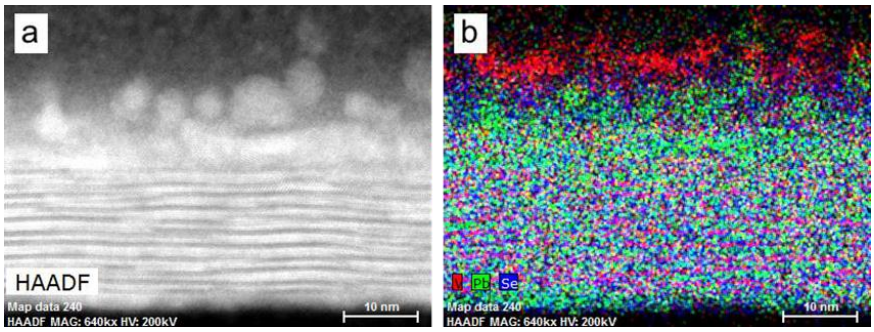

Figure D.2. (a) HAADF-STEM and (b) EDX analysis of the annealed q = 5 precursor shows that the film is defect-rich and already partially segregated. Large segregated V- and Pb-rich regions are found near the surface of the film.

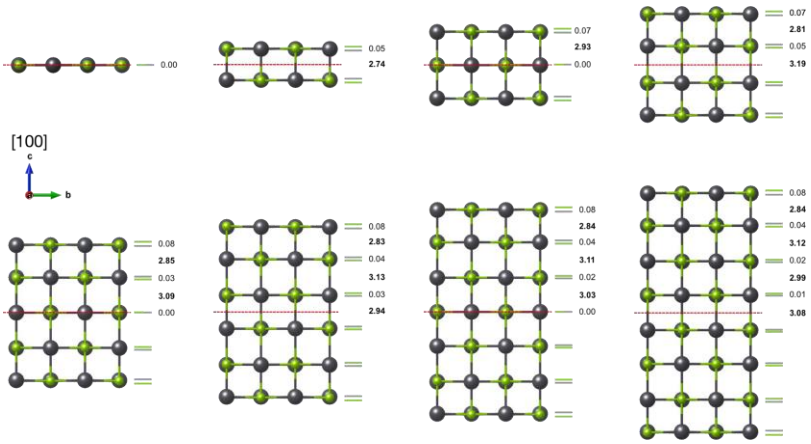

Figure D.3. Energy minimized structures of PbSe blocks with varying number of layers (Pb = gray, Se = green). Surfaces are normal tothe "z" direction that is aligned vertically in these representations. All structures contain a z-axis mirror plane indicated by the red dashedlines. The bold numbers are the distances between PbSe monolayers while the numbers in normal font represent distances between Pb and Se within the monolayers originating from the "puckering" displacements induced by the surface. An alternation of short and longmonolayer distances are observed as an indication of bilayer formation. Vacuum is placed along the z-direction to prevent interactions between blocks. All atomic plane distances are in Angstroms.

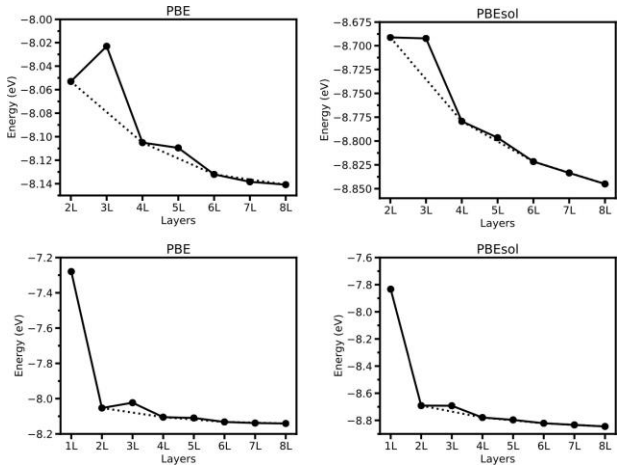

Figure D.4. Energies of PbSe blocks as a function of thickness computed using the PBE and PBEsol exchange-correlation functionals. The bottom two plots include the 1-layer system to emphasize its large difference in energy compared to slabs with larger layer thicknesses. Althoughthe absolute energies obtained by the two functionals differ, the presence of a convex hull formedby slabs with even layer thicknesses emerges from both results.

APPENDIX E

SUPPORTING INFORMATION FOR CHAPTER VIII

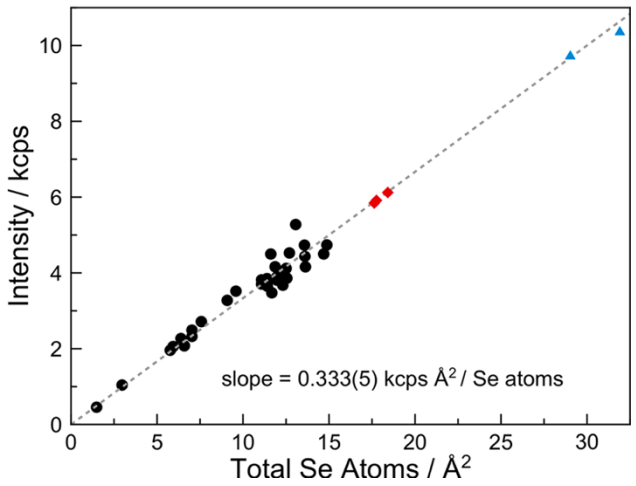

Figure E.1. The calibration curve relating the angle-integrated Se Lα XRF intensity to Se atoms per Å^2.

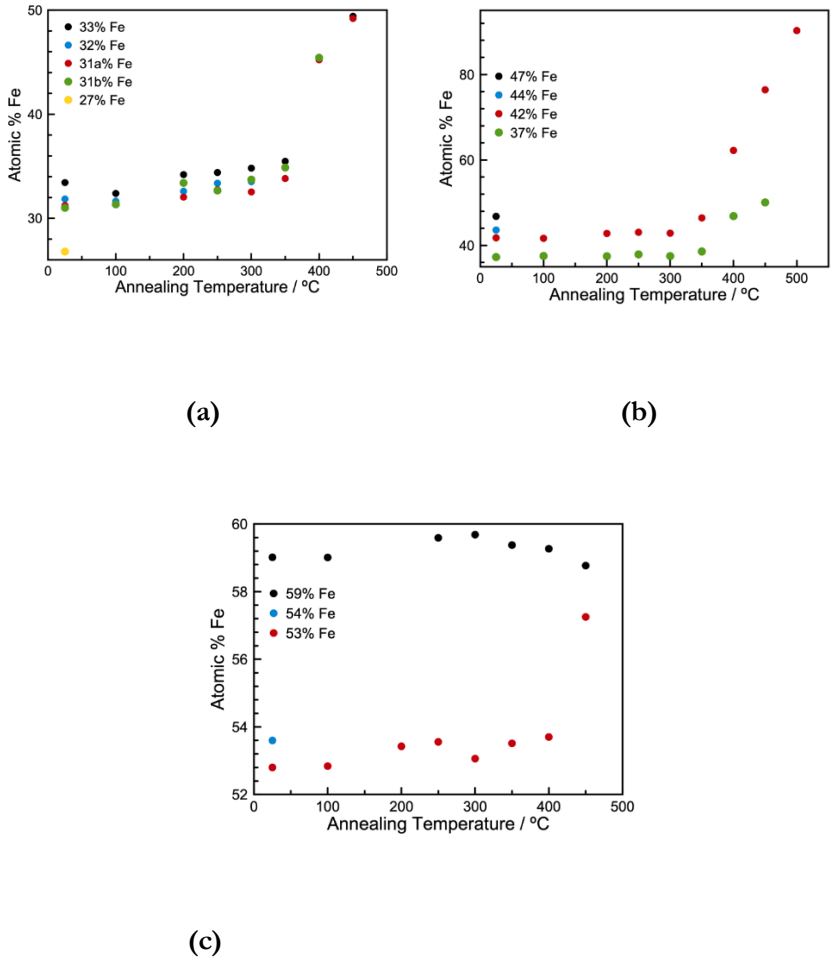

Figure E.2. Elemental composition of each film as a function of annealing temperature. In each case, the percent iron content was determined by (Fe atoms per Å^2)/(Fe atoms per Å^2 + Se atoms per Å^2). Note that film composition was not determined at every temperature for all samples.

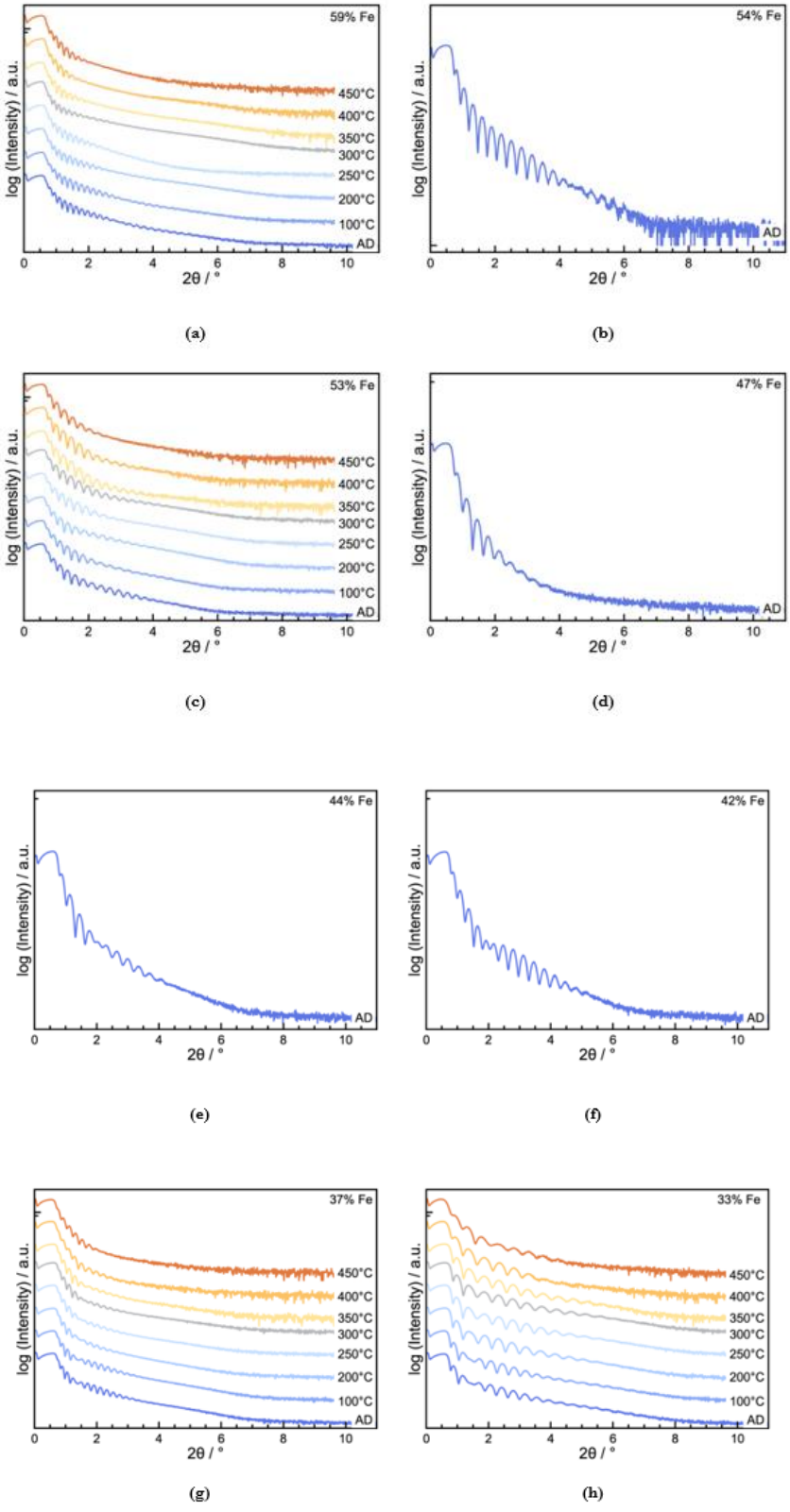
59% Fe
450°C
400°C
350°C
300°C
250°C
200°C
100°C
AD
log (Intensity) / a.u.
2θ / °
(a)
54% Fe
AD
log (Intensity) / a.u.
2θ / °
(b)
53% Fe
450°C
400°C
350°C
300°C
250°C
200°C
100°C
AD
log (Intensity) / a.u.
2θ / °
(c)
47% Fe
AD
log (Intensity) / a.u.
2θ / °
(d)
44% Fe
AD
log (Intensity) / a.u.
2θ / °
(e)
42% Fe
AD
log (Intensity) / a.u.
2θ / °
(f)
37% Fe
450°C
400°C
350°C
300°C
250°C
200°C
100°C
AD
log (Intensity) / a.u.
2θ / °
(g)
33% Fe
450°C
400°C
350°C
300°C
250°C
200°C
100°C
AD
log (Intensity) / a.u.
2θ / °
(h)

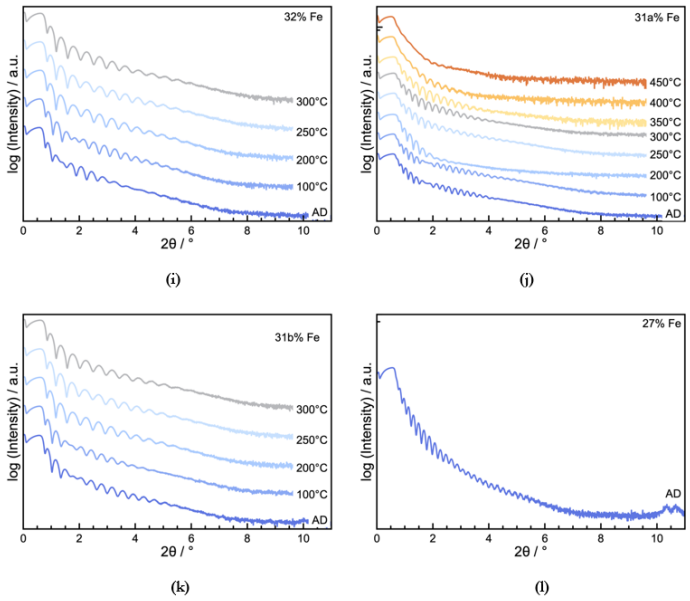

Figure E.3. XRR patterns of every sample explored in this investigation. Film thicknesses were determined from the Kiessig fringes as explained in the primary report.

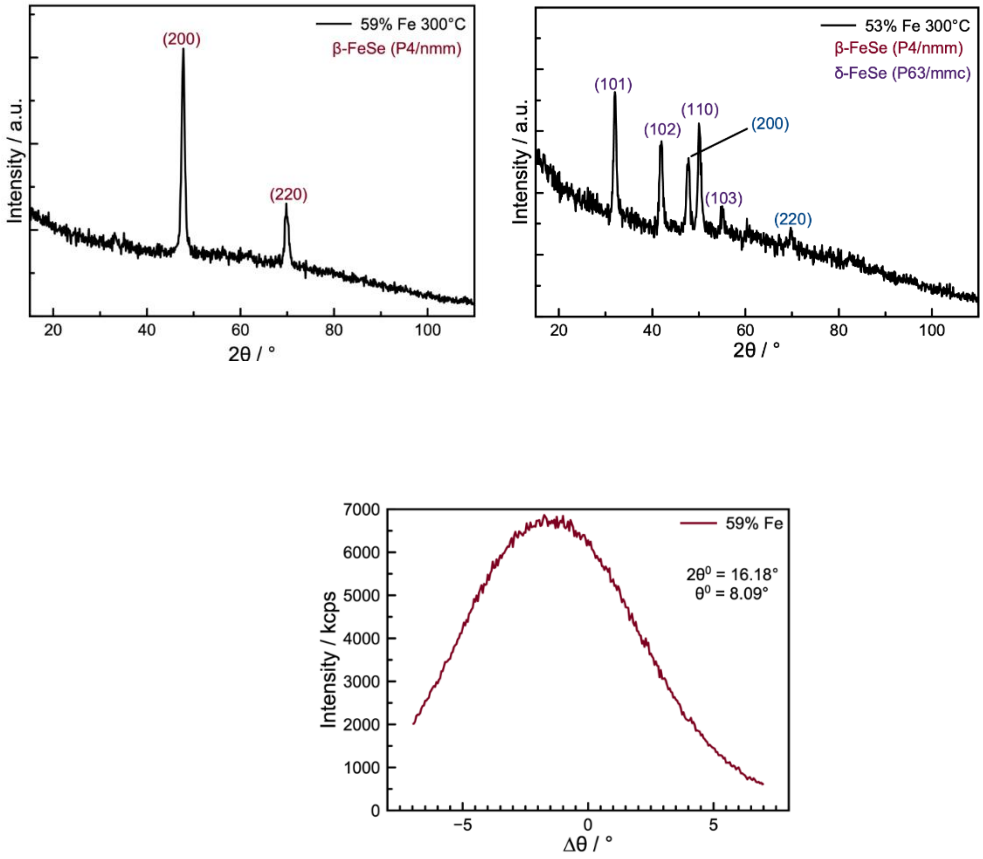

Figure E.4. In-plane X-ray diffraction patterns of **(a)** the 59% Fe sample and **(b)** the 53% Fe sample. **(c)** A rocking curve on the peak at 2θ = 16.18° in the as-deposited 59% Fe specular XRD pattern with a FWHM of approximately 8.4°.

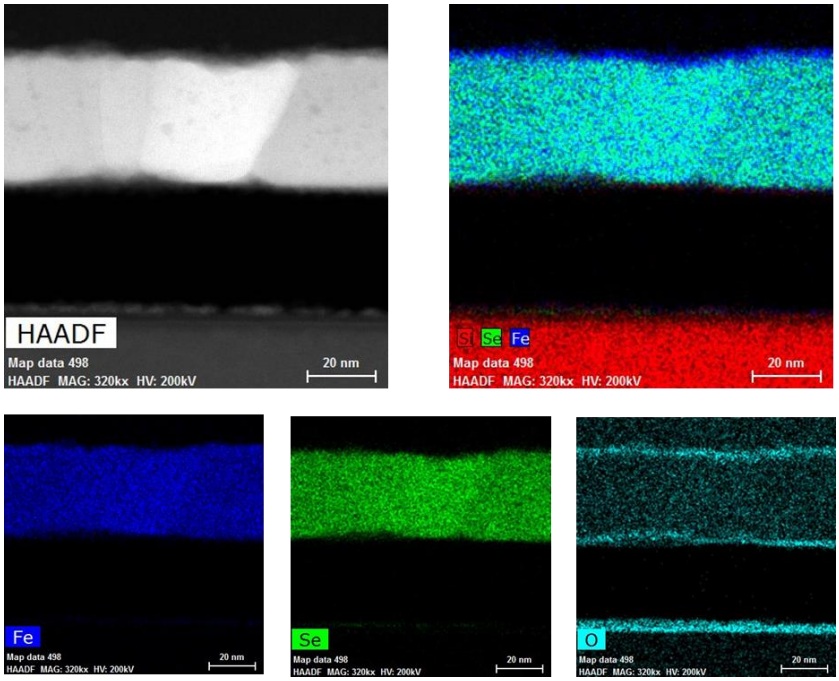

Figure E.5. Energy dispersive X-ray spectroscopy (EDS) maps obtained on a 37% Fe sample annealed to 350°C. The HAADF-STEM image from the region the maps were obtained is shown in the first image. The sample delaminated from the Si / native SiO_2 substrate during preparation of the cross-section. The sample contains homogeneous Fe and Se. An Fe-oxide is evident on the surface of the film.

APPENDIX F

SUPPORTING INFORMATION FOR CHAPTER IX

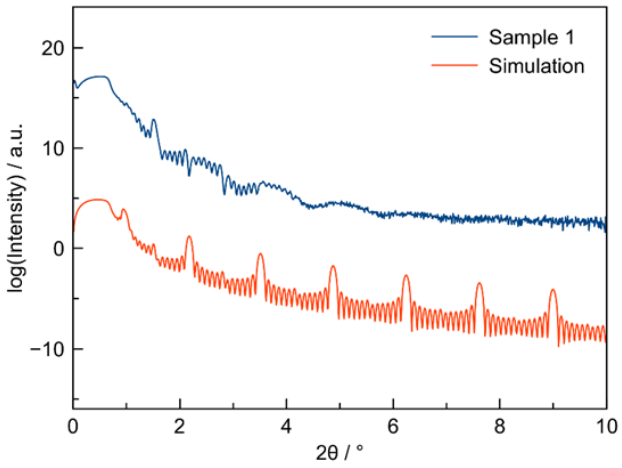

Figure F.1. XRR pattern for the Fe-rich multilayer sample (M1) and simulated XRR pattern for 7 repeating units of Fe|Se on Si with native SiO_2.

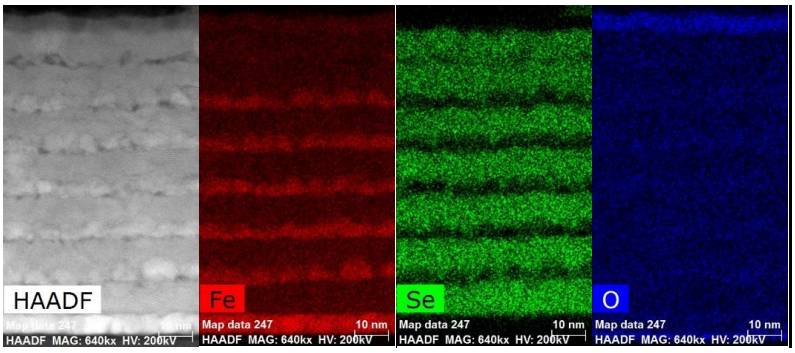

Figure F.2. HAADF-STEM image of the Fe-rich multilayer sample (M1) and corresponding EDS maps for each element from the same region.

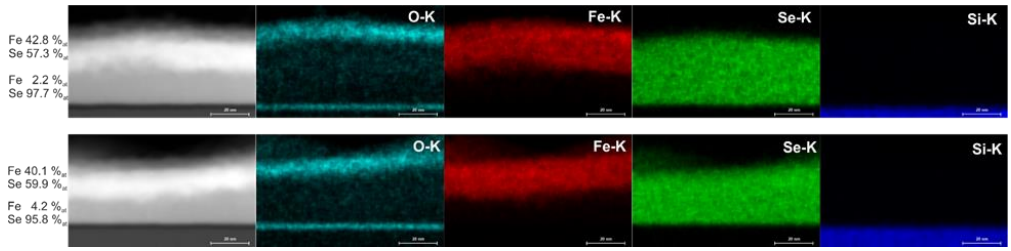

Figure F.3. HAADF-STEM image of the Se-rich bilayer sample (B2) and corresponding EDS maps for each element from the same region.

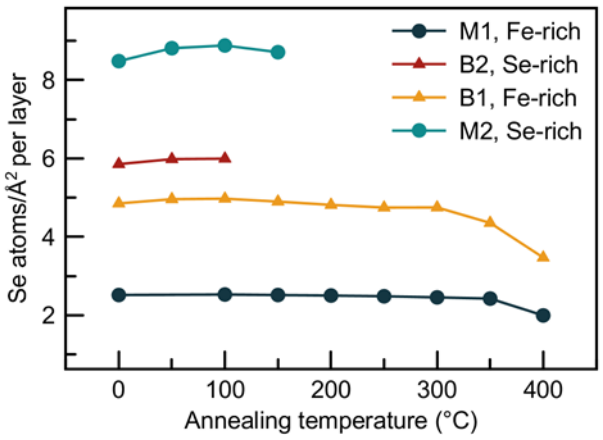

Figure F.4. Se atoms/Å^2 per layer measured by XRF as a function of annealing temperature

APPENDIX G

SUPPORTING INFORMATION FOR CHAPTER X

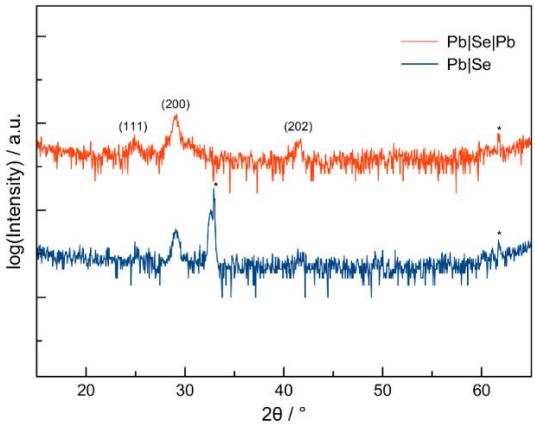

Figure G.1. Specular XRD of as-deposited Pb|Se|Pb and Pb|Se precursors, where labeled indices are applicable to both patterns and correspond to PbSe (Fm$\underline{3}$m).

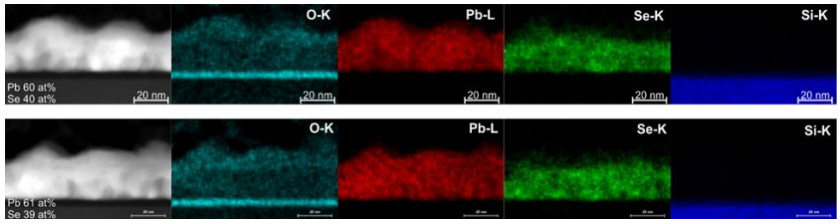

Figure G.2. HAADF-STEM image of a cross-section of the Pb|Se|Pb precursor (left) and EDS maps for each element present in the Pb|Se|Pb precursor, which show islands of PbSe and Pb-oxide on the surface.

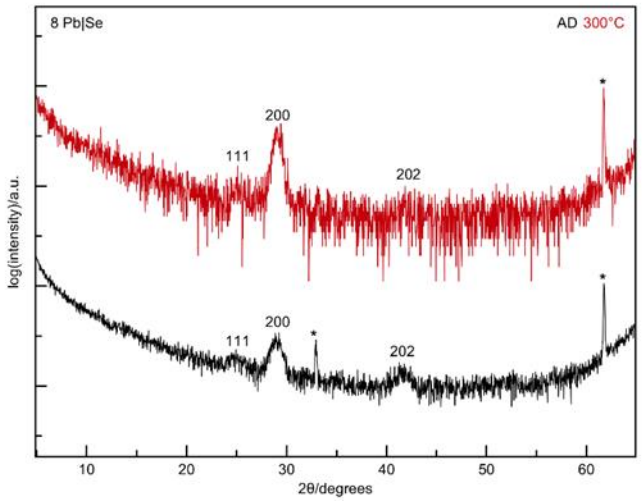

Figure G.3. Specular XRD pattern of the 8 Pb|Se sample as-deposited (black) and annealed to 300°C. Labeled indices are consistent with a PbSe ($Fm\bar{3}m$). Reflections marked with an asterisk are from the substrate.

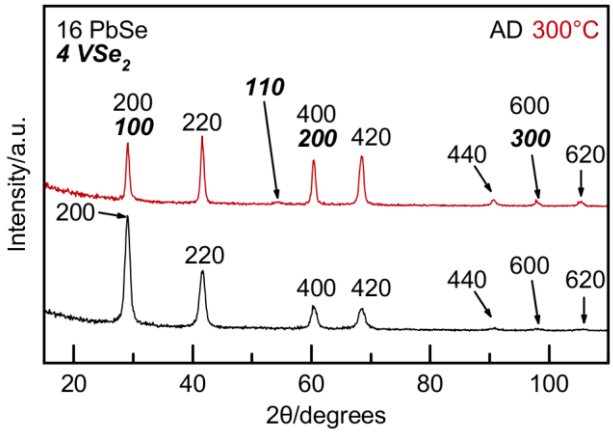

Figure G.4. In-plane XRD pattern of the 16 Pb|Se on 4 V|Se sample as-deposited (black) and annealed to 300°C. Labeled indices are consistent with a PbSe ($Fm\bar{3}m$) or hexagonal VSe_2 unit cell. Only PbSe reflections are present in the as-deposited sample, which is consistent with specular XRD.

Substrate	Precursor structure	Total Experimental Atoms/Å² after annealing			# PbSe layers possible	# $MoSe_2$ layers possible
		Pb	Se	Mo		
8 repeating units Mo|Se	128 Pb|Se	12.381	13.046	0.816	116	3
	64 Pb|Se	6.164	7.591	0.832	58	6
	32 Pb|Se	3.106	4.779	0.827	29	7
	16 Pb|Se	1.626	3.277	0.826	15	7
	8 Pb|Se	0.808	2.403	0.819	7	7

Table G.1. Total experimental atoms/Å² after annealing to 400°C were determined via X-ray fluorescence, where Se also includes the amount used in Mo|Se layers. The number of PbSe layers was calculated using the total Pb atoms/Å², where 0.1065 atoms/Å² are needed to form one bilayer of PbSe. The number of $MoSe_2$ layers possible was calculated using the remaining Se available after 0.1065 atoms/Å² of Se per PbSe is used, and assuming 0.2135 atoms/Å² is needed to form a trilayer of $MoSe_2$.

APPENDIX H

SUPPORTING INFORMATION FOR CHAPTER XIV

Thermo Fisher Scientific Helios Laser PFIB

The Laser PFIB system used for data collection was a pre-production prototype of a modified Helios PlasmaFocused Ion Beam (PFIB) DualBeam FIB/SEM that had been retrofitted with an optical feedthrough to deliver a focused, scanned, femtosecond laser beam coincident with both the SEM and PFIB. The laser itself and necessary optics were mounted to the chamber so that all components of the beam path were vibration isolated on the same air-sprung table on which the DualBeam resided. The entire beam path wasfully enclosed and interlocked to protect the sensitive optical components, maintain the beam alignment, and to reduce the risk of laser exposure. A schematic of the Laser PFIB concept is shown in Figure H.1. Figure H.2 is a photograph of the pre-production model used in this work.

The external (outside the vacuum chamber) optical components that comprise the laser beam path consist of coated, high power application steering mirrors to direct the beam to a final scanning mirror, which controls the beam angle as it enters the vacuum chamber via an optical feedthrough. This feedthrough wasmotorized in the axial direction (optical axis) to allow the user to change the focus of the laser on the sample.Polarization of the laser could be rotated by in-line half-waveplates. The laser itself was of the Carbide product line from Light Conversion. It consisted of a 1030 nm fundamental and a 515 nm second harmonicwavelength, with a pulse duration less than 300 fs. The laser was capable of operation at up to 600 kHz with a maximum average output power of 4 W.

Internally, the optical feedthrough mechanically held the focusing light objective in vacuum. The objective was designed for vacuum compatibility, high-power applications, and incorporated antireflective coatings for both fundamental and second harmonic wavelengths. The objective was protected from ablated debris by user replaceable, consumable glass coverslips. These components are visible in the in-chamber photograph of Figure H.3. Additionally, a mechanical, pneumatically-actuated shutter was automatically inserted during laser ablation to help protect the SEM pole tip and lower column from ablated debris.

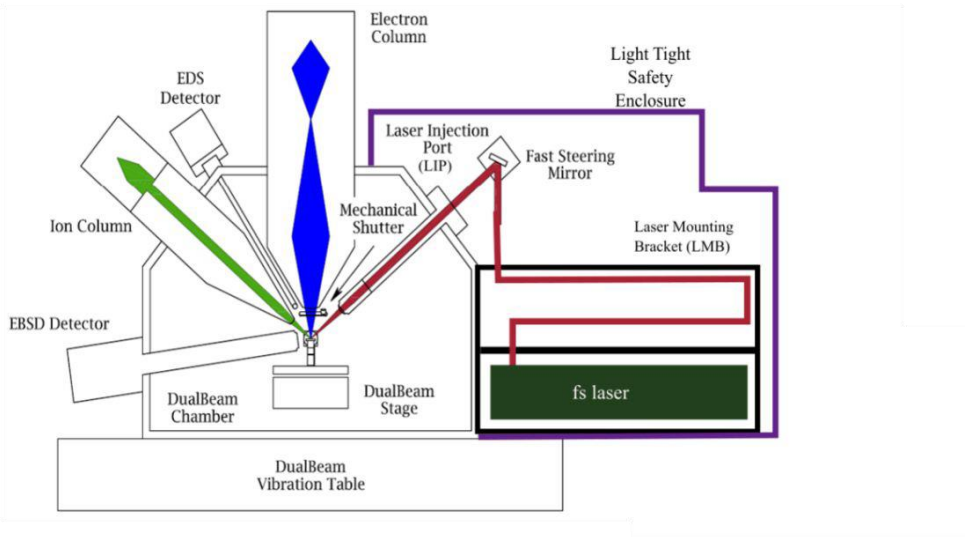

Figure H.1. Conceptual layout of the Laser PFIB System, which merges femtosecond laser / plasma FIB /SEM to a single point of coincidence, to enable multiscale and multimodal analysis.

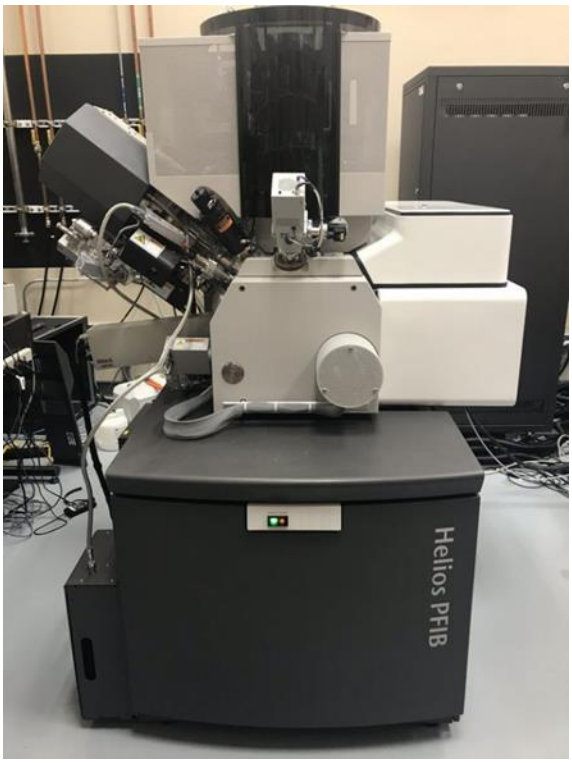

Figure H.2. Photograph of the pre-production prototype Laser PFIB used in this work.

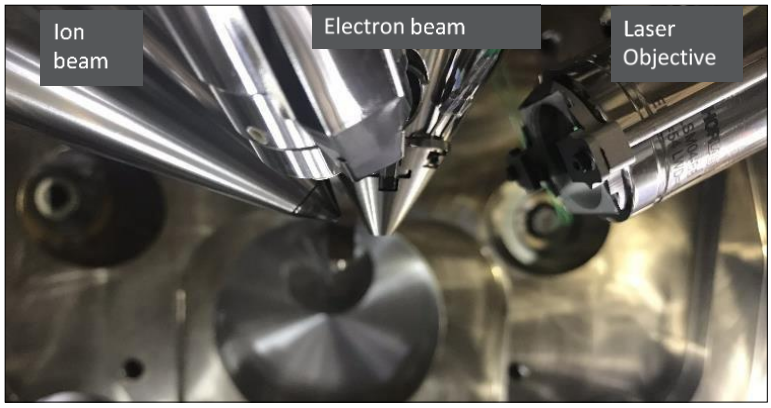

Figure H.3. In-chamber image showing three-beam coincidence as found in the Laser PFIB prototype. Thelaser objective was protected by replaceable and consumable glass coverslips to prevent debris collection on the light optics.

Cryogenic Stage in the Laser PFIB

During oblique cross-sectioning, an additional negative tilt of 8° was added to yield a 59° cut-face angle relative to horizontal. Ideally the laser could be used to cut normal to the surface, creating a vertical cross-section for the least amount of material removal to achieve a certain depth, but the coin cell geometry limitations kept this from being possible. Additionally, the oblique cross-section allowed for better EDS collection, given the tilt limitations imposed by the Quorum cryo-stage. Fortunately, the exceptional speedof the laser ablation process helped compensate for the need to remove more material to access a given depth in the battery. This allowed us to cut deeply (more than 1 mm) quickly enough to maximize the analytical time on the newly exposed, reactive lithium-containing structures. Figure H.4 also shows the polarization orientation as defined in our system when using the oblique cross-sectioning technique.

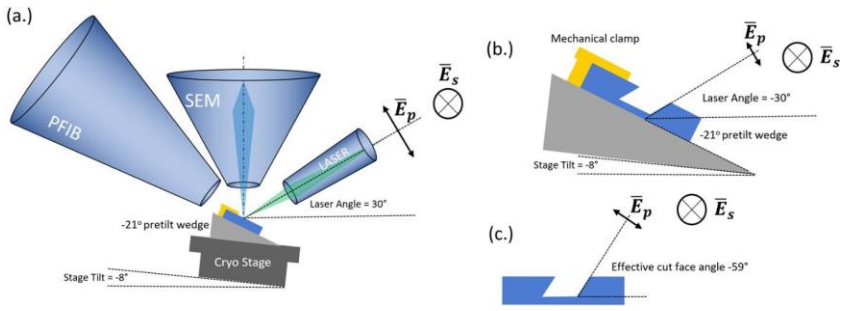

Figure H.4. Schematic illustrating the laser cut and SEM image geometries used in the current work, including the description of the polarization direction in relation to the system and sample geometry. Overview (a.) of the sample, and its mounting inside the chamber; Detail of

the cross-section (b.) geometryin its as-processed state; detail of the effective cut angle (c.) into the battery.

Sample Milling and Characterization

In order to optimize the time necessary to achieve a clean cross-section, the laser ablation was performed in several steps, similar to using regular and cleaning cross-section patterning in FIB techniques. Several experimental conditions were tested to determine what laser parameters would yield the best cut quality, including laser wavelength, repetition rate, pulse energy, and polarization. A bulk mill to remove a large volume was necessary to access the region of interest in the samples, Figure H.S5a. Due to the geometric limitations of the sample on the cryo-stage, the bulk mill needed to be large enough to reduce shadowing on the EDS detector.

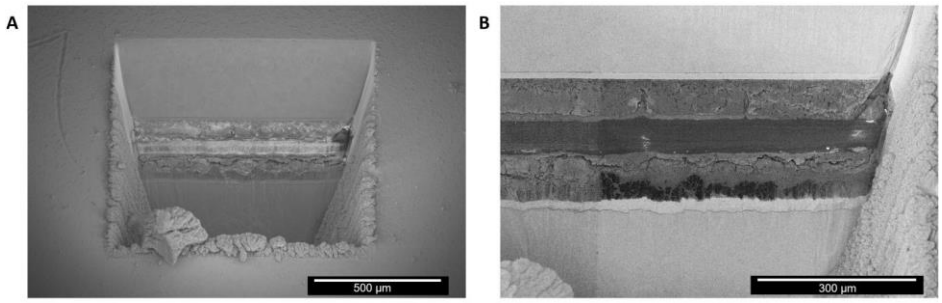

Figure H.5. Scanning electron micrographs of (a) coarse and (b) fine polished laser ablation faces of the 51stplating coin cell sample.

First, a coarse bulk cut was made using 1030 nm in order to remove a volume of ~1200 x 900 x 800 μm togain access to the region of interest. In this system, the pulse energy available and spot size were higher for1030 nm than 515 nm, which allowed for more rapid material removal. Next, this cross section was coarselypolished to remove ablation debris from the bulk mill on the ROI. After the coarse mill, the system was vented so that the protective coverslip could be replaced, due to the large amount of material coating the coverslip that reduced the transmission of laser light. The sample remained on the cooled cryo-stage duringthis vent and pump cycle.

The best cut quality for the final polishing step was achieved using low repetition rates and 515 nm p- polarized light, Figure S5b. These conditions were particularly optimal for the non-metal stacks in the sample. The focus of the laser was set to be just above the region of interest, or over focused approximately300 μm subsurface into the cross-section, which was done by moving the objective lens in towards the sample. This was done to reduce the time spent on polishing the stainless steel, by only polishing the regionof interest. All milling parameters are listed in Table H.1.

Table H.1. Ultrashort pulse laser ablation parameters used on each coin cell battery sample.

	Wavelength (nm)	**Repetition Rate** (kHz)	**Pulse Energy** (μJ)	**Dimensions** (μm)	**Pitch** (μm)	**Time** (min)
Coarse Bulk Cut	1030	20	40	1200 x 900	10 x 10	3:36
Coarse Polish	1030	7.5	40	1200 x 500	5 x 5	4:48
Fine Polish	515	1	10	600 x 20	2 x 2	1:35

Scanning electron micrographs of the fine polished oblique battery stack cross-sections are shown in Figure 1 (unprocessed images in Figures H.6-H.12), with measurements of the individual component layer thicknesses provided in Table H.2.

Table H.2. Measurements (in μm) of the layer thickness of individual components in coin cell samples, with thicknesses corrected for the oblique cross section of 59 degrees. Measurement error is +/- 3 μm

(um)	Pristine	1st Plate	1st Strip	11th Plate	51st Plate	101st Plate	Low Rate 101st Plate
Top Cu	11	12	12	11	10	10	10
Bottom Cu	14	15	15	12	12	13	12
Separator	53	58	57	55	50	--	49
Top Li + SEI	0	15	6	10	62	66	39
Bottom Li + SEI	53	48	74	64	72	42	77
Top to Bottom Cu Separation	116	125	119	133	191	192	165

Unprocessed SEM Images of Coin Cells

Figure 1 provides images of each oblique battery stack after fine polishing, while held at ~ -110°C. Each of these individual images were false colored to highlight the regions of lithium metal, separator, SEI/electrolyte, and copper, interpreted from the data provided in the EDS maps (Figures S18–S23). Raw images are provided in Figures S6-S11. Figure S12 was acquired from the low-rate cell cycled at 0.47 mA/cm^2 to the 101st plating step. Replicates of the 101st Li plating step in cells cycled at 1.88 mA/cm^2 are reported in Figures S13-S17. Note that

during milling with the ultrashort pulse laser, redeposition of iron from the stainless-steel casing caused cracks and gaps to be highlighted. These regions are most clear in theEDS maps. The iron redeposition is most apparent in the 51st and 101st Li plating cells, where cracks and crevices in the SEI were present.

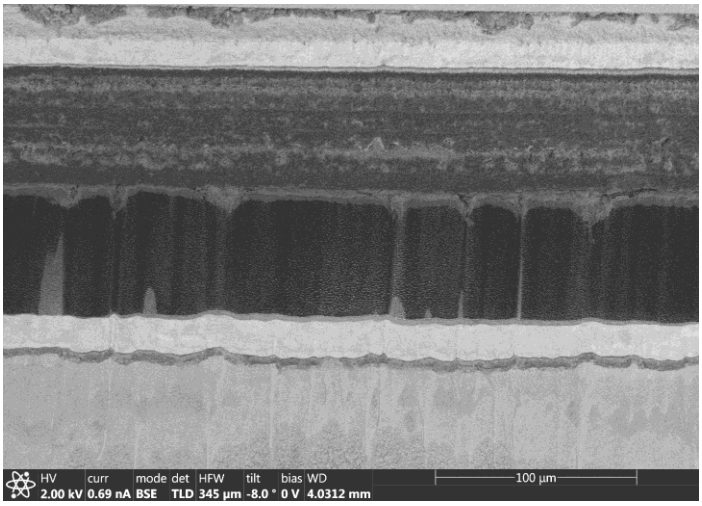

Figure H.6. Unprocessed SEM image of the uncycled cell.

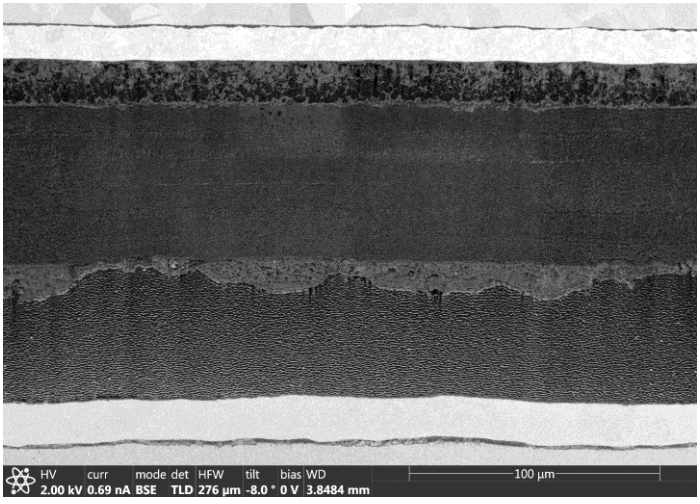

Figure H.7. Unprocessed SEM image of the 1st Li plating cell cycled at a high rate of 1.88 mA/cm^2 to acapacity of 1.88 mAh/cm^2.

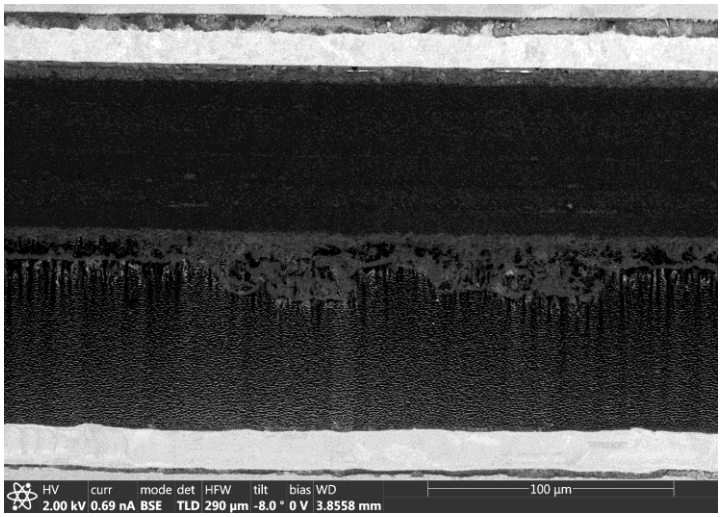

Figure H.8. Unprocessed SEM image of the 1st Li stripping cell cycled at a high rate of 1.88 mA/cm2 to acapacity of 1.88 mAh/cm2.

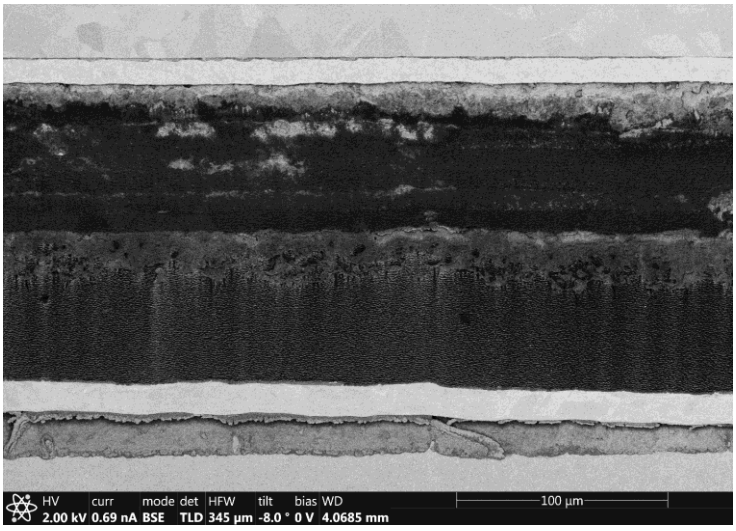

Figure H.9. Unprocessed SEM image of the 11th Li plating cell cycled at a high rate of 1.88 mA/cm2 to acapacity of 1.88 mAh/cm2.

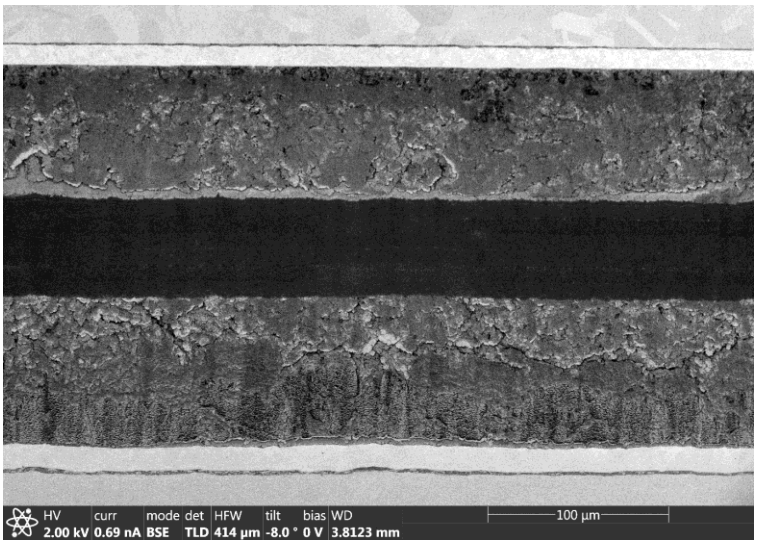

Figure H.10. Unprocessed SEM image of the 51st Li plating cell cycled at a high rate of 1.88 mA/cm^2 to acapacity of 1.88 mAh/cm^2.

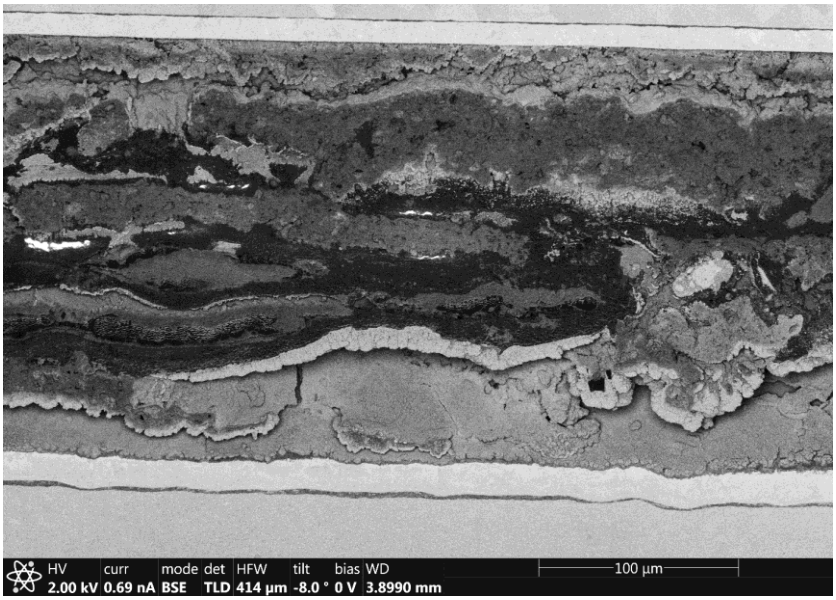

Figure H.11. Unprocessed SEM image of the 101st Li plating cell cycled at a high rate of 1.88 mA/cm^2 toa capacity of 1.88 mAh/cm^2.

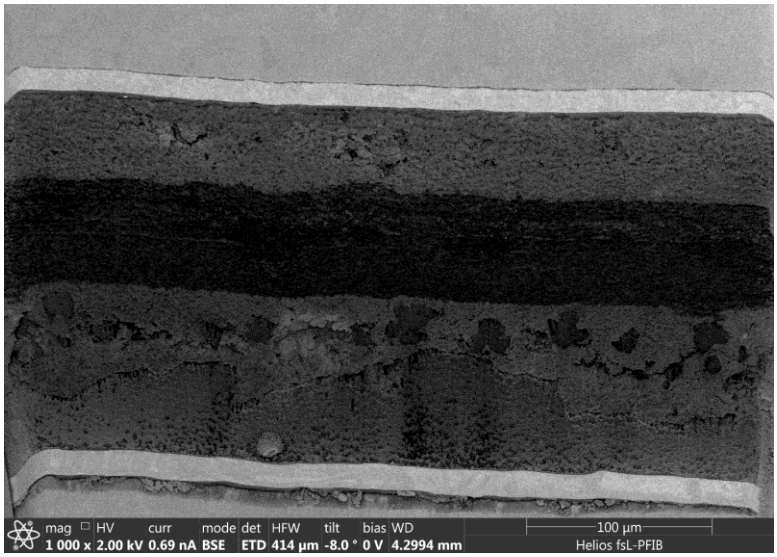

Figure H.12. Unprocessed SEM image of the 101st Li plating cell cycled at a low rate of 0.47 mA/cm^2 to acapacity of 1.88 mAh/cm^2.

Replicate Unprocessed SEM Images of Coin Cells

Not all images showed catastrophic separator failure as shown in Figure 13.1 of the main manuscript as failure is highly stochastic, but after sampling only one or two regions in each cell it was easy to find separator damage or failure. In two of four cells imaged that match the conditions in the manuscript, twoof them showed the separator shredding and the others showed signs of damage in the random locations chosen. We believe that separator shredding is widespread but may only occur in some regions within a cell, which agrees with the stochastic nature of the cycling data. All of the cells showed evidence of Li and SEI growing between the separator sheets or trilayers. Some cells were imaged in multiple

locations and it was more common for separator failure to occur near the edges of the cell stack than in the middleof the cell stack.

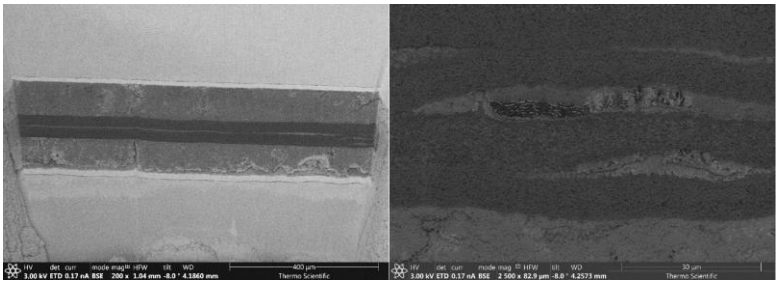

Figure H.13. First replicate, near center of coin cell, unprocessed SEM images of the 101st Li plating cell cycled at a high rate of 1.88 mA/cm^2. The bottom right part of the separator stack shows Li metal platingbetween the layers and SEI building up as shown in the image to the right.

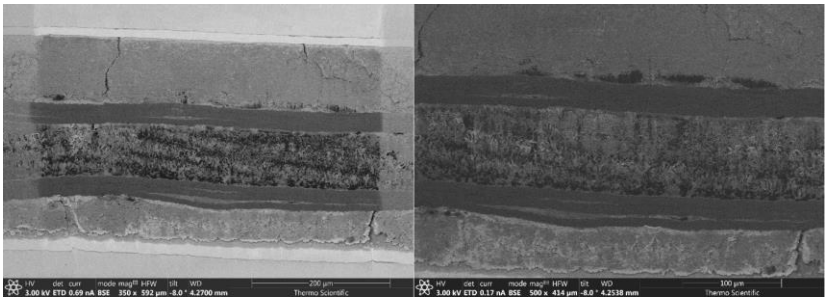

Figure H.14. First replicate, near edge of coin cell, unprocessed SEM images of the 101st Li plating cell cycled at a high rate of 1.88 mA/cm^2. Copious amounts of Li (evident from the laser induced pattern) andSEI have formed between the two separator sheets and the Celgard trilayers are beginning to delaminate.

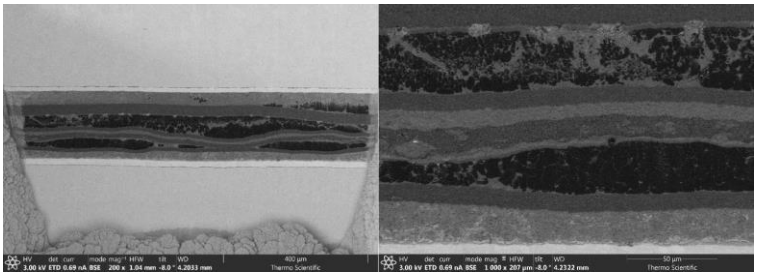

Figure H.15. Second replicate, near center of coin cell, unprocessed SEM images of the 101st Li plating cell cycled at a high rate of 1.88 mA/cm^2. Copious amounts of Li and SEI have formed between the twoseparator sheets and the Celgard trilayers have delaminated.

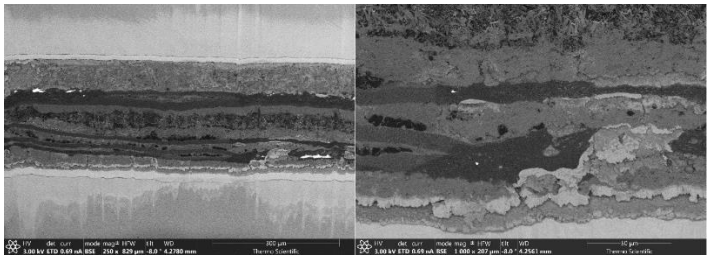

Figure H.16. Second replicate, near edge of coin cell, unprocessed SEM images of the 101st Li plating cellcycled at a high rate of 1.88 mA/cm^2. Copious amounts of Li and SEI have formed between the two separator sheets, the Celgard trilayers have delaminated, and separator shredding has begun (more detail showed in image on the right).

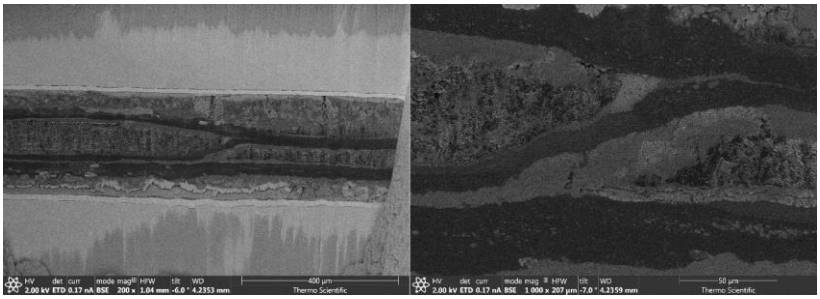

Figure H.17. Third replicate, near edge of coin cell, unprocessed SEM images of the 101st Li plating cellcycled at a high rate of 1.88 mA/cm^2. Copious amounts of Li and SEI have formed between the two separator sheets and the Celgard trilayers have delaminated.

Energy Dispersive X-ray Spectroscopy Maps

The pre-production Laser PFIB was equipped with an EDAX TEAM™ EDS/EBSD System. For EDS mapping, the stage was tilted to 16 degrees to bring the sample as close to flat as possible given the cryo- stage limitations. The SEM beam conditions were set to 20 kV, 2.8 nA. Elements of interest in EDS were C, O, S, F, Cu, and Fe. A medium resolution scan in TEAM software was used on all samples. The highestquality EDS map given time constraints were performed on the 11th lithiation sample with beam conditionsof 20 kV, 1.4 nA using medium resolution settings and drift correction in the TEAM software. EDS maps from each sample are shown in Figures H.18-H.23. The EDS maps were used to provide false color for component identification in the SEM images presented in Figure 1, as the carbon signal was strongly correlated to the separator, and very weak for the electrolyte and SEI. The lithium metal was identified in the mapped regions by the absence of an x-ray signal. This data provides some insight on the SEI regions,by the dominant oxygen and

fluoride signals from the inorganic structures that form, whereas the sulfur signal is more representative of the electrolyte. The SEI inclusions in the separator are identified as either small stranded pieces of Li covered with copious amounts of SEI, or solely SEI structures. Note that the blur in the copper signal from the bottom current collector is due to the angled cut face which released some out-of-plane copper x-rays through the above, thin Li metal or SEI layers, which dissimilarity did not escape through the topside of the top copper current collector that was shadowed by the stainless-steel cap.

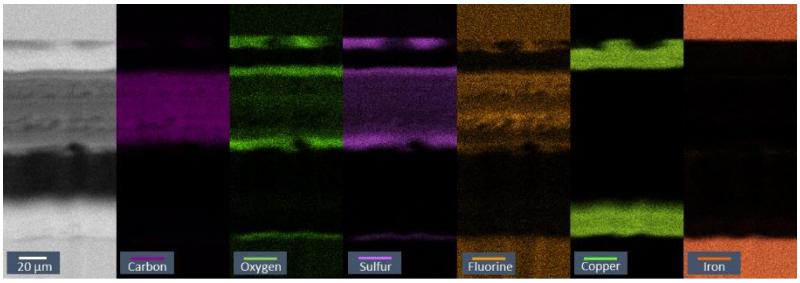

Figure H.18. Energy dispersive x-ray spectroscopy elemental maps of the uncycled cell.

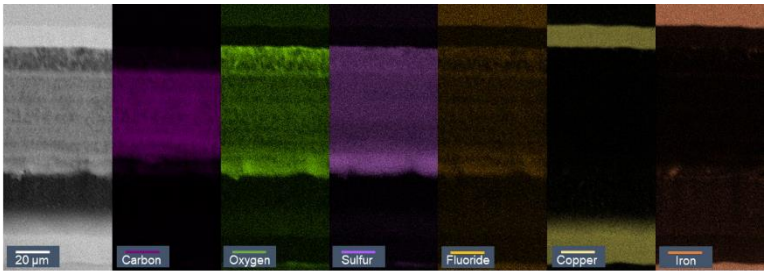

Figure H.19. Energy dispersive x-ray spectroscopy elemental maps of the 1st Li plating cell.

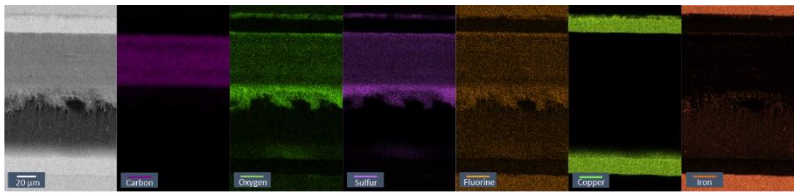

Figure H.20. Energy dispersive x-ray spectroscopy elemental maps of the 1st Li stripping cell.

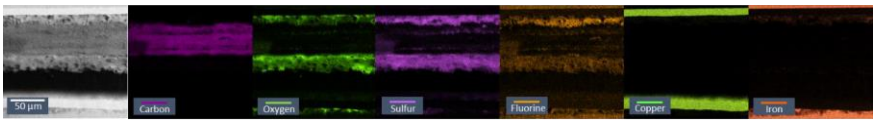

Figure H.21. Energy dispersive x-ray spectroscopy elemental maps of the 11th Li plating cell.

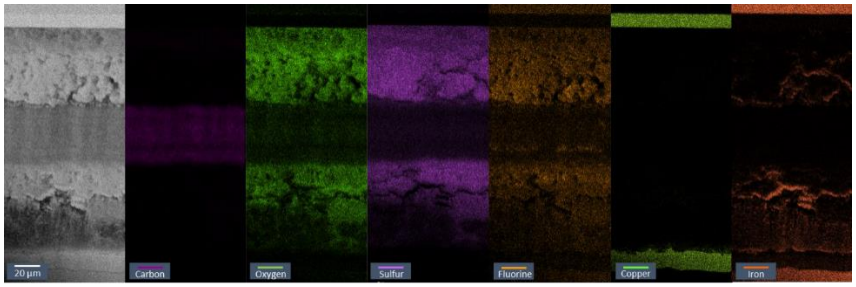

Figure H.22. Energy dispersive x-ray spectroscopy elemental maps of the 51st Li plating cell.

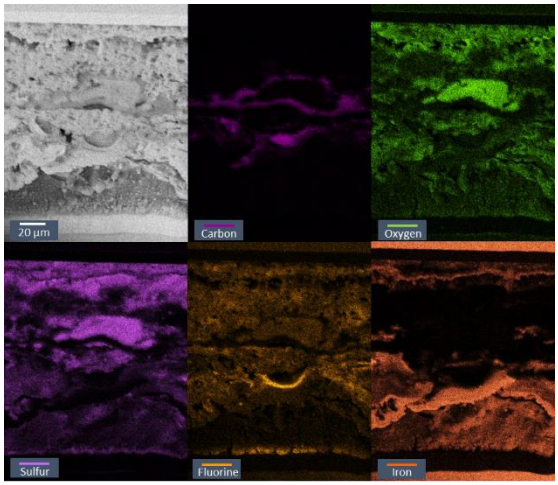

Figure H.23. Energy dispersive x-ray spectroscopy elemental maps of the 101st Li plating cell.

Analysis of the Electrochemical Data

The voltage versus time data shows that the overpotential grows with cycling with some sporadic changesfrom cycle to cycle, but the cell can supply 1.88 mAh/cm^2 reliably for a little over 150 hours (Figure H.24).After 150 hours (77 cycles) the cell began to fail catastrophically, such that it could no longer supply 1.88mAh/cm^2. The voltage versus time signal cannot be explained by a hard-short circuit, where the cell wouldstill be able to supply the programmed capacity, but the impedance would drop indicating that the current was carried across a dendrite instead of via charge transfer reactions. Instead, the voltage versus time curveis consistent with loss of active lithium in the cell, and a supply of electrons. In regard to the soft short discussion, replicates typically showed the behavior of the stripping capacity being higher than the plated capacity for some range over the 5-50 cycles.

Furthermore, this oscillation around 100% does not occur atother conditions such as lower current density, so it cannot easily be explained by random error in the battery cycler.

The cell maintained high average Coulombic efficiency up to cycle 71, at which point the Coulombic efficiency drops to 89.7%, but the cell is still able to plate the full specified capacity. The Coulombic efficiency recovers to 99.3% in cycle 72 and then drops again to 80-92% for the next 5 cycles, again with full plated capacity. Then, there is a sudden drop in the plating capacity on cycle 77, which is the first cyclewhere Li could not be plated to the specified capacity. The Coulombic efficiency was 90.1% for cycle 77 but then dropped to 72.8% on the subsequent cycle.

`

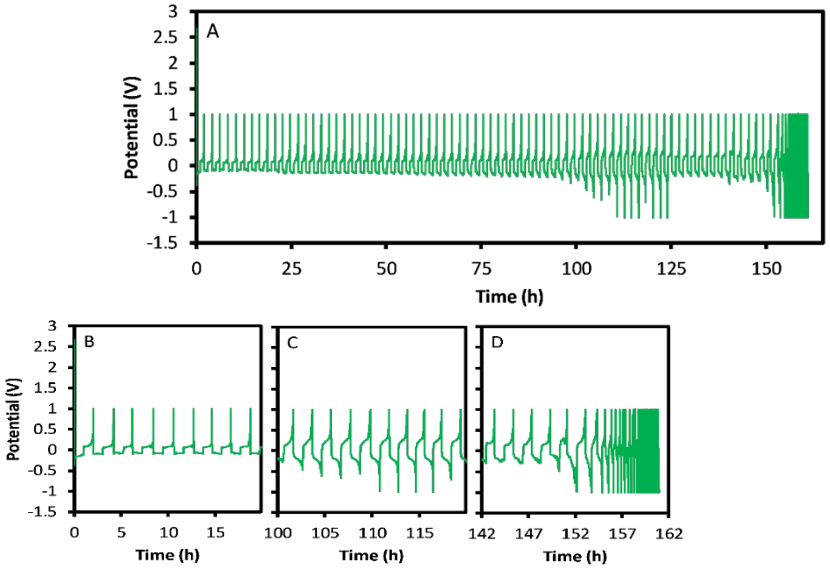

Figure H.24. (a) Voltage versus time profile for a cell at the 101st Li plating step cycled at a high rate of 1.88 mA/cm^2 to a capacity of 1.88 mAh/cm^2. (b-d) Zoomed in profiles for various time ranges to show more detail. This data was taken on the same cell depicted in Figure 13.1f and Figure 13.2a-b in the main manuscript.

Voltage versus time data are shown in Figure H.25 at the 0.47 mA/cm^2 low-rate condition (replicates in Figures H.41-H.43). In contrast to the cells cycled at high-current density (Figure H.24, and replicates in Figures H.26-H.40), the cells cycled at low-current density showed little variation in overpotential with cycling and much more stable behavior without signs of failure apparent in the electrochemical data. Note that the same number of cycles at low-current density required four times as long as at high-current density,because the capacity was held constant between these two data sets.

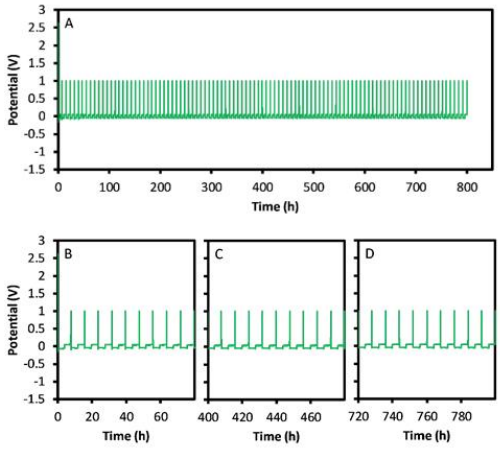

Figure H.25. (a) Voltage versus time profile for a cell at the 101st Li plating step cycled at a low rate of 0.47mA/cm^2 to a capacity of 1.88 mAh/cm^2. (b - d) Zoomed in profiles for various time ranges to show more detail. This data was taken on the same cell depicted in Figure 2c-e in the main manuscript.

Replicates of Electrochemical Data High Rate

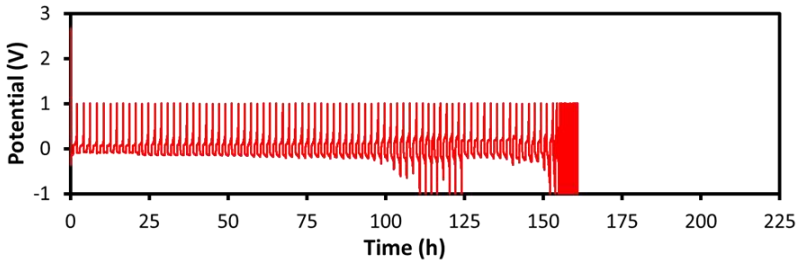

Figure H.26. First replicate of voltage versus time profile for a cell at the 101st Li plating step cycled at ahigh rate of 1.88 mA/cm^2 to a capacity of 1.88 mAh/cm^2.

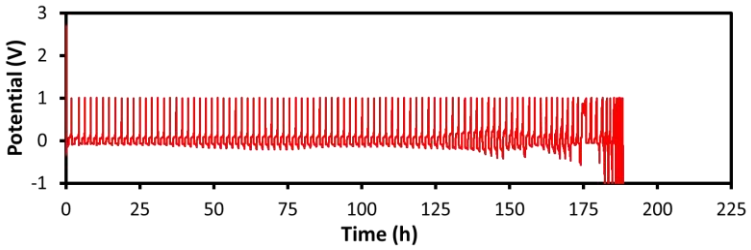

Figure H.27. Second replicate of voltage versus time profile for a cell at the 101st Li plating step cycled at ahigh rate of 1.88 mA/cm^2 to a capacity of 1.88 mAh/cm^2.

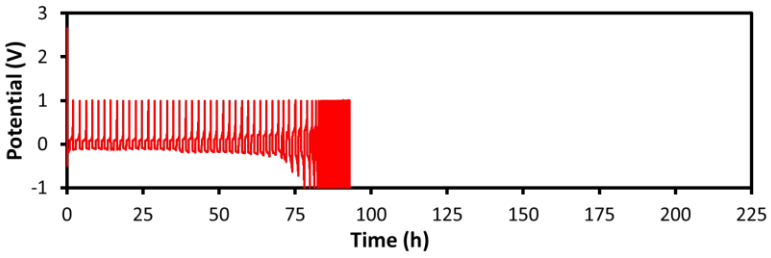

Figure H.28. Third replicate of voltage versus time profile for a cell at the 101st Li plating step cycled at ahigh rate of 1.88 mA/cm^2 to a capacity of 1.88 mAh/cm^2.

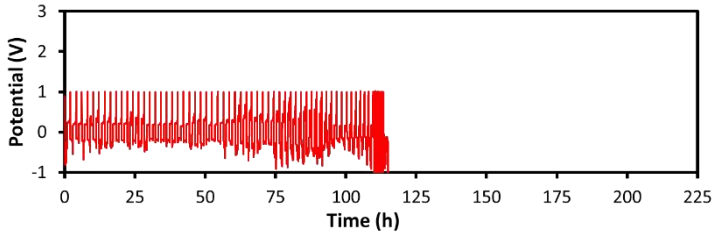

Figure H.29. Fourth replicate of voltage versus time profile for a cell at the 101st Li plating step cycled at ahigh rate of 1.88 mA/cm^2 to a capacity of 1.88 mAh/cm^2.

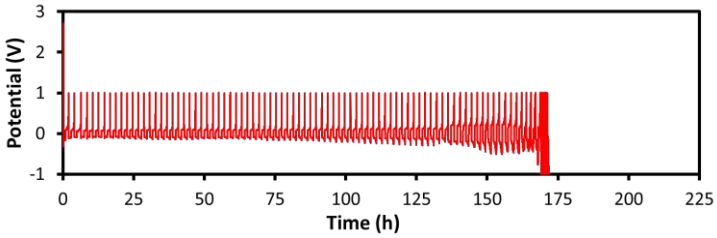

Figure H.30. Fifth replicate of voltage versus time profile for a cell at the 101st Li plating step cycled at ahigh rate of 1.88 mA/cm^2 to a capacity of 1.88 mAh/cm^2.

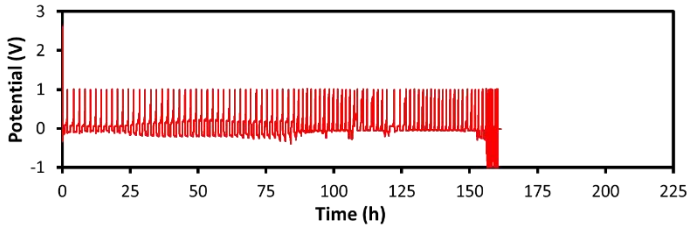

Figure H.31. Sixth replicate of voltage versus time profile for a cell at the 101st Li plating step cycled at ahigh rate of 1.88 mA/cm^2 to a capacity of 1.88 mAh/cm^2.

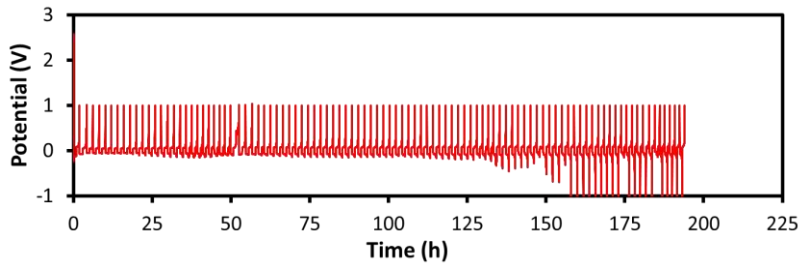

Figure H.32. Seventh replicate of voltage versus time profile for a cell at the 101st Li plating step cycled ata high rate of 1.88 mA/cm^2 to a capacity of 1.88 mAh/cm^2.

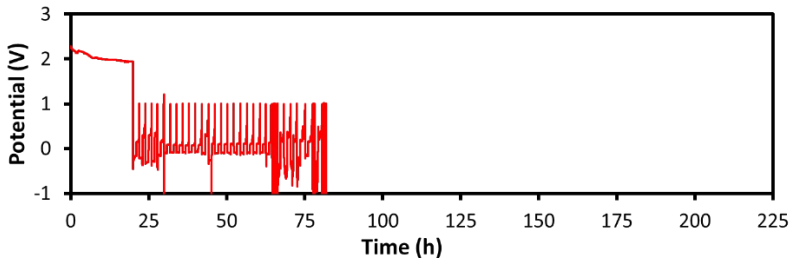

Figure H.33. Eighth replicate of voltage versus time profile for a cell at the 101st Li plating step cycled at ahigh rate of 1.88 mA/cm^2 to a capacity of 1.88 mAh/cm^2.

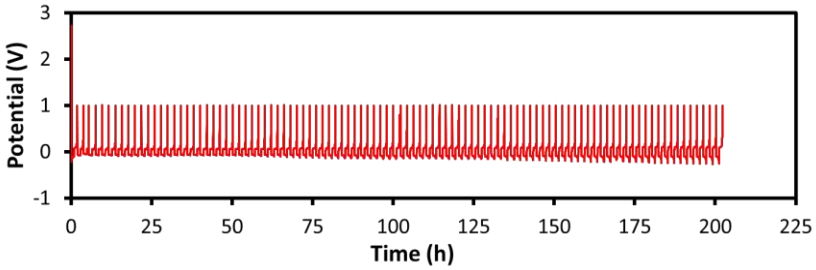

Figure H.34. Ninth replicate of voltage versus time profile for a cell at the 101st Li plating step cycled at ahigh rate of 1.88 mA/cm^2 to a capacity of 1.88 mAh/cm^2.

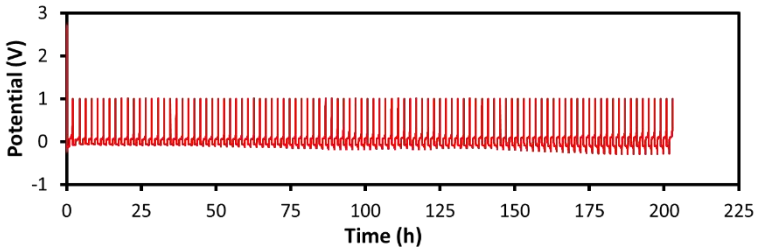

Figure H.35. Tenth replicate of voltage versus time profile for a cell at the 101st Li plating step cycled at ahigh rate of 1.88 mA/cm^2 to a capacity of 1.88 mAh/cm^2.

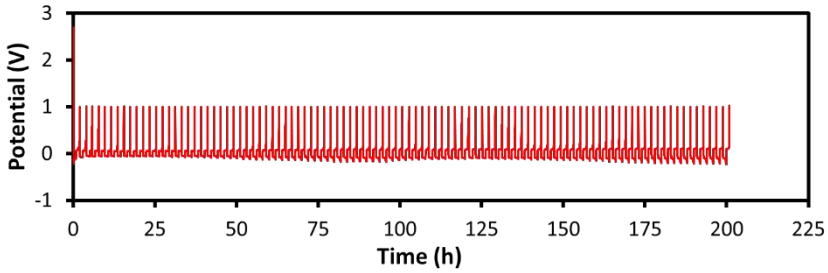

Figure H.36. Eleventh replicate of voltage versus time profile for a cell at the 101st Li plating step cycled ata high rate of 1.88 mA/cm^2 to a capacity of 1.88 mAh/cm^2.

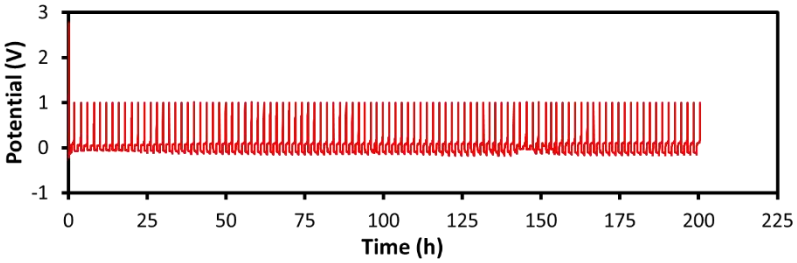

Figure H.37. Twelfth replicate of voltage versus time profile for a cell at the 101st Li plating step cycled ata high rate of 1.88 mA/cm^2 to a capacity of 1.88 mAh/cm^2.

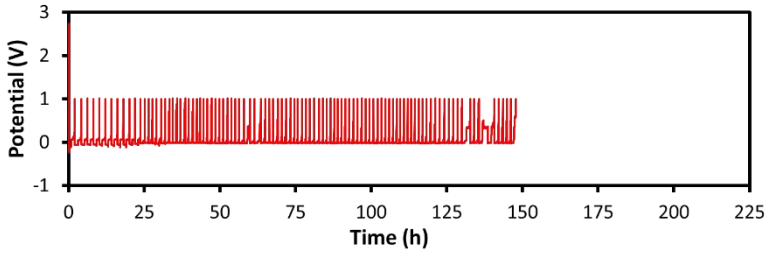

Figure H.38. Thirteenth replicate of voltage versus time profile for a cell at the 101st Li plating step cycledat a high rate of 1.88 mA/cm^2 to a capacity of 1.88 mAh/cm^2.

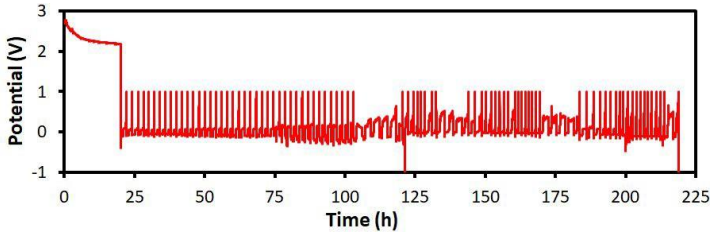

Figure H.39. Fourteenth replicate of voltage versus time profile for a cell at the 101st Li plating step cycledat a high rate of 1.88 mA/cm^2 to a capacity of 1.88 mAh/cm^2.

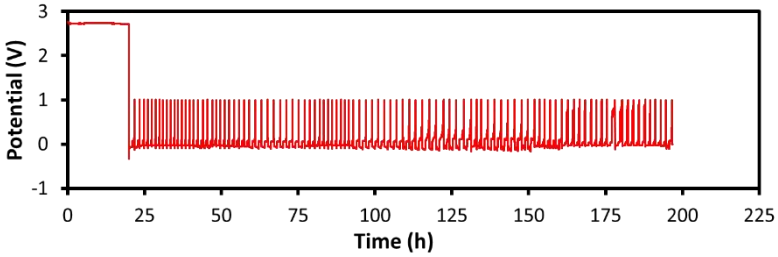

Figure H.40. Fifteenth replicate of voltage versus time profile for a cell at the 101st Li plating step cycled ata high rate of 1.88 mA/cm^2 to a capacity of 1.88 mAh/cm^2.

Low Rate

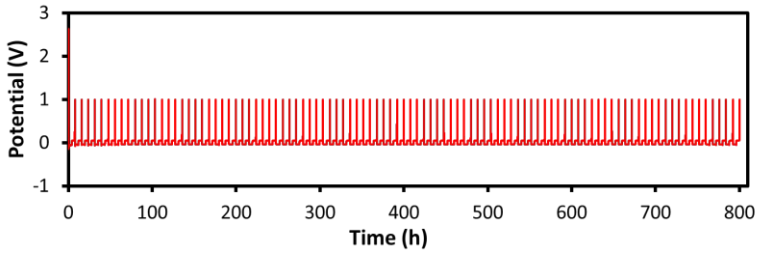

Figure H.41. First replicate of voltage versus time profile for a cell at the 101st Li plating step cycled at alow rate of 0.47 mA/cm^2 to a capacity of 1.88 mAh/cm^2.

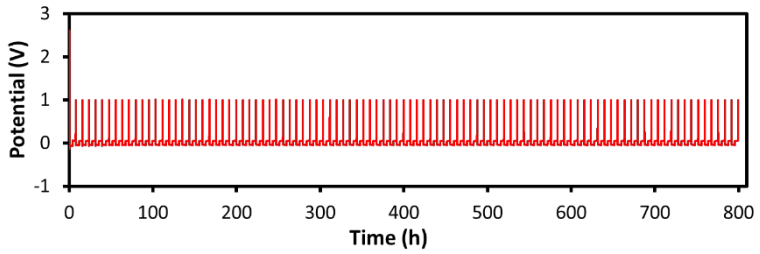

Figure H.42. Second replicate of voltage versus time profile for a cell at the 101st Li plating step cycled at alow rate of 0.47 mA/cm^2 to a capacity of 1.88 mAh/cm^2.

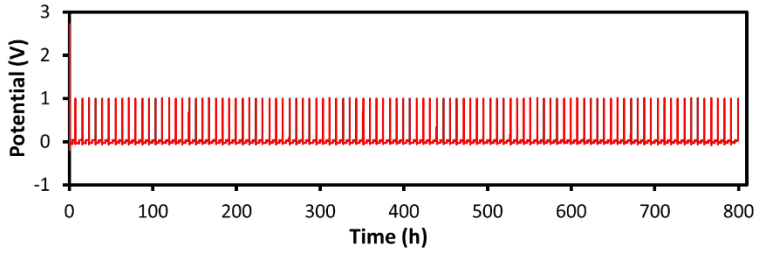

Figure H.43. Third replicate of voltage versus time profile for a cell at the 101st Li plating step cycled at a low rate of 0.47 mA/cm^2 to a capacity of 1.88 mAh/cm^2.

Optical Evidence of Li Plating within Stacked Separators

To provide further evidence that the material within and between the separator is comprised of SEI and Limetal, we have disassembled cells and peeled the separator layers apart from one another (Figure H.44). Theimage below shows a part of the top Celgard separator cut and peeled away from the other one, such that we imaged between the two separators. There is a very clear large patch of metallic Li metal as well as a lot of black material, which has been documented to be SEI in this electrolyte.

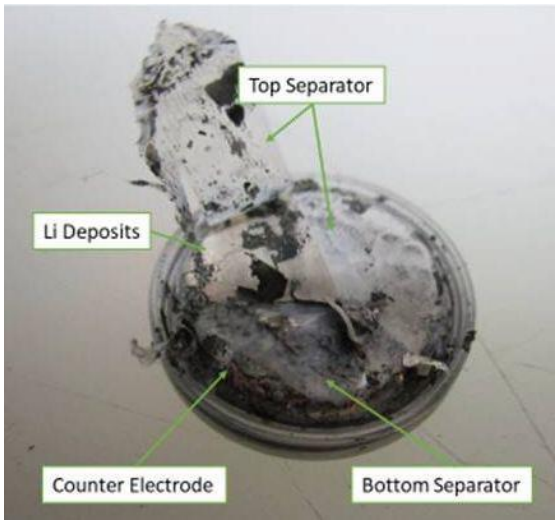

Figure H.44. Optical image during coin cell disassembly of separator being removed from a cell at the 101st Li plating step after cycling at a high rate of 1.88 mA/cm^2 to a capacity of 1.88 mAh/cm^2.

Analysis of Carbonate Electrolyte

Figure H.45 shows the plating results for 1 M LiPF6 in 3/7 ethyl carbonate/ethyl methyl carbonate with 10 wt.% fluoroethylene carbonate and 2 wt.% vinyl carbonate with two stacked Celgard 2325 separators. Thecell failed, though from the images we expect that the failure was related to the depleted supply of Li on the counter electrode rather than separator failure. Figure H.46 shows the potential vs time where the cell cycled at 0.94 mA/cm^2 then failed catastrophically after 29 cycles, as Li metal does not cycle well in carbonate electrolytes. The inefficiency of Li cycling, particularly at high current in carbonate electrolytes,causes failure to proceed by a different mechanism, the loss of Li inventory.

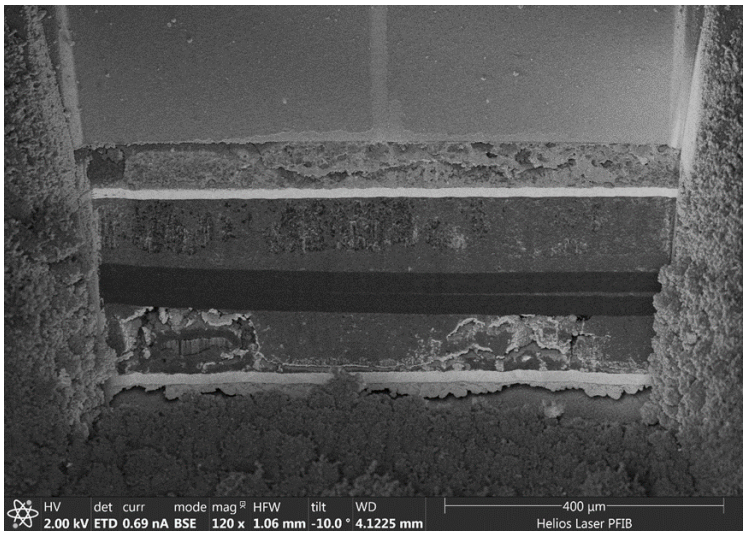

Figure H.45. Unprocessed SEM image of the 101st Li plating step in 1 M $LiPF_6$ in 3 EC/7 EMC with 10 wt.% FEC and 2 wt.% VC after cycling at a medium rate of 0.94 mA/cm^2 to a capacity of 1.88 mAh/cm^2.

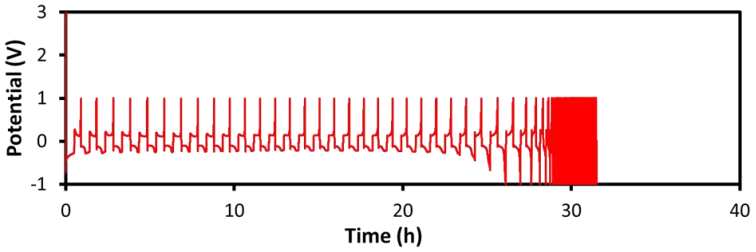

Figure H.46. Voltage versus time profile for a 1 M $LiPF_6$ in 3 EC/7 EMC with 10 wt.% FEC and 2 wt.% VC cell at the 101st Li plating step cycled at a medium rate of 0.94 mA/cm^2 to a capacity of 1.88 mAh/cm^2.

Analysis of Celgard 2400 Separator

We also examined several replicates with two Celgard 2400 separators rather than two Celgard 2325 separators, with 2.8 M LiFSI in DME electrolyte. Celgard 2325 is commonly used with Li metal cycling because the increased tortuosity of the trilayer polypropylene/polyethylene/polypropylene design could complicate the path for shorts. We show in the manuscript that the trilayers also delaminate and enable separator shredding. Celgard 2400 has a through-hole single layer separator design made up of polypropylene. With two stacked Celgard 2400 separators, we saw no evidence of the most common failure mechanism that was evident in cells made with Celgard 2325 (Figures H.47-H.48). We observed similar results with SEI building up between the two Celgard 2400 separators (lightened layers in the middle of stack) and some deformation of the Celgard, indicated by the uneven thickness of the Celgard layers on theleft of the image in Figure H.47. Four of the seven replicate Celgard 2400 cells cycled with an increase in polarization with cycling but did not fail to deliver capacity and did not polarize to -1 V (Figures H.49-H.55). The three remaining cells all suffered from very obvious short circuits. It appears that Celgard 2400 cells

are more likely to short due to the through-hole design and lack of tortuosity. However, several of the Celgard 2325 trilayers (Figures H.26-H.40) cause failure through more extreme polarization caused by loss of lithium inventory or SEI building up between the electrodes in the separator layers.

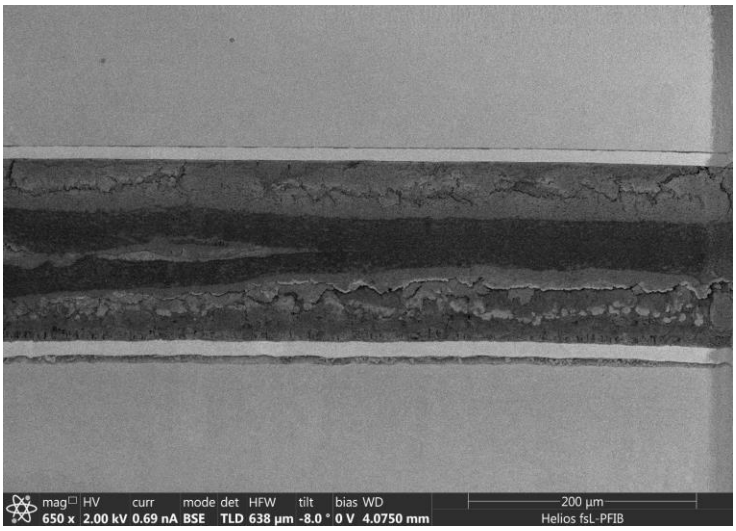

Figure H.47. Unprocessed SEM image of the 101st Li plating step assembled with two stacked Celgard 2400separators after cycling at a high rate of 1.88 mA/cm^2 to a capacity of 1.88 mAh/cm^2.

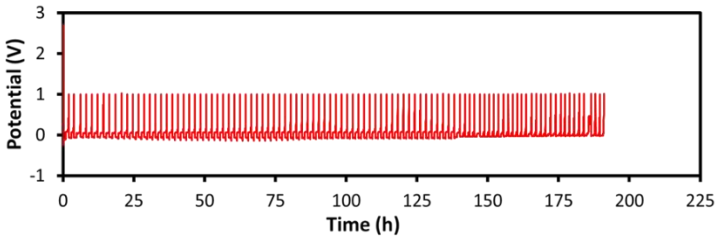

Figure H.48. Voltage versus time profile for a cell with Celgard 2400 separators at the 101st Li plating stepcycled at a high rate of 1.88 mA/cm^2 to a capacity of 1.88 mAh/cm^2.

Replicates of Electrochemical Data with Celgard 2400

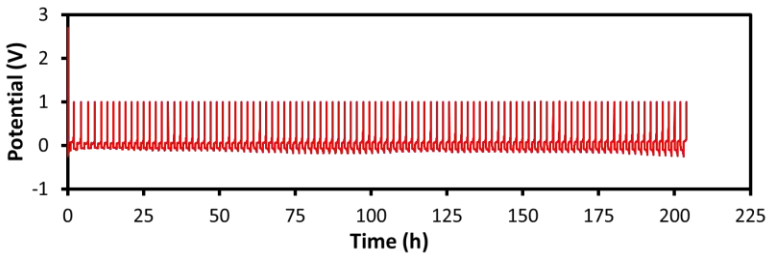

Figure H.49. First replicate voltage versus time profile for a cell with Celgard 2400 separators at the 101stLi plating step cycled at a high rate of 1.88 mA/cm^2 to a capacity of 1.88 mAh/cm^2

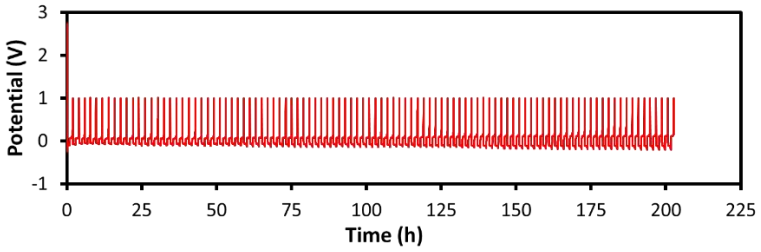

Figure H.50. Second replicate voltage versus time profile for a cell with Celgard 2400 separators at the 101stLi plating step cycled at a high rate of 1.88 mA/cm^2 to a capacity of 1.88 mAh/cm^2.

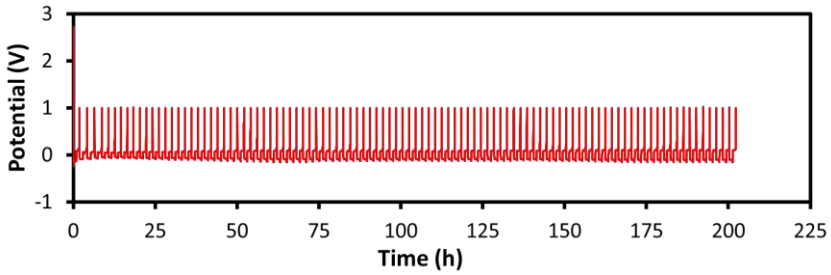

Figure H.51. Third replicate voltage versus time profile for a cell with Celgard 2400 separators at the 101st Li plating step cycled at a high rate of 1.88 mA/cm^2 to a capacity of 1.88 mAh/cm^2.

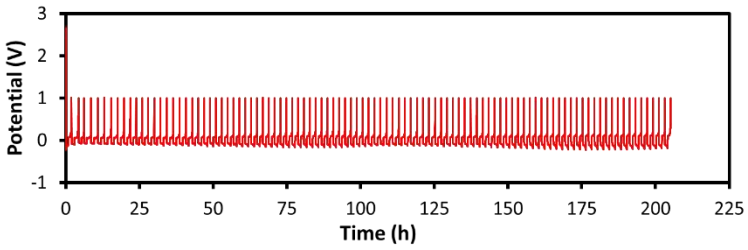

Figure H.52. Fourth replicate voltage versus time profile for a cell with Celgard 2400 separators at the 101st Li plating step cycled at a high rate of 1.88 mA/cm^2 to a capacity of 1.88 mAh/cm^2.

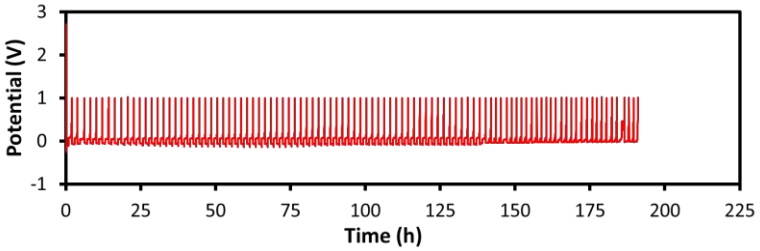

Figure H.53. Fifth replicate voltage versus time profile for a cell with Celgard 2400 separators at the 101st Li plating step cycled at a high rate of 1.88 mA/cm^2 to a capacity of 1.88 mAh/cm^2.

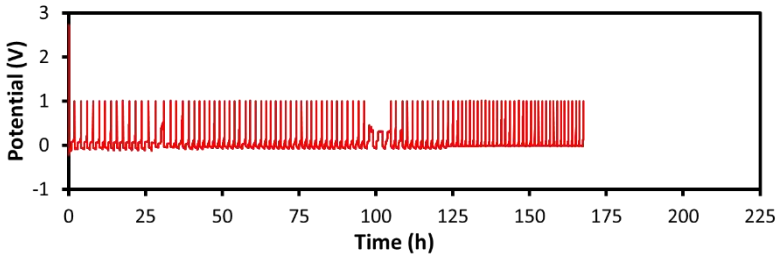

Figure H.54. Sixth replicate voltage versus time profile for a cell with Celgard 2400 separators at the 101stLi plating step cycled at a high rate of 1.88 mA/cm^2 to a capacity of 1.88 mAh/cm^2.

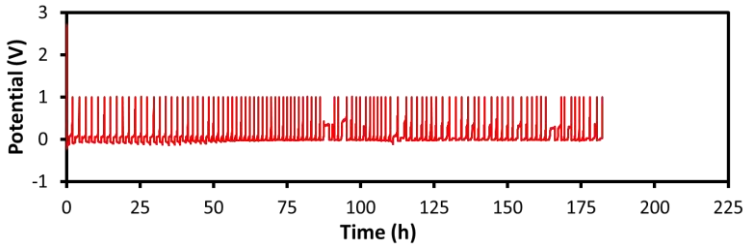

Figure H.55. Seventh replicate voltage versus time profile for a cell with Celgard 2400 separators at the101st Li plating step cycled at a high rate of 1.88 mA/cm^2 to a capacity of 1.88 mAh/cm^2

REFERENCES CITED

Chapter I

(1) Lin, Z.; McCreary, A.; Briggs, N.; Subramanian, S.; Zhang, K.; Sun, Y.; Li, X.; Borys, N. J.; Yuan, H.; Fullerton-Shirey, S. K.; Chernikov, A.; Zhao, H.; McDonnell, S.; Lindenberg, A. M.; Xiao, K.; Le Roy, B. J.; Drndić, M.; Hwang, J. C. M.; Park, J.; Chhowalla, M.; Schaak, R. E.; Javey, A.; Hersam, M. C.; Robinson, J.; Terrones, M. 2D Materials Advances: From Large Scale Synthesis and Controlled Heterostructures to Improved Characterization Techniques, Defects and Applications. In *2D Materials*; 2016.

(2) Yankowitz, M.; Ma, Q.; Jarillo-Herrero, P.; LeRoy, B. J. Van Der Waals Heterostructures Combining Graphene and Hexagonal Boron Nitride. *Nature Reviews Physics*. 2019.

(3) Mas-Ballesté, R.; Gómez-Navarro, C.; Gómez-Herrero, J.; Zamora, F. 2D Materials: To Graphene and Beyond. *Nanoscale*. 2011.

(4) Gao, E.; Lin, S. Z.; Qin, Z.; Buehler, M. J.; Feng, X. Q.; Xu, Z. Mechanical Exfoliation of Two-Dimensional Materials. *J. Mech. Phys. Solids* **2018**, *115*.

(5) Yi, M.; Shen, Z. A Review on Mechanical Exfoliation for the Scalable Production of Graphene. *Journal of Materials Chemistry A*. 2015.

(6) Cun, H.; Macha, M.; Kim, H. K.; Liu, K.; Zhao, Y.; LaGrange, T.; Kis, A.; Radenovic, A. Wafer-Scale MOCVD Growth of Monolayer MoS2 on Sapphire and SiO2. *Nano Res.* **2019**, *12* (10).

(7) Johnson, D. C. Controlled Synthesis of New Compounds Using Modulated Elemental Reactants. *Curr. Opin. Solid State Mater. Sci.* **1998**.

(8) Westover, R.; Atkins, R. A.; Falmbigl, M.; Ditto, J. J.; Johnson, D. C. Self-Assembly of Designed Precursors: A Route to Crystallographically Aligned New Materials with Controlled Nanoarchitecture. *J. Solid State Chem.* **2016**, *236*.

(9) De Pablo, J. J.; Jones, B.; Kovacs, C. L.; Ozolins, V.; Ramirez, A. P. The Materials Genome Initiative, the Interplay of Experiment, Theory and Computation. *Current Opinion in Solid State and Materials Science*. 2014.

(10) Kalil Tom And Wadia, C. Materials Genome Initiative for Global Competitiveness. *Genome* **2011**, No. June.

(11) Jain, A.; Ong, S. P.; Hautier, G.; Chen, W.; Richards, W. D.; Dacek, S.; Cholia, S.; Gunter, D.; Skinner, D.; Ceder, G.; Persson, K. A. Commentary: The Materials Project: A Materials Genome Approach to Accelerating Materials Innovation. *APL Materials*. 2013.

(12) Disalvo, F. J. Solid-State Chemistry: A Rediscovered Chemical Frontier. *Science (80-.).* **1990**, *247* (4943).

(13) Meredig, B.; Agrawal, A.; Kirklin, S.; Saal, J. E.; Doak, J. W.; Thompson, A.; Zhang, K.; Choudhary, A.; Wolverton, C. Combinatorial Screening for New Materials in Unconstrained Composition Space with Machine Learning. *Phys. Rev. B - Condens. Matter Mater. Phys.* **2014**, *89* (9).

(14) Narayan, A.; Bhutani, A.; Rubeck, S.; Eckstein, J. N.; Shoemaker, D. P.; Wagner, L. K. Computational and Experimental Investigation for New Transition Metal Selenides and Sulfides: The Importance of Experimental Verification for Stability. *Phys. Rev. B* **2016**, *94* (4).

(15) Balogun, M. S.; Qiu, W.; Luo, Y.; Meng, H.; Mai, W.; Onasanya, A.; Olaniyi, T. K.; Tong, Y. A Review of the Development of Full Cell Lithium-Ion Batteries: The Impact of Nanostructured Anode Materials. *Nano Research*.

(16) Gauthier, M.; Carney, T. J.; Grimaud, A.; Giordano, L.; Pour, N.; Chang, H. H.; Fenning, D. P.; Lux, S. F.; Paschos, O.; Bauer, C.; Maglia, F.; Lupart, S.; Lamp, P.; Shao-Horn, Y. Electrode-Electrolyte Interface in Li-Ion Batteries: Current Understanding and New Insights. *Journal of Physical Chemistry Letters*. 2015.

(17) Liu, B.; Zhang, J. G.; Xu, W. Advancing Lithium Metal Batteries. *Joule*. 2018.

(18) Jungjohann, K. L.; Gannon, R. N.; Goriparti, S.; Randolph, S. J.; Merrill, L. C.; Johnson, D. C.; Zavadil, K. R.; Harris, S. J.; Harrison, K. L. Cryogenic Laser Ablation Reveals Short-Circuit Mechanism in Lithium Metal Batteries. *ACS Energy Lett.* **2021**, *6*, 2138–2144.

Chapter II

(1) Fister, L.; Li, X.; McConnell, J.; Novet, T.; Johnson, D. C. Deposition System for the Synthesis of Modulated, Ultrathin-film Composites. *J. Vac. Sci. Technol. A Vacuum, Surfaces, Film.* **1993**, *11* (6).

(2) Westover, R.; Atkins, R. A.; Falmbigl, M.; Ditto, J. J.; Johnson, D. C. Self-Assembly of Designed Precursors: A Route to Crystallographically Aligned New Materials with Controlled Nanoarchitecture. *J. Solid State Chem.* **2016**, *236*.

(3) Esters, M. Deposition Software for the Inficon IC6 Deposition Controller.

(4) Lipson, H. S. X-Ray Diffraction by B. E. Warren . *Acta Crystallogr. Sect. A* **1971**, *27* (2).

(5) Parratt, L. G. Surface Studies of Solids by Total Reflection of X-Rays. *Phys. Rev.* **1954**, *95* (2).

(6) Chason, E.; Mayer, T. M. Thin Film and Surface Characterization by Specular X-Ray Reflectivity. *Crit. Rev. Solid State Mater. Sci.* **1997**, *22* (1).

(7) Björck, M.; Andersson, G. GenX: An Extensible X-Ray Reflectivity Refinement Program Utilizing Differential Evolution. *J. Appl. Crystallogr.* **2007**, *40* (6).

(8) Hamann, D. M.; Bardgett, D.; Cordova, D. L. M.; Maynard, L. A.; Hadland, E. C.; Lygo, A. C.; Wood, S. R.; Esters, M.; Johnson, D. C. Sub-Monolayer Accuracy in Determining the Number of Atoms per Unit Area in Ultrathin Films Using X-Ray Fluorescence. *Chem. Mater.* **2018**, *30* (18).

(9) Sohlberg, K.; Pennycook, T. J.; Zhou, W.; Pennycook, S. J. Insights into the Physical Chemistry of Materials from Advances in HAADF-STEM. *Physical Chemistry Chemical Physics*. 2015.

(10) Nellist, P. D.; Pennycook, S. J. The Principles and Interpretation of Annular Dark-Field Z-Contrast Imaging. *Adv. Imaging Electron Phys.* **2000**, *113* (C), 147–203.

(11) Schneider, C. A.; Rasband, W. S.; Eliceiri, K. W. NIH Image to ImageJ: 25 Years of Image Analysis. *Nature Methods*. 2012.

(12) Mohammed, A.; Abdullah, A. Scanning Electron Microscopy (SEM): A Review. *Int. Conf. Hydraul. Pneum.* **2018**, *7* (January).

(13) Sezen, M. Focused Ion Beams (FIB) — Novel Methodologies and Recent Applications for Multidisciplinary Sciences. In *Modern Electron Microscopy*

(14) Schaffer, M.; Schaffer, B.; Ramasse, Q. Sample Preparation for Atomic-Resolution STEM at Low Voltages by FIB. *Ultramicroscopy* **2012**.

(15) D'Alfonso, A. J.; Freitag, B.; Klenov, D.; Allen, L. J. Atomic-Resolution Chemical Mapping Using Energy-Dispersive x-Ray Spectroscopy. *Phys. Rev. B - Condens. Matter Mater. Phys.* **2010**, *81* (10).

(16) Echlin, M. P.; Straw, M.; Randolph, S.; Filevich, J.; Pollock, T. M. The TriBeam System: Femtosecond Laser Ablation in Situ SEM. *Materials Characterization*. 2015.

(17) Echlin, M. P.; Mottura, A.; Torbet, C. J.; Pollock, T. M. A New TriBeam System for Three-Dimensional Multimodal Materials Analysis. *Rev. Sci. Instrum.* **2012**, *83* (2), 23701.

(18) Randolph, S. J.; Filevich, J.; Botman, A.; Gannon, R.; Rue, C.; Straw, M. In Situ Femtosecond Pulse Laser Ablation for Large Volume 3D Analysis in Scanning Electron Microscope Systems. *J. Vac. Sci. Technol. B, Nanotechnol. Microelectron. Mater. Process. Meas. Phenom.* **2018**, *36* (6), 06JB01.

Chapter III

(1) Lin, Z.; McCreary, A.; Briggs, N.; Subramanian, S.; Zhang, K.; Sun, Y.; Li, X.; Borys, N. J.; Yuan, H.; Fullerton-Shirey, S. K.; Chernikov, A.; Zhao, H.; McDonnell, S.; Lindenberg, A. M.; Xiao, K.; Le Roy, B. J.; Drndić, M.; Hwang, J. C. M.; Park, J.; Chhowalla, M.; Schaak, R. E.; Javey, A.; Hersam, M. C.; Robinson, J.; Terrones, M. 2D Materials Advances: From Large Scale Synthesis and Controlled Heterostructures to Improved Characterization Techniques, Defects and Applications. In *2D Materials*; **2016**, *3*(4), 042001.

(2) Novoselov, K. S.; Mishchenko, A.; Carvalho, A.; Castro Neto, A. H. 2D Materials and van Der Waals Heterostructures. *Science.* **2016**, *353*(6298).

(3) Dean, C.; Young, A. F.; Wang, L.; Meric, I.; Lee, G. H.; Watanabe, K.; Taniguchi, T.; Shepard, K.; Kim, P.; Hone, J. Graphene Based Heterostructures. *Solid State Commun.* **2012,** *152*(15), 1275-1282.

(4) Zou, X.; Yakobson, B. I. An Open Canvas - 2D Materials with Defects, Disorder, and Functionality. *Acc. Chem. Res.* **2015**, *48*(1)*,* 73-80.

(5) Jiang, J.; Xu, T.; Lu, J.; Sun, L.; Ni, Z. Defect Engineering in 2D Materials: Precise Manipulation and Improved Functionalities. *Research* **2019**, *2019*.

(6) Yao, W.; Wu, B.; Liu, Y. Growth and Grain Boundaries in 2D Materials. *ACS Nano.* **2020**, *14*(8), 9320-9346.

(7) Hus, S. M.; Li, A. P. Spatially-Resolved Studies on the Role of Defects and Boundaries in Electronic Behavior of 2D Materials. *Progress in Surface Science.* **2017**, *92*(3), 176-201.

(8) Merrill, D. R.; Moore, D. B.; Bauers, S. R.; Falmbigl, M.; Johnson, D. C. Misfit Layer Compounds and Ferecrystals: Model Systems for Thermoelectric Nanocomposites. *Materials.* **2015**, *8*(4), 2000-2029.

(9) Merrill, D. R.; Moore, D. B.; Ditto, J.; Sutherland, D. R.; Falmbigl, M.; Winkler, M.; Pernau, H. F.; Johnson, D. C. The Synthesis, Structure, and Electrical Characterization of $(SnSe)_{1.2}TiSe_2$. *Eur. J. Inorg. Chem.* **2015,** *2015*(1), 83-91.

(10) Hamann, D. M.; Merrill, D. R.; Bauers, S. R.; Mitchson, G.; Ditto, J.; Rudin, S. P.; Johnson, D. C. Long-Range Order in $[(SnSe)_{1.2}]_1[TiSe_2]_1$ Prepared from Designed Precursors. *Inorg. Chem.* **2017**, *56*(6), 3499-3505.

(11) Hamann, D. M.; Bardgett, D.; Bauers, S. R.; Kasel, T. W.; Mroz, A. M.; Hendon, C. H.; Medlin, D. L.; Johnson, D. C. Influence of Nanoarchitecture on Charge Donation and the Electrical-Transport Properties in $[(SnSe)_{1+\delta}][TiSe_2]$QHeterostructures. *Chem. Mater.* **2020**, *32*(13), 5802-5813.

(12) Göhler, F.; Hamann, D. M.; Rösch, N.; Wolff, S.; Logan, J. T.; Fischer, R.; Speck, F.; Johnson, D. C.; Seyller, T. Electronic Structure of Designed $[(SnSe)_{1+\delta}]_m[TiSe_2]_2$ Heterostructure Thin Films with Tunable Layering Sequence. *J. Mater. Res.* **2019**, *34*(12), 1965-1975.

(13) Hamann, D. M.; Lygo, A. C.; Esters, M.; Merrill, D. R.; Ditto, J.; Sutherland, D. R.; Bauers, S. R.; Johnson, D. C. Structural Changes as a Function of Thickness in $[(SnSe)_{1+\delta}]_mTiSe_2$ Heterostructures. *ACS Nano* **2018**, *12*(2), 1285-1295.

(14) Li, Z.; Bauers, S. R.; Poudel, N.; Hamann, D.; Wang, X.; Choi, D. S.; Esfarjani, K.; Shi, L.; Johnson, D. C.; Cronin, S. B. Cross-Plane Seebeck Coefficient Measurement of Misfit Layered Compounds $(SnSe)_n(TiSe_2)_n$ (n = 1,3,4,5). *Nano Lett.* **2017,** *17*(3), 1978-1986.

(15) Johnson, D. C. Controlled Synthesis of New Compounds Using Modulated Elemental Reactants. *Curr. Opin. Solid State Mater. Sci.* **1998,** *3*(2), 159-167.

(16) Schaffer, M.; Schaffer, B.; Ramasse, Q. Sample Preparation for Atomic-Resolution STEM at Low Voltages by FIB. *Ultramicroscopy.* **2012**, *114*, 62-71.

(17) Park, Y. C.; Park, B. C.; Romankov, S.; Park, K. J.; Yoo, J. H.; Lee, Y. B.; Yang, J. M. Use of Permanent Marker to Deposit a Protection Layer against FIB Damage in TEM Specimen Preparation. *J. Microsc.* **2014**, *255*(3), 180-187.

(18) Miller, A. M.; Hamann, D. M.; Hadland, E. C.; Johnson, D. C. Investigating the Formation of MoSe2and TiSe2Films from Artificially Layered Precursors. *Inorg. Chem.* **2020**, *59*(17), 12536-12544.

(19) Choi, W.; Choudhary, N.; Han, G. H.; Park, J.; Akinwande, D.; Lee, Y. H. Recent Development of Two-Dimensional Transition Metal Dichalcogenides and Their Applications. *Materials Today.* **2017**, *20*(3), 116-130.

(20) Vishwanath, S.; Liu, X.; Rouvimov, S.; Basile, L.; Lu, N.; Azcatl, A.; Magno, K.; Wallace, R. M.; Kim, M.; Idrobo, J. C.; Furdyna, J. K.; Jena, D.; Xing, H. G. Controllable Growth of Layered Selenide and Telluride Heterostructures and Superlattices Using Molecular Beam Epitaxy. *J. Mater. Res.* **2016**, *31*(7), 900-910.

(21) Yankowitz, M.; Ma, Q.; Jarillo-Herrero, P.; LeRoy, B. J. Van Der Waals

Heterostructures Combining Graphene and Hexagonal Boron Nitride. *Nature Reviews Physics*. **2019,** *1*(2), 112-125.

(22) Rouxel, J.; Meerschaut, A.; Wiegers, G. A. Chalcogenide Misfit Layer Compounds. *J. Alloys Compd.* **1995**, *229*(1), 144-157.

(23) Kalläne, M.; Rossnagel, K.; Marczynski-Bühlow, M.; Kipp, L.; Starnberg, H. I.; Stoltz, S. E. Stabilization of the Misfit Layer Compound $(PbS)_{1.13}TaS_2$ by Metal Cross Substitution. *Phys. Rev. Lett.* **2008**, *100*(6), 065502.

(24) Song, Y. J.; Kim, M. J.; Jung, W. G.; Kim, B. J.; Rhyee, J. S. Superconducting Properties of the Misfit-Layer Compound (SnSe)1.18(TiSe2)2. *Phys. Status Solidi Basic Res.* **2016**, *253*(8), 1517-1522.

(25) Schnering, H. G. von; Wiedemeier, H. The High Temperature Structure of β-SnS and ß-SnSe and the B16-to-B33 Type λ-Transition Path. *Zeitschrift für Krist. - Cryst. Mater.* **1981**, *156*(1-4), 143-150.

(26) Chattopadhyay, T.; Pannetier, J.; Von Schnering, H. G. Neutron Diffraction Study of the Structural Phase Transition in SnS and SnSe. *J. Phys. Chem. Solids* **1986**, *47*(9), 879-885.

(27) Sist, M.; Zhang, J.; Brummerstedt Iversen, B. Crystal Structure and Phase Transition of Thermoelectric SnSe. *Acta Crystallogr. Sect. B Struct. Sci. Cryst. Eng. Mater.* **2016**, *72*(3), 310-316.

(28) Falmbigl, M.; Alemayehu, M. B.; Merrill, D. R.; Beekman, M.; Johnson, D. C. In-Plane Structure of Ferecrystalline Compounds. *Cryst. Res. Technol.* **2015**, *50*(6), 464-472.

(29) Hirth, J. P. Dislocations, Steps and Disconnections at Interfaces. *J. Phys. Chem. Solids* **1994**, *55*(10), 985-989.

(30) Hirth, J. P.; Pond, R. C. Steps, Dislocations and Disconnections as Interface Defects Relating to Structure and Phase Transformations. *Acta Mater.* **1996**, *44*(12), 4749-4763.

(31) Roberts, D. M.; Bardgett, D.; Gorman, B. P.; Perkins, J. D.; Zakutayev, A.; Bauers, S. R. Synthesis of Tunable SnS-TaS_2 Nanoscale Superlattices. *Nano Lett.* **2020**, *20*(10), 7059-7067.

(32) Roberts, D. M.; Perkins, J. D.; Norman, A. G.; Stoldt, C. R.; Zakutayev, A.; Bauers, S. R. Amorphous Sulfide Heterostructure Precursors Prepared by Radio Frequency Sputtering. *J. Vac. Sci. Technol. B* **2019**, *37*(5), 051201.

(33) Lin, Q.; Tepfer, S.; Heideman, C.; Mortensen, C.; Nguyen, N.; Zschack, P.; Beekman, M.; Johnson, D. C. Influence of Selenium Vapor Postannealing on the Electrical Transport Properties of PbSe-WSe_2 Nanolaminates. *J. Mater. Res.* **2011**, *26*(15), 1866.

(34) Zhao, C.; Li, Z.; Fan, T.; Xiao, C.; Xie, Y. Defects Engineering with Multiple Dimensions in Thermoelectric Materials. *Research* **2020**, *2020*.

Chapter IV

(1) Disalvo, F. J. Solid-state chemistry: A rediscovered chemical frontier. *Science (80-.).* **247**, (1990).

(2) Fister, L. & Johnson, D. C. Controlling Solid-State Reaction Mechanisms Using Diffusion Length in Ultrathin-Film Superlattice Composites. *J. Am. Chem. Soc.* **114**, (1992).

(3) Kovnir, K. Predictive Synthesis. *Chem. Mater.* **0**, (2021).

(4) Zheleva, T., Jagannadham, K. & Narayan, J. Epitaxial growth in large-lattice-mismatch systems. *J. Appl. Phys.* **75**, (1994).

(5) Amsler, M. *et al.* Ternary mixed-anion semiconductors with tunable band gaps from machine-learning and crystal structure prediction. *Phys. Rev. Mater.* (2019)

(6) Hite, O. K. *et al.* Charge Density Wave Transition in (PbSe)1+δ(VSe2)n Compounds with n = 1, 2, and 3. *Chem. Mater.* (2017)

(7) Grosse, C. *et al.* Superconducting ferecrystals: Turbostratically disordered atomic-scale layered (PbSe) 1.14 (NbSe 2) n thin films. *Sci. Rep.* **6**, (2016).

(8) Falmbigl, M. *et al.* Influence of Defects on the Charge Density Wave of $([SnSe]_{1+\delta})_1(VSe_2)_1$ Ferecrystals. *ACS Nano* (2015)

(9) Smeller, M. M. *et al.* Structure of turbostratically disordered misfit layer compounds [(PbSe)0.99]1[WSe2]1, $[(PbSe)_{1.00}]_1[MoSe_2]_1$, and [(SnSe) 1.03]1[MoSe2]1. *Zeitschrift fur Anorg. und Allg. Chemie* **638**, (2012).

(10) Anderson, M. D. *et al.* Size-dependent structural distortions in one-dimensional nanostructures. *Angew. Chemie - Int. Ed.* **52**, (2013).

(11) Heideman, C. L. *et al.* Designed synthesis, structure, and properties of a family of ferecrystalline compounds [(PbSe)1.00]m(MoSe 2)n. *J. Am. Chem. Soc.* **135**, (2013).

(12) Heideman, C. L. & Johnson, D. C. Structural influence on transport properties in [(PbSe)1.00] m(MoSe2)n misfit layered compounds. *Semicond. Sci. Technol.* **29**, (2014).

(13) Johnson, D. C. Controlled synthesis of new compounds using modulated

elemental reactants. *Curr. Opin. Solid State Mater. Sci.* **3**, (1998).

(14) Hamann, D. M. *et al.* Sub-Monolayer Accuracy in Determining the Number of Atoms per Unit Area in Ultrathin Films Using X-ray Fluorescence. *Chem. Mater.* **30**, (2018).

(15) Schaffer, M., Schaffer, B. & Ramasse, Q. Sample preparation for atomic-resolution STEM at low voltages by FIB. *Ultramicroscopy* (2012)

(16) Morris, M. C. *et al.* STANDARD X-RAY DIFFRACTION POWDER PATTERNS. *NBS Monogr. (United States)* (1982)

(17) Bronsema, K. D., De Boer, J. L. & Jellinek, F. On the structure of molybdenum diselenide and disulfide. *ZAAC - J. Inorg. Gen. Chem.* **540**, (1986).

(18) Beekman, M. *et al.* Detection of nanoscale embedded layers using laboratory specular X-ray diffraction. *J. Appl. Phys.* **117**, (2015).

Chapter V

(1) Laursen, A. B.; Kegnas, S.; Dahl, S.; Chorkendorff, I. Molybdenum sulfides – efficient and viable materials for electroand photoelectocatalytic hydrogen evolution. *Energy Environ. Sci.* **2012**, *5*, 5577-5591.

(2) Ambrosi, A.; Sofer, Z.; Pumera, M. 2H → 1T phase transition and hydrogen evolution activity of MoS_2, $MoSe_2$, WS_2 and WSe_2 strongly depends on the MX_2 composition. *Chem. Commun*. **2015**, *51*, 8450.

(3) Yin, Y.; Zhang, Y.; Gao, T.; Yao,, T.; Zhang, X.; Han, J.; Wang, X.; Zhang, Z.; Xu, P.; Zhang, P.; Cao, X.; Song, B.; Jin, S. Synergistic Phase and Disorder Engineering in 1T-$MoSe_2$ Nanosheets for Enhanced Hydrogen-Evolution Reaction. *Adv. Mater.* **2017**, *29*, 1700311.

(4) Puthussery, J.; Seefeld, S.; Berry, N.; Gibbs, M.; Law, M. Colloidal Iron Pyrite (FeS_2) Nanocrystal Inks for Thin-Film Photovoltaics. *J. Am. Chem. Soc.* **2011**, *133*, 716.

(5) Feng, J.; Sun, X.; Wu, C. Z.; Peng, L. L.; Lin, C. W.; Hu, S. L.; Yang, J. L.; Xie, Y. Metallic Few-Layered VS_2 Ultrathin Nanosheets: High Two-Dimensional Conductivity for In-Plane Supercapacitors. *J. Am. Chem. Soc.* **2011**, *133*, 17832.

(6) Ding, S. J.; Zhang, D. Y.; Chen, J. S.; Lou, X. W. Facile synthesis of hierarchical MoS_2 microspheres composed of few-layered nanosheets and their lithium storage properties. *Nanoscale* **2012**, *4*, 95.

(7) Wilson, J. A.; Yoffe, A. D. The transition metal dichalcogenides discussion and interpretation of the observed optical, electrical, and structural properties. *Adv. Phys.*, **1969**, *18*, 193–335.

(8) Chhowalla, M.; Shin, H. S.; Eda, G.; Li, L. -J.; Loh, K. P.; Zhang, H. The chemistry of two-dimensionbal layered transition metal dichalcogenide nanosheets. *Nature Chemistry*. **2013**, *5*, 263.

(9) Kobayashi, K.; Yamauchi, J. Electronic structure and scanning-tunneling-microscopy image of molybdenum dichalcogenide surfaces. *Phys. Rev. B.* **1995**, *51*, 17085.

(10) Ding, Y.; Wang, Y.; Ni, J.; Shi, L.; Shi, S.; Tang, W. First principles study of structural, vibrational, and electrica properties of graphene-like MX2 (M = Mo, Nb, W, Ta; X = S, Se, Te) monolayers. *Physica B* **2011**, *406*, 2254–2260.

(11) Tongay, S.; Zhou, J.; Ataca, C.; Lo, K.; Matthews, T. S.; Li, J.; Grossman, J. C.; Wu, J. Thermally driven crossover from indirect toward direct bandgap in 2D semiconductors: MoSe2 versus MoS2. *Nano Lett.* **2012**, *12*, 5576−5580.

(12) Splendiani, A.; Sun, L.; Zhang, Y.; Li, T.; Kim, T.; Chim, C.-Y.; Galli, G.; Wang, F. Emergin Photoluminescences in Monolayer MoS2. *Nano Lett.* **2010**, *10*, 1271–1275.

(13) Yu, Z. G.; Yakosen, B. I.; Zhang, Y.-W. Realizing Indirect-to-Direct Band Gap Transition in Few-Layer Two-Dimensional MX2 (M = Mo, W; X = S, Se). *ACS Appl. Energy Mater.* **2018**, *1*, 4115−4121

(14) Steinhoff, A.; Kim, J. -H.; Jahnke, F.; Rosner, M.; Kim, D. -S.; Lee, C.; Han, G. H.; Jeong, M. S.; Wehling, T. O.; Gies, C. Efficient Excitonic Photoluminescence in Direct and Indirect Band Gap Monolayer MoS_2. *Nano Lett.* **2015**, *15*, 6841−6847.

(15) Zhao, W.; Ghorannevis, Z.; Chu, L.; Toh, M.; Kloc, C.; Tan, P. -H.; Eda, G. Evolution of electronic structure in atomically thin sheets of WS_2 and WSe_2. *ACS Nano.* **2013**, *7*, 791-797.

(16) McCreary, K. M.; Hanbicki, A. T.; Jernigan, G. G.; Culbertson, J. C.; Jonker, B. T. The effect of Preparation Conditions on Raman and Photoluminescence of Monolayer WS_2. *Sci. Rep.* **2016**, *6*, 19159.

(17) Hermann, A. M.; Somoano, R.; Hadek, V.; Rembaum, A. Electrical

Resistivity of Intercalated Molybdenum Disulfide. *Solid State Communications*. **1973**, *13*, 1065.

(18) Py, M. A.; Haering, R. R. Structureal destabilization induced by lithium intercalation in MoS_2 and related compounds. *Can. J. Phys.* **1983**, *61*, 76.

(19) Kappera, R.; Voiry, D.; Yalcin, S. E.; Branch, B.; Gupta, G.; Mohite, A. D.; Chhowalla, M. Phase-engineered low-resistance constacts for ultrathin MoS_2 transistors. *Nat. Materials*. **2014**, *12*, 1128.

(20) Friedman, A. L.; Hanbicki, A. T.; Perkins, F. K.; Jernigan, G. G.; Culbertson, J. C.; Campbell, P. M. Evidence for Chemical Vapor Induced 2H to 1T Phase Transition in MoX_2 (X = Se, S) Transition Metal Dichalcogenide Films. *Scientific Reports*. **2017**, *7*, 3836.

(21) Rudorff, W. Alkali Metal Intercalation Compounds of Transition Metal Chalcogenides: TX_2, TX_3, and TX_4 Chalcogenides. *Chimia*, **1965**, *489*.

(22) Schöllhorn, R.; Weiss, A. Cation exchange reactions and layer solvate complexes of ternary phases M_xMoS_2. *Journal of the Less-Common Metals*, **1974**, *36*, 229-236.

(23) Murphy, D.; Di Salvo, F.; Hull, G.; Waszczak, J. Convenient Preparation and Physical Properties of Lithium Intercalation Compounds of Group 4B and 5B Layered Transition Metal Dichalcogenides. *Inorg. Chem.* **1976**, *15*, 17.

(24) Schöllhorn, R.; Meyer, H. Cathodic reduction of layered transition metal chalcogenides. *Mat. Res. Bull.* **1974**, *9*, 1237.

(25) Haering, R. R.; Stiles, J. A. R.; Brandt, K. Lithium Molybdenum Disulphide Battery Cathode. US Patent 4, 224, 390, September 23, 1980.

(26) Radisavljevic, B.; Whitwick, M. B.; Kis, A. Integrated Circuits and Logic Operations Based on Single-Layer MoS2. *ACS Nano* **2011**, *5*, 9934–9938.

(27) Cheng, X.B.; Zhang, R.; Zhao, C.Z.; Zhang Q. Toward Safe Lithium Metal Anode in Rechargeable Batteries: A Review. *Chem. Rev.*, **2017**, *117*, 10403-10473.

(28) Weigers, G. A. Misfit layer compounds: Structures and physical properties. *Prog. Solid. St. Chem*. **1996**, *24*, 1-139.

(29) Hadland, E. C.; Gohler, F.; Mitchson, G.; Fender. S. S.; Schmidt, C.;

Zahn, D. R. T.; Seyller, T.; Johnson, D. C. Synthesis and Properties of $(BiSe)_{0.97}MoSe_2$: A Heterostructure Containing Both 2H-$MoSe_2$ and 1T-$MoSe_2$. *Chem. Mater.* **2019**, *31*, 5824.

(30) Lygo, A. C.; Hamann, D. M.; Moore, D. B.; Merrill, D. R.; Ditto, J.; Esters, M.; Orlowicz, J.; Wood, S. R.; Johnson, D. C. Kinetically Controlled Formation and Decomposition of Metastable $[(BiSe)_{1+\delta}]_m[(TiSe_2)]_m$ Compounds. *J. Am. Chem. Soc.* **2018**, *140*, 3385−3393.

(31) Lygo, A. C.; Wood, S. R.; Ditto, J.; Johnson, D. C. Syntheis of $(BiSe)_{1+\delta}(Bi_2Se_3)1+\gamma(BiSe)_{1+\delta}TiSe_2$ by Directed Self-Assembly of a Designed Precursor. *Chem. Mater.* **2019**, *31*, 216.

(32) Hamann, D. M., Bardgett, D., Cordova, D. L. M., Maynard, L. A., Hadland, E. C, Lygo, A. C., Wood, S. R., Esters, M., and Johnson, D. C. Sub-Monolayer Accuracy in Determining the Number of Atoms per Unit Area in Ultrathin Films Using X-ray Fluorescence. *Chem. Mater.* **2018**, *30*, 6209.

(33) Schaffer, M.; Schaffer, B.; Ramasse, Q. Sample preparation for atomic-resolution STEM at low voltages by FIB. *Ultramicroscopy*, **2012**, *114*, 62-71.

(34) Miller, A. M.; Hamann, D. M.; Hadland, E. C.; Johnson, D. C. Investigating the Formation of $MoSe_2$ and $TiSe_2$ Films form Artificially Layered Precursors. *Inorg. Chem.* **2020**, *59*, 12536–12544.

(35) Mitchson, G.; Falmbigl, M.; Ditto, J.; Johnson, D. C. Antiphase Boundaries in the Turbostratically Disordered Misfit Compound $(BiSe)_{1+\delta}NbSe_2$. *Inorg. Chem.* **2015**, *54*, 10309.

(36) Smeller, M. M.; Heideman, C. L.; Lin, Q.; Beekman, M. Anderson, M. D.; Zschack, P.; Anderson, I, M.; Johnson, D. C. Structure of Turbostratically Disordered Misfit Layer Compounds $[(PbSe)_{0.99}]_1[WSe_2]_1$, $[(PbSe)_{1.00}]_1[MoSe_2]_1$, and $[(SnSe)_{1.03}]1[MoSe_2]_1$. *Z. Anorg. Allg. Chem.* **2012**, *638*, 2632.

(37) Moore, D. B.; Beekman, M.; Disch, S.; Zschack, P.; Hausler, I.; Neumann, W.; Johnson, D. C. Synthesis, Structure, and Properties of Turbostratically Disordered $(PbSe)_{1.18}(TiSe_2)_2$. *Chem. Mater.* **2013**, *25*, 2404.

(38) Grosse, C.; Alemayehu, M. B.; Falmbigl, M.; Mogilatenko, A.; Chiatti, O.; Johnson, D. C.; Fischer, S. F. Superconducting ferecrystals: turbostratically disordered atomic-scale layered $(PbSe)_{1.14}(NbSe_2)_n$ thin

films. *Sci. Rep.* **2016**, *6*, 33457.

(39) Yu, Y.; Nam, G.-H.; He, Q.; Wu, X.-J.; Zhang, K.; Yang, Z.; Chen, J.; Ma, Q.; Zhao, M.; Liu, Z.; Ran, F.-R.; Wang, X.; Li, H.; Huang, X.; Li, B.; Xiong, Q.; Zhang, Q.; Liu, Z.; Gu, L.; Du, Y.; Huang, W.; Zhang, H. High phase-purity 1T'-MoS_2- and 1T'-$MoSe_2$-layered crystals. *Nat. Chem*, **2018**, 10(6), 638.

(40) Esters, M.; Henning, R. G.; Johnson, D. C. Insights into the Charge-Transfer Stabilization of Heterostructure Components with Unstable Bulk Analogs. *Chem. Mater.* **2018**, *30*, 4738.

(41) Mitchson, G.; Hadland, E. C.; Gohler, F.; Wanke, M.; Esters, M.; Ditto, J.; Bigwood, E.; Ta, K.; Henning, R. G.; Seyller, T.; Johnson, D. C. Structur Changes in 2D BiSe Bilayers as n Increases in $(BiSe)_{1+\delta}(NbSe2)_n$ (n = 1-4) Heterostructures. *ACS Nano* **2016**, *10*, 9489.

(42) Hadland, E. C.; Jang, H.; Wolff, N.; Fischer, R.; Lygo, A. C.; Mitchson, G.; Li, D.; Kienle, L.; Cahill, D. G.; Johnson, D. C. Ultralow thermal conductivity of turbostratically disordered $MoSe_2$ ultrathin films an implications for heterostructures. *Nanotechnology*. **2019**, *30*, 285401.

Chapter VI

(1) Trost, B. M.; Dong, G. Total Synthesis of Bryostatin 16 Using Atom-Economical and Chemoselective Approaches. *Nature* **2008**, *456* (7221), 485−488.

(2) Langmuir, I. The Arrangement of Electrons in Atoms and Molecules. *J. Am. Chem. Soc.* **1919**, *41* (6), 868−934.

(3) Pyykkö, P. Understanding the Eighteen-Electron Rule. *J. Organomet. Chem.* **2006**, *691* (21), 4336−4340.

(4) Wu, Y.; D'Agostino, C.; Holland, D. J.; Gladden, L. F. In Situ Study of Reaction Kinetics Using Compressed Sensing NMR. *Chem. Commun.* **2014**, *50* (91), 14137−14140.

(5) Capocasa, G.; Sessa, F.; Tavani, F.; Monte, M.; Olivo, G.; Pascarelli, S.; Lanzalunga, O.; Di Stefano, S.; D'Angelo, P. Coupled X-Ray Absorption/UV-Vis Monitoring of Fast Oxidation Reactions Involving a Nonheme Iron-Oxo Complex. *J. Am. Chem. Soc.* **2019**, *141* (6), 2299−2304.

(6) Huang, Z.; Dong, G. Site-Selectivity Control in Organic Reactions: A Quest To Differentiate Reactivity among the Same Kind of Functional Groups. *Acc. Chem.*

Res. **2017**, *50*, 465−471.

(7) Corey, E. J. The Logic of Chemical Synthesis: Multistep Synthesis of Complex Carbogenic Molecules (Nobel Lecture). *Angew. Chem., Int. Ed. Engl.* **1991**, *30* (5), 455−465.

(8) Disalvo, F. J. Solid-State Chemistry: A Rediscovered Chemical Frontier. *Science (Washington, DC, U. S.)* **1990**, *247*, 649−655.

(9) Jansen, M. A Concept for Synthesis Planning in Solid-State Chemistry. *Angew. Chem., Int. Ed.* **2002**, *41* (20), 3746−3766.

(10) Pienack, N.; Bensch, W. In-Situ Monitoring of the Formation of Crystalline Solids. *Angew. Chem., Int. Ed.* **2011**, *50* (9), 2014−2034.

(11) Kanatzidis, M. G.; Pöttgen, R.; Jeitschko, W. The Metal Flux: A Preparative Tool for the Exploration of Intermetallic Compounds. *Angew. Chem., Int. Ed.* **2005**, *44* (43), 6996−7023.

(12) Xu, Y.; Musumeci, V.; Aymonier, C. Chemistry in Supercritical Fluids for the Synthesis of Metal Nanomaterials. *React. Chem. Eng.* **2019**, *4* (12), 2030−2054.

(13) Hagenmuller, P. *Preparative Methods in Solid State Chemistry*; Academic Press: New York, 1972.

(14) Shoemaker, D. P.; Chung, D. Y.; Mitchell, J. F.; Bray, T. H.; Soderholm, L.; Chupas, P. J.; Kanatzidis, M. G. Understanding Fluxes as Media for Directed Synthesis: In Situ Local Structure of Molten Potassium Polysulfides. *J. Am. Chem. Soc.* **2012**, *134* (22), 9456−9463.

(15) Kohlmann, H. Looking into the Black Box of Solid-State Synthesis. *Eur. J. Inorg. Chem.* **2019**, *2019* (39−40), 4174−4180.

(16) Marbella, L. E.; Millstone, J. E. NMR Techniques for Noble Metal Nanoparticles. *Chem. Mater.* **2015**, *27* (8), 2721−2739.

(17) Mi, J. L.; Jensen, K. M. Ø.; Tyrsted, C.; Bremholm, M.; Iversen, B. B. In Situ Total X-Ray Scattering Study of the Formation Mechanism and Structural Defects in Anatase TiO_2 Nanoparticles under Hydrothermal Conditions. *CrystEngComm* **2015**, *17* (36), 6868−6877.

(18) Xu, H.; Sommer, S.; Broge, N. L. N.; Gao, J.; Iversen, B. B. The Chemistry of Nucleation: In Situ Pair Distribution Function Analysis of

Secondary Building Units During UiO-66 MOF Formation. *Chem. - Eur. J.* **2019**, *25* (8), 2051−2058.

(19) Bøjesen, E. D.; Jensen, K. M. Ø.; Tyrsted, C.; Mamakhel, A.; Andersen, H. L.; Reardon, H.; Chevalier, J.; Dippel, A. C.; Iversen, B. B. The Chemistry of $ZnWO_4$ Nanoparticle Formation. *Chem. Sci.* **2016**, *7* (10), 6394−6406.

(20) Bauers, S. R.; Wood, S. R.; Jensen, K. M. Ø.; Blichfeld, A. B.; Iversen, B. B.; Billinge, S. J. L.; Johnson, D. C. Structural Evolution of Iron Antimonides from Amorphous Precursors to Crystalline Products Studied by Total Scattering Techniques. *J. Am. Chem. Soc.* **2015**, *137* (30), 9652−9658.

(21) Bøjesen, E. D.; Iversen, B. B. The Chemistry of Nucleation. *CrystEngComm* **2016**, *18* (43), 8332−8353.

(22) Dippel, A.-C.; Bindzus, N.; Saha, D.; Delitz, J. T.; Liermann, H.-P.; Wahlberg, N.; Becker, J.; Bøjesen, E. D.; Brummerstedt Iversen, B. Synchrotron Powder Diffraction at P02.1 at PETRA III: From Electron Density Distributions to in Situ Total Scattering. *Z. Anorg. Allg. Chem.* **2014**, *640* (15), 3094−3099.

(23) Bayer, B. C.; Kaindl, R.; Monazam, M. R. A.; Susi, T.; Kotakoski, J.; Gupta, T.; Eder, D.; Waldhauser, W.; Meyer, J. C. Atomic-Scale in Situ Observations of Crystallization and Restructur- ing Processes in Two-Dimensional MoS_2 Films. *ACS Nano* **2018**, *12* (8), 8758−8769.

(24) Nielsen, M. H.; Aloni, S.; De Yoreo, J. J. In Situ TEM Imaging of $CaCO_3$ Nucleation Reveals Coexistence of Direct and Indirect Pathways. *Science (Washington, DC, U. S.)* **2014**, *345* (6201), 1158−1162.

(25) Liu, C.; Malladi, S. K.; Xu, Q.; Chen, J.; Tichelaar, F. D.; Zhuge, X.; Zandbergen, H. W. In-Situ STEM Imaging of Growth and Phase Change of Individual CuAlX Precipitates in Al Alloy. *Sci. Rep.* **2017**, *7* (1), 1−8.

(26) West, A. R. *Solid State Chemistry and Its Applications*, 2nd ed.; John Wiley & Sons, Ltd: West Sussex, UK, 2014.

(27) Lau, S. S.; Feng, J. S. Y.; Olowolafe, J. O.; Nicolet, M. A. Iron Silicide Thin Film Formation at Low Temperatures. *Thin Solid Films* **1975**, *25* (2) 415−422.

(28) Stein, A.; Keller, S. W.; Mallouk, T. E. Turning down the Heat: Design and Mechanism in Solid-State Synthesis. *Science (Washington, DC, U. S.)*

1993, *259* (5101), 1558−1564.

(29) Chamorro, J. R.; Mcqueen, T. M. Progress toward Solid State Synthesis by Design. *Acc. Chem. Res.* **2018**, *51*, 2918−2925.

(30) Schafer, H. Preparative Solid State Chemistry: The Present Position. *Angew. Chem., Int. Ed. Engl.* **1971**, *10* (1), 43−50.

(31) De Yoreo, J.; Mandrus, D.; Soderholm, L.; Forbes, T.; Kanatzidis, M.; Wiesner, U.; Xu, T.; Tolbert, S.; Zawarotko, M.; Chan, J.; Mitchell, J.; Erlebacher, J.; Laskin, J.; Billinge, S.; Galli, G. *Report of the Basic Energy Sciences Workshop on Synthesis Science for Energy Relevant Technology*; US DOE, **2016**.

(32) Hamann, D. M.; Hadland, E. C.; Johnson, D. C. Heterostructures Containing Dichalcogenides-New Materials with Predictable Nanoarchitectures and Novel Emergent Properties. *Semicond. Sci. Technol.* **2017**, *32* (9), 093004.

(33) Hernan, L.; Morales, J.; Pattanayak, J.; Tirado, J. L. Preparation and Characterization of New Misfit Layer Selenides SnVSe 3 and SnNb 2 Se 5. *Chem. Lett.* **1991**, *20* (11), 1981−1984.

(34) Falmbigl, M.; Alemayehu, M. B.; Merrill, D. R.; Beekman, M.; Johnson, D. C. In-Plane Structure of Ferecrystalline Compounds. *Cryst. Res. Technol.* **2015**, *50* (6), 464−472.

(35) Bayard, M.; Sienko, M. J. Anomalous Electrical and Magnetic Properties of Vanadium Diselenide. *J. Solid State Chem.* **1976**, *19*, 325−329.

(36) Evans, B. L.; Hazelwood, R. A. Optical and Electrical Properties of SnSe2. *J. Phys. D: Appl. Phys.* **1969**, *2* (11), 1507−1516.

(37) Cottrell, A. *An Introduction to Metallurgy*, 2nd ed.; Edward Arnold Publishers, Ltd.: London, UK, **1975**.

(38) Fister, L.; Li, X.; McConnell, J.; Novet, T.; Johnson, D. C. Deposition System for the Synthesis of Modulated, Ultrathin-film Composites. *J. Vac. Sci. Technol., A* **1993**, *11* (6), 3014−3019.

(39) Hamann, D. M.; Bardgett, D.; Cordova, D. L. M.; Maynard, L. A.; Hadland, E. C.; Lygo, A. C.; Wood, S. R.; Esters, M.; Johnson, D. C. Sub-Monolayer Accuracy in Determining the Number of Atoms per Unit Area in Ultrathin Films Using X-Ray Fluorescence. *Chem. Mater.* **2018**, *30*

(18), 6209−6216.

(40) Toby, B. H.; Von Dreele, R. B. GSAS-II: The Genesis of a Modern Open-Source All Purpose Crystallography Software Package. *J. Appl. Crystallogr.* **2013**, *46* (2), 544−549.

(41) Rodríguez-Carvajal, J. FULLPROF: A Program for Rietveld Refinement and Pattern Matching Analysis. In *Abstracts of the Satellite Meeting on Powder Diffraction of the XV Congess of the IUCr*, Toulouse, France, **1990**; p 127.

(42) Schneemeyer, L. F.; Stacy, A.; Sienko, M. J. Effect of Nonstoichiometry on the Periodic Lattice Distortion in Vanadium Diselenide. *Inorg. Chem.* **1980**, *19* (9), 2659−2662.

(43) Holy, V.; Pietsch, U.; Baumbach, T. *High-Resolution X-Ray Scattering from Thin Films and Multilayers*; Springer Berlin Heidelberg: Germany, 1999.

(44) Stierle, A.; Vlieg, E. Surface Sensitive X-Ray Diffraction Methods. *In Modern Diffraction Methods;* Mittemeijer, E. J., Welsel, U., Eds.; Wiley-VCH Verlag & Co.: Weinheim, Germany, 2013; pp 221−258.

(45) Woolfson, M. M. *An Introduction to X-Ray Crystallography*, 2nd ed.; Cambridge University Press: Cambridge, UK, 1997.

(46) Callister, W. D. J.; Rethwisch, D. G. *Materials Science and Engineering: An Introduction*, 8th ed.; John Wiley and Sons Inc.: Hoboken, NJ, 2010.

(47) Shimada, T.; Ohuchi, F. S.; Parkinson, B. A. Thermal Decomposition of SnS_2 and $SnSe_2$: Novel Molecular-beam Epitaxy Sources for Sulfur and Selenium. *J. Vac. Sci. Technol., A* **1992**, *10* (3), 539−542.

(48) Cordova, D. L. M.; Kam, T. M.; Fender, S. S.; Tsai, Y. H.; Johnson, D. C. Strong Non-Epitaxial Interactions: Crystallographi- cally Aligned PbSe on VSe_2. *Phys. Status Solidi A* **2019**, *216* (15), 1800896.

(49) Atkins, R.; Disch, S.; Jones, Z.; Haeusler, I.; Grosse, C.; Fischer, S. F.; Neumann, W.; Zschack, P.; Johnson, D. C. Synthesis, Structure and Electrical Properties of a New Tin Vanadium Selenide. *J. Solid State Chem.* **2013**, *202*, 128−133.

(50) Beekman, M.; Rodriguez, G.; Atkins, R.; Kunert, J.; Moore, D. B.; Johnson, D. C. Detection of Nanoscale Embedded Layers Using

Laboratory Specular X-Ray Diffraction. *J. Appl. Phys.* **2015**, *117* (18), 185306.

(51) Atkins, R.; Dolgos, M.; Fiedler, A.; Grosse, C.; Fischer, S. F.; Rudin, S. P.; Johnson, D. C. Synthesis and Systematic Trends in Structure and Electrical Properties of $[(SnSe)_{1.15}]_m(VSe_2)_1$, m = 1, 2, 3, and 4. *Chem. Mater.* **2014**, *26* (9), 2862−2872.

(52) Björck, M.; Andersson, G. GenX: An Extensible X-Ray Reflectivity Refinement Program Utilizing Differential Evolution. *J. Appl. Crystallogr.* **2007**, *40* (6), 1174−1178.

(53) Hite, O. K.; Falmbigl, M.; Alemayehu, M. B.; Esters, M.; Wood, S. R.; Johnson, D. C. Charge Density Wave Transition in $(PbSe)_{1+\delta}(VSe_2)_n$ Compounds with n = 1, 2, and 3. *Chem. Mater.* **2017**, *29* (13) 5646−5653.

(54) Hite, O. K.; Nellist, M.; Ditto, J.; Falmbigl, M.; Johnson, D. C. Transport Properties of VSe2 Monolayers Separated by Bilayers of BiSe. *J. Mater. Res.* **2016**, *31* (7), 886−892.

(55) Hadland, E.; Jang, H.; Falmbigl, M.; Fischer, R.; Medlin, D. L.; Cahill, D. G.; Johnson, D. C. Synthesis, Characterization, and Ultralow Thermal Conductivity of a Lattice-Mismatched $SnSe_2(MoSe_2)_{1.32}$ Heterostructure. *Chem. Mater.* **2019**, *31* (15), 5699−5705.

(56) Van Aert, S.; Verbeeck, J.; Erni, R.; Bals, S.; Luysberg, M.; Van Dyck, D.; Van Tendeloo, G. Quantitative Atomic Resolution Mapping Using High-Angle Annular Dark Field Scanning Transmission Electron Microscopy. *Ultramicroscopy* **2009**, *109* (10), 1236−1244.

(57) Hamann, D. M.; Merrill, D. R.; Bauers, S. R.; Mitchson, G.; Ditto, J.; Rudin, S. P.; Johnson, D. C. Long-Range Order in $[(SnSe)_{1.2}]_1[TiSe_2]_1$ Prepared from Designed Precursors. *Inorg. Chem.* **2017**, *56* (6), 3499−3505.

(58) Falmbigl, M.; Putzky, D.; Ditto, J.; Esters, M.; Bauers, S. R.; Ronning, F.; Johnson, D. C. Influence of Defects on the Charge Density Wave of $([SnSe]_{1+\delta})_1(VSe_2)_1$ Ferecrystals. *ACS Nano* **2015**, *9* (8), 8440−8448.

(59) Westover, R.; Atkins, R. A.; Falmbigl, M.; Ditto, J. J.; Johnson, D. C. Self-Assembly of Designed Precursors: A Route to Crystallo- graphically Aligned New Materials with Controlled Nanoarchitecture. *J. Solid State Chem.* **2016**, *236,* 173−185.

(60) Falmbigl, M.; Esters, M.; Johnson, D. C. Formation of a Selenide-Based Heterostructure From a Designed Precursor†. *Cryst. Res. Technol.* **2017**, *52* (10), 1700067.

Chapter VII

(1) Hamann, D. M.; Hadland, E. C.; Johnson, D. C. Heterostructures Containing Dichalcogenides-New Materials with Predictable Nanoarchitectures and Novel Emergent Properties. *Semicond. Sci. Technol.* **2017**, *32*, No. 093004.

(2) Cheon, G.; Duerloo, K. A. N.; Sendek, A. D.; Porter, C.; Chen, Y.; Reed, E. J. Data Mining for New Two- and One-Dimensional Weakly Bonded Solids and Lattice-Commensurate Heterostructures. *Nano Lett.* **2017**, *17*, 1915−1923.

(3) Butler, S. Z.; Hollen, S. M.; Cao, L.; Cui, Y.; Gupta, J. A.; Gutierrez, H. R.; Heinz, T. F.; Hong, S. S.; Huang, J.; Ismach, A. F.; et al. Progress, Challenges, and Opportunities in Two-Dimensional Materials beyond Graphene. *ACS Nano* **2013**, *7*, 2898−2926.

(4) Khan, K.; Tareen, A. K.; Aslam, M.; Wang, R.; Zhang, Y.; Mahmood, A.; Ouyang, Z.; Zhang, H.; Guo, Z. Recent Developments in Emerging Two-Dimensional Materials and Their Applications. *J. Mater. Chem. C* **2020**, *8*, 387−440.

(5) Bernevig, B. A.; Zhang, S. C. Quantum Spin Hall Effect. *Phys. Rev. Lett.* **2006**, *96*, 106802.

(6) Marrazzo, A.; Gibertini, M.; Campi, D.; Mounet, N.; Marzari, N. Prediction of a Large-Gap and Switchable Kane-Mele Quantum Spin Hall Insulator. *Phys. Rev. Lett.* **2018**, *120*, 117701.

(7) Burkov, A. A.; Balents, L. Weyl Semimetal in a Topological Insulator Multilayer. *Phys. Rev. Lett.* **2011**, *107*, 127205.

(8) Mak, K. F.; Lee, C.; Hone, J.; Shan, J.; Heinz, T. F. Atomically Thin MoS2: A New Direct-Gap Semiconductor. *Phys. Rev. Lett.* **2010**, *105*, 2−5.

(9) Mu̇chler, L.; Zhang, H.; Chadov, S.; Yan, B.; Casper, F.; Ku̇bler, J.; Zhang, S. C.; Felser, C. Topological Insulators from a Chemist's Perspective. *Angew. Chem., Int Ed.* **2012**, *51*, 7221−7225.

(10) Ju, L.; Velasco, J.; Huang, E.; Kahn, S.; Nosiglia, C.; Tsai, H. Z.; Yang, W.; Taniguchi, T.; Watanabe, K.; Zhang, Y.; et al. Photoinduced Doping in Heterostructures of Graphene and Boron Nitride. *Nat. Nanotechnol.* **2014**, *9*, 348−352.

(11) Xu, K.; Wang, Y.; Zhao, Y.; Chai, Y. Modulation Doping of Transition Metal Dichalcogenide/Oxide Heterostructures. *J. Mater. Chem. C* **2017**, *5*, 376−381.

(12) Hadland, E. C.; Göhler, F.; Mitchson, G.; Fender, S. S.; Schmidt, C.; Zahn, D. R. T.; Seyller, T.; Johnson, D. C. Synthesis and Properties of (BiSe)0.97MoSe2: A Heterostructure Containing Both 2H-MoSe2 and 1T-MoSe2. *Chem. Mater.* **2019**, *31*, 5824−5831.

(13) Wu, W.; Wang, L.; Li, Y.; Zhang, F.; Lin, L.; Niu, S.; Chenet, D.; Zhang, X.; Hao, Y.; Heinz, T. F.; et al. Piezoelectricity of SingleAtomic-Layer MoS2 for Energy Conversion and Piezotronics. *Nature* **2014**, *514*, 470−474.

(14) Xin, C.; Zheng, J.; Su, Y.; Li, S.; Zhang, B.; Feng, Y.; Pan, F. Few-Layer Tin Sulfide: A New Black-Phosphorus-Analogue 2D Material with a Sizeable Band Gap, Odd-Even Quantum Confinement Effect, and High Carrier Mobility. *J. Phys. Chem. C* **2016**, *120* ,22663−22669.

(15) Lavini, F.; Calo, A.; Gao, Y.; Albisetti, E.; De Li, T.; Cao, T.; Li,`G.; Cao, L.; Aruta, C.; Riedo, E. Friction and Work Function Oscillatory Behavior for an Even and Odd Number of Layers in Polycrystalline MoS2. *Nanoscale* **2018**, *10*, 8304−8312.

(16) Guo, H.; Xiao, J.; Qu, J.; Legut, D.; Zhang, Q. Odd-Even Layer Effect of Bismuth Oxychalcogenide Nanosurfaces: A First-Principles Study. *J. Phys. Chem. C* **2019**, *123*, 24024−24030.

(17) Xiao, J.; Wang, Y.; Wang, H.; Pemmaraju, C. D.; Wang, S.; Muscher, P.; Sie, E. J.; Nyby, C. M.; Devereaux, T. P.; Qian, X.; et al. Berry Curvature Memory via Electrically Driven Stacking Transitions. *Nat. Phys.* **2020**, No. 01037.

(18) Frindt, R. F. Superconductivity in Ultrathin NbSe2 Layers. *Phys. Rev. Lett.* **1972**, *28*, 299−301.

(19) Novoselov, K. S.; Geim, A. K.; Morozov, S. V.; Jiang, D.; Zhang, Y.; Dubonos, S. V.; Grigorieva, I. V.; Firsov, A. A. Electric Field in Atomically Thin Carbon Films. *Science* **2004**, *306*, 666−669.

(20) Roddaro, S.; Pingue, P.; Piazza, V.; Pellegrini, V.; Beltram, F. The Optical Visibility of Graphene: Interference Colors of Ultrathin Graphite on SiO2. *Nano Lett.* **2007**, *7*, 2707−2710.

(21) Li, M. Y.; Chen, C. H.; Shi, Y.; Li, L. J. Heterostructures Based on Two-Dimensional Layered Materials and Their Potential Applications. *Mater. Today* **2016**, 322−335.

(22) Wang, J.; Zhang, Y. Topologic Connection between 2-D Layered Structures and 3-D Diamond Structures for Conventional Semiconductors. *Sci. Rep.* **2016**, *6*, 1−9.

(23) Wang, F. Q.; Zhang, S.; Yu, J.; Wang, Q. Thermoelectric Properties of Single-Layered SnSe Sheet. *Nanoscale* **2015**, *7*, 15962−15970.

(24) Tyagi, K.; Waters, K.; Wang, G.; Gahtori, B.; Haranath, D.; Pandey, R. Thermoelectric Properties of SnSe Nanoribbons: A Theoretical Aspect. *Mater. Res. Express* **2016**, *3*, No. 035013.

(25) Zhang, L. C.; Qin, G.; Fang, W. Z.; Cui, H. J.; Zheng, Q. R.; Yan, Q. B.; Su, G. Tinselenidene: A Two-Dimensional Auxetic Material with Ultralow Lattice Thermal Conductivity and Ultrahigh Hole Mobility. *Sci. Rep.* **2016**, *6*, 1−9.

(26) Sun, Y.; Luo, S.; Zhao, X. G.; Biswas, K.; Li, S. L.; Zhang, L. InSe: A Two-Dimensional Material with Strong Interlayer Coupling. *Nanoscale* **2018**, *10*, 7991−7998.

(27) Yuan, X.; Tang, L.; Liu, S.; Wang, P.; Chen, Z.; Zhang, C.; Liu, Y.; Wang, W.; Zou, Y.; Liu, C.; et al. Arrayed van Der Waals Vertical Heterostructures Based on 2d GaSe Grown by Molecular Beam Epitaxy. *Nano Lett.* **2015**, *15*, 3571−3577.

(28) Morrison, S. R. *The Chemical Physics of Surfaces*; Springer Science+Business Media LLC: New York, 1990.

(29) Wrasse, E. O.; Schmidt, T. M. Prediction of Two-Dimensional Topological Crystalline Insulator in PbSe Monolayer. *Nano Lett.* **2014**, *14*, 5717−5720.

(30) Shao, Z.; Zheng, F.; Zhang, Z.; Sun, H.; Li, S.; Yuan, H.; Li, Q.; Zhang, P.; Pan, M. Epitaxial Growth of PbSe Few-Layers on $SrTiO_3$: The Effect of Compressive Strain and Potential Two-Dimensional Topological Crystalline Insulator. *ACS Nano* **2019**, *13*, 2615−2623.

(31) Mariano, A. N.; Chopra, K. L. Polymorphism in Some IV-VI Compounds

Induced by High Pressure and Thin-Film Epitaxial Growth. *Appl. Phys. Lett.* **1967**, *10*, 282−284.

(32) Cordova, D. L. M.; Kam, T. M.; Fender, S. S.; Tsai, Y. H.; Johnson, D. C. Strong Non-Epitaxial Interactions: Crystallographically Aligned PbSe on VSe_2. *Phys. Status Solidi Appl. Mater. Sci* **2019**, *216*, 1800896.

(33) Wang, N. Z.; Yuan, S. F.; Cong, R.; Lu, X. F.; Meng, F. B.; Shang, C.; Chen, X. H. Structure and Physical Properties of the Misfit Compounds (PbSe)1.16($TiSe_2$)m (m = 1, 2). *EPL* **2015**, *112*, 67007.

(34) Cordova, D. L. M.; Fender, S. S.; Kam, T. M.; Seyd, J.; Albrecht, M.; Lu, P.; Fischer, R.; Johnson, D. C. Designed Synthesis and Structure-Property Relationships of Kinetically Stable [(PbSe)- 1+I´]m(VSe2)1 (m = 1, 2, 3, 4) Heterostructures.́ *Chem. Mater.* **2019**, *31*, 8473−8483.

(35) Hamann, D. M.; Bardgett, D.; Cordova, D. L. M.; Maynard, L. A.; Hadland, E. C.; Lygo, A. C.; Wood, S. R.; Esters, M.; Johnson, D. C. Sub-Monolayer Accuracy in Determining the Number of Atoms per Unit Area in Ultrathin Films Using X-Ray Fluorescence. *Chem. Mater.* **2018**, *30*, 6209−6216.

(36) Holy, V.; Pietsch, U.; Baumbach, T. *High-Resolution X-Ray Scattering from Thin Films and Multilayers*; Springer Berlin Heidelberg: Germany, 1999.

(37) Stierle, A.; Vlieg, E. Surface Sensitive X-Ray Diffraction Methods. In *Modern Diffraction Methods*; Mittemeijer, E. J., Welsel, U.; Wiley-VCH Verlag & Co.: Weinheim, Germany, 2013; 221−258.

(38) Schneemeyer, L. F.; Stacy, A.; Sienko, M. J. Effect of Nonstoichiometry on the Periodic Lattice Distortion in Vanadium Diselenide. *Inorg. Chem.* **1980***, 19,* 2659−2662.

(39) Tao, F.; Bernasek, S. L. Understanding Odd-Even Effects in Organic Self-Assembled Monolayers. *Chem. Rev.* **2007**, *107*, 1408−1453.

(40) Burnett, E. K.; Ai, Q.; Cherniawski, B. P.; Parkin, S. R.; Risko, C.; Briseno, A. L. Even-Odd Alkyl Chain-Length Alternation Regulates Oligothiophene Crystal Structure. *Chem. Mater.* **2019**, *31*, 6900−6907.

(41) Thuo, M. M.; Reus, W. F.; Nijhuis, C. A.; Barber, J. R.; Kim, C.; Schulz, M. D.; Whitesides, G. M. Odd-Even Effects in Charge Transport across Self-Assembled Monolayers. *J. Am. Chem. Soc.* **2011**, *133*, 2962−2975.

(42) Yang, K.; Cai, Z.; Jaiswal, A.; Tyagi, M.; Moore, J. S.; Zhang, Y. Dynamic Odd-Even Effect in Liquid n -Alkanes near Their Melting Points. *Angew. Chem., Int. Ed.* **2016**, *55*, 14090−14095.

(43) Fister, L.; Li, X.; McConnell, J.; Novet, T.; Johnson, D. C. Deposition System for the Synthesis of Modulated, Ultrathin-film Composites. *J. Vac. Sci. Technol A Vacuum, Surfaces, Film.* **1993**, *11*, 3014−3019.

(44) Rodríguez-Carvajal, J. FULLPROF: A Program for Rietveld Refinement and Pattern Matching Analysis. In *Abstracts of the Satellite Meeting on Powder Diffraction of the XV Congress of the IUCr* Toulouse, France; 1990;127.

(45) Blöchl, P. E. Projector Augmented-Wave Method. *Phys. Rev. B* **1994**, *50*, 17953−17979.

(46) Kresse, G.; Furthmüller, J. Efficient Iterative Schemes for Ab Initio Total-Energy Calculations Using a Plane-Wave Basis Set. *Phys. Rev. B – Condens. Matter Mater Phys.* **1996**, *54*, 11169−11186.

(47) Perdew, J. P.; Burke, K.; Ernzerhof, M. Generalized Gradient Approximation Made Simple. *Phys. Rev. Lett.* **1996**, *77*, 3865−3868.

(48) Perdew, J. P.; Ruzsinszky, A.; Csonka, G. I.; Vydrov, O. A.; Scuseria, G. E.; Constantin, L. A.; Zhou, X.; Burke, K. Restoring the Density-Gradient Expansion for Exchange in Solids and Surfaces. *Phys. Rev. Lett.* **2008**, *100*, 136406.

(49) Deringer, V. L.; Dronskowski, R. Stabilities and Reconstructions of Clean PbS and PbSe Surfaces: DFT Results and the Role of Dispersion Forces. *J. Phys. Chem. C* **2016**, *120*, 8813−8820.

(50) Schafer, T.; Fan, Z.; Grünwald, M.; Kresse, G. Ab Initio Phase Diagram of PbSe Crystals Calculated with the Random Phase Approximation. *Phys. Rev. B* **2018**, *98*, 144103.

(51) Noda, Y.; Masumoto, K.; Ohba, S.; Saito, Y.; Toriumi, K.; Iwata, Y.; Shibuya, I. Temperature Dependence of Atomic Thermal Parameters of Lead Chalcogenides, PbS, PbSe and PbTe. *Acta Crystallogr. Sect. C Cryst. Struct. Commun.* **1987**, *43*, 1443−1445.

Chapter VIII

(1) Jain, A.; Ong, S. P.; Hautier, G.; Chen, W.; Richards, W. D.; Dacek, S.; Cholia, S.; Gunter, D.; Skinner, D.; Ceder, G.; Persson, K. A. (*=equal contributions). The Materials Project: A materials genome approach to accelerating materials innovation. *APL Mater.* **2013**, *1*, No. 011002.

(2) de Pablo, J. J.; et al. The Materials Genome Initiative, the Interplay of Experiment, Theory and Computation. *Curr. Opin. Solid State Mater. Sci.* **2014**, *18*, 99−117.

(3) Amsler, M.; Ward, L.; Hegde, V. I.; Goesten, M. T.; Yi, X.; Wolverton, C. Ternary Mixed-Anion Semiconductors with Tunable Band Gaps from Machine-Learning and Crystal Structure Prediction. *Phys. Rev. Mater.* **2019**, *3*, No. 035404.

(4) Sun, W.; Bartel, C. J.; Arca, E.; Bauers, S. R.; Matthews, B.; Orvananos, B.; Chen, B.; Toney, M. F.; Schelhas, L. T.; Tumas, W.; Tate, J.; Zakutayev, A.; Lany, S.; Holder, A.; Ceder, G. A Map of the Inorganic Ternary Metal Nitrides. *Nat. Mater.* **2019**, *18*, 732−739.

(5) Stein, A.; Keller, S. W.; Mallouk, T. E. Turning Down the Heat: Design and Mechanism in Solid-State Synthesis. *Science* **1993**, *259*, 1558−1564.

(6) Aykol, M.; Dwaraknath, S. S.; Sun, W.; Persson, K. A. Thermodynamic Limit for Synthesis of Metastable Inorganic Materials. *Sci. Adv.* **2018**, *4*, No. eaaq0148.

(7) Bauer, E. G.; Dodson, B. W.; Ehrlich, D. J.; Feldman, L. C.; Flynn, C. P.; Geis, M. W.; Harbison, J. P.; Matyi, R. J.; Peercy, P. S.; Petroff, P. M.; Phillips, J. M.; Stringfellow, G. B.; Zangwill, A. Fundamental Issues in Heteroepitaxy − A Department of Energy, Council on Materials Science Panel Report. *J. Mater. Res.* **1990**, *5*, 852−894.

(8) Jansen, M. A Concept For Synthesis Planning in Solid-State Chemistry. *Angew. Chem., Int. Ed.* **2002**, *41*, 3746−3766.

(9) Cordova, D. L. M.; Johnson, D. C. Synthesis of Metastable Inorganic Solids with Extended Structures. *ChemPhysChem* **2020**, *21*, 1345−1386.

(10) Haindl, S.; Kidszun, M.; Oswald, S.; Hess, C.; Buchner, B.; Kolling, S.; Wilde, L.; Thersleff, T.; Yurchenko, V. V.; Jourdan, M.; Hiramatsu, H.; Hosono, H. Thin Film Growth of Fe-Based Superconductors From Fundamental Properties to Functional Devices. A Comparative Review. *Rep. Prog. Phys.* **2014**, *77*, No. 046502.

(11) Narayan, A.; Bhutani, A.; Rubeck, S.; Eckstein, J. N.; Shoemaker, D. P.;

Wagner, L. K. Computational and Experimental Investigation for New Transition Metal Selenides and Sulfides: The Importance of Experimental Verification for Stability. *Phys. Rev. B* **2016**, *94*, No. 045105.

(12) Coh, S.; Lee, D.-H.; Louie, S. G.; Cohen, M. L. Proposal for a bulk material based on a monolayer FeSe on $SrTiO_3$ HighTemperature Superconductor. *Phys. Rev. B* **2016**, *93*, No. 245138.

(13) Wu, X. J.; Zhang, Z. Z.; Zhang, J. Y.; Ju, Z. G.; Li, B. H.; Li, B. S.; Shan, C. X.; Zhao, D. X.; Yao, B.; Shen, D. Z. Growth of FeSe on General Substrates by Metal-Organic Chemical Vapor Deposition and the Application in Magnet Tunnel Junction Devices. *Thin Solid Films* **2008**, *516*, 6116−6119.

(14) Liu, X.; Zhao, L.; He, S.; He, J.; Liu, D.; Mou, D.; Shen, B.; Hu, Y.; Huang, J.; Zhou, X. J. Electronic Structure and Superconductivity of FeSe-Related Superconductors. *J. Phys.: Condens. Matter* **2015**, *27*, No. 183201.

(15) Chen, Y.; Zhang, J.; Guo, P.; Liu, H.; Wang, Z.; Liu, M.; Zhang, T.; Wang, S.; Zhou, Y.; Lu, X.; Zhang, J. Coupled Heterostructure of Mo-Fe Selenide Nanosheets Supported on Carbon Paper as an Integrated Electrocatalyst for Efficient Hydrogen Evolution. *ACS Appl. Mater. Interfaces* **2018**, *10*, 27787−27794.

(16) Mazin, I. I. The FeSe Riddle. *Nat. Mater.* **2015**, *14*, 755−756.

(17) Zhang, H.; Dong, W.; Meng, Q.-L.; Yin, N.; Liu, Z.; Lu, X.; Ge, B.; Li, Y.; Shi, Q.; Wang, L.; Xue, Q.-K.; Jiang, P.; Bao, X. InterfaceEnhanced Superconductivity in Multi-Grain $(FeSe)_{\eta}(SrTiO_3)_{1-\eta}$ Composites. *Supercond. Sci. Technol.* **2021**, *34*, No. 035002.

(18) Qiu, W.; Ma, Q.; Ma, Z.; Tang, J.; Sang, L.; Cai, C.; Hossain, M. S.; Cheng, Z.; Wang, X.; Liu, Y.; Dou, S. X. Enhanced Superconductivity Induced by Several-Unit-Cells Diffusion in an FeTe/FeSe Bilayer Heterostructure. *Phys. Rev. B* **2019**, *99*, No. 064502.

(19) Ghasemi, A.; Kepaptsoglou, D.; Galindo, P. L.; Ramasse, Q. M.; Hesjedal, T.; Lazarov, V. K. Van der Waals Epitaxy Between the Highly Lattice Mismatched Cu-Doped FeSe and Bi_2Te_3. *NPG Asia Mater.* **2017**, *9*, No. e402.

(20) Wu, M.-K.; Wang, M.-J.; Yeh, K.-W. Recent Advances in β-$FeSe_{1-x}$ and Related Superconductors. *Sci. Technol. Adv. Mater.* **2013**, *14*, No.

014402.

(21) Williams, J. R.; Smalley, A. L. E.; Sellinschegg, H.; DanielsHafer, C.; Harris, L.; Johnson, M. B.; Johnson, D. C. Synthesis of Crystalline Skutterudite Superlattices Using the Modulated Elemental Reactant Method. *J. Am. Chem. Soc.* **2003**, *125*, 10335−10341.

(22) Hamann, D. M.; Bardgett, D.; Cordova, D. L. M.; Maynard, L. A.; Hadland, E. C.; Lygo, A. C.; Wood, S. R.; Esters, M.; Johnson, D. C. Sub-Monolayer Accuracy in Determining Number of Atoms per Unit Area in Ultrathin Films using X-ray Fluorescence. *Chem. Mater.* **2018**, *30*, 6209−6216.

(23) Okamoto, H. The Fe-Se (Iron-Selenium) System. *J. Phase Equilib.* **1991**, *12*, 383−389.

(24) Li, Z.; Ju, J.; Tang, J.; Sato, K.; Watahiki, M.; Tanigaki, K. Structural and Superconductivity study on α-$FeSe_x$. *J. Phys. Chem. Solids* **2010**, *71*, 495−498.

(25) Bauers, S. R.; Wood, S. R.; Jensen, K. M.; Blichfeld, A. B.; Iversen, B. B.; Billinge, S. J.; Johnson, D. C. Structural evolution of iron antimonides from amorphous precursors to crystalline products studied by total scattering techniques. *J. Am. Chem. Soc.* **2015**, *137*, 9652−9658.

(26) Williams, J. R.; Johnson, M.; Johnson, D. C. Composition dependence of the nucleation energy of iron antimonides from modulated elemental reactants. *J. Am. Chem. Soc.* **2001**, *123*, 1645−1649.

(27) Pickardt, J.; Reuter, B.; Riedel, E.; Soechtig, J. On the Formation of $FeSe_2$ Single Crystals by Chemical Transport Reactions. *J. Solid State Chem.* **1975**, *15*, 366−368.

(28) Buryanova, E. Z.; Komkov, A. I. A New Mineral − Ferroselite. *Dokl. Akad. Nauk SSSR* **1955**, *105*, 812−813.

(29) Schuster, W.; Mikler, H.; Komarek, K. L. Transition Metal − Chalcogen Systems. VII. The Iron-Selenium Phase Diagram. *Monatsh. Chem.* **1979**, *110*, 1153−1170.

(30) Okazaki, A.; Hirakawa, K. Structural Study of Iron Selenides $FeSe_x$. I Ordered Arrangement of Defects of Fe Atoms. *J. Phys. Soc. Jpn.* **1956**,

11, 930−936.

(31) Kumar, R. S.; Zhang, Y.; Sinogeikin, S.; Xiao, Y.; Kumar, S.; Chow, P.; Cornelius, A. L.; Chen, C. F. Crystal and Electronic Structure of FeSe at High Pressure and Low Temperature. *J. Phys.Chem. B* **2010**, *114*, 12597−12606.

(32) Gawryluk, D. J.; Fink-Finowicki, J.; Wisniewski, A.; Puzniak, R.; Domukhovski, V.; Diduszko, R.; Berkowski, M. Structure and Superconductivity of $FeSe_{1-x}$ and $FeTe_{1-y}$ Crystals: Dependence on the Synthesis Methods, Starting Composition, and Growth Conditions. *Acta Phys. Pol., A* **2010**, *118*, 331−334.

(33) Shivastava, M. M.; Srivastava, O. N. Studies of Structural Transformation and Electrical Behavior of FeSe Films. *Thin Solid Films* **1975**, *29*, 275−284.

(34) Anderson, M. D.; Thompson, J. O.; Johnson, D. C. Avoiding Binary Compounds as Reaction Intermediates in Solid State Reactions. *Chem. Mater.* **2013**, *25*, 3996−4002.

Chapter IX

(1) Disalvo, F. J. Solid-State Chemistry: A Rediscovered Chemical Frontier. *Science (80-.).* **1990**, *247* (4943). https://doi.org/10.1126/science.247.4943.649.

(2) De Pablo, J. J.; Jones, B.; Kovacs, C. L.; Ozolins, V.; Ramirez, A. P. The Materials Genome Initiative, the Interplay of Experiment, Theory and Computation. *Current Opinion in Solid State and Materials Science*. 2014. https://doi.org/10.1016/j.cossms.2014.02.003.

(3) Narayan, A.; Bhutani, A.; Rubeck, S.; Eckstein, J. N.; Shoemaker, D. P.; Wagner, L. K. Computational and Experimental Investigation for New Transition Metal Selenides and Sulfides: The Importance of Experimental Verification for Stability. *Phys. Rev. B* **2016**, *94* (4). https://doi.org/10.1103/PhysRevB.94.045105.

(4) Chen, L. J. Metal Silicides: An Integral Part of Microelectronics. *JOM*. 2005. https://doi.org/10.1007/s11837-005-0111-4.

(5) Zhang, S. L.; Östling, M. Metal Silicides in CMOS Technology: Past, Present, and Future Trends. *Critical Reviews in Solid State and Materials Sciences*. 2003. https://doi.org/10.1080/10408430390802431.

(6) D'Heurle, F. M.; Gas, P.; Lavoie, C.; Philibert, J. Diffusion in Intermetallic Compounds: The Ordered Cu3Au Rule, Its History. *Zeitschrift fuer Metallkunde/Materials Research and Advanced Techniques*. 2004.

https://doi.org/10.3139/146.018042.

(7) Bardgett, D.; N. Gannon, R.; M. Hamann, D.; M. Roberts, D.; R. Bauers, S.; Lu, P.; C. Johnson, D. Understanding the Reactions Between Fe and Se Binary Diffusion Couples. *Chem. Mater.* **2021**, *0* (0). https://doi.org/10.1021/acs.chemmater.1c00303.

(8) Li, Z.; Ju, J.; Tang, J.; Sato, K.; Watahiki, M.; Tanigaki, K. Structural and Superconductivity Study on α-FeSex. *J. Phys. Chem. Solids* **2010**, *71* (4). https://doi.org/10.1016/j.jpcs.2009.12.020.

(9) Pietrokowsky, P. Lattice Parameter of Alpha Iron by Divergent Beam Diffraction. *J. Appl. Phys.* **1966**, *37* (12). https://doi.org/10.1063/1.1708081.

(10) Montoro, V. Miscibilita Fra Gli Ossidi Salini Di Ferro e Di Manganese. *Gaz Chim Ital* **1938**, *68*, 728–733.

(11) Kjekshus, A.; Rakke, T.; Andresen, A. F.; Southern, J. T. Compounds with the Marcasite Type Crystal Structure. IX. Structural Data for FeAs2, FeSe2, NiAs2, NiSb2, and CuSe2. *Acta Chem. Scand.* **1974**, *28a*. https://doi.org/10.3891/acta.chem.scand.28a-0996.

(12) Okazaki, A.; Hirakawa, K. Structural Study of Iron Selenides FeSeax. I Ordered Arrangement of Defects of Fe Atoms. *J. Phys. Soc. Japan* **1956**, *11* (9). https://doi.org/10.1143/JPSJ.11.930.

Chapter X

(1) Mueller, P.; Fach, A.; John, J.; Tiwari, A. N.; Zogg, H.; Kostorz, G. Structure of Epitaxial PbSe Grown on Si(111) and Si(100) without a Fluoride Buffer Layer. J. Appl. Phys. 1996, 79 (4), 1911–1916.

(2) Zhang, K.; Ramalingom Pillai, A. D.; Nminibapiel, D.; Tangirala, M.; Chakravadhanula, V. S.; Kubel, C.; Baumgart, H.; Kochergin, V. ALD Growth of PbTe and PbSe Superlattices for Thermoelectric Applications. ECS Trans. 2013, 58 (10), 131–139.

(3) Pillai, A. D. R.; Zhang, K.; Bollenbach, K.; Nminibapiel, D.; Cao, W.; Baumgart, H.; Chakravadhanula, V. S. K.; Kubel, C.; Kochergin, V. ALD Growth of PbTe and PbSe Superlattices for Thermoelectric Applications. ECS Trans. 2013, 58 (10, Atomic Layer Deposition Applications 9), 131–139, 10 pp.

(4) Jang, M. H.; Yoo, S. S.; Kramer, M. T.; Dhar, N. K.; Gupta, M. C. Properties of Chemical Bath Deposited and Sensitized PbSe Thin Films for IR Detection. Semicond. Sci. Technol. 2019, 34 (11), 115010.

(5) El-Shazly, E. A. A.; Zedan, I. T.; Abd El-Rahman, K. F. Determination and Analysis of Optical Constants for Thermally Evaporated PbSe Thin Films. Vacuum 2011, 86 (3), 318–323.

(6) Manga, K. K.; Wang, J.; Lin, M.; Zhang, J.; Nesladek, M.; Nalla, V.; Ji, W.; Loh, K. P. High-Performance Broadband Photodetector Using Solution-Processible PbSe-TiO2-Graphene Hybrids. Adv. Mater. (Weinheim, Ger. 2012, 24 (13), 1697–1702.

(7) Luther, J. M.; Law, M.; Song, Q.; Perkins, C. L.; Beard, M. C.; Nozik, A. J. Structural, Optical, and Electrical Properties of Self-Assembled Films of PbSe Nanocrystals Treated with 1,2-Ethanedithiol. ACS Nano 2008, 2 (2), 271–280.

(8) Kar, A. I. Amorphous Pbse Thin Film Produced by Chemical Bath Deposition at Ph of 5-8. Surf. Rev. Lett. 2019, 27 (4), 1950128.

(9) Androulakis, J.; Todorov, I.; He, J.; Chung, D. Y.; Dravid, V.; Kanatzidis, M. Thermoelectrics from Abundant Chemical Elements: High-Performance Nanostructured PbSe-PbS. J. Am. Chem. Soc. 2011, 133 (28), 10920–10927.

(10) Wang, H.; Pei, Y.; Lalonde, A. D.; Snyder, G. J. Heavily Doped P-Type PbSe with High Thermoelectric Performance: An Alternative for PbTe. Adv. Mater. 2011, 23 (11), 1366–1370.

(11) Rogacheva, E. I.; Nashchekina, O. N.; Ol'khovskaya, S. I.; Dresselhaus, M. S. Thermoelectric Transport in PbSe Quantum Wells. AIP Conf. Proc. 2012, 1449 (9th European Conference on Thermoelectrics, 2011), 151–154.

(12) Luo, P.; Zhuge, F.; Wang, F.; Lian, L.; Liu, K.; Zhang, J.; Zhai, T. PbSe Quantum Dots Sensitized High-Mobility Bi2O2Se Nanosheets for High-Performance and Broadband Photodetection beyond 2 Mm. ACS Nano 2019, 13 (8).

(13) Schaller, R. D.; Klimov, V. I. High Efficiency Carrier Multiplication in PbSe Nanocrystals: Implications for Solar Energy Conversion. Phys. Rev. Lett. 2004, 92 (18).

(14) Fang, X. M.; Chao, I.-N.; Strecker, B. N.; McCann, P. J.; Yuan, S.; Liu, W. K.; Santos, M. B. Molecular Beam Epitaxial Growth of Bi2Se3- and Tl2Se-Doped PbSe and PbEuSe on CaF2/Si(111). J. Vac. Sci. Technol. B

Microelectron. Nanom. Struct. 1998, 16 (3), 1459–1462.

(15) Freik, D. M.; Voitkiv, V. V; Gaiduchok, G. M.; Brodin, I. I. X-Ray Diffraction Studies of Lead Chalcogenide-Based Compositions in Thin Layers. Izv. Vyss. Uchebnykh Zaved. Fiz. 1972, 15 (11), 132–134.

(16) Jensen, J. D.; Schoolar, R. B. Surface Charge Transport in Lead Sulfur Selenide (PbSxSe1-x) and Lead Tin Selenide (Pb1-YSnySe) Epitaxial Films. J. Vac. Sci. Technol. 1976, 13 (4), 920–925.

(17) Tedenac, J. C.; Dal Corso, S.; Liautard, B.; Brun, G.; Charar, S.; Ohadi, A.; Fau, C.; El Kholdi, M. Heterostructures of Ternary IV-VI Semiconductors of Lead Selenide Telluride/Barium Difluoride and Lead Tin Selenide/Barium Difluoride. Proc. - Electrochem. Soc. 1993, 93–10 (Logic and Functional Devices for Photonics and the Seventeenth State-of-the-Art Program on Compound Semiconductors, 1992), 255–268.

(18) Wu, H. Z.; Fang, X. M.; Salas Jr., R.; McAlister, D.; McCann, P. J. Molecular Beam Epitaxy Growth of PbSe on BaF2-Coated Si(111) and Observation of the PbSe Growth Interface. J. Vac. Sci. Technol. B Microelectron. Nanom. Struct. 1999, 17 (3), 1263–1266.

(19) Hohnke, D. K.; Hurley, M. D. Growth and Electrical Properties of Epitaxial Lead Selenide Telluride (PbSexTe1-x) Layers. J. Appl. Phys. 1976, 47 (11), 4975–4979.

(20) Sachar, H. K.; Chao, I.; McCann, P. J.; Fang, X. M. Growth and Characterization of PbSe and Pb1-XSnxSe on Si (100). J. Appl. Phys. 1999, 85 (10), 7398–7403.

(21) Pashaev, A. M.; Davarashvili, O. I.; Akhvlediani, Z. G.; Enukashvili, M. I.; Bychkova, L. P.; Dzagania, M. A. Study on the Forbidden Gap Width of Strained Epitaxial Lead Selenide Layers by Optical Transmission. J. Mater. Sci. Eng. B 2012, 2 (2), 142–150.

(22) McLane, G.; Zemel, J. N. Surface Interaction of Atomic Hydrogen and Molecular Oxygen on Thin Lead Selenide Epitaxic Films. Thin Solid Films 1971, 7 (3/4), 229–246.

(23) A, B. M.; D, I. B.; D, T. G.; A, Y. A.; V, S. R.; U, M. E. Some Studies on Chemically Deposited N-PbSe Thin Films. Res. J. Chem. Sci. 2011, 1 (9), 37–41.

(24) Hone, F. G.; Dejene, F. B. Tuning the Optical Band Gap and Stoichiometric Ratio of Chemically Synthesized Lead Selenide Thin Films

by Controlling Film Thickness. J. Mater. Sci. Mater. Electron. 2017, 28 (8), 5979–5989.

(25) Wrasse, E. O.; Schmidt, T. M. Prediction of Two-Dimensional Topological Crystalline Insulator in PbSe Monolayer. Nano Lett. 2014, 14 (10).

(26) Sachar, H. K.; Chao, I.; Fang, X. M.; McCann, P. J. Growth and Characterization of Pbse and Pbl-Sn1 Se Layers on Si (100). MRS Proc. 1997, 487.

(27) Strecker, B. N.; McCann, P. J.; Fang, X. M.; Hauenstein, R. J.; O'Steen, M.; Johnson, M. B. LPE Growth of Crack-Free PbSe Layers on Si(100) Using MBE-Grown PbSe/BaF2/CaF2 Buffer Layers. J. Electron. Mater. 1997, 26 (5).

(28) Zhao, F.; Ma, J.; Weng, B.; Li, D.; Bi, G.; Chen, A.; Xu, J.; Shi, Z. MBE Growth of PbSe Thin Film with a 9×105 Cm-2 Etch-Pits Density on Patterned (1 1 1)-Oriented Si Substrate. J. Cryst. Growth 2010, 312 (19), 2695–2698.

(29) Zogg, H.; Maissen, C.; Blunier, S.; Teodoropol, S.; Overney, R. M.; Richmond, T.; Tomm, J. W. Thermal-Mismatch Strain Relaxation Mechanisms in Heteroepitaxial Lead Chalcogenide Layers on Silicon Substrates. Semicond. Sci. Technol. 1993, 8 (1S), S337–S341.

(30) Xu, T. N.; Wu, H. Z.; Si, J. X.; Cao, C. F. Observation of Triangle Pits in PbSe Grown by Molecular Beam Epitaxy. Appl. Surf. Sci. 2007, 253 (12), 5457–5461.

(31) Freik, D. M.; Chobanyuk, V. M.; Sokolov, O. L.; Lopyanko, M. A. Misfit Dislocations and Electronic Processes in the Two-Layer Epitaxial Structures of Lead Chalcogenides. Fiz. i Khimiya Tverd. Tila 2009, 10 (1), 9–18.

(32) Osherov, A.; Shandalov, M.; Ezersky, V.; Golan, Y. EPITAXY and Orientation Control in Chemical Solution Deposited PbS and PbSe Monocrystalline Films. J. Cryst. Growth 2007, 304 (1), 169–178.

(33) Zogg, H.; Tiwari, A. N.; Blunier, S.; Maissen, C.; Masek, J. Heteroepitaxy of II-VI and IV-VI Semiconductors on Silicon Substrates. Proc. SPIE-The Int. Soc. Opt. Eng. 1991, 1361 (Phys. Concepts Mater. Novel Optoelectron. Device Appl. 1, Pt. 1), 406–413.

(34) Sachar, H. K.; Chao, I.; Fang, X. M.; McCann, P. J. Growth and Characterization of PbSe and Pb1-XSnxSe Layers on Si (100). Mater. Res.

Soc. Symp. Proc. 1998, 487 (Semiconductors for Room-Temperature Radiation Detector Applications II), 651–656.

(35) Breton, G.; Maurice, T.; Masri, P.; Charar, S.; Averous, M. Epitaxy Induced Phase Stabilization: A Comparative Experimental and Elasticity-Based Theoretical Study on MBE Grown PbSe/CaF2/Si Epilayer. Int. J. Inorg. Mater. 2001, 3 (8), 1237–1239.

(36) Chen, T.; Fan, C.; Zhou, W.; Zou, X.; Xu, X.; Wang, S.; Wan, Q.; Zhang, Q. Epitaxial Growth of Non-Layered PbSe Nanoplates on MoS2 Monolayer for Infrared Photoresponse. Appl. Phys. Express 2019, 12 (5).

(37) Smeller, M. M.; Heideman, C. L.; Lin, Q.; Beekman, M.; Anderson, M. D.; Zschack, P.; Anderson, I. M.; Johnson, D. C. Structure of Turbostratically Disordered Misfit Layer Compounds [(PbSe)0.99]1[WSe2]1, [(PbSe) 1.00]1[MoSe2]1, and [(SnSe) 1.03]1[MoSe2]1. Zeitschrift fur Anorg. und Allg. Chemie 2012, 638 (15).

(38) Moore, D. B.; Stolt, M. J.; Atkins, R.; Sitts, L.; Jones, Z.; Disch, S.; Beekman, M.; Johnson, D. C. Structural and Electrical Properties of (PbSe) 1·16 TiSe 2 . Emerg. Mater. Res. 2012, 1 (6).

(39) B. Moore, D.; Beekman, M.; Disch, S.; Zschack, P.; Häusler, I.; Neumann, W.; C. Johnson, D. Synthesis, Structure, and Properties of Turbostratically Disordered (PbSe)1.18(TiSe2)2. Chem. Mater. 2013, 25 (12), 2404–2409.

(40) Hite, O. K.; Falmbigl, M.; Alemayehu, M. B.; Esters, M.; Wood, S. R.; Johnson, D. C. Charge Density Wave Transition in (PbSe)1+δ(VSe2)n Compounds with n = 1, 2, and 3. Chem. Mater. 2017.

(41) Cordova, D. L. M.; Kam, T. M.; Fender, S. S.; Tsai, Y. H.; Johnson, D. C. Strong Non-Epitaxial Interactions: Crystallographically Aligned PbSe on VSe2. Phys. Status Solidi Appl. Mater. Sci. 2019, 216 (15).

(42) Grosse, C.; Alemayehu, M. B.; Falmbigl, M.; Mogilatenko, A.; Chiatti, O.; Johnson, D. C.; Fischer, S. F. Superconducting Ferecrystals: Turbostratically Disordered Atomic-Scale Layered (PbSe) 1.14 (NbSe 2) n Thin Films. Sci. Rep. 2016, 6.

(43) Parratt, L. G. Surface Studies of Solids by Total Reflection of X-Rays. Phys. Rev. 1954, 95 (2).

(44) Mariano, A. N.; Chopra, K. L. Polymorphism in Some IV-VI Compounds

Induced by High Pressure and Thin-Film Epitaxial GROWTH. Appl. Phys. Lett. 1967, 10 (10).

(45) Hohnke, D. K.; Kaiser, S. W. Epitaxial PbSe and Pb1-XSnxSe: Growth and Electrical Properties. J. Appl. Phys. 1974, 45 (2).

(46) Miller, A. M.; Hamann, D. M.; Hadland, E. C.; Johnson, D. C. Investigating the Formation of MoSe2 and TiSe2Films from Artificially Layered Precursors. Inorg. Chem. 2020.

(47) Bronsema, K. D.; De Boer, J. L.; Jellinek, F. On the Structure of Molybdenum Diselenide and Disulfide. ZAAC - J. Inorg. Gen. Chem. 1986, 540 (9–10).

Chapter XI

(1) Kovnir, K. Predictive Synthesis. *Chem. Mater.* **2021**, *0* (0). https://doi.org/10.1021/acs.chemmater.1c01484.

(2) de Pablo, J. J.; Jackson, N. E.; Webb, M. A.; Chen, L. Q.; Moore, J. E.; Morgan, D.; Jacobs, R.; Pollock, T.; Schlom, D. G.; Toberer, E. S.; Analytis, J.; Dabo, I.; DeLongchamp, D. M.; Fiete, G. A.; Grason, G. M.; Hautier, G.; Mo, Y.; Rajan, K.; Reed, E. J.; Rodriguez, E.; Stevanovic, V.; Suntivich, J.; Thornton, K.; Zhao, J. C. New Frontiers for the Materials Genome Initiative. *npj Computational Materials*. 2019. https://doi.org/10.1038/s41524-019-0173-4.

(3) Kalil Tom And Wadia, C. Materials Genome Initiative for Global Competitiveness. *Genome* **2011**, No. June.

(4) Jain, A.; Ong, S. P.; Hautier, G.; Chen, W.; Richards, W. D.; Dacek, S.; Cholia, S.; Gunter, D.; Skinner, D.; Ceder, G.; Persson, K. A. Commentary: The Materials Project: A Materials Genome Approach to Accelerating Materials Innovation. *APL Materials*. 2013. https://doi.org/10.1063/1.4812323.

(5) Mitchell, K.; Ibers, J. A. Rare-Earth Transition-Metal Chalcogenides. *Chem. Rev.* **2002**, *102* (6). https://doi.org/10.1021/cr010319h.

(6) Yuan, H.; Kong, L.; Li, T.; Zhang, Q. A Review of Transition Metal Chalcogenide/Graphene Nanocomposites for Energy Storage and Conversion. *Chinese Chem. Lett.* **2017**, *28* (12). https://doi.org/10.1016/j.cclet.2017.11.038.

(7) Manzeli, S.; Ovchinnikov, D.; Pasquier, D.; Yazyev, O. V.; Kis, A. 2D Transition Metal Dichalcogenides. *Nature Reviews Materials*. 2017. https://doi.org/10.1038/natrevmats.2017.33.

(8) Narayan, A.; Bhutani, A.; Rubeck, S.; Eckstein, J. N.; Shoemaker, D. P.; Wagner, L. K. Computational and Experimental Investigation for New Transition Metal

Selenides and Sulfides: The Importance of Experimental Verification for Stability. *Phys. Rev. B* **2016**, *94* (4). https://doi.org/10.1103/PhysRevB.94.045105.

(9) Johnson, D. C. Controlled Synthesis of New Compounds Using Modulated Elemental Reactants. *Curr. Opin. Solid State Mater. Sci.* **1998**. https://doi.org/10.1016/S1359-0286(98)80082-X.

(10) Westover, R.; Atkins, R. A.; Falmbigl, M.; Ditto, J. J.; Johnson, D. C. Self-Assembly of Designed Precursors: A Route to Crystallographically Aligned New Materials with Controlled Nanoarchitecture. *J. Solid State Chem.* **2016**, *236*. https://doi.org/10.1016/j.jssc.2015.08.018.

(11) Fister, L.; Li, X.; McConnell, J.; Novet, T.; Johnson, D. C. Deposition System for the Synthesis of Modulated, Ultrathin-film Composites. *J. Vac. Sci. Technol. A Vacuum, Surfaces, Film.* **1993**, *11* (6). https://doi.org/10.1116/1.578290.

(12) Hamann, D. M.; Bardgett, D.; Cordova, D. L. M.; Maynard, L. A.; Hadland, E. C.; Lygo, A. C.; Wood, S. R.; Esters, M.; Johnson, D. C. Sub-Monolayer Accuracy in Determining the Number of Atoms per Unit Area in Ultrathin Films Using X-Ray Fluorescence. *Chem. Mater.* **2018**, *30* (18). https://doi.org/10.1021/acs.chemmater.8b02591.

(13) Hohnke, D. K.; Kaiser, S. W. Epitaxial PbSe and $Pb_{1-X}Sn_xSe$: Growth and Electrical Properties. *J. Appl. Phys.* **1974**, *45* (2). https://doi.org/10.1063/1.1663334.

(14) Cordova, D. L. M.; Fender, S. S.; Kam, T. M.; Seyd, J.; Albrecht, M.; Lu, P.; Fischer, R.; Johnson, D. C. Designed Synthesis and Structure-Property Relationships of Kinetically Stable $[(PbSe)_{1+\delta};]_m(VSe_2)_1$ (m = 1, 2, 3, 4) Heterostructures. *Chem. Mater.* **2019**, *31* (20). https://doi.org/10.1021/acs.chemmater.9b02826.

(15) Pietrokowsky, P. Lattice Parameter of Alpha Iron by Divergent Beam Diffraction. *J. Appl. Phys.* **1966**, *37* (12). https://doi.org/10.1063/1.1708081.

(16) Okazaki, A.; Hirakawa, K. Structural Study of Iron Selenides FeSeax. I Ordered Arrangement of Defects of Fe Atoms. *J. Phys. Soc. Japan* **1956**, *11* (9). https://doi.org/10.1143/JPSJ.11.930.

(17) Kjekshus, A.; Rakke, T.; Andresen, A. F.; Southern, J. T. Compounds with the Marcasite Type Crystal Structure. IX. Structural Data for $FeAs_2$, $FeSe_2$, $NiAs_2$, $NiSb_2$, and $CuSe_2$. *Acta Chem. Scand.* **1974**, *28a*. https://doi.org/10.3891/acta.chem.scand.28a-0996.

(18) Hite, O. K.; Falmbigl, M.; Alemayehu, M. B.; Esters, M.; Wood, S. R.; Johnson, D. C. Charge Density Wave Transition in $(PbSe)_{1+\delta}(VSe_2)_n$ Compounds with n = 1, 2, and 3. *Chem. Mater.* **2017**. https://doi.org/10.1021/acs.chemmater.7b01383.

(19) Schneemeyer, L. F.; Stacy, A.; Sienko, M. J. Effect of Nonstoichiometry on the

Periodic Lattice Distortion in Vanadium Diselenide. *Inorg. Chem.* **1980**, *19* (9). https://doi.org/10.1021/ic50211a036.

(20) M. Hamann, D.; P. Rudin, S.; Asaba, T.; Ronning, F.; Leo M. Cordova, D.; Lu, P.; C. Johnson, D. Predicting and Synthesizing Interface Stabilized 2D Layers. *Chem. Mater.* **2021**, *33* (13), 5076–5084. https://doi.org/10.1021/acs.chemmater.1c01064.

Chapter XII

(1) Chhowalla, M.; Shin, H. S.; Eda, G.; Li, L.-J.; Loh, K. P.; Zhang, H. The Chemistry of Two-Dimensional Layered Transition Metal Dichalcogenide Nanosheets. *Nat. Chem.* **2013**, *5* (4), 263–275.

(2) Krasnok, A.; Lepeshov, S.; Alú, A. Nanophotonics with 2D Transition Metal Dichalcogenides [Invited]. *Opt. Express* **2018**, *26* (12), 15972.

(3) Kong, D.; Cha, J. J.; Wang, H.; Lee, H. R.; Cui, Y. First-Row Transition Metal Dichalcogenide Catalysts for Hydrogen Evolution Reaction. *Energy Environ. Sci.* **2013**, *6* (12), 3553.

(4) Pumera, M.; Loo, A. H. Layered Transition-Metal Dichalcogenides (MoS2 and WS2) for Sensing and Biosensing. *TrAC Trends Anal. Chem.* **2014**, *61*, 49–53.

(5) Wang, H.; Yuan, H.; Sae Hong, S.; Li, Y.; Cui, Y. Physical and Chemical Tuning of Two-Dimensional Transition Metal Dichalcogenides. *Chem. Soc. Rev.* **2015**, *44* (9), 2664–2680.

(6) Wang, Z.; Li, R.; Su, C.; Loh, K. P. Intercalated Phases of Transition Metal Dichalcogenides. *SmartMat* **2020**, *1* (1).

(7) Loh, L.; Zhang, Z.; Bosman, M.; Eda, G. Substitutional Doping in 2D Transition Metal Dichalcogenides. *Nano Res.* **2021**, *14* (6), 1668–1681.

(8) Shi, Y.; Li, H.; Li, L.-J. Recent Advances in Controlled Synthesis of Two-Dimensional Transition Metal Dichalcogenides via Vapour Deposition Techniques. *Chem. Soc. Rev.* **2015**, *44* (9), 2744–2756.

(9) Wang, S.; Robertson, A.; Warner, J. H. Atomic Structure of Defects and Dopants in 2D Layered Transition Metal Dichalcogenides. *Chem. Soc. Rev.* **2018**, *47* (17), 6764–6794.

(10) Marseglia, E. A. Transition Metal Dichalcogenides and Their Intercalates. *Int. Rev. Phys. Chem.* **1983**, *3* (2), 177–216.

(11) Tedstone, A. A.; Lewis, D. J.; O'Brien, P. Synthesis, Properties, and Applications of Transition Metal-Doped Layered Transition Metal Dichalcogenides. *Chem. Mater.* **2016**, *28* (7), 1965–1974.

(12) Wang, C.; Wu, X.; Zhang, X.; Mu, G.; Li, P.; Luo, C.; Xu, H.; Di, Z. Iron-Doped VSe_2 Nanosheets for Enhanced Hydrogen Evolution Reaction. *Appl. Phys. Lett.* **2020**, *116* (22), 223901.

(13) Di Salvo, F. J.; Waszczak, J. V. THE EFFECT OF Fe SUBSTITUTION ON THE CHARGE DENSITY WAVE IN VSe_2. *J. Phys. Colloq.* **1976**, *37* (C4), C4-157-C4-161.

(14) Yadav, C. S.; Rastogi, A. K. Transport and Magnetic Properties of $Fe_{1/3}VSe_2$. *J. Phys. Condens. Matter* **2008**, *20* (41), 415212.

(15) Hamann, D. M.; Bardgett, D.; Cordova, D. L. M.; Maynard, L. A.; Hadland, E. C.; Lygo, A. C.; Wood, S. R.; Esters, M.; Johnson, D. C. Sub-Monolayer Accuracy in Determining the Number of Atoms per Unit Area in Ultrathin Films Using X-Ray Fluorescence. *Chem. Mater.* **2018**, *30* (18), 6209–6216.

(16) Cordova, D. L. M.; Kam, T. M.; Fender, S. S.; Tsai, Y. H.; Johnson, D. C. Strong Non-Epitaxial Interactions: Crystallographically Aligned PbSe on VSe_2. *Phys. Status Solidi A* **2019**, *216* (15), 1800896.

(17) *Inorganic Crystal Structure Database*.

(18) Sassi, S.; Candolfi, C.; Delaizir, G.; Migot, S.; Ghanbaja, J.; Gendarme, C.; Dauscher, A.; Malaman, B.; Lenoir, B. Crystal Structure and Transport Properties of the Homologous Compounds $(PbSe)_5(Bi_2Se_3)_{3m}$ ($m = 2, 3$). *Inorg. Chem.* **2018**, *57* (1), 422–434.

(19) Dresselhaus, M. S.; Chen, G.; Tang, M. Y.; Yang, R. G.; Lee, H.; Wang, D. Z.; Ren, Z. F.; Fleurial, J.-P.; Gogna, P. New Directions for Low-Dimensional Thermoelectric Materials. *Adv. Mater.* **2007**, *19* (8), 1043–1053.

(20) Snyder, G. J.; Toberer, E. S. Complex Thermoelectric Materials. *Nat. Mater.* **2008**, *7*, 105–114.

(21) Shelimova, L. E.; Karpinskii, O. G.; Zemskov, V. S. X-Ray Diffraction Study of Ternary Layered Compounds in the PbSe-Bi2Se3 System. *Inorg. Mater.* **2008**, *44* (9), 927–931.

(22) Shelimova, L. E.; Karpinskii, O. G.; Konstantinov, P. P.; Avilov, E. S.; Kretova, M. A.; Lubman, G. U.; Nikhezina, I. Yu.; Zemskov, V. S. Composition and Properties of Compounds in the PbSe-Bi2Se3 System. *Inorg. Mater.* **2010**, *46*

(2), 120–126.

(23) Kanatzidis, M. G. Structural Evolution and Phase Homologies for "Design" and Prediction of Solid-State Compounds. *Acc. Chem. Res.* **2005**, *38* (4), 359–368.

(24) Segawa, K.; Taskin, A. A.; Ando, Y. Pb5Bi24Se41: A New Member of the Homologous Series Forming Topological Insulator Heterostructures. *J. Solid State Chem.* **2015**, *221*, 196–201.

(25) Zemskov, V. S.; Shelimova, L. E.; Konstantinov, P. P.; Avilov, E. S.; Kretova, M. A.; Nikhezina, I. Y. Thermoelectric Materials with Low Heat Conductivity Based on PbSe-Bi2Se3 Compounds. *Inorg. Mater. Appl. Res.* **2011**, *2* (5), 405–413.

(26) Zhang, Y.; Wilkinson, A. P.; Lee, P. L.; Shastri, S. D.; Shu, D.; Chung, D.-Y.; Kanatzidis, M. G. Determining Metal Ion Distributions Using Resonant Scattering at Very High-Energy *K* -Edges: Bi/Pb in $Pb_5Bi_6Se_{14}$. *J. Appl. Crystallogr.* **2005**, *38* (3), 433–441.

Chapter XIII

(1) Zhang, Y.; Zuo, T. T.; Popovic, J.; Lim, K.; Yin, Y. X.; Maier, J.; Guo, Y. G. Towards Better Li Metal Anodes: Challenges and Strategies. *Materials Today*. 2020.

(2) Kim, K. J.; Balaish, M.; Wadaguchi, M.; Kong, L.; Rupp, J. L. M. Solid-State Li–Metal Batteries: Challenges and Horizons of Oxide and Sulfide Solid Electrolytes and Their Interfaces. *Advanced Energy Materials*. 2021.

(3) Ding, Z.; Li, J.; Li, J.; An, C. Review—Interfaces: Key Issue to Be Solved for All Solid-State Lithium Battery Technologies. *J. Electrochem. Soc.* **2020**, *167* (7).

(4) Xiang, Y.; Li, X.; Cheng, Y.; Sun, X.; Yang, Y. Advanced Characterization Techniques for Solid State Lithium Battery Research. *Mater. Today* **2020**, *36*, 139–157.

(5) Frisco, S.; Liu, D. X.; Kumar, A.; Whitacre, J. F.; Love, C. T.; Swider-Lyons, K. E.; Litster, S. Internal Morphologies of Cycled Li-Metal Electrodes Investigated by Nano-Scale Resolution X-Ray Computed Tomography. *ACS Appl. Mater. Interfaces* **2017**, *9* (22).

(6) Zachman, M. J.; Tu, Z.; Choudhury, S.; Archer, L. A.; Kourkoutis, L. F. Cryo-STEM Mapping of Solid–Liquid Interfaces and Dendrites in Lithium-Metal Batteries. *Nature* **2018**, *560* (7718).

(7) Vogel, A.; Venugopalan, V. Mechanisms of Pulsed Laser Ablation of Biological Tissues. *Chemical Reviews*. 2003.

(8) Ravi-Kumar, S.; Lies, B.; Zhang, X.; Lyu, H.; Qin, H. Laser Ablation of Polymers: A Review. *Polymer International*. 2019.

(9) Shirk, M. D.; Molian, P. A. A Review of Ultrashort Pulsed Laser Ablation of Materials. *J. Laser Appl.* **1998**, *10* (1).

(10) Förster, D. J.; Jäggi, B.; Michalowski, A.; Neuenschwander, B. Review on Experimental and Theoretical Investigations of Ultra-Short Pulsed Laser Ablation of Metals with Burst Pulses. *Materials (Basel).* **2021**, *14* (12).

(11) Fazio, E.; Gökce, B.; De Giacomo, A.; Meneghetti, M.; Compagnini, G.; Tommasini, M.; Waag, F.; Lucotti, A.; Zanchi, C. G.; Ossi, P. M.; Dell'aglio, M.; D'urso, L.; Condorelli, M.; Scardaci, V.; Biscaglia, F.; Litti, L.; Gobbo, M.; Gallo, G.; Santoro, M.; Trusso, S.; Neri, F. Nanoparticles Engineering by Pulsed Laser Ablation in Liquids: Concepts and Applications. *Nanomaterials*. 2020.

(12) Echlin, M. P.; Straw, M.; Randolph, S.; Filevich, J.; Pollock, T. M. The TriBeam System: Femtosecond Laser Ablation in Situ SEM. *Materials Characterization*. 2015.

(13) Randolph, S. J.; Filevich, J.; Botman, A.; Gannon, R.; Rue, C.; Straw, M. In Situ Femtosecond Pulse Laser Ablation for Large Volume 3D Analysis in Scanning Electron Microscope Systems. *J. Vac. Sci. Technol. B, Nanotechnol. Microelectron. Mater. Process. Meas. Phenom.* **2018**, *36* (6), 06JB01.

(14) Bonse, J.; Gräf, S. Maxwell Meets Marangoni—A Review of Theories on Laser-Induced Periodic Surface Structures. *Laser and Photonics Reviews*. 2020.

(15) Jungjohann, K.; Long, D.; Gannon, R.; Randolph, S.; Goriparti, S.; Merrill, L.; Harrison, K. Cryo-EM of Li Metal Battery Aging and Failure Mechanisms. *Microsc. Microanal.* **2020**, *26* (S2), 1652–1653.

Chapter XIV

(1) Yoshino, A. The birth of the lithium-ion battery. *Angew. Chem., Int. Ed.* **2012**, *51* (24), 5798-5800.

(2) Yoshino, A.; Sanechika, K.; Nakajima, T. Secondary battery. US 4668595 A, 1987.

(3) Besenhard, J.; Eichinger, G. High energy density lithium cells: Part I. Electrolytes and anodes. *J. Electroanal. Chem. Interfacial Electrochem.* **1976**, *68* (1), 1-18.

(4) Fang, C.; Wang, X.; Meng, Y. S. Key issues hindering a practical lithium-metal anode. *Trends in Chemistry* **2019**, *1* (2), 152-158.

(5) Tikekar, M. D.; Choudhury, S.; Tu, Z.; Archer, L. A. Design principles for electrolytes and interfaces for stable lithium-metal

batteries. *Nature Energy* **2016**, *1* (9), 16114.

(6) Xu, W.; Wang, J.; Ding, F.; Chen, X.; Nasybulin, E.; Zhang, Y.; Zhang, J.-G. Lithium metal anodes for rechargeable batteries. *Energy Environ. Sci.* **2014**, *7* (2), 513-537.

(7) Zhang, X.; Wang, Q. J.; Harrison, K. L.; Jungjohann, K.; Boyce, B. L.; Roberts, S. A.; Attia, P. M.; Harris, S. J. Rethinking how external pressure can suppress dendrites in lithium metal batteries. *J. Electrochem. Soc.* **2019**, *166* (15), A3639.

(8) Monroe, C.; Newman, J. Dendrite growth in lithium/polymer systems: A propagation model for liquid electrolytes under galvanostatic conditions. *J. Electrochem. Soc.* **2003**, *150* (10), A1377.

(9) Wang, H.; Liu, Y.; Li, Y.; Cui, Y. Lithium metal anode materials design: interphase and host. *Electrochemical Energy Reviews* **2019**, *2* (4), 509-517.

(10) Fincher, C. D.; Ojeda, D.; Zhang, Y.; Pharr, G. M.; Pharr, M. Mechanical properties of metallic lithium: from nano to bulk scales. *Acta Mater.* **2020**, *186*, 215-222.

(11) Peled, E.; Golodnitsky, D.; Ardel, G. Advanced model for solid electrolyte interphase electrodes in liquid and polymer electrolytes. *J. Electrochem. Soc.* **1997**, *144* (8), L208-L210.

(12) Frisco, S.; Liu, D. X.; Kumar, A.; Whitacre, J. F.; Love, C. T.; Swider-Lyons, K. E.; Litster, S. Internal Morphologies of Cycled LiMetal Electrodes Investigated by Nano-Scale Resolution X-ray Computed Tomography. *ACS Appl. Mater. Interfaces* **2017**, *9* (22), 18748-18757.

(13) Shearing, P.; Brandon, N.; Gelb, J.; Bradley, R.; Withers, P.; Marquis, A.; Cooper, S.; Harris, S. Multi length scale microstructural investigations of a commercially available Li-ion battery electrode. *J. Electrochem. Soc.* **2012**, *159* (7), A1023.

(14) Zachman, M. J.; Tu, Z.; Choudhury, S.; Archer, L. A.; Kourkoutis, L. F. Cryo-STEM mapping of solid-liquid interfaces and dendrites in lithium-metal batteries. *Nature* **2018**, *560* (7718), 345.

(15) Zhang, X.; Sahraei, E.; Wang, K. Deformation and failure characteristics of four types of lithium-ion battery separators. *J. Power Sources* **2016**, *327*, 693-701.

(16) Qian, J.; Henderson, W. A.; Xu, W.; Bhattacharya, P.; Engelhard, M.; Borodin, O.; Zhang, J.-G. High rate and stable cycling of lithium metal anode. *Nat. Commun.* **2015**, *6*, 6362.

(17) Echlin, M. P.; Straw, M.; Randolph, S.; Filevich, J.; Pollock, T. M. The TriBeam system: Femtosecond laser ablation in situ SEM. *Mater. Charact.* **2015**, *100*, 1-12.

(18) Rahbani, J.; Behzad, A. R.; Khashab, N. M.; Al-Ghoul, M. Characterization of internal structure of hydrated agar and gelatin matrices by cryo-SEM. *Electrophoresis* **2013**, *34* (3), 405-408.

(19) Chen, K.-H.; Wood, K. N.; Kazyak, E.; LePage, W. S.; Davis, A. L.; Sanchez, A. J.; Dasgupta, N. P. Dead lithium: mass transport effects on voltage, capacity, and failure of lithium metal anodes. *J. Mater. Chem. A* **2017**, *5* (23), 11671-11681.

(20) Fang, C.; Li, J.; Zhang, M.; Zhang, Y.; Yang, F.; Lee, J. Z.; Lee, M.-H.; Alvarado, J.; Schroeder, M. A.; Yang, Y.; et al. Quantifying inactive lithium in lithium metal batteries. *Nature* **2019**, *572* (7770), 511-515.

(21) Lu, D.; Shao, Y.; Lozano, T.; Bennett, W. D.; Graff, G. L.; Polzin, B.; Zhang, J.; Engelhard, M. H.; Saenz, N. T.; Henderson, W. A.; et al. Failure mechanism for fast-charged lithium metal batteries with liquid electrolytes. *Adv. Energy Mater.* **2015**, *5* (3), 1400993.

(22) Lin, D.; Liu, Y.; Cui, Y. Reviving the lithium metal anode for high-energy batteries. *Nat. Nanotechnol.* **2017**, *12* (3), 194.

(23) Wang, W.; Hao, F.; Mukherjee, P. P. Mechanistics of LithiumMetal Battery Performance by Separator Architecture Design. *ACS Appl. Mater. Interfaces* **2020**, *12* (1), 556-566.

(24) Kalnaus, S.; Wang, Y.; Turner, J. A. Mechanical behavior and failure mechanisms of Li-ion battery separators. *J. Power Sources* **2017**, *348*, 255-263.

(25) Gor, G. Y.; Cannarella, J.; Leng, C. Z.; Vishnyakov, A.; Arnold, C. B. Swelling and softening of lithium-ion battery separators in electrolyte solvents. *J. Power Sources* **2015**, *294*, 167-172.

(26) Bai, P.; Li, J.; Brushett, F. R.; Bazant, M. Z. Transition of lithium growth mechanisms in liquid electrolytes. *Energy Environ. Sci.* **2016**, *9* (10), 3221-3229